INFORMATION TO USERS

This manuscript has been reproduced from the microfilm master. UMI films the text directly from the original or copy submitted. Thus, some thesis and dissertation copies are in typewriter face, while others may be from any type of computer printer.

The quality of this reproduction is dependent upon the quality of the copy submitted. Broken or indistinct print, colored or poor quality illustrations and photographs, print bleedthrough, substandard margins, and improper alignment can adversely affect reproduction.

In the unlikely event that the author did not send UMI a complete manuscript and there are missing pages, these will be noted. Also, if unauthorized copyright material had to be removed, a note will indicate the deletion.

Oversize materials (e.g., maps, drawings, charts) are reproduced by sectioning the original, beginning at the upper left-hand corner and continuing from left to right in equal sections with small overlaps. Each original is also photographed in one exposure and is included in reduced form at the back of the book.

Photographs included in the original manuscript have been reproduced xerographically in this copy. Higher quality 6" x 9" black and white photographic prints are available for any photographs or illustrations appearing in this copy for an additional charge. Contact UMI directly to order.

UMI

A Bell & Howell Information Company
300 North Zeeb Road, Ann Arbor MI 48106-1346 USA
313/761-4700 800/521-0600

Reproduced with permission of the copyright owner. Further reproduction prohibited without permission.

Spatio-temporal Dynamics Study of Wave Patterns in Binary Fluid Convection

by

SAID SLIMANI

A dissertation submitted to the Graduate Faculty in Engineering
in partial fulfillment of the requirements for the
degree of Doctor of Philosophy, The City University of New York.

1998

UMI Number: 9908364

UMI
300 North Zeeb Road
Ann Arbor, MI 48103

This manuscript has been read and accepted for the Graduate Faculty in Engineering in satisfaction of the dissertation requirement for the degree of Doctor of Philosophy.

5/21/98
Date

Nadine
Chair of Examining Committee

5/22/98
Date

Gerard G. Lowen
Executive Officer

Prof. Andreas Acrivos

Dr. Paul Kolodner

Prof. George Triantafyllou

Prof. Yannis Andreopoulos
Supervisory Committee

THE CITY UNIVERSITY OF NEW YORK

Abstract

Spatio-temporal Dynamics Study of Wave Patterns in Binary Fluid Convection

by

Said Slimani

Advisor: Professor Nadine Aubry

The present thesis is devoted to studying spatio-temporal dynamics of nonlinear traveling waves. We develop theoretical tools using Bi-Orthogonal Decompositions to understand nonlinear interactions between different components of the wave field under consideration. We study the possible evolutions of uniformly traveling wave as a control parameter varies. Two scenarios have been identified: one involving superpositions of uniformly traveling waves and bifurcations, and one consisting of spatio-temporal modulations of the uniformly traveling waves. We have applied such techniques to convection in binary fluid mixtures in an annular cell, a system which exhibits chaotic wave phenomena. More precisely, we have analyzed sets of experimental data and performed a parameter study of this data base. This experiment has the advantage to be performed with extreme precision and stability. We have shown how our (generic) tools provide quantitative characterization of the complexity arising in this system and how the previous scenarios of uniformly traveling wave destabilization take place. We have studied in detail the Counterpropagating Wave Packets regime and modeled the wave patterns through spatio-temporal modulations model, the dynamics of which agreed well.

Contents

List of Tables

List of Figures

Chapter 1

Introduction

In the past several years, the study of spatio-temporal phenomena has been the subject of an enormous amount of scientific activity. The principal reason for this is that these phenomena are of fundamental importance in many physical systems, particularly in turbulence. The understanding of spatio-temporal dynamics will further our insight into turbulence.

Small confined experimental systems are known to exhibit temporal chaos. Classical examples of such systems are Rayleigh-Bénard convection, flow between concentric cylinders, etc. Dynamical systems theory has been developed to deal with such systems, providing universal concepts such as bifurcations, strange attractors, etc. Dynamical systems theory allows the dynamics of complicated behaviors to be embedded in low-dimensional phase spaces and modeled through low-dimensional dynamical systems.

In contrast to confined systems, spatially extended (or infinite) systems allow chaotic behavior to manifest itself in space as well as in time. This spatial complexity gives rise to the notion of spatio-temporal chaos, which adds a new level of difficulty. Spatiotemporal chaos is not rigorously defined, but a definition based upon coherence length ξ seems to be practical. For a system of size L, if, on the one hand, $\xi \approx L$, then the dynamics are correlated throughout the system, and chaos can exist only in the temporal domain. If, on the other hand, $\xi << L$, then the dynamics of different spatial regions are uncorrelated, and spatio-temporal chaos is possible.

Characterization of spatio-temporal chaos was another challenge for understanding these phenomena. For the case of temporal chaos, Lyapunov exponents are used to indicate the divergence of trajectories and permit the study of sensitivity to initial conditions. Other techniques are used to study the topology of attractors such as their dimension, symbolic dynamics, etc. The generalization of these methods to spatio-temporal chaos has not been made.

Other areas of research for the understanding of turbulence and transition to turbulence include the study of the role of 'coherent structures' in the dynamics. However, a definition of such structures is still a subjective issue and is dependent on the observer and the systems observed. In recent literature, there have been several attempts to deal with this problem. One that has attracted much attention is the approach based upon the Karhunen-Loève technique, introduced by Lumley in turbulence. He proposed that a coherent structure is an entity that contains most of the energy in an optimal sense, that is based on a variational principle. This method, based on a statistical approach, has an enormous appetite for data, and the information extracted is only characteristic of second order correlations. The success of this method is due to its ability to describe the apparently chaotic flow of *a priori* high-dimensional phase space, in low-dimensional spaces. This method, although applicable to any flow field, would fail to extract isolated 'coherent structures' such as solitary waves, which undoubtedly represent the most simplistic pattern one can have.

Progress in all these subjects has always advanced through an interplay between theory and experiments. The latter have progressed by improving many aspects, such as parameter control, providing 'clean' data, reducing the influence of boundary conditions and three-dimensional effects, etc. As far as the theory is concerned, many scientist have focused on devising new methods and developing techniques which would be appropriate for the understanding of these phenomena. Their common goal is to provide an understanding of the appearence of complicated behavior as some stress parameters are varied. Under the influence of these variations, systems can undergo several bifurcations before exhibiting spatio-temporal chaos.

There are indeed many experimental systems which undergo a transition from a trivial state to one exhibiting complex spatio-temporal behavior as some parameter is increased through a threshold. These systems typically exhibit increasingly complex spatio-temporal dynamics as the parameter is further increased. Such behavior can be seen in the Faraday experiment, for instance, in which a free surface of a liquid becomes unstable to the appearence of an erratic pattern of capillary waves as the container is vibrated vertically with increasing amplitude. Another example is provided by the experiment on convection in thin, horizontal layers of gas at high pressure, giving rise to "spiral chaos".

In these two experiments and in many others in which spatio-temporal chaos is possible, the systems are three-dimensional and exhibit complex, two- or three-dimensional patterns. In two- as well as three-dimensional systems, data acquisition still presents difficulties, and, even when they are overcome, one has to obtain a large amount of data whose storage and analysis is impractical. However, the situation in one-dimensional systems is more tractable, and the possibility of obtaining large space-time domains conveniently sampled allows one to focus on the spatio-temporal behavior itself.

In this thesis, we deal with some of the aspects of spatio-temporal behavior we have described. We are particularly concerned with nonlinear wave phenomena observed in a one-dimensional experimental system: traveling-wave convection in a binary fluid mixture. Scores of data from this system were kindly provided to us by Dr. P. Kolodner, Bell Laboratories. We develop methods based upon the biorthogonal decompositions recently introduced [4] to resolve some of the previous difficulties such as the characterization of spatio-temporal complexity and the study of the mechanisms of transition. In the remainder of this introduction, we give a few more details regarding the experimental system as well as our theoretical approaches and goals.

1.1 Experimental System

Convection in binary fluid mixtures, usually performed by using either He^3/He^4 or alcohol/water, is interesting and nontrivial. In a binary fluid, the parameters affecting the flow are the ***Rayleigh number*** R, which is the dimensionless temperature difference ΔT, imposed across the fluid layer, and the ***separation ratio*** ψ, which measures the coupling between the temperature and the concentration gradient induced by the Soret effect. The magnitude of the nonlinearity in this system is controlled by varying R and ψ. We are interested in negative values of ψ, for which the system gives rise to an oscillatory instability as R is increased above a critical R_{co}. For increasingly negative ψ, the onset of convection is delayed to higher and higher Rayleigh numbers. Regions of instability in the (R, ψ) plane are shown in Figure 1a. These experiments illustrate a wealth of fascinating traveling wave patterns, ranging from simple uniform traveling waves to space-time chaotic patterns, which exist even near threshold. The series of experiments we focus on lies in the range $0 \geq \psi \geq -0.07$, specifically $\psi = -0.02$. A bifurcation diagram for this case is shown in Figure 1b. The higher curve in Figure 1b corresponds to a convective state where spatially-uniform rolls are stationary or traveling depending on R. For higher values of R, the system undergoes a transition to a spatially uniform state in which steady rolls fill the entire cell; the mixture simply acts like a pure fluid.

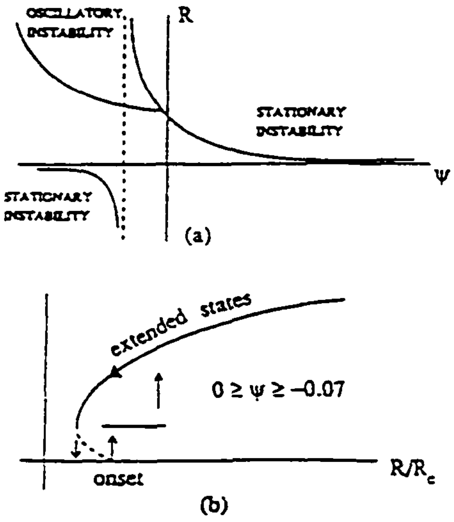

Figure 1.1: Regions of instability (a), Bifurcation diagram (b).

These experiments were first conducted in a rectangular geometry. In this case, the convective state consisted of right- and left-going disturbances which interact by exchanging energy and lead to a blinking state. Cross [21] has used models based upon coupled Ginzburg-Landau (GL) equations and has succeeded in reproducing blinking states. Endwall effects seem to have a dominating role on the dynamics. By using an annular geometry, endwall influences are removed. Yet, time-dependent behavior of right- and left-traveling wave persists. The interaction between both components, left and right, of the wave field yields various patterns ranging from regular or periodic pulses to others dominated by dispersive bursting, leading to an irregular appearance and a sudden collapse of spatially-localized bursts of traveling waves. This behavior was termed ***dispersive chaos*** [34] owing to an analogy with similar behavior seen in the numerical integration of the complex GL equation and attributed to the nonlinear dispersion term.

Convection in binary fluid mixtures was our system of choice because of a number of advantages over other pattern-forming systems. First, it is one-dimensional. As noted above, data-management problems are much easier to handle in one dimension. Second, this particular experiment has been developed into an exceptionally clean system: drifts, nonuniformities, and distortions has been reduced to extremely low levels. Third, the diversity of patterns produced constitute a broad range of input to test the applicability of our methods. This system is thus well adapted for studying some aspects of spatio-temporal nonlinear wave phenomena.

1.2 Theoretical Approaches

Ginzburg-Landau equations. In most spatio-temporal pattern-forming systems, such as the previously described experiments, the Ginzburg-Landau equations emerge as model equations. For some systems, their derivation can be deduced directly from governing (basic laws) equations. For others, this is not a trivial procedure, and one has to rely on symmetry considerations for determining the appropriate coefficients in the equations.

For binary fluid mixtures, it appears that Ginzburg-Landau equations are not quite consistent with the experimental observations and a quantitative comparison is still far from being complete, especially far above onset in strongly nonlinear regimes. Since concentration effects are important, a coupled system of GL and an equation governing the concentration field is emerging as a promising model. Riecke [47] has been able to account, at least semi-quantitatively, for the dynamics seen further above onset.

Statistical analyses such as spectral analysis and probability distribution functions are commonly used. Unfortunately, these methods have limited ability to fully characterize the nonlinear dynamics. A general deficiency of such analyses is that they are basically descriptive and take no particular advantage of the dynamical structure of the system under study. Still, they can be particularly helpful for preliminary data analysis.

Modal expansion. Our viewpoint in dealing with such systems, for which models have not been derived yet, relies on dealing directly with data acquired from the experiment, thus analyzing in a sense the 'solution' itself rather than the evolution equation, and trying to understand the dynamics and the mechanisms of interaction.

Bi-Orthogonal Decompositions (BOD), a deterministic approach to study spatio-temporal dynamics, is based on an integral operator whose kernel is precisely the field under investigation, say a space-time signal $u(x,t)$. The spectral decomposition of the integral operator, noted U, if assumed compact, yields two sets of discrete, orthonormal eigenmodes, one spatial $\{\varphi_n(x),\ n = 1,..\}$ and the other one, temporal $\{\psi_n(t),\ n = 1,..\}$. The space-time function $u(x,t)$ can then be written as a sum of products of these spatial and temporal modes which converges in norm:

$$u(x,t) = \sum_n^N A_n \varphi_n(x) \psi_n(t), \tag{1.1}$$

with

$$A_1 \geq A_2 \geq \ldots \geq A_N > 0.$$

Here, N, the number of non-zero eigenvalues, is known as the *global dimension* of $u(x,t)$.

One advantage of the BOD over other methods such as Fourier or the wavelet transforms resides in the fact that the summation in the relation (1.1) is carried out over one index only. Therefore, related through a one-to-one correspondence, the spatial and temporal modes are such that $U\varphi_n = A_n\psi_n$. Another advantage is that the BOD does not assume *a priori* a given basis; rather, it is extracted, intinsically, from the dynamics under consideration. These modes have the potential of spanning the lowest dimensional spaces called *characteristic spaces.* These characteristic spaces are the best adapted to capture the interesting part of the dynamics and allow 'easy' recognition of any bifurcations occurring as the control parameter is varied. Bifurcations are attributed, generally, to the lack of smoothness, as some parameter is varied, of some quantities, such as the entropy, the energy, etc. The latter are among many other physical quantities which have been defined by the BOD. Additional investigations in the characteristic spaces are usually needed to investigate the occurrence of bifurcations.

Since many complicated behaviors are attributed to broken symmetries, having a method which conveniently represents them to study their effects is highly desirable. The BOD permits a natural introduction of spatio-temporal symmetries. They are introduced through a pair of operators, one acting on the space of spatial functions, the other one acting on the space of temporal functions. Not only do spatio-temporal symmetries play important roles in the transition, but their presence also helps a further characterization of the dynamics in the characteristic spaces. Their role extends to being characteristic of some specific phenomena. For instance, translation symmetries are associated with traveling waves, dilation symmetries are associated with self-similairty, etc. These are some examples of the utilities of the BOD method, and this list is by no means exhaustive. More details will be given later.

On the one hand, our goals in this work include providing a full characterization of the spatiotemporal complexity arising in the experiments on binary fluid convection and understanding the dynamics and structures of the different patterns observed. On the other hand, the tools we used, which were mainly based on biorthogonal decompositions, have to be developed further to accomodate the particularities of the system considered. We have achieved such goals through a combination of theoretical and experimental efforts over a long period of time. For the realization of this work, Dr. P. Kolodner has kindly made available to us scores of data formatted according to our requests.

The organization of this thesis is as follows. The next chapter describes the mathematical formalism of biorthogonal decompositions (BOD). We present new developements especially carried out for the study of wave propagation phenomena.

In Chapter 3, a full study of the experiments on binary fluid convection is presented. We describe the experimental apparatus, and we give a detailed overview of the different dynamical states observed, with an emphasis on those of interest to us. Classical methods are then used to describe the experiments. The BOD method is used to fully characterize those dynamical states. The focus of Chapter 4 is the dynamics and structures of a periodic regime observed just above onset in these experiments, the reason being that the apparent regularity of this state hides many intriguing and nontrivial dynamics.

Because of the large number of figures used, especially in chapters 3 and 4, we append them at the end of each chapter.

Chapter 2

Bi-Orthogonal Decompositions

Introduction

Many dynamical systems tools used in this work are based upon bi-orthogonal decompositions (BOD). These allow us to study the dynamics of spatio-temporal dynamical systems in the smallest linear space and lead to a description of space-time complexity through the analysis of several suitable physical quantities. BOD's can be considered as derived versions of the proper orthogonal decomposition (POD), also known as the Karhunen-Loève (K-L) expansion or the principal component analysis, a well-known classical probability theory tool [42]. Lumley (1967) was the first to introduce the POD in the field of hydrodynamics in an effort to identify 'coherent structures' in a random turbulent flow [44]. For many years, the use of the POD was limited to Lumley and his collaborators, essentially because of the enormous amount of data needed and the belief that the information extracted was characteristic of second order statistics only (the two-point correlation tensor). It is only recently that the fluid mechanics community adapted the method, after the low dimensional study of the boundary layer [7], demonstrating the efficiency of the first few POD modes from a dynamical point of view. The derivation of BOD's for the study of spatio-temporal dynamical systems was then another important step in the history of such methods. While there is some overlap between the POD and BOD's, they are conceptually and fundamentally different: the POD is, by definition, statistical whereas the BOD's concept is deterministic.

However, in all cases, the blindness of such methods regarding both the nature of the data and the systems that produced them made them interdisciplinary techniques used in many fields (e.g. signal analysis, image processing, meteorology, oceanography, compression of data ...).

In this chapter, we introduce both the BOD technique and its properties, and present some new related developments and results. The organization is as follows.

In Section 1, we briefly review the mathematical formalism of the BOD, which is based upon linear operator theory. An operator is thus introduced, the spectral decomposition of which achieves a bi-modal expansion. In Section 2, we discuss how effective the BOD is in dealing with data acquired from systems with imperfections, such as background noise. Also, among other important applications of the BOD are dynamics study and bifurcation analysis. These concepts are reviewed in Sections 3 and 4. A survey of some recent applications of the BOD in many different systems is presented in Section 5. Spatio-temporal symmetries are discussed in Section 6. In Section 7, we start our study of wave propagation phenomena. In this chapter, we restrict ourselves to the case of simple traveling waves; the case of many traveling waves is deferred to the next chapter. We then discuss in Section 8 the problem of degeneracies and quasidegeneracies which are related to symmetry breaking and the choice of the space-time domain. Then, in Section 9, we relate the BOD to the Fourier transform by means of a commutative diagram, which will be helpful for the study of wave propagation phenomena. In Section 10, we deal with the problem of extending signals defined on finite domains to duplicated signals in space-time domain and discuss its effects on the BOD components. In the final section of this chapter, we study the property of asymptotic degeneracy as the time domain tends to infinity and its importance for permitting a quantitative characterization of space-time signals.

2.1 Mathematical Formalism

BOD's decompose space-time functions -or signals- that represent the output from an experimental apparatus (velocity, concentration, temperature, etc ...) or solutions of a nonlinear dynamical system (partial differential equations, coupled map lattices, etc ...). The evolution of such systems may obey complicated laws, sometimes unknown, and it is often difficult to predict or even quantify the resulting complexity. BOD's can be efficiently used for this purpose.

Bi-Orthogonal Decompositions generally refer to any decomposition consisting of expanding a signal $u(x,t)$ into orthogonal spatial modes in a Hilbert space $\mathcal{H}(X)$ ($x \in X$), and orthogonal temporal modes in a Hilbert space $\mathcal{H}(T)$ ($t \in T$). These two sets of modes span two characteristic spaces, a spatial one, $\chi(X)$, and a temporal one, $\chi(T)$, the two being related via an isomorphism. We now present the mathematical formalism of the BOD, which has its foundation in linear operator theory, and the related physical quantities.

2.1.1 Mathematical setting

We will consider a dynamical system whose state is described by a measurable complex-valued function $u = u(x,t)$ in a space $\mathcal{H}(X) \times \mathcal{H}(T)$. In some cases, the space variable, x, and the time variable, t, vary continuously in $\mathbb{R}$ or in some interval of $\mathbb{R}$, and in other cases, x and t will take only discrete values. We denote by X a subset of $\mathbb{R}$ (usually a spatial domain), and T a subset of $\mathbb{R}_+$ (usually a temporal domain). Let us consider $u(x,t)$ which is defined on $X \times T$ ($x \in X$, $t \in T$). The signal $u(x,t)$ is associated with a linear operator U which defines an isomorphism between $\mathcal{H}(X)$ and $\mathcal{H}(T)$ such that:

$$\begin{aligned} & U : \mathcal{H}(X) & \rightarrow & \ \mathcal{H}(T) \\ \forall \varphi \in \mathcal{H}(X), \quad & (U\varphi)(t) & = & \int_X u(x,t)\varphi(x)d\mu(x), \end{aligned}$$

the adjoint operator being

$$\begin{aligned} & U^* : \mathcal{H}(T) & \rightarrow & \ \mathcal{H}(X) \\ \forall \psi \in \mathcal{H}(T), \quad & (U^*\psi)(x) & = & \int_T \overline{u(x,t)}\psi(t)d\tilde{\mu}(t), \end{aligned}$$

where the bar denotes the complex conjugate, and $d\mu(x)$ (resp. $d\tilde{\mu}(t)$) the measure defining the scalar product in $\mathcal{H}(X)$ (resp. $\mathcal{H}(T)$).

The bi-orthogonal decomposition of the signal $u(x,t)$ is achieved by the spectral decomposition of the self-adjoint operator V:

$$V = \begin{pmatrix} 0 & U^* \\ U & 0 \end{pmatrix} \tag{2.1}$$

defined on $\mathcal{H}(X) \oplus \mathcal{H}(T)$. When V is compact, the following theorem establishes the bi-orthogonal decomposition of the signal $u(x,t)$.

Theorem 2.1 *Let $u(x,t)$ be a measurable, square-integrable complex-valued function. There exists a canonical decomposition such that*

$$\begin{aligned} u(x,t) &= \sum_{k=1}^{K} A_k \overline{\varphi_k(x)} \psi_k(t) \\ \textit{with} \quad & A_1 \geq A_2 \geq \ldots > 0, \\ & \lim_{n \to \infty} A_n = 0 \\ \textit{and} \quad & (\varphi_k, \varphi_l) = (\psi_k, \psi_l) = \delta_{k,l}. \end{aligned} \tag{2.2}$$

The sum in (2.2) converges in norm.

PROOF.

The proof is classical in the theory of linear operators. We refer the interested readers to Aubry *et al.* [4]. ∎

We now make some remarks on this important theorem.

Remark 2.2 *Some terminology. The elements of the spatial orthonormal sequence $\{\varphi_i\}_{i=1}^{\infty}$ are called topos, and the elements of the temporal orthonormal sequence $\{\psi_i\}_{i=1}^{\infty}$ are called chronos. Hereafter, we use also 'spatial mode' to refer to a topo and 'temporal mode' to denote a chrono.*

Remark 2.3 *An advantage presented by the BOD over other decompositions, such as the Fourier Transform, is that there is only one summation index in (2.2). This is due to the fact that the spatial modes and the temporal modes are in one-to-one correspondence.*

Remark 2.4 *The bi-modal expansion (2.2) is not unique if degeneracies occur. This simply follows from the fact that the subspace associated with each degenerate eigenvalue is not spanned by a unique basis. This, however, does not affect the BOD since this subspace is unique, has a finite dimension, and the one-to-one correspondence of vectors between these subspaces is preserved.*

Remark 2.5 *The series (2.2) enjoys the property that, for any finite order N, the truncated sequence*

$$u_N(x,t) = \sum_{k=1}^{N} A_k \overline{\varphi_k(x)} \psi_k(t)$$

is the best approximation (in the norm topology) of $u(x,t)$ among all sums of N products of a function of x by a function of t. Furthermore, in doing such truncation an upper bound on the error is given by

$$||u - u_N|| \leq A_{N+1}.$$

Two particular examples of such a decomposition are the two-dimensional Fourier decomposition for plane waves and the proper orthogonal decomposition (POD), when the statistical average is chosen to be the time average. We should, however, mention that the latter is formally statistical and corresponds, in our formalism, to the spectral decomposition of the operator V^2:

$$V^2 = \begin{pmatrix} U^*U & 0 \\ 0 & UU^* \end{pmatrix} \tag{2.3}$$

where U^*U (resp. UU^*) is the operator whose kernel is the spatial two-point correlation (resp. the temporal two-point correlation), hereafter denoted by $\mathcal{R}$ and $\mathcal{L}$ respectively. These correlations are nonnegative operators and define the following endomorphisms.

First, $\mathcal{R}$ is defined as:

$$\begin{aligned} \mathcal{R} : \mathcal{H}(T) &\rightarrow \mathcal{H}(T) \\ \forall \psi \in \mathcal{H}(T), \qquad (\mathcal{R}\psi)(t) &= \int_T r(t,s)\psi(s)ds, \end{aligned}$$

where $r(t,s)$ is the temporal two-point correlation function of $u(x,t)$:

$$r(t,s) = \int_X u(x,t)\overline{u(x,s)}dx. \tag{2.4}$$

This is easy to show by simply considering the action of the operator $\mathcal{R}$ on a function $\psi \in \mathcal{H}(T)$:

$$\begin{aligned}(\mathcal{R}\psi)(t) &= (UU^*\psi)(t)\\ &= \int_X u(x,t)(U^*\psi)(x)dx\\ &= \int_X\int_T u(x,t)\overline{u(x,s)}\psi(s)dxds\\ &= \int_T r(t,s)\psi(s)ds,\end{aligned}$$

the integrals being rearranged using Fubini's theorem.

Second, $\mathcal{L}$ is defined as:

$$\begin{aligned}\mathcal{L}:\mathcal{H}(X) &\to \mathcal{H}(X)\\ \forall\varphi \in \mathcal{H}(X), \qquad (\mathcal{L}\varphi)(x) &= \int_X l(x,y)\varphi(y)dy,\end{aligned}$$

where $l(x,y)$ is the spatial two-point correlation of the operator $\mathcal{L}$. In a similar way, we can show that:

$$l(x,y) = \int_T u(x,t)\overline{u(y,t)}dt. \tag{2.5}$$

The eigenvalue problem that gives the spectral decomposition of V^2 is:

$$\begin{pmatrix} U^*U & 0 \\ 0 & UU^* \end{pmatrix}\begin{pmatrix} \varphi_k \\ \psi_k \end{pmatrix} = A_k^2\begin{pmatrix} \varphi_k \\ \psi_k \end{pmatrix}. \tag{2.6}$$

Solutions of (2.6) are what is referred to as the POD. In contrast, the BOD uses the operator V instead of the correlation operators, the eigenvalue problem reading:

$$\begin{pmatrix} 0 & U^* \\ U & 0 \end{pmatrix}\begin{pmatrix} \varphi_k \\ \psi_k \end{pmatrix} = A_k\begin{pmatrix} \varphi_k \\ \psi_k \end{pmatrix}, \tag{2.7}$$

where two coupled equations have to be solved simultaneously. The eigensolutions of (2.7), the $\{\varphi_k\}_{k=1}^{K}$ and $\{\psi_k\}_{k=1}^{K}$, satisfy the property of being in one-to-one correspondence, the latter being given by either one of the equations in (2.7), for example

$$\psi_k = A_k^{-1} U \varphi_k. \tag{2.8}$$

This is a very special property in the sense that it defines a unique dispersion relation. Furthermore, the eigensolutions of (2.6) are necessarily eigensolutions of (2.7), but the converse is not true.

Remark 2.6 *BOD's have been generalized in Aubry et al. [6] to the case of non-compact operators. This generalization was shown to be useful for theoretical deductions and model derivations to account for certain physical situations, such as the presence of a continuous component in the spectrum, infinite domains and in case where singularities occur. Such a situation may arise, for instance, in fully developed turbulence where the operator does not need to be compact. In these cases, various Hilbert spaces were used. Otherwise,* $\mathcal{L}^2$ *spaces are often more convenient and straightforward to use, especially for data analysis for which they are sufficient.*

Remark 2.7 *It is worth mentioning that higher space-time correlations, auto- as well as cross-correlations, can be also obtained in the BOD formalism.*

We end this subsection by noting that the BOD can be viewed as a transformation to global variables which define (spatial and temporal) phase spaces well-adapted to the signal itself, in which dynamical studies can be easily undertaken.

2.1.2 Measures of Spatio-temporal Complexity

In this section, we introduce BOD related technical tools which provide the basis for our dynamical approach throughout this study. These tools are not only quantitative but also geometric. Their elegance and simplicity lie in the fact that there is no need *a priori* for a model. However, the analysis provided may serve as a prelude for the construction of a model, see Chapter 5.

The method offers several quantities which characterize spatio-temporal behaviors. These quantities are of three kinds: energies, entropies and dimension. Since the information contained in a signal is spatial as well as temporal, the previous quantities ought to be likewise. Also, they may be either spatial or temporal, except the dimension, which is necessarily global, that is, characteristic of both space and time.

The universal character of the BOD makes it applicable to any signal, whether it is ordered or disordered, laminar or turbulent, regular or chaotic. We now introduce the definition of physical quantities and reserve the geometric phase space description essential for dynamical studies and bifurcation analysis for Sections 2.3 and 2.4.

Global quantities

- **Global Energy**

The global energy of the signal is given by:

$$\begin{aligned} E(u) &= \int_X \int_T u(x,t)\overline{u(x,t)}dxdt \\ &= \sum_{k=1}^{K} A_k^2, \end{aligned} \tag{2.9}$$

which can be expressed in term of the operators V, such as

$$E(u) = \frac{1}{2} Tr(V^2),$$

or in terms of the operators U and U^*, such as: $E(u) = Tr(UU^*) = Tr(U^*U)$.

This can be readily checked using the expansion (2.2) and the orthogonality property of the topos and the chronos. From (2.9) we see that each space-time mode, i.e. pair (φ_k, ψ_k), contributes independently to the energy of the signal.

The term 'energy' is rather confusing in many cases. In hydrodynamics, however, the signal is often the velocity field, in which case the global energy does coincide with the kinetic energy.

- **Global Entropy**

First, let us define the relative energy, or the fraction of energy contained in each mode:

$$p_k = \frac{A_k^2}{\sum_{k=1}^{K} A_k^2}. \tag{2.10}$$

The global entropy is then expressed as:

$$H(u) = -\frac{1}{logK} \sum_{k=1}^{K} p_k log p_k. \tag{2.11}$$

This quantity is of great interest as it enables us to first, quantify the full space-time structure of the signal, and second, quantify the complexity of the physical system for that particular value of the control parameter(s) at which the signal was recorded.

We recall that the highest value of $H(u)$ is one, corresponding to a uniform distribution of the energy among all the modes, and the lowest value is zero, corresponding to the case where the whole energy is captured by one mode.

- **Signal Dimension**

The characteristic dimension of the signal is defined as the common dimension of the spaces $\chi(X)$ and $\chi(T)$, these two spaces being related via an isomorphism through the operator U:

$$\begin{pmatrix} 0 & U^* \\ U & 0 \end{pmatrix} \begin{pmatrix} \chi(X) \\ \chi(T) \end{pmatrix} = \begin{pmatrix} \chi(X) \\ \chi(T) \end{pmatrix}.$$

As a consequence of this isomorphism, it follows that

$$\chi(X) = Ker(U)^{\perp} \tag{2.12}$$

$$\chi(T) = Ker(U^*)^{\perp} \tag{2.13}$$

where

$$Ker(U) = \{\varphi \in \mathcal{H}(X) /\ U\varphi = 0\}.$$

(or, equivalently, $\chi(X) \oplus \chi(T) = Ker(V)^{\perp}$.)

As we will see later, this dimension is nothing more than the minimal number of degrees of freedom needed to recover the signal $u(x,t)$: $\chi(X)$ and $\chi(T)$ are the smallest Euclidean spaces which contain the temporal dynamics and the spatial configuration.

The connection between this characteristic dimension, noted $dim(u)$, and other geometric characterizations of the attractor such as the Liapunov dimension, dim_A, was discussed in [4]; these two dimensions are related by the following relation:

$$dim(u) = [dim_A] + 1$$

where $[dim_A]$ refers to the integer part of the Liapunov dimension. The Hausdorff dimension, of which the Liapunov dimension is an upper bound, is therefore related to $dim(u)$ as well.

Other quantities

- **Temporal and Spatial Energies**

We now define two energy quantities, one temporal, the other one spatial. Such quantities are useful to trace, for instance, intermittent and bursting events. The spatial energy indicates the activity at spatial points during the time evolution of the physical system. Likewise, the temporal energy indicates major events occuring during the time evolution.

The temporal energy, denoted as $Es(t)$, is defined as

$$\begin{aligned} Es(t) &= \int_X u(x,t)\overline{u(x,t)}dx \\ &= \sum_{k=1}^{K} A_k^2 |\psi_k(t)|^2. \end{aligned} \tag{2.14}$$

In a similar way, the spatial energy, denoted as $Et(x)$, is defined as

$$\begin{aligned} Et(x) &= \int_T u(x,t)\overline{u(x,t)}dt \\ &= \sum_{k=1}^{K} A_k^2 |\varphi_k(x)|^2. \end{aligned} \tag{2.15}$$

- **Temporal and Spatial Entropies**

A pair of quantities representative of the degree of order of the signal is now presented. One of them is temporal, the other one is spatial. The former indicates the emergence of coherent events in time while the latter represents the degree of order of the spatial component of the signal. It can be useful in evaluating the distribution of disorder in various domains of the flow.

The temporal entropy, $Hs(t)$, is

$$Hs(t) = \frac{1}{logK} \sum_{k=1}^{K} p_k(t) log p_k(t), \tag{2.16}$$

where

$$p_k(t) = \frac{A_k |\psi_k(t)|}{\sum_{k=1}^{K} A_k |\psi_k(t)|}. \tag{2.17}$$

The spatial entropy, $Ht(x)$, is

$$Ht(x) = -\frac{1}{logK} \sum_{k=1}^{K} p_k(x) log p_k(x), \tag{2.18}$$

where

$$p_k(x) = \frac{A_k |\varphi_k(x)|}{\sum_{k=1}^{K} A_k |\varphi_k(x)|}. \tag{2.19}$$

2.2 Characteristic Spaces and Dynamics

In (temporal) dynamical systems theory, one is concerned with global and/or local aspects of the dynamics. For a given dynamical system, the objective is to characterize the geometry of the structure of the orbit. When the dynamical system depends on parameters, one would like to characterize the change of the structure of the orbit as the parameters vary. Such goal can still fit into the BOD's framework. How? Through the alternative of viewing the signal as a vector quantity, rather than a scalar. In this context, the BOD is viewed as a geometrical tool, an important point in bifurcation analysis (see next section). Hence, this viewpoint establishes a connection between the bi-orthogonal decomposition and the underlying dynamical properties of the physical system under consideration. In the following subsections, we review the fundamental points of this approach in some detail.

Characteristic Spaces

The symmetric treatment of the two variables, namely space and time, present in the signal that is analyzed, is an intrinsic property of the BOD and is also enjoyed by any related quantities. This symmetry manifests itself in the following way.

On the one hand, the signal can be considered as the temporal evolution of spatial configurations, written as

$$\forall t \in T, \qquad \xi_t(x) = u(x,t), \quad x \in X. \tag{2.20}$$

As time runs, ξ_t defines a time orbit of the system in the space $\mathcal{H}(X)$. An important property of the BOD is that it permits the localization of the dynamics in a much smaller subspace $\chi(X) \subset \mathcal{H}(X)$ - see the following theorem. More importantly, it is possible to find bounded regions of $\chi(X)$ in which the system spends most of the time. The latter suggests that the density of presence would be an appropriate measure. Indeed, in [4], an estimation of the time spent by the dynamics in a bounded subset of the characteristic space was given.

On the other hand, the signal can be viewed as the spatial variation of the time series, that is

$$\forall x \in X, \qquad \eta_x(t) = u(x,t), \quad t \in T. \tag{2.21}$$

This will enable us to analyze the spatial complexity of the system, as $\eta_x \in \mathcal{H}(T)$ in the temporal configuration space $\chi(T) \subset \mathcal{H}(T)$. This latter contains the time evolution of all local sites.

Theorem 2.8 *$\chi(X)$ is the smallest closed linear subspace of the phase space $\mathcal{H}(X)$, containing all the spatial configurations ξ_t, $t \in T$. Similarly, $\chi(T)$ is the smallest closed linear subspace of $\mathcal{H}(T)$, containing all the time series η_x, $x \in X$.*

PROOF.

First, let us recall that

$$\chi(X) = Ker(U)^{\perp},$$

$$\chi(T) = Ker(U^{*})^{\perp}.$$

Since all topos φ_k are in $\chi(X)$, Theorem 2.1 implies that $\xi_t \in \chi(X)\ \forall t$. Conversely, we want to show that $\chi(X) \subset \{\xi_t\}$ where

$$\{\xi_t\}_{t\in T}^{\perp} \subset \chi(X)^{\perp} = Ker(U).$$

Let us take $\xi \in \mathcal{H}(X)$ and $\xi \in \{\xi_t\}^{\perp}$. Then we can write

$$\begin{aligned}(U\xi)(t) &= \int_X u(x,t)\xi(x)dx \\ &= (\xi_t, \xi)_X \\ &= 0,\end{aligned}$$

Consequently, $\xi \in Ker(U)$, and the theorem follows. The same approach, for symmetry reasons, is used to show that $\eta \in ker(U^{*})$. ■

Dynamics

These characteristic spaces are the smallest spaces containing the dynamics. In addition to being intrinsically related to the signal under consideration, they provide a distinctive tool for dynamics study. Properties of these spaces have some features of the well-known normal forms and manifolds theorems in dynamical systems theory.

On the one hand, the BOD is regarded as a transformation to global variables, thus catching some of the spirit of the normal forms. On the other hand, in view of the optimality of the dimension of the space involved, the dynamics of the system can be therefore confined. Symmetry arguments can be used to further localize the interesting part of the dynamics. Examples of such features are presented below.

2.2.1 Bifurcation Analysis

Bifurcations are changes that may occur in the qualitative structure of solutions for certain parameter values when parameters are varied. While bifurcation analysis for temporal systems can be easily conducted using classical tools, such as the Poincaré section, Lyapunov exponents, .. etc, spatio-temporal systems are generally difficult and are not amenable to such tools. In this section we try to shed some light on how the BOD's tools can be used to track possible bifurcations in spatio-temporally evolving systems. It is also the purpose of this section to discuss generic conditions under which a bifurcation, in the BOD's context, would occur.

Therefore, to perform a bifurcation analysis in the BOD framework, we use the BOD's components that we have recalled above. The lack of smoothness in many quantities such as the entropy and energy as a function of control parameters can be a strong indicator of the occurence of bifurcations, which generally should be supported by other investigations. These include looking into changes in other BOD components: characteristic spaces could be subjected to rotations or a change in their dimension, change of the repartition of energy in the different spatial and temporal modes, just to name a few.

Because the symmetries are suitably represented in the BOD's framework and their effects could extend to the BOD's component, such as the spectrum and the modes, it is therefore efficient to rely on symmetry considerations to track possible bifurcations, since in many cases they occur when symmetry breakings are imminent. This interplay between the presence of space-time symmetries and the occurrence of bifurcations can, in some cases, be used to predict the qualitative nature of solutions which bifurcate at critical parameter values due to symmetry considerations alone. Conversely, the occurrence of a bifurcation may lead to the emergence of new symmetries. The latter are the subject of the next section.

2.3 Spatio-Temporal Symmetries

Several physical systems (the Rayleigh-Bénard system, the Navier-Stokes equations, etc ...) are invariant under different symmetry groups (Euclidean group, scaling group, etc ...). The present section explores the effects of these symmetries on the BOD [5].

As was pointed out in Section 2.3, the introduction of the space/time symmetry concept links the spatial behavior to the temporal one.

The action of a spatio-temporal symmetry, which leaves $u(x,t)$ invariant, requires the dual action of two operators, $(\tilde{S}, S)$, $\tilde{S}$ acting on $\mathcal{H}(T)$ and S acting on $\mathcal{H}(X)$. These operators intertwine the operator U:

$$\tilde{S}U = US. \tag{2.22}$$

Likewise, the adjoint operators $(\tilde{S}^*, S^*)$ satisfy

$$\tilde{S}^*U = US^*. \tag{2.23}$$

These properties can be equivalently written as the commutation of the operator V and the symmetry operator C, defined as

$$C = \begin{pmatrix} S & 0 \\ 0 & \tilde{S} \end{pmatrix}, \tag{2.24}$$

that is,

$$[V, C] = VC - CV = 0.$$

A trivial calculation shows that S is a symmetry of the spatial correlation U^*U and, likewise, $\tilde{S}$ is a symmetry of the temporal correlation UU^*. In a compact form we have

$$[V^2, C] = 0. \tag{2.25}$$

Corollary 2.9 *The relation (2.25) implies that characteristic spaces, $\chi(X)$ and $\chi(T)$, are invariant under the action of S and $\tilde{S}$, respectively.*

PROOF

The characteristic space $\chi(X)$ (resp. $\chi(T)$) spanned by the sequence $\{\varphi_i\}_{i=1}^K$ (resp. $\{\psi_i\}_{i=1}^K$) is invariant under the action of the symmetry operator S (resp. $\tilde{S}$). In order to show this corollary, it suffices to note that if φ (resp. ψ) is a topo (resp. a chrono) associated with the eigenvalue A, then $S\varphi$ (resp. $\tilde{S}\psi$) is also a topo (resp. a chrono) associated with the same eigenvalue. ■

Therefore, the presence of degeneracies could be used to detect symmetries that may not be explicit in the signal under consideration.

2.4 BOD Applications

In this section, we survey some spatio-temporal systems to which the BOD was applied.

- **Coupled Map Lattices**

Coupled map lattices (CML) have been proposed as models for space-time complexity. The dynamics of CML was studied in one-dimensional lattice defined by a chain of maps with diffusive coupling [41, 4].

The spatial configuration of the system is described by the set u_i, $0 < i \leq L$ and $u_i \in [0, 1]$. The dynamics is defined as

$$u_i^{t+1} = (1 - \epsilon) f(u_i^t) + \frac{\epsilon}{2}(f(u_{i-1}^t) + f(u_{i+1}^t)), \tag{2.26}$$

ϵ is the coupling parameter, $0 \leq \epsilon \leq 1$, t is the discrete time, and f is a nonlinear map, taken here as the logistic map

$$f(x) = ax(1 - x). \tag{2.27}$$

A characteristic behavior of these spatially extended systems is the coexistence of different dynamical regimes. In Refs [41, 4] dynamics study was carried out using BOD techniques. The study focussed on two different values of the parameter a where chaotic behavior was exhibited. In both cases, a stable fixed point occurs between two values of ϵ, $\epsilon_1(a) < \epsilon < \epsilon_2(a)$. At $\epsilon = \epsilon_2(a)$, a Hopf bifurcation occurs. These bifurcations were carefully studied by means of symmetry and characteristic spaces, $\chi(X)$ and $\chi(T)$. The Hopf bifurcation was clearly indicated by the presence of a limit cycle lying in two-dimensional characteristic spaces. Taking advantage of the BOD, $u_i(t)$ can be written as

$$u_i(t) = \sum_{k=1,2} \alpha_k \phi_k(i) \psi_k(t), \tag{2.28}$$

This simplified expansion enabled the authors to follow the position of the space $\chi_\epsilon(X)$ inside $L^2(X)$. The authors were also able to study the growing complexity of the dynamics in these spaces.

- **Kuramoto-Sivashinsky Equation**

The Kuramoto-Sivashinsky equation (KSE), which has been the subject of many studies, was analyzed by the BOD [40]. It reads

$$\frac{\partial u}{\partial t} + 4\frac{\partial^4 u}{\partial x^4} + \alpha\left(\frac{\partial^2 u}{\partial x^2} + \frac{1}{2}\left(\frac{\partial u}{\partial x}\right)^2\right) = 0; \quad 0 \le x \le 2\pi. \qquad (2.29)$$

It was derived as an amplitude equation for a variety of physical problems. It is known to exhibit various bifurcations and solutions with space-time complexity. An example of complexity that arises in this dynamical system was attributed to the breaking of space-time symmetries. First, at some value of α, a stable fixed point occurs. Then, as α is further increased, a bifurcation to traveling waves was seen to occur, after which the symmetry breaks, and then a spatio-temporal complex regime follows.

The study of space-time symmetries as α is varied suggests their important role in the route to spatio-temporal complexity and proved very useful in studying the spatial and temporal structure of the attractor.

- **Turbulent Wake Flow**

Recently, BOD techniques were also applied to the turbulent wake flow problem [16]. The complexity of the structures is seen to increase considerably as the Reynolds number, the only control parameter of the problem, is increased to high values. Although many experiments and numerical computations were conducted in different Reynolds number regimes, there has not been a complete understanding of large-scale motion and space-time symmetries. In this regard, BOD has been used to further some understanding of the mechanisms governing the routes to turbulence as well as the spatio-temporal structures involved.

For low Reynolds numbers, space-time symmetries were used to characterize the primary instability (Karman vortex street) seen in numerical computation of two-dimensional Naviers-Stokes equations for the wake behind a cylinder. Reflection symmetry was characteristic of the chronos and topos.

2.5 Traveling Waves

The role played by traveling waves (TW), particularly spatially localized solitary waves is well-known in the transition to spatio-temporal complexity. Solitons, which have been observed in nonlinear differential equations modeling physical phenomena such as the Korteweg-De-Vries equation and the nonlinear Shrödinger equation [53], can break down and lead to turbulence (Moon, 1991). In the transition process, the TW first formed often bifurcates into a more complex solution consisting of several waves with various speeds and amplitudes, interacting nonlinearly with each other. Recently, a method for identifying the speeds of the various traveling features has been presented, based on the Fourier transform [45].

Bi-orthogonal decompositions of superpositions of patterns traveling at various speeds and exhibiting different amplitudes will be studied in the upcoming chapter. Of particular interest in the following is the study of a simple traveling wave in the BOD framework. We study the breaking of spatio-temporal symmetries associated with the presence of traveling wave in an arbitrary domain.

2.5.1 Definition

First, let us define a pure traveling wave.

Definition 2.10 *A traveling wave of a speed c is defined as*

$$u(x - x_0, t) = u(x, t + t_0), \tag{2.30}$$

$\forall x, x_0 \in X, t, t_0 \in T$ *such that* $x_0 + ct_0 = 0$.

Proposition 2.11 $u(x,t)$ *is a pure traveling wave of the form (2.30) if and only if it can be equivalently written as*

$$u(x,t) = f(x - ct). \tag{2.31}$$

PROOF

The necessary condition can be shown readily by a simple transformation. If we put

$$f(z) = u(z, 0),$$

and by means of the following change of variables,

$$\begin{cases} x = y \\ t = 0 \\ t_0 = s \Rightarrow x_0 = cs \end{cases}$$

we obtain

$$u(y - cs, 0) = u(y, s) = f(y - cs).$$

The converse is even simpler: it suffices to write f as

$$u(x, t) = f(x - ct).$$

■

2.5.2 Translation Symmetries

We now apply the properties of symmetries that we have recalled above (see section 2.3) to the case of spatio-temporal translations symmetries.

Definition 2.12 *We define the spatial translation operator S_{x_0} defined on $\mathcal{H}(X)$ by*

$$(S_{x_0}\varphi)(x) = \varphi(x - x_0).$$

Definition 2.13 *The temporal translation operator $\tilde{S}_{t_0}$ defined on $\mathcal{H}(T)$ is given by*

$$(\tilde{S}_{t_0}\psi)(t) = \psi(t - t_0).$$

The following theorem characterizes the symmetry of the structures of the BOD [5].

Theorem 2.14 *Let $u(x, t)$ be a signal, U the associated operator. The following statements are equivalent.*

(i) $u(x, t)$ is a simple traveling wave in the sense of Definition 2.10.

(ii) $u(x,t)$ satisfies the symmetry relation

$$US_{x_o} = \tilde{S}_{t_o}U, \ \forall x_o, t_o \ \text{such that} \ x_o + ct_o = 0. \tag{2.32}$$

(iii) the bi-orthogonal structures are degenerate with respect to the group of translations; that is,

$$\text{if } U\varphi = A\psi \text{ then } US_{x_o}\varphi = A\tilde{S}_{t_o}\psi, \ \text{with} \ x_o + ct_o = 0. \tag{2.33}$$

PROOF

The first and second statements are equivalent. This is a direct implication of Definition 2.10.

Using Corollary 2.9, the third statement is a straightforward implication of the second statement.

The converse can be shown as follows. The third statement implies that $Ker(U) = Ker(U^*U)$ is invariant under the action of S_{x_o}, and thus (2.32) is satisfied when it is restricted to $Ker(U)$. The orthogonal of $Ker(U)$, namely $\chi(X)$, is spanned by the topos. Then, the relation (2.32) for each topos $\varphi \in \chi(X)$ results directly from (2.33). ■

Remark 2.15 *It is worthwhile reminding the reader that the definition of a traveling wave (2.30) and Theorem 2.14 are valid only if the spatio-temporal domain is infinite. For finite domains, for (2.30) and Theorem 2.14 to hold, $u(x,t)$ must be supplemented with spatial periodicity, that is*

$$u(0,t) = u(L,t), \quad \forall t \in T,$$

where 0 and L are the limiting boundaries of X.

2.6 Degeneracy and Quasidegeneracy

2.6.1 Degeneracy for TW

For the sake of simplicity, we now restrict ourselves to the case of spatially and temporally periodic signals defined on finite domains. Indeed, in this case, spatial (resp. temporal) Fourier functions are in $\mathcal{L}^2(X)$ (resp. in $\mathcal{L}^2(T)$). Thus the case of continuum spectrum does not arise in the discussion.

Proposition 2.16 *Let $u(x,t)$ be a signal. If $u(x,t)$ is a simple traveling wave then biorthogonal modes are Fourier modes, and the associated spectrum presents a degeneracy of at least a multiplicity of two.*

PROOF

Using the condition (ii) of Theorem 2.14, we can conclude that all the spatial and temporal modes are Fourier modes, since they have to satisfy the symmetry relation.

The degeneracy is shown as follows.

Condition (iii) of Theorem 2.14 implies that each space is invariant under the action of translation operators S_{x_o} in $\chi(X)$ and translation operators $\tilde{S}_{t_o}$ in $\chi(T)$. Since each topo φ_k (resp. chrono ψ_k) is a Fourier mode, then there exists at least one x_o (resp. t_o) such that $S_{x_o}\varphi_k \neq \varphi_k$ (resp. $\tilde{S}_{t_o}\psi_k \neq \psi_k$), and thus the space is at least of dimension two. ■

We should mention that, for the case of simple traveling waves, spatial correlation functions are homogeneous, and temporal correlation functions are stationary. These facts can also be used to show the proposition 2.16.

Remark 2.17

The reader might think that the converse of the proposition is true, namely that if the biorthogonal modes are Fourier modes and the spectrum has a degeneracy of order two, then the signal would describe a simple traveling wave. The following example shows that it is not the case. Let us consider the signal $u(x,t)$ given by

$$u(x,t) = cosxsint + sinxcost + cos2xsin3t + sin2xcos3t$$

For a convenient spatio-temporal domain, functions can be made orthogonal and normalized. The above signal has indeed a degeneracy of order 4 and Fourier modes as topos and chronos. However, the signal does not represent a simple traveling wave.

Remark 2.18

In addition to the degeneracy and the fact that the biorthogonal modes are Fourier modes, the property of being a simple traveling wave imposes a constant ratio of the rotation number in each eigenspace.

2.6.2 High order degeneracies

In the absence of other symmetries, the order two degeneracy in the proposition 2.16 is generic for a traveling wave. However, high order degeneracies may occur. In the following we discuss the dilation symmetry, which is used to characterize self-similarity. However, it is not sufficient to have higher order degeneracy, say of order 4, as shown in the following example. Let $u(x,t)$ be a signal defined by

$$u(x,t) = cosxsint + sinxcost + cos\lambda xsin\lambda t + sin\lambda xcos\lambda t$$

In order to have a sufficient condition, spatial and temporal characteristic spaces ought to be invariant under the action of a one parameter dilation symmetry group i.e.

$$\begin{aligned} D_\lambda \chi(X) &= \chi(X) & (2.34) \\ \tilde{D}_\lambda \chi(T) &= \chi(T). & (2.35) \end{aligned}$$

where the operator D_λ is defined from $\mathcal{L}^2(X)$ to $\mathcal{L}^2(X)$, by

$$(D_\lambda \phi)(x) = \frac{1}{\sqrt{\lambda}} \phi(\lambda^{-1}x). \tag{2.36}$$

2.6.3 Signal with non-zero averages

If the signal has a non-zero temporal average (resp. non-zero spatial average), then among the temporal (resp. spatial) bi-orthogonal modes one is a constant being the temporal (resp. spatial) average of the signal if and only if the associated temporal mode (resp. spatial mode) is the only non-zero mode (see [5], Theorem 2.3).

The importance of breaking this symmetry for the bi-orthogonal decomposition is illustrated by the following example.

2.6.4 Temporal period

We consider a simple traveling wave of the type (2.31), which is localized in space, see Figure 2.2.

As illustrated in Figure 2.3, the spectrum presents degeneracies of multiplicity two as well as quasidegeneracies, that is pairs of closed eigenvalues. The simultaneous degeneracies appear to occur at regular intervals. Thus, we have the following definition:

Definition 2.19 *T_p is defined as the smallest temporal domain for which a total degeneracy occurs, namely all the eigenvalues have simultaneously a multiplicity of order two.*

Lemma 2.20 *Let $u(x,t)$ be a simple traveling wave defined on a spatially periodic domain. The spectrum presents total degeneracy for $nT_p, \forall n \in I\!N$ if and only if we have:*

$$u(x,t) = u(x, t + T_p); \; \forall (x,t) \in X \times T,$$

namely T_p coincides with the temporal period of the signal.

PROOF

If T_p represents the temporal period of the signal $u(x,t)$, then the property (2.33) of Theorem 2.14, shows that each eigenvalue has mutiplicity two: its corresponding eigenspace is two dimensional.

Conversely, let L_p be the period of the spatial domain. Then, the function f of Proposition 2.11 is also periodic of period L_p. We then have

$$\begin{aligned} u(x,t) &= f(x - ct) && (2.37)\\ &= f(x - ct - L_p) && (2.38)\\ &= u(x, t + \frac{L_p}{c}) && (2.39) \end{aligned}$$

Performing the BOD in a domain $L_p \times T_p$ and considering a degenerate subspace, spanned by Fourier modes of the same wave number k and same frequencies ω, the orthogonality of both topos and both chronos imposes that

$$L_p = cT_p \tag{2.40}$$

and thus

$$u(x,t) = u(x, t + T_p). \tag{2.41}$$

■

Remark 2.21

Often, signals acquired from experiments or simulations may present temporal periods which are generally not known a priori. The above Lemma allows us to know if such periods exist. It is done by computing the running spectrum of the signal $u(x,t)$ *and checking for enventual total degeneracies.*

Moreover, the spectrum is totally degenerate each time the domain of $u(x,t)$ is of the form $qL_p \times pL_p$ où $p, q \in \mathbb{N}^*$.

If the temporal interval is of the form $T \neq nT_p$, then the eigenvalues are quasidegenerate. This quasi-degeneracy seems to fade away as we increase the temporal domain and eventually leads to an asymtotic degeneracy. The proof of this important property is deferred to the last section in this chapter, because some results related to the concept of *unfolding*, discussed in section 2.8, will be needed. We should mention that the eigenvectors associated with the quasi-degenerate eigenvalues will no longer enjoy translation symmetries.

2.7 Commutative Diagram

It is very useful to broaden our perspective of spatio-temporal symmetries from the standpoint of the Fourier transform, particularly because both approaches can lead, in some specific cases, to the same description. Recall for instance the case of a homogeneous correlation function, for which the BOD yields precisely Fourier modes. We now focus on the symmetry relation in the case of a traveling wave. In this situation, we give the corresponding symmetry relation in Fourier space and draw a commutative diagram illustrating the relation between both decompositions.

The spatial Fourier transform pair is defined on the space $\mathcal{L}^2(X)$ to $\mathcal{L}^2(K)$ by:

$$\tilde{\phi}(k) = \frac{1}{2\pi}\int_{-\infty}^{+\infty} \phi(x) exp(ikx)dx, \tag{2.42}$$

and its inverse, from $\mathcal{L}^2(K)$ to $\mathcal{L}^2(X)$, by

$$\phi(x) = \int_{-\infty}^{+\infty} \tilde{\phi}(x) exp(-ikx)dk, \tag{2.43}$$

The temporal Fourier transform, defined from $\mathcal{L}^2(T)$ to $\mathcal{L}^2(\Omega)$, is given by

$$\tilde{\psi}(\omega) = \frac{1}{2\pi}\int_{-\infty}^{+\infty} \psi(t) exp(-i\omega t) dt,$$

and its inverse, from $\mathcal{L}^2(\Omega)$ to $\mathcal{L}^2(T)$, by

$$\psi(t) = \int_{-\infty}^{+\infty} \tilde{\psi}(\omega) exp(i\omega t) d\omega.$$

Consequently, we associate unitary operators to the spatial and temporal Fourier transforms as follows:

$$\mathcal{F} : \mathcal{L}^2(X) \longrightarrow \mathcal{L}^2(K)$$

$$\mathcal{G} : \mathcal{L}^2(T) \longrightarrow \mathcal{L}^2(\Omega)$$

Definition 2.22 *We define $\widehat{u}(k,\omega)$ as the Fourier transform (spatial and temporal) of $u(x,t)$. $\widehat{u}(k,\omega)$ defines a linear operator $\widehat{U}: \mathcal{L}^2(K) \to \mathcal{L}^2(\Omega)$ in the same way as $u(x,t)$ in the physical space defines U.*

Proposition 2.23 *The operator $\widehat{U}$ can be expressed in terms of the operators $\mathcal{F}, U$ and $\mathcal{G}$ in the following way:*

$$\widehat{U} = \mathcal{G} U \mathcal{F}^{-1}. \tag{2.44}$$

PROOF

The relation (2.44) is always true, and we have the following commutation diagram

$$\begin{tikzcd} \mathcal{L}^2(X) \arrow[r, "\mathcal{F}"] \arrow[d, "U"] & \mathcal{L}^2(K) \arrow[d, "\widehat{U}"] \\ \mathcal{L}^2(T) \arrow[r, "\mathcal{G}"] & \mathcal{L}^2(\Omega) \end{tikzcd} \tag{2.45}$$

In order to show the proposition, it suffices to rewrite both sides of the equation (2.44) applied to a function $\hat{\varphi}(k)$. The right-hand side becomes:

$$
\begin{aligned}
[\mathcal{G}U\mathcal{F}^{-1}\hat{\varphi}](\omega) &= \int_T e^{i\omega t}[U\mathcal{F}^{-1}\hat{\varphi}](t)dt \\
&= \int_T e^{i\omega t}\int_X u(x,t)[\mathcal{F}^{-1}\hat{\varphi}](x)dxdt \\
&= \int_{\hat{X}}\int_T\int_X e^{i(\omega t-kx)}u(x,t)dxdt\ \hat{\varphi}(k)dk \\
&= \int_{\hat{X}}\hat{u}(k,\omega)\hat{\varphi}(k)dk \\
&= (\hat{U}\hat{\varphi})(\omega).
\end{aligned}
$$

■

Definition 2.24 *We define the pair of operators* $(\tilde{R}_{t_o}, R_{x_o})$ *through the following relations:*

$$(R_{x_o}\hat{\varphi})(k) = e^{ikx_o}\hat{\varphi}(k) \tag{2.46}$$

$$(\tilde{R}_{t_o}\tilde{\psi})(\omega) = e^{i\omega t_o}\tilde{\psi}(\omega) \tag{2.47}$$

Lemma 2.25 $u(x,t)$ *is a simple traveling wave traveling with the speed c if and only if:*

$$\hat{U}R_{x_o} = \tilde{R}_{t_o}\hat{U} \quad \text{for all } (x_o,t_o) \text{ such that } x_o = ct_o. \tag{2.48}$$

Remark 2.26 *Notice that the operators* $\tilde{R}_{t_o}$ *and* R_{x_o} *are unitary; therefore we have*

$$R^*_{x_o} = R_{-x_o} = R^{-1}_{x_o},$$

$$\tilde{R}^*_{t_o} = \tilde{R}_{-t_o} = \tilde{R}^{-1}_{t_o}.$$

As a consequence of Lemma 2.25, we have the following commutative diagram:

$$\begin{tikzcd}
\mathcal{L}^2(X) \arrow[r, "\mathcal{F}"] \arrow[d, "S_{x_o}"] & \mathcal{L}^2(K) \arrow[d, "R_{x_o}"] \\
\mathcal{L}^2(X) \arrow[r, "\mathcal{F}"] \arrow[d, "U"] & \mathcal{L}^2(K) \arrow[d, "\widehat{U}"] \\
\mathcal{L}^2(T) \arrow[r, "\mathcal{G}"] \arrow[d, "\tilde{S}_{t_o}^{-1}"] & \mathcal{L}^2(\Omega) \arrow[d, "\tilde{R}_{t_o}^{-1}"] \\
\mathcal{L}^2(T) \arrow[r, "\mathcal{G}"] & \mathcal{L}^2(\Omega)
\end{tikzcd} \tag{2.49}$$

PROOF OF LEMMA 2.25.

It suffices to explicitly write both sides of the relation (2.48). The left hand side gives

$$\begin{aligned}
(\widehat{U} R_{x_o} \tilde{\varphi})(\omega) &= \int \widehat{u}(k,\omega) R_{x_o} \tilde{\varphi}(k) dk \\
&= \int \widehat{u}(k,\omega) e^{ikx_o} \tilde{\varphi}(k) dk,
\end{aligned}$$

while the right hand side reads

$$\begin{aligned}
(\tilde{R}_{t_o} \widehat{U} \tilde{\varphi})(\omega) &= e^{i\omega t_o} \widehat{U} \tilde{\varphi}(\omega) \\
&= e^{i\omega t_o} \int \widehat{u}(k,\omega) \tilde{\varphi}(k) dk \\
&= e^{i\omega \frac{x_o}{c}} \int \widehat{u}(k,\omega) \tilde{\varphi}(k) dk.
\end{aligned}$$

Identifying the kernels of the integrals of both sides, we get

$$\forall \omega, \forall k \quad e^{i\omega \frac{x_o}{c}} \widehat{u}(k,\omega) = e^{ikx_o} \widehat{u}(k,\omega). \tag{2.50}$$

Hence, only two cases are possible for (2.50) to hold:

- If $\omega = ck$, then $\widehat{u}(k,\omega)$ is an arbitrary function.
- If $\omega \neq ck$, then $\widehat{u}(k,\omega)$ must be zero.

Therefore, we get the following well-known result: the support of $\widehat{u}(k,\omega)$ is a straight line in the (k,ω) plane. This line is called a *spoke* (Figure 2.1).

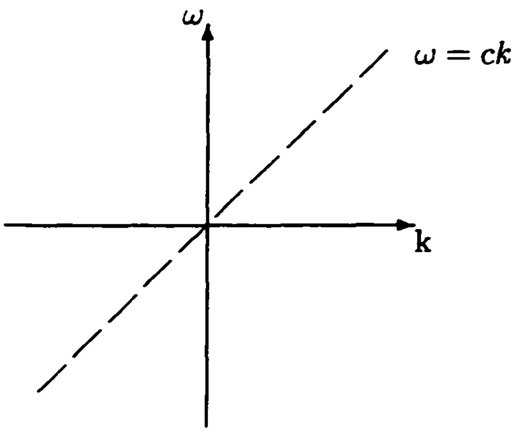

Figure 2.1: Radial spoke, linear dispersion relation

This could be expressed alternately as follows

$$\hat{u}(k,\omega) = \tilde{u}(k)\delta(\omega - ck). \tag{2.51}$$

where the inverse Fourier transform of $\tilde{u}(k)$ determines the shape of the TW in physical space. ∎

2.8 Unfoldings and the BOD

In the numerical implementation of the BOD, one deals often with signals acquired from experimental devices or produced by numerical computations, and, thus, are of finite spatial and temporal domains.

However, in the case where the physical system that produces signal is not spatially confined and temporally finite, physical considerations have to be taken to choose a convenient space-time window. Generally, this choice can be dictated by many factors, such as the geometry of the system, symmetry considerations, etc ... For instance, the experiment on binary fluid convection performed in annular geometry possesses a natural spatial periodicity. Likewise, the time domain depends on many factors as well, such as the physical process, the state of the system, etc ... Thus, if the system is in a chaotic state, it is generally not obvious to estimate the time of observation, especially if no attractor is known for the system. In such a case, a criterion for an estimate of the time interval is presented below which is based upon the variation of the global entropy, Hu with respect to the running time interval.

In the present section, however, we focus on studying how to extend signals defined on finite domains, not necessarily periodic, to even larger domains through spatio-temporal unfoldings. This problem is of relevance to us because it is important to distinguish which of the effects seen in BOD components is related to the physical phenomenon.

A signal can be represented by either one of the operators, its associated operator V, the spatial correlation operator, or the temporal correlation operator. Without loss of generality, we will use the spatial correlation which we denote by $\mathcal{A}$. Its associated dimension is d.

Two cases of unfoldings are of interest to us. The first case corresponds to unfoldings in space-time domain. In the second case, we deal with an unfolding performed only diagonally in the space-time domain.

2.8.1 Unfoldings of type I

We consider an extended signal constructed through an unfolding of a signal originally defined on a domain $D = L \times T$.

Some notations:

We denote by $U_{p,q}$ the operator associated with the unfolded signal $u(x,t)$, defined on the domain $pL \times qT$, namely, a signal duplicated p times in space and q times in time.

We denote by $\vec{e_i}$ the i^{th} element of the canonical base of $\mathbb{R}^p$:

$$\vec{e_i} = \begin{pmatrix} 0 \\ \vdots \\ 1 \\ \vdots \\ 0 \end{pmatrix},$$

where 1 is placed at the i^{th} position.

Proposition 2.27 *In terms of the correlation operator $\mathcal{A}$ associated with U, the correlation operator of the unfolded signal is expressed as follows:*

$$\tilde{\mathcal{A}} = q \overbrace{\begin{pmatrix} \mathcal{A} & \dots & \mathcal{A} \\ \vdots & \ddots & \vdots \\ \mathcal{A} & \dots & \mathcal{A} \end{pmatrix}}^{p \text{ times}}$$

where we have assumed that an unfolding of p times in space and q times in time was carried out. The matrix $\tilde{\mathcal{A}}$ is a block matrix.

PROOF

The correlation matrix, $\tilde{\mathcal{A}}$ associated with the operator $U_{p,q}$, corresponding to the extended signal, is obtained by a simple expansion. ∎

We now construct an isomorphism, denoted by Φ, between $\mathcal{H} \otimes \mathcal{L}^2(\mathbb{R}^n)$ and $\mathcal{L}^2(\mathbb{R}^{nd})$ in the following manner.

We define by $\mathcal{W}$ the square matrix of order p with all elements being unity

$$\mathcal{W} = \begin{pmatrix} 1 & \dots & 1 \\ \vdots & \ddots & \vdots \\ 1 & \dots & 1 \end{pmatrix}.$$

Thus, we have the following conjugate diagram

$$\begin{tikzcd} \mathcal{H} \otimes \mathcal{L}^2(\mathbb{R}^n) \arrow[r, "\Phi"] \arrow[d, "(\mathcal{A}\otimes\mathcal{W})"] & \mathcal{L}^2(\mathbb{R}^{nd}) \arrow[d, "\tilde{\mathcal{A}}"] \\ \mathcal{H} \otimes \mathcal{L}^2(\mathbb{R}^n) \arrow[r, "\Phi"] & \mathcal{L}^2(\mathbb{R}^{nd}) \end{tikzcd}$$

that is,

$$\Phi[\mathcal{A} \otimes \mathcal{W}]\Phi^{-1} \equiv \tilde{\mathcal{A}}. \tag{2.52}$$

Proposition 2.28 *If $\lambda_1 > .. > \lambda_i > .. > \lambda_d$ represent the associated spectrum of the operator U, then the spectrum of the unfolding $U_{p,q}$ is given by*

$$\begin{cases} \tilde{\lambda}_i = \sqrt{pq}\lambda_i, & \text{for } 1 \le i \le d, \\ 0, & \text{degenerate } (n-1)d \text{ times.} \end{cases}$$

If φ_i (resp. ψ_i) a BOD spatial mode (resp. a BOD temporal mode) of U associated with λ_i, then $\varphi_i \otimes \bigoplus_{j=1}^{n} e_j$, (resp. $\psi_i \otimes \bigoplus_{j=1}^{n} e_j$,) represents the spatial mode (resp. the temporal mode) of $U_{p,q}$ associated with the eigenvalue $\tilde{\lambda}_i$.

PROOF

Due to the isomorphism (2.52), the BOD components of $U_{p,q}$ are obtained from those of $\mathcal{A} \otimes \mathcal{W}$.

The eigenvalues of $\mathcal{A}$ are denoted λ_i^2, the associated eigenvectors associated with them are the φ_i's and the ψ_i's. The matrix $\mathcal{W}$ possesses two eigenvalues, namely p and 0, 0 being degenerated $(p-1)$ times. The eigenvector associated with the nonzero eigenvalue, p, reads:

$$\vec{\omega}_p = \bigoplus_{j=1}^{p} \vec{e}_j. \tag{2.53}$$

Thus, we obtain the eigenvalues and the eigenmodes associated with $\mathcal{A} \otimes \mathcal{W}$:

$$\tilde{\lambda}_i^2 = pq\lambda_i^2, \quad \vec{\omega}_p = \bigoplus_{j=1}^{p} \vec{e}_j, \; for\ i = 1, .., d. \tag{2.54}$$

In consequence, one obtains for $U_{p,q}$:

$$\tilde{\lambda}_i = \sqrt{pq}\lambda_i, \quad \vec{\omega}_p = \bigoplus_{j=1}^{p} \vec{e}_j, \; for\ i = 1, .., d. \tag{2.55}$$

■

Remark 2.29 *It is interesting to note that the projector P_p associated with the eigenvalue p of $\mathcal{W}$ projects onto the diagonal.*

The associated projector with zero eigenvalue, noted P_0, projects onto the kernel of $\tilde{A}$ and the modes corresponding to the zero eigenvalue are not relevant to the BOD analysis.

2.8.2 Unfoldings of type II

In this type of unfolding, one performs a duplication on the diagonal. The unfolded signal, noted U_n, where n is the number of unfoldings performed. The correlation matrix associated with the operator U_n is given by

$$\bar{\mathcal{A}} = \overbrace{\begin{pmatrix} \mathcal{A} & 0 & \dots & 0 \\ 0 & \mathcal{A} & \dots & 0 \\ \vdots & & \ddots & \vdots \\ 0 & 0 & \dots & \mathcal{A} \end{pmatrix}}^{n \ fois}$$

In this case $\mathcal{W}$ is simply the identity matrix:

$$\mathcal{W} = \mathbb{1}_n.$$

Proposition 2.30 *If $\lambda_1 > .. > \lambda_i > .. > \lambda_d$ represent the spectrum associated with the operator U, then the unfoldings of U_n is given by*

$$\bar{\lambda}_i = \lambda_i, \ \ for \ i = 1, .., d,$$

where each of the eigenvalues is n-fold degenerate n.

If φ_i (resp. ψ_i) is a BOD spatial mode (resp. a BOD temporal mode) of U associated with λ_i, then $\varphi_i \otimes e_j, j = 1, .., n$ (resp. $\psi_i \otimes e_j, j = 1, .., n$) represent the spatial modes (resp. temporal modes) which span the spatial (resp. temporal) eigenspace associated with the eigenvalue $\bar{\lambda}_i$.

Proof.

The proof is similar to the previous one, *i.e.* that of Proposition 2.28. The matrix $\mathcal{W}$ is the identity and thus we have only one eigenvalue, 1, degenerate n times. The corresponding eigenvectors are simply the elements of the canonical base of $\mathbb{R}^p$. Therefore, the eigenvalues and eigenvectors of the operator U_n are

$$\bar{\lambda}_i = \lambda_i, \ \ for \ i = 1, .., d, \tag{2.56}$$

and

$$\varphi_i \otimes e_j, j = 1, .., n. \tag{2.57}$$

■

2.9 Asymptotic Degeneracy

Proposition 2.31 *For a simple traveling wave, defined on a spatially periodic domain, the normalized eigenvalues show asymptotic degeneracy as the time of observation is increased to infinity.*

PROOF

Before proceeding to show this proposition, we establish some preliminary results and give some notations.

We denote by B_T the temporal correlation matrix corresponding to the signal $u(x,t)$ which is defined on $T \times X$, its associated eigenvalues being denoted by $(A_k^T)^2$. The temporal correlation matrix for the spatio-temporal domain $(T+1) \times X$ is denoted by B_{T+1}, and $(A_k^{T+1})^2$ refer to its corresponding eigenvalues.

The matrix P which denotes the difference between B_{T+1} and B_T reads

$$P = \begin{pmatrix} 0 & \dots & 0 & b_1 \\ \vdots & \ddots & \vdots & \vdots \\ 0 & \dots & 0 & b_n \\ b_1 & \dots & b_n & a \end{pmatrix} \tag{2.58}$$

where the quantity b_t represents $(\vec{\xi}_t, \vec{\xi}_{T+1}) = \sum_x u(x,t)u(x,T+1)$, $t = 1, \dots, n = T$, and $a = ||\vec{\xi}_{T+1}||^2$.

The eigenvalue problem for the matrix P reads

$$P\vec{v} = \mu\vec{v} \tag{2.59}$$

By writing $\vec{v}$ such that

$$\vec{v} = \begin{pmatrix} \vec{\xi} \\ x \end{pmatrix},$$

the equation (2.59) can be equivalently written as a scalar and vectorial equation such that

$$\vec{b}x - \mu\vec{\xi} = 0 \tag{2.60}$$

$$(\vec{b},\vec{\xi}) + (a-\mu)x = 0 \tag{2.61}$$

where

$$\vec{b} = \begin{pmatrix} b_1 \\ \vdots \\ b_n \end{pmatrix}, \ \vec{\xi} \in \mathbf{C}, \ x \in \mathbf{C}. \tag{2.62}$$

It can be readily noticed that one of the eigenvalues of the matrix P is 0, with multiplicity (T-1), the eigenvectors being

$$\begin{pmatrix} \vec{\xi}_i \\ 0 \end{pmatrix}, \quad i = 1, ..., n = T, \tag{2.63}$$

with $\vec{\xi}_i$ being orthogonal to $\vec{b}$:

$$(\vec{b},\vec{\xi}_i) = 0, \quad i = 1, ..., n = T. \tag{2.64}$$

For an eigenvalue μ other than 0, the equation (2.60) shows that $\vec{b}$ and $\vec{\xi}$ are colinear. The equation (2.61) gives

$$\mu^2 - a\mu - ||\vec{b}||^2 = 0, \tag{2.65}$$

whose solutions are

$$\mu_{1,2} = \frac{1}{2}\{a \pm \sqrt{a^2 + 4||\vec{b}||^2}\}. \tag{2.66}$$

Their associated eigenvectors read

$$\vec{u}_{1,2} = \begin{pmatrix} 0 \\ 1 \end{pmatrix} + \begin{pmatrix} \beta_{1,2}\vec{b} \\ 0 \end{pmatrix} \tag{2.67}$$

where the $\beta_{1,2}$ are given by

$$\beta_{1,2} = \frac{1}{||\vec{b}||^2}\{\mu_{1,2} - a\}. \tag{2.68}$$

Now, let us majorate the largest eigenvalue. This upper bound majoration will be useful later. We know that the b_i's satisfy Schwartz inequality

$$\begin{aligned} b_i^2 &= |(\vec{\xi}_i, \vec{\xi}_{T+1})|^2 \\ &\leq ||\vec{\xi}_i||^2 \, ||\vec{\xi}_{T+1}||^2 \\ &\leq ||\vec{\xi}_{T+1}||^4 \end{aligned}$$

since a simple traveling wave satisfies $||\vec{\xi}_t|| = ||\vec{\xi}_s||, \forall t, s$. Consequently,

$$\sum_{i=1}^{T} b_i^2 = ||\vec{b}||^2 \leq T||\vec{\xi}_{T+1}||^4 \tag{2.69}$$

$$\leq Ta^2. \tag{2.70}$$

Hence, since μ_1 is the majorant of P's eigenvalues, we have the following upper bound

$$\mu_1 \leq \frac{1}{2}\{a + a\sqrt{1+4T}\} \tag{2.71}$$

$$\leq \frac{a}{2}\{2 + 2\sqrt{T}\} \tag{2.72}$$

$$\leq a\{1 + \sqrt{T}\}. \tag{2.73}$$

Weil's inequality for the eigenvalues of the matrices B_T, B_{T+1} and P gives

$$(A_i^T)^2 + \mu_i \leq (A_i^{T+1})^2 \leq (A_i^T)^2 + \mu_1, \ \forall i. \tag{2.74}$$

Hence, we note the explicit dependence of μ_1 with respect to T. Note as well that the total energy of the traveling wave at the instant T equals

$$Eu = \sum_{i=1}^{N}(A_i^T)^2 = T\sum_{i=1}^{X} u(i,T)^2 = Ta. \tag{2.75}$$

Normalizing the inequality (2.74), we obtain

$$\frac{T}{T+1}p_i^T + \frac{T}{a\{T+1\}}\mu_i \leq p_i^{T+1} \leq \frac{T}{T+1}p_i^T + \frac{1}{a\{T+1\}}\mu_1(T+1). \tag{2.76}$$

- For $i = 1$, we have

$$p_1^{T+1} = \frac{T}{T+1} p_1^T + \frac{\mu_1(T+1)}{a\{T+1\}}$$

At the initial state, $p_1^1 = 1$, and we obtain

$$p_1^T = \frac{1}{T} + \frac{1}{aT}\sum_{j=2}^{T} \mu_1(j);\ T > 1.$$

- For $i = 2$, we have

$$\frac{T}{T+1} p_2^T + \frac{T}{a\{T+1\}}\mu_2 \leq p_2^{T+1} \leq \frac{T}{T+1} p_2^T + \frac{\mu_1(T+1)}{a\{T+1\}}$$

or

$$|p_2^{T+1} - \frac{T}{T+1} p_2^T| \leq \frac{\mu_1(T+1)}{a\{T+1\}}$$

- For $i > 2$, $\mu_i = 0$ and we get

$$\frac{T}{T+1} p_i^T \leq p_i^{T+1} \leq \frac{T}{T+1} p_i^T + \frac{\mu_1}{a\{T+1\}},$$

or in a compact form,

$$|p_i^{T+1} - \frac{T}{T+1} p_i^T| \leq \frac{\mu_1(T+1)}{a\{T+1\}}.$$

Since all $p_i^T \leq 1,\ \forall T$, the last inequality reads

$$\begin{aligned} |p_i^{T+1} - p_i^T| &\leq 2\frac{\mu_1}{a(T+1)} && (2.77)\\ &\leq 2\frac{\sqrt{T}+1}{T+1}. && (2.78) \end{aligned}$$

Let us show now that the normalized eigenvalues p_k^T have a finite limit as time T increases indefinitely.

According to the results established earlier in Section (2.8), the p_k^T's have the same values for temporal domains of the form nT_p, for all $n \in \mathbb{N}^*$,

$$p_i^{T_p} = p_i^{nT_p} = p_i, \ \forall i.$$

If we set

$$T = nT_p + \ell, \ 0 \leq \ell \leq T_p \ and \ n \in \mathbb{N}^*,$$

then the inequality (2.78) reads

$$|p_i^{nT_p+\ell+1} - p_i^{nT_p+\ell}| \leq 2\frac{\sqrt{nT_p+\ell}+1}{nT_p+\ell+1}$$

For an upper bound of the quantity

$$|p_i^{nT_p+\ell} - p_i^{nT_p}|,$$

we proceed as follows

$$\begin{aligned} |p_i^{nT_p+\ell} - p_i^{nT_p}| &= |p_i^{nT_p+\ell} - p_i^{nT_p+\ell-1} + \ldots + p_i^{nT_p+\ell-(\ell-1)} - p_i^{nT_p}| \\ &\leq |p_i^{nT_p+\ell} - p_i^{nT_p+\ell-1}| + \ldots + |p_i^{nT_p+1} - p_i^{nT_p}| \\ &\leq 2\ell\frac{\sqrt{T}+1}{T+1}. \end{aligned}$$

The last inequality shows that

$$\lim_{T\to\infty} p_i^T = p_i.$$

In addition, we know that the eigenvalues asssociated with a simple traveling wave are 2-fold degenerate (see proposition 2.16.) each time the temporal domain is of the form nT_p, we thus have

$$p_{2i}^{nT_p} = p_{2i-1}^{nT_p} = p_{2i} = p_{2i-1}.$$

Hence, the limit of the difference tends to zero:

$$\lim_{T\to\infty} |p_{2i}^T - p_{2i-1}^T| = 0.$$

This ends the proof of the proposition. ∎

An illustration of this result is shown in figure 2.3.

Consequence for the entropy

A very important consequence of the last result, namely the normalized eigenvalues exhibit an asymptotic degeneracy, is that a similar behavior is expected from quantities calculated based upon these eigenvalues. Particularly, the entropy which is defined as

$$H(u) = - \lim_{N \to \infty} \frac{1}{logN} \sum_{k=1}^{N} p_k log p_k, \tag{2.79}$$

converges to a limit when the time of observation is sufficiently increased. This phenomenon of *saturation* is crucial for quantifying the state of a signal for the viewpoint of space-time complexity. This will be illustrated in chapter 3 in the experiment on binary fluid convection.

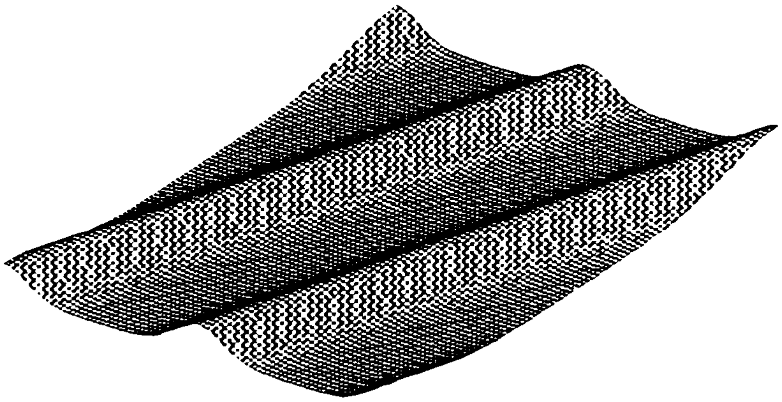

Figure 2.2: Three dimensional representation of a soliton in a periodic domain, two spatial periods are shown.

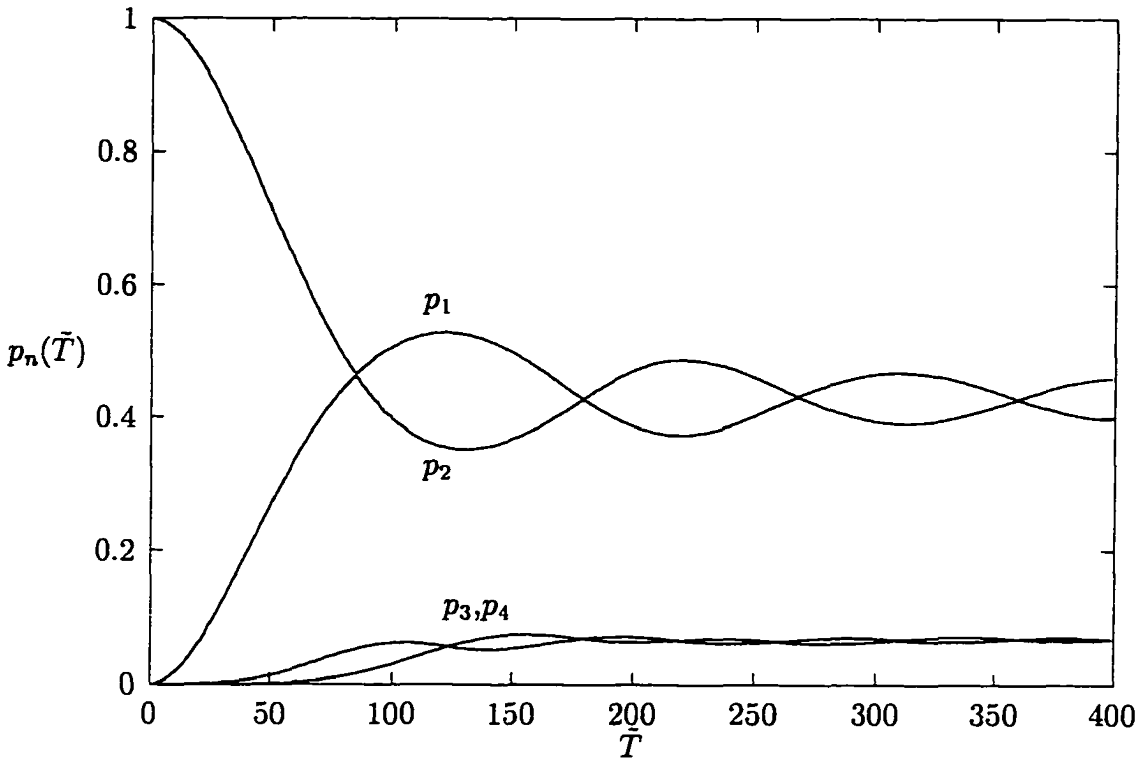

Figure 2.3: Normalized eigenvalues evolving with $\tilde{T}$. In this specific example the eigenvalue corresponding to the average of the signal was omitted.

Chapter 3

Characterization of Spatiotemporal Chaos in Binary Fluid Convection

3.1 Introduction

While more and more experiments report the presence of erratic behaviors, only a few have the advantage of enabling quantitative characterization. The lack of clean experimental systems and applicable techniques that allow such characterization has been a major obstacle, especially systems which exhibit space-time complexity. In this chapter[1], the objective is twofold. First, we describe an extensive series of experiments on traveling-wave convection in an ethanol/water mixture performed in a long, narrow, annular container. Second, complex dynamical states exhibited by this system are analyzed using a number of classical statistical techniques, such as correlation functions and Fourier spectra, with a particular focus on the techniques presented in Chapter 2, which are mainly appropriate for measuring space-time complexity.

In these experiments, as the Rayleigh number — the main control parameter — is quasi-statically increased through the range 0-2% above onset, the system evolves through a series of complex spatio-temporal states before settling into an extended pattern of steady, spatially-uniform convective rolls. Several other spatio-temporal states occur depending on stress parameters, and the ones we intend to focus on are

---

[1] This chapter is partially extracted from Ref. [60].

described in detail in Section 3.3. Much of the dynamical behavior is influenced by strong nonlinear dispersion, which causes the repeated and often irregular appearance and sudden collapse of spatially-localized bursts of traveling waves. We use the biorthogonal decomposition technique in an effort to extract the basic features of the patterns and to characterize the complexity of their dynamics.

This chapter is organized as follows: First, thermal convection in binary fluid mixtures is introduced. Then, in Section 3.2, the apparatus and experimental techniques are described. In this section, we also discuss the classical statistical analyses that have been applied to the data collected from the experiments. A detailed description of dynamical states exhibited by the system is reviewed in Section 3.3. Section 3.4 discusses the results of the analyses of the observed dynamics over the entire range of Rayleigh numbers explored in these experiments. Section 3.5 follows with a summary and discussion.

3.2 Thermal Convection in Binary Fluid Mixtures

3.2.1 Basic Ideas and Parameterization

The usual Rayleigh-Bénard convection consists of pure viscous fluid contained in a rectangular box with a gradient of temperature imposed vertically across the horizontal layer. If the gradient of temperature is small, the fluid remains at rest, and the equilibrium solution corresponds to a pure conductive state, with a linear distribution of the temperature along the vertical axis. When the applied gradient of temperature is large enough, the pure conduction state loses its stability, the stabilizing effects of diffusion and dissipation being overcome by the destabilizing effect of buoyancy, and convection follows. The ratio of the characteristic times of the stabilizing effects to the destabilizing effect defines a non-dimensional parameter, proportional to the temperature difference, called the *Rayleigh number* R,

$$R = k\Delta T.$$

The Rayleigh number represents the main stress parameter in this system. As R is increased above a certain critical Rayleigh number R_c, steady roll patterns are formed. As R is further increased, a variety of other bifurcations occur, and the resulting flow patterns exhibit complicated space-time evolution. Subsequently, we use the reduced Rayleigh number which measures the fractional distance from the onset:

$$\epsilon = \frac{R - R_c}{R_c}.$$

Double Diffusive Systems

The standard Rayleigh-Bénard instability is caused by density variations due to thermal expansion. Density variations can be generated by diffusive quantities other than the temperature field. Examples of such cases are thermohaline convection, a salt/water mixture with the salt concentration providing the second diffusivity, and in binary-fluid mixtures such as $^3He -^4 He$ mixtures or ethanol-water mixtures, where the presence of a second fluid, ethanol in pure water for instance, influences the density due to a strong dependence on concentration fluctuations. In this work, we deal exclusively with binary mixtures of ethanol and water.

In these mixtures, concentration gradients are induced by the applied gradient of temperature across the layer of fluid. This phenomenon of thermally induced concentration diffusion is known as the Soret effect. The ratio of the induced vertical density gradient to that caused by thermal expansion defines the *separation ratio* ψ:

$$\psi = -c(1-c)\frac{(\partial\rho/\partial c)_T}{(\partial\rho/\partial T)_c}S_T,$$

where S_T is the Soret coefficient. The separation ratio measures the extent to which the Soret effect stabilizes or destabilizes the fluid layer against convection.

Concentration diffusion is much slower than heat diffusion. This effect is parameterized by the Lewis number: $\mathcal{L} = D/\kappa$, where D is the mass-diffusion coefficient and κ is the thermal diffusivity. The fourth parameter is the *Prandtl number* $P = \nu/\kappa$, which is the ratio of the viscosity ν to thermal diffusivity.

Unlike steady convection of pure fluid, in binary fluid mixtures the primary instability can be either oscillatory or stationary. The separation ratio is the parameter determining which of these two behaviors is observed. In fact, linear instability analysis shows that, for $\psi \leq -\mathcal{L}^2$, convection is expected to begin as an oscillatory state with a well-defined frequency. This degenerate point is referred to as a codimension two point.

3.2.2 Binary Fluid Experiments

In the following section we briefly describe the apparatus and techniques used in the experiments performed by P. Kolodner. The data acquired from this system constitute a major input for the formalism we have developed and the analyses we intend to carry out. For the interested readers, more details about this experimental system can be found in other recent publications [29, 31, 38]. We also discuss some data manipulations and representations, such as complex demodulation.

Apparatus and Procedures

The cell has the shape of an annular channel of height $d = 0.2737cm$, radial width 1.677d, and mean circumference $82.47d$, formed by a concentric disk and ring. These are clamped between an electrically-heated, mirror-polished silicon bottom plate and a transparent, water-cooled sapphire top plate. By means of 24 adjustable trim heaters arranged in a circle on the underside of the bottom plate of the cell, the applied temperature difference can be made uniform. The fluid used in these experiments had the following properties, at a mean temperature of 27.26°C :

- 0.4 wt-% solution of ethanol.
- Separation ratio $\psi = -0.0204$.
- Prandtl number $P = 5.969$.
- Lewis number $\mathcal{L} = 0.0085$.

The flow patterns studied consist of superpositions of one-dimensional TW which propagate azimuthally around the cell in directions that we refer to as "left" and "right". The data is acquired through shadowgraphic flow-visualization. A refractive image of the flow pattern is produced and projected onto an annular array of 720 photodiodes controlled by a computer which digitizes the signals on a fine spacetime mesh and stores them for later analyses.

Data Collection

A total of 50 data sets were recorded from these experiments in the range $0 < \epsilon < 0.0192$. These data sets were 37 hours long, recorded after an equilibrium period that varied from 18 to 24 hours. The meshes we have considered were a spacing of 2° in space - an equivalent of 0.458d, d being the cell height, and 20 sec in time or $0.390\tau_v$, $\tau_v = 51.2$ sec being the vertical thermal diffusion time. The selected mesh had approximately 4 points per spatial wavelength, while the fastest temporal oscillation was covered with approximately 5 points per cycle. Before we performed our quantitative analyses, two corrections were applied to these data. First, the dc background components of the signals were removed, and then small distortions in the optical system were corrected.

Complex Demodulation

One method of analysis we used in this work is complex demodulation. This technique is applicable to signals that can be written in the form:

$$u(x,t) = Re\{A_L(x,t)e^{i(\omega_L(x,t)t+k_L(x,t)x)} + A_R(x,t)e^{i(\omega_R(x,t)t-k_R(x,t)x)}\}. \qquad (3.1)$$

Complex demodulation allows the real amplitudes $A_{L,R}(x,t)$, wavenumbers $k_{L,R}(x,t)$ and frequencies $\omega_{L,R}(x,t)$ to be extracted. The reader is referred to Ref. [38] for more details. Here we merely point out that the conditions under which this procedure is valid are statisfied by most of our data.

This procedure is quite useful for qualitative examination of the data; see next subsection on data representation. A special application of this technique is developed for quantitatively analyzing the evolution of the slowly-varying complex amplitudes. This is important for extracting the coefficients in the Complex Ginzburg-Landau equations [38].

Data Representation

Space-time diagrams are very useful for qualitative examination of the data. They show the trajectories of all individual convective rolls; for instance one may choose to plot the paths of constant TW phase velocity. Also, an amplitude threshold needs to be applied so that only significant TW amplitudes are seen.

Another very useful representation is a hidden-line graph of the spatially varying amplitudes extracted through complex demodulation, as they reveal the bursting and propagating effects that are the heart of dispersive chaos. Also useful is the application of spatial demodulation of the raw signal at the measured mean wavenumber at each time step. This analysis reveals dynamical behavior without separating the left- and right-TW components, as can be seen in Figs 3.6 and 3.8 below.

3.3 Dynamical States: Overview

In this section, we give a brief description of the dynamical states observed in these experiments. We will concentrate on the three states following the onset transients. These transients, linear at onset and nonlinear near onset, are particularly useful for measuring dispersive properties of TW in this system. For instance, in this system, the critical Rayleigh number $r_{co} = 1.18044(6)$, the critical wave number $k_c = 3.0505(50)$ and the Hopf frequency $\omega_o = 3.143828(25)$.

Following these onset transients and after their decay, persistent nonlinear state termed *counterpropagating quasilnear wave packets* (CPWP) are seen. They consist of a pair of broad, slightly asymmetric wave packets of small-amplitude TW which propagate around the cell in opposite directions at high velocity. This state persists up to $\epsilon = 0.0019$.

As ϵ is increased, dispersive chaos sets in. Spatially-localized bursts characterized by erratic, repeated appearance and subsequent decay are produced in this state. These bursts appear more frequently in time and more densely in space as ϵ is increased through the range $0.0019 \leq \epsilon \leq 0.0111$. At $\epsilon = 0.0111$, more spatially correlated bursts with decreasing temporal frequency and increasing temporal duration appear, which lead to a state characterized by persistent steady convective rolls at a certain spatial location. Their spatial extent expands linearly with ϵ. As ϵ is further increased, these steady convective rolls fill the entire cell at $\epsilon = 0.0192$.

Each of the following subsections deals with an individual dynamical state seen in its own range of ϵ. We give sufficient description to characterize the state and to be suitable for our purposes for the later discussion of the ϵ dependence of the behavior of all the dynamical states.

3.3.1 Counterpropagating Wave Packets

Given sufficient time, linear and nonlinear transients always decay into the CPWP state for $\epsilon < 0.0019$. Figure 3.1 shows the resulting state for $\epsilon = 0.00065(7)$. The power spectrum computed from the time series signal measured at any single spatial point in this state exhibits discrete, narrow peaks which are due to both amplitude and frequency modulation.

Full complex demodulation of the shadowgraph signals yields the amplitude profiles in Figure 3.2, showing explicitly that this state consists of a pair of wave packets which circulate around the cell at approximately constant velocity and no long-term change in shape. The wave-packet amplitude profiles are slightly asymmetric, and the phase velocity in each wave packet is approximately constant. Using spectral measurements, the group velocity, v_g, is found to decrease smoothly from the linear value at onset by several percent. By following the paths of points of constant TW phase in spacetime, a phase velocity v_{ph} can also be measured.

Figure 3.3 shows the evolution with ϵ of the time-averaged amplitude profile of the right-going wave packet. These were calculated by shifting the profiles computed by complex demodulation at time t to the left by an amount $v_{gr}t$ - thus transforming to a comoving frame - and then time averaging. At the lowest ϵ, TW fill the cell with an amplitude profile that exhibits only a weak, sinusoidal spatial modulation. As ϵ is increased, the amplitude profiles grow stronger, narrower and more asymmetric. Importantly, the wave packets seen in these experiments are substantially weaker than any other nonlinear state in this system. The amplitude profiles of slow, spatially-uniform, nonlinear TW have an average value of 0.12 near onset, which is also comparable to the peak amplitude seen in the weakest persistent dispersive-chaos state at $\epsilon = 0.00195$. By comparison, Fig. 3.5 shows that the strongest wave packet exhibits a peak amplitude of only 0.020.

The small TW amplitudes and small group and phase velocities observed in these experiments are indications that nonlinearities are very weak in the CPWP state - in Ref. [30], these states were referred to as *quasilinear*.

When the two wave packets are far from one another, they propagate with nearly the linear group and phase velocities and grow up at the linear growth rate.

When they pass through each other, their amplitudes slightly damp, compensating the linear growth and leading to a regular state of small amplitude and no long-term change in wave-packet shape. Other signatures of these weak nonlinear effects are quite difficult to detect. In particular, we have not been able to measure any modulations in the height or the width of the wave packets that are phase-coherent with their circulation.

CPWP states have been observed for $0.00018(7) \leq \epsilon \leq 0.00166(7)$. At the upper end of this range, these states can be somewhat irregular. An example is shown in Fig. 3.4, where the right-TW amplitude in a CPWP state at $\epsilon = 0.00123(7)$ is shown in hidden-line format. In the very middle of the bottom of Fig. 3.4, the right-going wave packet splits into two, and the leading wave packet decays. In addition, the peak amplitude of the wave packet is not steady in Fig. 3.4: observe the abrupt decrease in amplitude in the upper left-hand corner of the bottom frame of Fig. 3.4. By contrast, the left-going wave packet (upper frame of Fig. 3.4) displays regular behavior during this run. While the hidden-line presentation of the TW amplitude profiles in Fig. 3.4 reveals this instance of gross dynamical irregularity quite well, we have found in general that the irregularities in the counterpropagating regime are quite weak and difficult to detect using spectral or demodulation techniques. Dynamical analysis based on the BOD reveals these weak effects more clearly, and they are the subject of the next chapter. Part of this analysis is presented in Section 3.4.2 below.

Increasing ϵ from 0.00166 to 0.00195 causes a transition to persistent dispersive chaos. The reverse transition is seen on dropping ϵ from 0.00197 to 0.00178. Thus, we quote the upper limit of the CPWP state as $\epsilon_b = 0.00187(12)$.

3.3.2 Dispersive Chaos

Figure 3.5 shows a hidden-line plot of the full TW amplitude field in a state of dispersive chaos (DC) at $\epsilon = 0.0048$. This representation shows very clearly that this state consists of repeated bursts in both the left- and right-TW components. However, the duration of the bursts, the phase velocity of the underlying TW, and the general qualitative evolution of this state with ϵ are better revealed in spacetime diagrams. A series of dispersive-chaos data sets, separated in ϵ by approximately 0.0022, have been recorded. Fig. 3.6(a) shows the first well-equilibrated DC state studied in this system, at $\epsilon = 0.00200(6)$. This run exhibits infrequent, broad, double-humped bursts in both TW components. Note that the TW phase velocity changes very little in these bursts, except in the right-TW burst at time 26000 sec. Also note that there are substantial regions in which both left and right TW are seen. As ϵ is increased (Figs. 3.6(b)), the bursts become more localized in space and appear more frequently in time and more densely in space. Regions of lower phase velocity become more apparent, and regions of overlap between left and right TW grow smaller. These trends continue as ϵ is further increased. At higher ϵ (Fig. 3.6(c); $\epsilon = 0.00744(5)$), a new trend is observed: the TW bursts begin to last longer in time, to appear in spatially-correlated locations, and to exhibit extremely low phase velocity for long periods of time. The evolution of these features culminates in the run of Fig. 3.6(d) at $\epsilon = 0.01098(8)$; this is the highest value of ϵ at which DC dynamics are exhibited, although we classify this run as exhibiting a mixture of TW and steady rolls (TW/SR) dynamics part of the time as well (There are three such part DC-part TW/SR data sets). Thus, the nearly-steady convective rolls between locations 120^o and 190^o in the bottom half of the frame coexist with very long-lived bursts of much faster TW which appear in nearby locations; in the top half of the frame, the regular TW bursts characteristic of the TW/SR state are seen.

The decrease of the TW phase velocity with ϵ is undoubtedly caused by the stronger pumping of the convective concentration field at higher TW amplitude. This effect tends to “dig a hole” in the concentration field which can only diffuse away slowly after the collapse of a TW burst, due to the small Lewis number in this system. Because of the increased buoyancy in this “concentration hole”, subsequent bursts grow preferentially in the locations of previous bursts.

3.3.3 Coexisting Traveling Waves and Steady Rolls.

The evolution in the dispersive-chaos regime towards longer-lived, correlated spatial regions of ever-slower TW documented in Fig. 3.6 ultimately leads to the TW/SR state. Figure 3.7 shows a spacetime diagram of this state for $\epsilon = 0.01212(5)$.

The region between locations 190° and 280° is occupied by almost perfectly steady rolls; in the rest of the cell, strikingly regular TW bursts are observed. We have performed most of the analysis of these states by removing the SR component with a temporal hipass filter. The structure of the TW component isolated in this way exhibit trailing-edge phase defect which results in the burst-splitting scenario.

We note that the amplitude profiles reveal weak left-going (right-going) TW on the right (left) side of the TW region. Spectral analysis shows that the weak TW are *reflections* of the strong, incident TW from the edges of the SR region. The reflection coefficient is roughly $r = 0.1$. The reflected TW, however, are completely attenuated by the incident TW.

The TW profiles seen in this state are reminiscent of the profiles seen in the regular "blinking states" seen in short, rectangular cells at the same separation ratio [34], exhibiting the approximately exponential growth in the TW direction that is characteristic of convective instability. The TW amplitudes decay near the edges of the SR region - such "healing regions" are also seen in blinking states [34, 21]. However, unlike the weakly-nonlinear blinking states, the incident TW in the TW/SR state are strongly nonlinear and completely absorb the reflected waves. The source of the TW bursts must therefore lie in the center of the TW region.

Figure 3.9 shows the evolution of the TW/SR state with ϵ. The most obvious feature is the decrease with ϵ of the length Γ_{TW} of the TW region. With further increase in ϵ, this trend causes the cell to fill with steady rolls. The bursting appears to be regular in all three of these runs, although a more detailed analysis of the run in Fig. 3.9(c) at $\epsilon = 0.01535(5)$ shows these events to be slightly erratic - see below.

The regions of steady rolls in the three runs shown in Fig. 3.9 are centered at the same spatial location. As mentioned above, this is caused by convective "self-trapping": once a SR region is formed, it "digs a hole" in the convective concentration field which pins it spatially. Subsequent small changes in ϵ, as in the series of experiments in Fig. 3.9, change only the size of the region, but not its location. However, in experiments in which the pattern was quenched by reducing ϵ far below onset and then re-made by increasing ϵ again, the SR region reappeared at apparently random positions. These locations do not seem to be related to fixed inhomogeneities in the convection cell.

Erratic behavior in the TW/SR state can take several forms. In Fig. 3.9(c), while the TW bursts are somewhat irregular, the steady rolls are essentially motionless, as they are in TW/SR states which exhibit regular TW bursts - compare Fig. 3.9(c) with Figs. 3.9(a,b). A more extreme case of this type is observed at $\epsilon = 0.01650$, in which very steady rolls coexist with TW bursts that are so irregular that no value for ω_{mod} can be extracted. TW/SR states which exhibit motionless or nearly motionless SR are grouped together and represented with open triangles in Table 3.1 and in graphs below, even if their TW bursts do not exhibit regular dynamics. In contrast, it was observed in some runs that the SR themselves exhibited irregular dynamics. An example of such behavior is given in Fig. 3.10. Here, the nominally steady rolls exhibit occasional defects, and the SR region sometimes moves and/or changes in spatial extent. We reserve the name *erratic TW/SR states* and closed triangular symbol for TW/SR states in which the "steady" rolls are irregular in this way. In a third class of dynamical states, the system exhibits DC dynamics part of the time and TW/SR dynamics at other times. The state at $\epsilon = 0.01098(8)$ in Fig. 3.6(d) is such a state; two other runs of this type were recorded, just below the transition to the TW/SR state. These three runs are represented by half-open circles in Table 3.1 and in graphs below. The possibility of exhibiting these two new types of erratic dynamical behavior near the transition between dispersive chaos and the TW/SR state gives this transition a hysteretic character. This is discussed further in Section 3.5.1.

3.4 Biorthogonal Decomposition

3.4.1 Correlation Functions

We have studied correlation functions in a number of ways. We have computed the equal-time spatial correlation function at each time step in a data set and then averaged all time steps together to produce the time-averaged spatial correlation matrix $C_s(x, x')$. The diagonal of this matrix, denoted $C_s(\Delta x)$, with $\Delta x = x - x'$, is referred to as the time-averaged spatial correlation function. An example is shown in Fig. 3.11 below. Similarly, the space-averaged temporal correlation function $C_t(\Delta t)$ has been computed - see Fig. 3.15 for three examples. It has also been useful to compute correlation functions from the demodulated amplitude profiles $A_{L,R}(x,t)$ as well as from the raw signals $u(x,t)$ (Figs. 3.17). Finally, we have computed the time-averaged spatial cross-correlation function from the demodulated left- and right-TW amplitudes for selected data sets - see Figs. 3.13-3.14. All correlation functions have been normalized to unit peak amplitude.

Spatial Correlations

The oscillatory curve in Fig. 3.11(a) shows the time-averaged spatial correlation function $C_s(\Delta x)$ computed from the dispersive-chaos data at $\epsilon = 0.00323(5)$. Basically, this measurement reveals the time-averaged spatial burst shape in dispersive chaos. To quantify this shape, we computed the amplitude and wave-number profiles for this correlation function using spatial demodulation; these are the smooth curves in Figs. 3.11(a) and 3.11(b), respectively. Moving away from $\Delta x = 0$, the amplitude profile decays approximately as a Gaussian until the amplitude drops by about a factor of 3 from its value at the peak; further away from the peak, sharp minima are caused by phase defects. These appear as singularities in the wave-number profile.

Exploiting the lack of an amplitude cusp at $\Delta x = 0$ and the reasonably flat shape of the wave-number profile there, we fit the main body of the correlation function using the function $C_s(\Delta x) = A\exp(-2\Delta x^2/\sigma^2)cos(k\Delta x)$. This fit worked well for all TW data in this work. Figure 3.12 shows the fitted values of the spatial width σ and the central wave number k as functions of ϵ. The width initially shows a sharp decrease with ϵ in the dispersive-chaos regime (full circles), quantifying a trend of increased complexity noted above. Thereafter, σ increases again, decreasing once more in the TW/SR region. The wave number exhibits a consistent increasing trend with ϵ, or, more properly, with TW amplitude. This dependence of wave number on TW amplitude explains the presence of phase defects in the spatial correlation function observed in Fig. 3.11 and many other DC data sets: the presence of high-amplitude TW at $\Delta x = 0$ is strongly correlated with the presence of small-amplitude TW far away. These have a lower wave number; hence, there must be phase defects at intermediate distances.

Spatial Cross-Correlations

Figure 3.13 shows time-averaged spatial cross-correlation functions computed from the demodulated left- and right-TW amplitude profiles of several runs in the dispersive-chaos regime. With increasing ϵ, the cross-correlation function grows weaker and exhibits an increasing asymmetry. This asymmetry reflects the nature of the interaction between weak, convectively-amplified TW and strong, spatially-localized TW bursts in the opposite TW component, see Ref. [60].

Figure 3.14 shows time-averaged spatial cross-correlation functions computed from the demodulated left- and right-TW amplitude profiles of several runs in the TW/SR regime. In this state, the opposite TW components always occur in spatially-separated bursts; as ϵ is increased and the TW region shrinks, these bursts grow narrower (open triangles in Fig. 3.12(a)) and move closer together (Fig. 3.9.) Thus, the cross-correlation functions exhibit well-defined peaks which move closer to $\Delta x = 0$ and grow narrower as ϵ increases.

Temporal Correlations

Figure 3.15 shows the space-averaged temporal correlation function $C_t(\Delta t)$ computed from the raw signal in three dispersive-chaos data sets. The envelope of $C_t(\Delta t)$ decays rapidly with Δt; this decay becomes faster as ϵ increases. The very short phase correlation time is caused by the nonlinear dependence of TW frequency on amplitude in this system: as a typical burst forms in space and grows in amplitude, its frequency drops. Thus later TW are not in phase with earlier TW. This interference becomes more pronounced as ϵ is increased.

To eliminate the interference which limits the coherence of temporal correlation functions computed from the raw signals, we also performed these calculations starting from the demodulated TW amplitudes. Figure 3.16 shows the sum of the space-averaged temporal correlation functions computed for the left- and right-TW amplitude profiles in three dispersive-chaos data sets. In all cases, $C_t(\Delta t)$ decays to a level of about 0.3 at large delays Δt. This behavior reflects that essentially trivial fact that the presence of a burst at $\Delta x = 0$ is strongly correlated with the existence of bursts at other times; since demodulation has stripped off the carrier frequency from the signal, distant bursts cannot interfere to produce an asymptotic value of zero. However, these three data sets differ in the manner in which C_t approaches this asymptote. The two curves for $\epsilon = 0.00200(6)$ and $0.00634(11)$ exhibit a sharp initial decay whose characteristic time $\Delta t = 30$ represents the duration of a typical burst. For larger delays, these two curves differ. The run at $\epsilon = 0.00200(6)$ contained so few bursts that they can be seen individually in the dotted curve, and their characteristic double-humped shape can be discerned. There are many more bursts in the data set at $\epsilon = 0.00634(11)$ represented by the full curve; their shapes average out more completely, producing smaller features in the correlation function. The dashed curve, computed for the data set of Fig. 3.6(d) at $\epsilon = 0.01098(8)$, decays much more slowly, reflecting the presence in this data set of long-lived bursts of very slow TW as well as short bursts of fast TW.

Figure 3.17 presents temporal correlation functions computed from the demodulated TW amplitude profiles for regular TW/SR states. The fast oscillations in these curves represent the periodic appearance of TW bursts. The slowly-decaying envelope in Fig. 3.17(a) represents the regular, nearly-phase-coherent left- and right-TW bursts. The correlation function in Fig. 3.17(b) exhibits slow modulations due to fact that the left- and right-TW bursts exhibit different modulation frequencies. Fig. 3.17(c) corresponds to a data set in which the left- and right-TW bursts are not modulation-phase-coherent.

3.4.2 Biorthogonal Decomposition

Entropy Saturation

Before presenting detailed descriptions of the dynamical behavior measured using the BOD technique, we discuss an important systematic issue. In applying this technique, we must ensure that the duration T of each data set is long enough that further data acquisition would not affect results of the decomposition. We assess this by computing the spectral energy E and entropy H for subsets $t \in (0, \tilde{T})$ of the total time domain T ($\tilde{T} < T$), and studying their saturation with increasing $\tilde{T}$ as a function of ϵ. Typical results are shown in Figs. 3.19 and 3.20. Figure 3.19(a) shows the saturation of the spectral entropy for several CPWP data sets. After an initial sharp increase from 0 at small $\tilde{T}$, $H(\tilde{T})$ exhibits temporal oscillations corresponding to the circulation of the wave packets around the cell. These oscillations die out as time progresses; $H(\tilde{T})$ exhibits further slow evolution for some data sets. To average out the oscillations and to ensure saturation of subsequent slow drifts, all data sets had length > 55000 sec, and we quote global results computed from subsets of length T equal to the time taken for the wave packets to make exactly nine round trips.

Figure 3.19(b) illustrates the saturation of the spectral entropy for several DC data sets (curves g-j) and several TW/SR data sets (curves k-n). In the DC regime, the entropy is seen to increase sharply from 0 at very small $\tilde{T}$ and then to continue increasing very slowly before saturating. On average, the time required for saturation increases with ϵ in this regime. All of our DC data sets were sufficiently long (length 132000 sec) for the entropy to be completely saturated. In addition to these long-time trends, $H(\tilde{T})$ exhibits jumps with increasing $\tilde{T}$, corresponding to the inclusion of individual TW bursts in the time domain. Because new bursts are not coherent with previous bursts, they add to the complexity of the data set and increase the spectral entropy. For the regular TW/SR data sets shown in curves k-n in Fig. 3.19(b), the entropy saturates rapidly. Irregular TW/SR states, however, required an enormous time to saturate; in these cases, we used data sets of length 140000 sec instead of 132000 sec.

Spectral Energy

Figure 3.20 shows the evolution of the spectral energy E with time domain $\tilde{T}$. $E(\tilde{T})$ increases in jumps caused by the inclusion of new TW bursts. Averaging over these jumps, an approximately linear trend with $\tilde{T}$ is observed in almost all cases. The saturation of the "power" or global slope of these curves is much faster than that of the entropy.

Spectra

Figure 3.21(a) shows seven fully-saturated spectra computed in the DC regime, with ϵ increasing from the bottom curve to the top curve. At the lowest value of ϵ, the spectrum exhibits an inflection point separating a rapid, nearly exponential decay at low n from a flatter region at high n. As ϵ increases, the spectra become smoother, flatter, and stronger; the spectral entropy increases with ϵ in this state, and the spectral energy increases. In Fig. 3.21(b), we show spectra computed in six regular TW/SR states, with ϵ now increasing from the top curve to the bottom curve. In this dynamical state the spectral entropy decreases with ϵ. In some of these curves, quasi-two-fold degeneracies can be seen, as represented by pairs of nearly equal adjacent eigenvalues. Such near-degeneracies are related to the presence of TW in the system; they are present in all the BOD spectra computed in this work but are visible in only a few instances in Figs. 3.21(a,b) because of the small format of these graphs.

Dynamics

In Figs. 3.22-3.23, we illustrate the dynamics observed in the CPWP, DC, and TW/SR states by plotting the spatial and temporal energies and entropies extracted from the BOD. Recall from chapter 2, the spatial energy and entropy, $E_S(t)$ and $H_S(t)$, are functions of instantaneous time t that reflect the complexity of the spatial pattern recorded at that time. The introduction of an ordered spatial structure into a previously featureless pattern at a given time step will cause a sudden increase in the spatial energy and a corresponding decrease in the spatial entropy, as compared to the values computed at the previous time step. These signatures, which we see in all of our data, are essentially the opposite of the jumps seen in the growth of both the global energy $E(\tilde{T})$ and entropy $H(\tilde{T})$ shown in Figs. 3.19 and 3.20. There, new bursts are added in with all previous bursts as the computation is carried out over larger time domains $\tilde{T}$. The spectral energy and entropy associated with this growing collection of incoherent dynamical structures both tend to increase in jumps with $\tilde{T}$. Analogous comments apply in the spatial domain to the temporal energy and entropy, $E_T(x)$ and $H_T(x)$. At each spatial point, these functions measure the complexity of the time series signal measured at that point, independently of the signal at other spatial points.

Figure 3.22 shows the profiles of the spatial and temporal energy and entropy for a CPWP state at $\epsilon = 0.00095(7)$. In this regime, the spatial energy and entropy $E_S(t)$ and $H_S(t)$ (Fig. 3.22(a,b)) exhibit fast temporal oscillations at twice the frequency of the underlying TW; these are modulated on a slower time scale with a modulation period equal to half the time taken for the wave packets to circulate around the cell. Careful inspection shows that the fast carrier oscillations in $H_S(t)$ are out of phase with those in $E_S(t)$. These observations are easily explained. Twice per round trip, the wave packets overlap and interfere to produce localized standing waves. The nature of standing waves is to oscillate in time at the carrier frequency between a featureless pattern (which has low spectral energy and high entropy) and a coherent pattern of spatial oscillations (which has high spectral energy and low entropy). Thus, at the times when the wave packets overlap, $H_S(t)$ and $E_S(t)$ exhibit fast, out-of-phase temporal oscillations. Since the BOD is not sensitive to the sign of the signal, the spatial pattern is in effect rectified, and the temporal oscillations in $E_T(t)$ and $H_T(t)$ occur at twice the TW frequency. At other times during the wave-packet circulation, the pattern consists of spatially-separated left and right TW which do not interfere; thus at those times in the modulation cycle, $E_S(t)$ and $H_S(t)$ attain intermediate values and exhibit only weak oscillations on the fast time scale.

These features are also reflected in the spatial profiles of the temporal energy and entropy $H_T(x)$ and $E_T(x)$ plotted in Figs 3.22(c,d). These profiles once again exhibit out-of-phase oscillations, localized in regions centered at the points x_1 and x_2 where the wave packets overlap and produce standing waves. Since the spatial phase of the standing waves is not exactly the same each time the wave packets pass through each other, the spatial oscillations in $E_T(x)$ and $H_T(x)$ are washed out by averaging over many circulation cycles. Thus, the contrast in the time-averaged oscillations is weak, and the profiles appear noisy. In the language of dynamical systems, we would say that the temporal energy $E_T(x)$ represents the norm of the vector $\eta_x(t)$ in the temporal configuration space $\chi(T)$; $\eta_x(t)$ makes large excursions from the origin at the locations $x_{1,2}$ and approaches the origin as one moves away from $x_{1,2}$.

Figure 3.23 shows the corresponding profiles for the dispersive-chaos state shown in Fig. 3.6(c) ($\epsilon = 0.00744(5)$). In this regime, the spatial energy $E_S(t)$ exhibits erratic bursts corresponding to the appearance of new TW bursts (Fig. 3.23(a)). Some of these exhibit the characteristic double-humped shape. Because there is little spatial overlap of left- and right-TW bursts in this regime, the fast oscillations in

$E_S(t)$ caused by standing waves in the CPWP regime are essentially absent in dispersive chaos. Each TW burst adds a coherent spatial structure to the pattern; thus, the bursts in $E_S(t)$ coincide with dips in $H_S(t)$ (Fig. 3.23(b)). These characteristics of the DC regime have been noted previously [56]. The profile of the temporal energy $E_T(x)$ shown in Fig. 3.23(c) exhibits large-scale spatial structure. The temporal entropy $H_T(x)$ (Fig. 3.23(d)) shows corresponding nonuniformities; once again, regions of high temporal energy exhibit low temporal entropy. The reason for the nonuniformity of the dynamics is that, even though this data set is long enough to completely saturate the BOD in the sense defined in Figs. 3.19 and 3.20, it still contains only a finite number (approximately 120) of TW bursts. At the end of this section, we will have more to say about the nonuniformities revealed by these time-averaged spectral measures.

Figure 3.24 illustrates the spatiotemporal dynamics of a regular TW/SR state at $\epsilon = 0.01370(5)$. The spatial energy and entropy shown in Figs. 3.24(a,b) were computed using temporal-hipass-filtered versions of the data, to eliminate the influence of the localized SR on the dynamics. These profiles exhibit out-of-phase oscillations at a modulation frequency corresponding to the regular emission of TW bursts. Since the left- and right-TW bursts are spatially separated in this state, there are no standing waves and thus no oscillations on faster time scales in $H_S(t)$ or $E_S(t)$. Including the lopass component of the data shifted these profiles vertically without altering their oscillatory behavior. The temporal dynamics of this state are illustrated in Figs. 3.24(c,d). Here we show $H_T(x)$ and $E_T(x)$ computed from both the temporal-hipass-filtered version without SR (labeled "HF" in these graphs) and the spatial-hipass-filtered version which retains the SR component. The strong spatial oscillations in the profiles computed from the spatially-filtered data correspond to the SR; the temporal energy in the data without the SR component drops to zero in this spatial region, since the temporal filtering suppresses the low-frequency signal there. In the TW region, the shape of the temporal energy curve is the same for both versions and reflects the convective growth of TW bursts as they propagate out from location 50^o. Once again, the profile of the temporal entropy is out of phase with that of the temporal energy.

Global Behavior

Figure 3.25 shows the evolution of the global properties of the BOD with stress parameter ϵ. All the results in these graphs were computed using temporal-hipass-filtered data, so that, in the case of states which exhibited regions of steady rolls (triangles and half-filled circles in Fig. 3.25), the contribution of the SR component to the dynamics has been suppressed. The spectral energy E, shown in Fig. 3.25(a), exhibits an increasing trend up to $\epsilon \approx 0.0130$ in the TW/SR regime. $E(\epsilon)$ is a linear function in the CPWP regime (open squares) but increases approximately exponentially in the DC regime (circles and first triangular symbols in Fig. 3.25(a)). A fit of the data in the range $0.0020 < \epsilon < 0.0110$ to a functional form $E(\epsilon) = E_0 e^{\epsilon/\epsilon_E}$ gave an inverse log slope $\epsilon_E = 0.00423(15)$ and a prefactor $E_0 = 62.1(3.5)$. Below, it will useful to recall that the fitted spectral energy increases by a factor F = 6.63 on increasing ϵ from 0.0020 to 0.0100 in the DC regime. The decrease of the global energy in the TW/SR regime above $\epsilon \approx 0.0130$ is associated with the shrinking of the TW region documented in Fig. 3.9.

The behavior of the global entropy $H(\epsilon)$, shown in Fig. 3.25(b), is markedly different for the three dynamical states. In the CPWP regime, H increases linearly with ϵ. The scatter in these points is noteworthy and is discussed below. In the DC regime, $H(\epsilon)$ increases linearly with ϵ up to $\epsilon \approx 0.0080$ and then flattens out slightly. A fit of the data in the range $0.0020 < \epsilon < 0.0080$ to a linear dependence $H(\epsilon) = H_0 + (\epsilon/\epsilon_H)$ gave an inverse slope $\epsilon_H = 0.085(5)$ and an intercept $H_0 = 0.5800(37)$. Below, we will use some specific values taken from this fit: H = 0.604 at $\epsilon = 0.0020$, and H = 0.698 at $\epsilon = 0.0100$. In the TW/SR regime, $H(\epsilon)$ decreases again. As the TW region shrinks in this regime, the TW bursts become more ordered, in a spectral sense, even though their timing becomes erratic at the highest values of ϵ studied.

In reconstructing a dynamical state using the BOD, one would often like to truncate the expansion in Eq. (2.2) at the lowest possible order in order to conserve memory. The global entropy is an indirect measure of the number of terms required to reconstruct the data to within a desired precision. Another measure is simply to find the limit $n_f < N$ for which the energy sum in Eq. (2.9) equals a given fraction f of the global energy E. Figure 3.25(c) shows the ϵ dependence of n_{90}, the number of terms required to recover 90% of the spectra energy in this sum. n_{90} depends on the stress parameter in a way that is similar to the dependence of the global entropy. Indeed, in a plot of *ln* n_{90} *vs.* H, the data points in the different regimes are found to lie on slightly offset, nearly parallel straight lines. The weakest DC data evolve in a space of dimension $n_{90} = 18$.

In the discussion of Fig. 3.4 in Section 3.3.2 above, it was noted that some of the data sets acquired in the CPWP regime exhibit weakly erratic dynamics. The BOD has turned out to be a very sensitive way to reveal such behavior. In Fig. 3.26, we plot for these data the dependence on ϵ of the global energy and entropy calculated not from the raw data but separately from the demodulated left- and right-TW amplitudes. For $\epsilon < 0.00095$, both components exhibit identical global entropy and energy. However, the entropies of the two components differ for all data above this value, and the energies begin to separate for $\epsilon > 0.00123$, indicating that the two TW components are evolving independently. This is not too surprising, given the extremely weak nonlinear coupling between them and the tendency for isolated TW to burst and collapse at higher amplitudes. The greatest L-R energy difference is exhibited by the state of Fig. 3.4 at $\epsilon = 0.00123(7)$. Fig. 3.25(b) shows that the raw data in this run exhibited an anomalously high global entropy as well. These tiny manifestations of spatiotemporal complexity did not have perceivable effects on the statistical measures discussed in Sections 3.4 above.

In Fig. 3.27, we compare the global energy and entropy computed from data sets at high ϵ in which the low-temporal-frequency component due to slow TW and steady rolls is retained (large symbols) with those computed using temporal hipass filtering to remove that component of the signal (small symbols, copied from Figs. 3.25(a,b)). The presence of high-amplitude steady rolls increases the spectral energy and decreases the entropy in all cases. As ϵ increases in the TW/SR regime, the SR region grows in space, and the SR contribution to the energy grows correspondingly larger. Since the steady rolls exhibit very weak dynamical behavior in regular TW/SR states (open triangular symbols), the spectral entropy decreases rapidly at the highest values of ϵ.

Because of the marked differences in spectral entropy and energy associated with erratic TW bursts and regions of steady rolls, switching between DC and TW/SR dynamics (in data sets represented by half-filled circles in the graphs in this chapter) causes corresponding changes in the time evolution of the spatial energy and entropy $E_X(t)$ and $H_X(t)$. Figure 3.28 shows an example, at $\epsilon = 0.01097(8)$. At the beginning of this run ($t < 8000$ sec), a region of nearly steady convective rolls was in the process of disappearing from the system. This is reflected in a small increase in the spatial entropy in Fig. 3.28(b). The spatial energies computed retaining the SR component and suppressing it with temporal hipass filtering (labeled "HF" in Fig. 3.28(a)) were noticeably different until this transition. In the resulting pure DC state, the dynamics looked qualitatively similar to that exhibited in Figs. 3.23(a,b). Then, at time $t = 101000$ sec, a large TW burst evolved into another region of steady rolls, producing a sharp drop in the spectral entropy and a jump in the spatial energy computed from the unfiltered data. After this transition, regular TW bursts dominate the evolution of the temporal-hipass-filtered spatial energy.

3.5 Discussion

In this chapter, we have reviewed detailed and precise observations of one-dimensional TW patterns in a well-characterized, stable, and uniform experimental system. We have explored some of the possible dynamical states in an annular geometry of a particular size at this separation ratio. And, we have explored various techniques for the analysis of these data. We have divided our discussion of this work into two sections. Section 3.5.1 briefly summarizes the experimental observations. In Section 3.5.2, we present a discussion of the characterization of the observed dynamics.

3.5.1 Summary of Experimental Observations

As ϵ is increased above onset, this system evolves through dynamical states of three basic types before making a final transition to a spatially-uniform state of steady convective rolls. The first state, abbreviated CPWP, consists of pairs of broad, quasilinear wave packets which circulate around the cell at high velocity and with no long-term change in spatial structure. With increasing ϵ, these wave packets become narrower, stronger, and more asymmetric, and they begin to exhibit weakly erratic and independent dynamical behavior. Above a threshold $\epsilon_b = 0.0019$, the CPWP states gives way to dispersive chaos. In this state, both TW components exhibit irregular sequences of growth, bursting, and collapse. With increasing ϵ, the global behavior of this state becomes more erratic, and the spatiotemporal character of the TW bursts themselves evolve in ways which have been documented in detail, principally by computing correlation functions. At the highest values of ϵ for which this bursting behavior is seen, the system exhibits extended periods in which localized regions of extremely slow or stationary convective rolls are seen. Above a threshold $\epsilon = 0.0111$, this behavior culminates in the TW/SR state, in which part of the cell is filled with perfectly steady rolls, and the rest of the cell exhibits TW bursts whose timing is strikingly regular. As ϵ is further increased in this state, the spatial extent of the TW region decreases, vanishing at $\epsilon_c = 0.0192$. Above this threshold, the cell is filled with steady convective rolls of spatially-uniform amplitude. This transition is hysteretic; ϵ must be reduced to below $\epsilon_s = -0.016$ in order to induce a subsequent transition back to the quiescent state.

In all of these dynamical states, TW tend to take the form of localized bursts or wave packets which have an asymmetric structure. There is a universal tendency for the wave-number gradient seen in this structure to develop into a trailing-edge phase defect. By this process, the burst splits into two, and the leading burst decays. This scenario, as in Fig. 3.5, is seen in all the dynamical states described here and has been observed in other weakly-nonlinear [38] and strongly-nonlinear TW states as well.

3.5.2 Characterization of the Data

We have attempted to extract as much quantitative and qualitative information as possible from our data using the tools of classical statistical analysis. Demodulation techniques, used in various guises, have been extremely useful, because they extract the complex TW amplitudes, which, for instance, are described by the CGLE model. Correlation functions and spectra have revealed systematic trends in the structure of the TW bursts that constitute dispersive chaos. The spatial width and central wave number in Fig. 3.12 are good examples of the kind of precision that can be obtained using these diagnostic tools. However, these techniques certainly have their limits. For example, the asymmetric structure typically seen in TW bursts easily evades detection by $C_s(\Delta x)$. In addition, we have not found any way to estimate the average temporal duration of the TW bursts in dispersive chaos that is any more reliable than simply inspecting the spacetime diagrams of Fig. 3.6.

The biorthogonal decomposition has been an extremely powerful tool for studying some aspects of the dynamics of dispersive chaos. Some of the features in the BOD spectra (Fig. 3.21) are related to general symmetry properties of the system. For example, it was pointed out in the discussion of Fig. 3.21 that quasi-two-fold degeneracies in the BOD spectra are related to the presence of TW in the dynamics $u(x,t)$. It was also pointed out that the spectrum computed from the weakest DC data set exhibited a nearly exponential decay law. In general, exponential decays in the BOD spectra are the manifestations of space-time quasi-symmetries [5, 6]. In the case of fully developed, three-dimensional turbulence in the Navier-Stokes equations, such a quasi-symmetry is related to a scale invariance of $u(x,t)$ manifesting itself among the topos and chronos [6]. This quasi-symmetry is also equivalent to a spectrum law which can be understood as the generalization of the Kolmogorov $k^{-5/3}$ law for homogeneous, isotropic turbulence [6, 40]. Dispersive chaos, of course, does not exhibit the scale invariance of turbulence: TW convection always exhibits a narrow range of wave numbers, and, correspondingly, most of the BOD spectra in Fig. 3.21 deviate strongly from an exponential shape.

The global complexity of the spatiotemporal dynamics is reflected in the spectral energy E and entropy H computed from the BOD spectra. As shown in Figs. 3.25(a,b), transitions between the three main dynamical states seen in these experiments are clearly reflected in the ϵ dependence of these global quantities. Such transitions have been observed in the BOD spectra of coupled-map lattices [4, 41] and indeed were predicted in our early work on the present system [56]. An open question is whether they correspond to bifurcations in the mathematical sense. A *spatiotemporal bifurcation* [3, 2], in analogy with Poincaré's terminology for bifurcations in temporal dynamical systems, corresponds to a lack of smoothness in the dependence of the flow on the stress parameter. The perturbation theory of linear operators, applied to the biorthogonal operator V, reveals that such a lack of smoothness can only be due to the appearence of a new degeneracy in the BOD spectrum as a parameter is varied. Since the appearence of a new degeneracy causes a decrease in the spectral entropy H, a bifurcation necessarily occurs at a local maximum of H. This is indeed the case at, for example, the boundary between the dispersive-chaos and coexistence regimes in these experiments. While a local entropy maximum is a necessary condition and therefore is a good indicator of the possibility of a bifurcation, it is not a sufficient condition, and a more detailed analysis of the transition is needed. This question will be addressed in Ref. [49].

The spatial and temporal energies and entropies $E_S(t)$, $H_S(t)$, $E_T(x)$, and $H_T(x)$ are less "global" properties of the dynamics than the spectral energy E and entropy H. These functions reveal features which can be directly related to the properties of TW bursts and other details of the dynamical behavior. For example the growth of individual TW bursts are reflected in sudden increases in the spatial energy correlated with dips in the spatial entropy. This is the characteristic signature that a coherent spatiotemporal structure has appeared in the system.

Beyond these measures of dynamical complexity, there remain two important open problems in our characterization of this system. First, as mentioned above, while we can easily appreciate the qualitative spatiotemporal shape of the TW bursts in dispersive chaos from their shapes in the spacetime diagrams in Fig. 3.5, we have not found a way, based on the BOD or any other technique, to quantitatively extract the average spatiotemporal shapes of these bursts. This is analogous to the problem of identifying coherent structures in turbulence. The second open issue relates to the application of the tools of the theory of dynamical systems to these data - a point mentioned in the very first paragraph of this chapter. The BOD is a method for representing complex spatiotemporal dynamics as the orbit described by a vector in a spatial characteristic space as time evolves and as the orbit described by a corresponding vector in a temporal characteristic space as the spatial location moves. These two spaces are the spatiotemporal counterparts of the notion of phase space in temporal dynamical systems theory. Although these two spaces are the smallest linear spaces which contain the dynamics of $u(x,t)$ (viewed as a set of spatial or temporal vectors), a difficult problem presented by most of our data is one of high dimensionality: the weakest dispersive-chaos data set exhibits a dimension which we can estimate as

$n_{90} = 18$ from Fig. 3.25(c). The essential challenge in understanding dispersive chaos lies in finding ways to characterize high-dimensional dynamical systems. Although it is clear that we have already significantly decreased the dimensionality of the dynamics by the application of the BOD itself, as compared to other bases such as the Fourier basis [3, 8, 19], it is obvious that a further reduction is needed if progress is to be made. As a start on this problem, we have begun a dynamical-systems analysis of data in the CPWP regime, where $3 < n_{90} < 12$. The dimension of the dynamics is reduced still further by analyzing the demodulated TW amplitude fields rather than the raw data - see Fig. 3.27. Furthermore, the BOD localizes the subspace in which a spatiotemporal bifurcation may take place to that spanned by degenerate eigenfunctions, therefore providing a technique for still further dimension reduction similar to that of the center manifold theorem of temporal dynamical systems theory.

Section	**State**	ϵ **Range**	**Symbol**
	linear TW	0	□
	nonlinear onset transients	0.0004 - 0.0017	
3.3.1	counterpropagating wave packets	0 - 0.0019	■ , □
3.3.2	dispersive chaos (DC)	0.0019 - 0.0111	●
3.3.2, 3.3.3	part DC, part TW/SR a	0.0103 - 0.0110	•
3.3.3	regular TW/SR	0.0111 - 0.0192	△
3.3.3	erratic TW/SR	0.0097 - 0.0122	▲

Table 3.1: Dynamical states

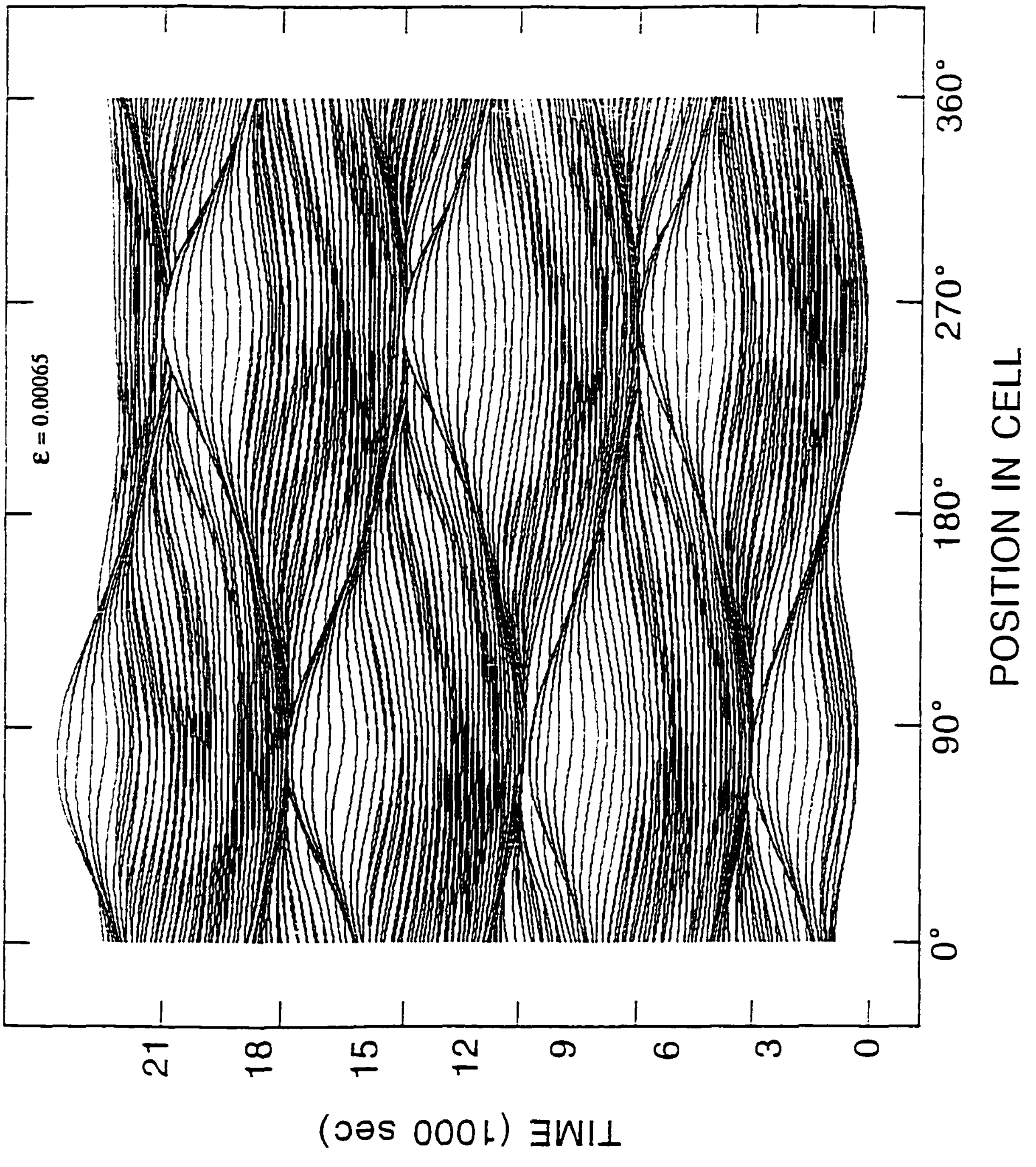

Figure 3.1: The spatiotemporal evolution of the CPWP state is shown for ϵ = 0.00065(7).

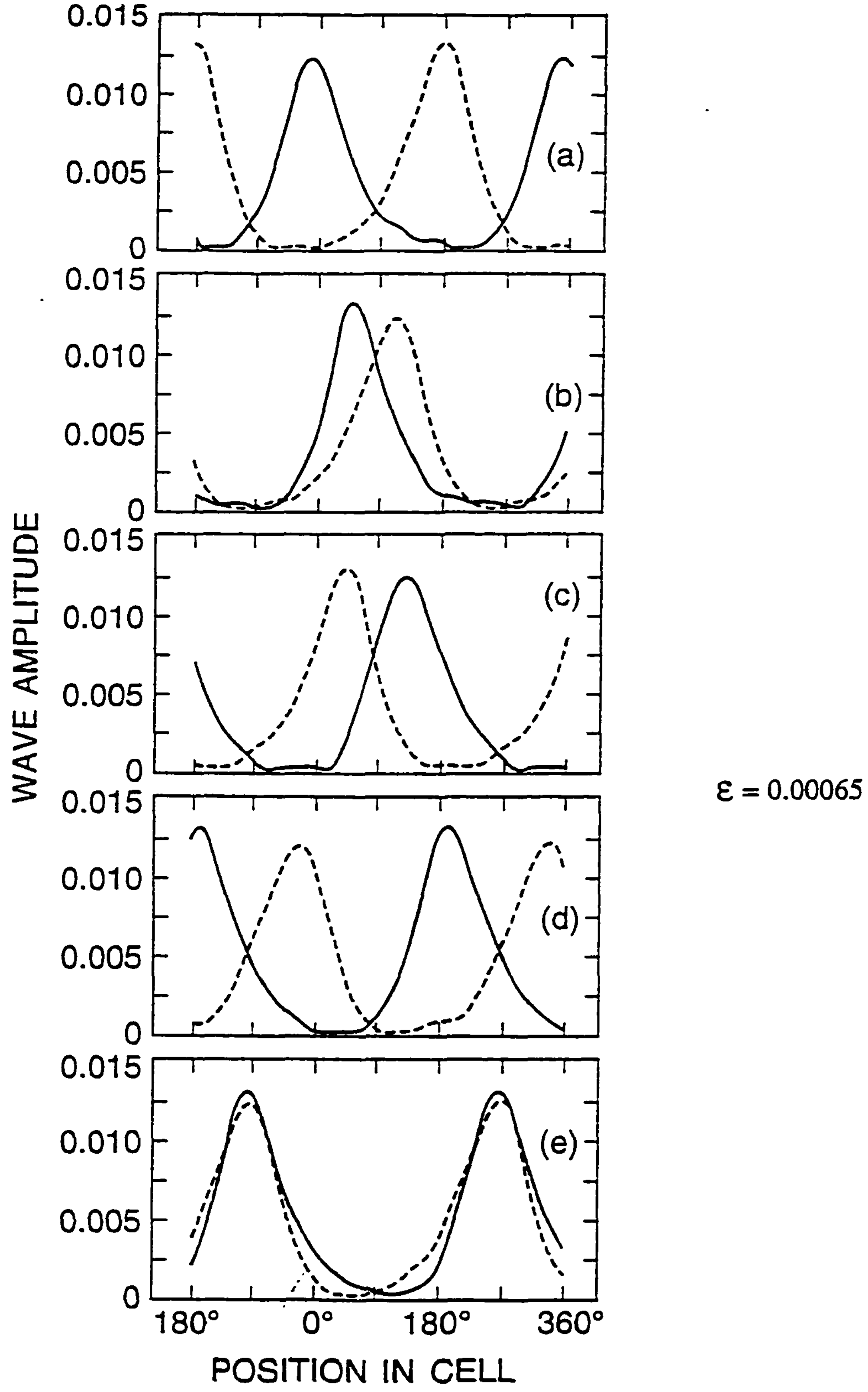

Figure 3.2: Frames (a)-(e) show the spatial profiles of the right- (full curves) and left-TW (dashed) amplitude profiles at times separated by 25.0 τ_v, with time increasing from (a) to (e).

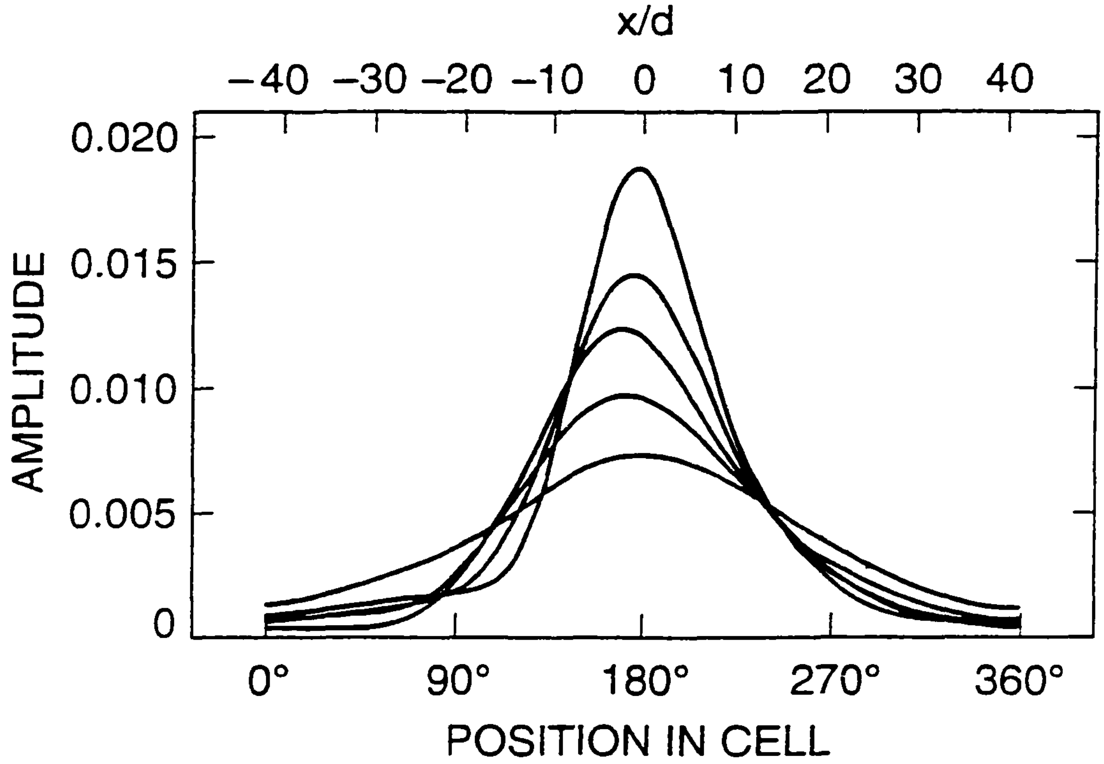

Figure 3.3: The time-averaged right-TW amplitude profiles are shown for CPWP states at several values of ϵ. From weakest to strongest amplitude profiles: $\epsilon = 0.00018(7)$, $\epsilon = 0.00043(7)$, $\epsilon = 0.00065(7)$, $\epsilon = 0.00095(7)$, and $\epsilon = 0.00166(7)$. With increasing ϵ, the amplitude profiles become stronger, narrower, and more asymmetric.

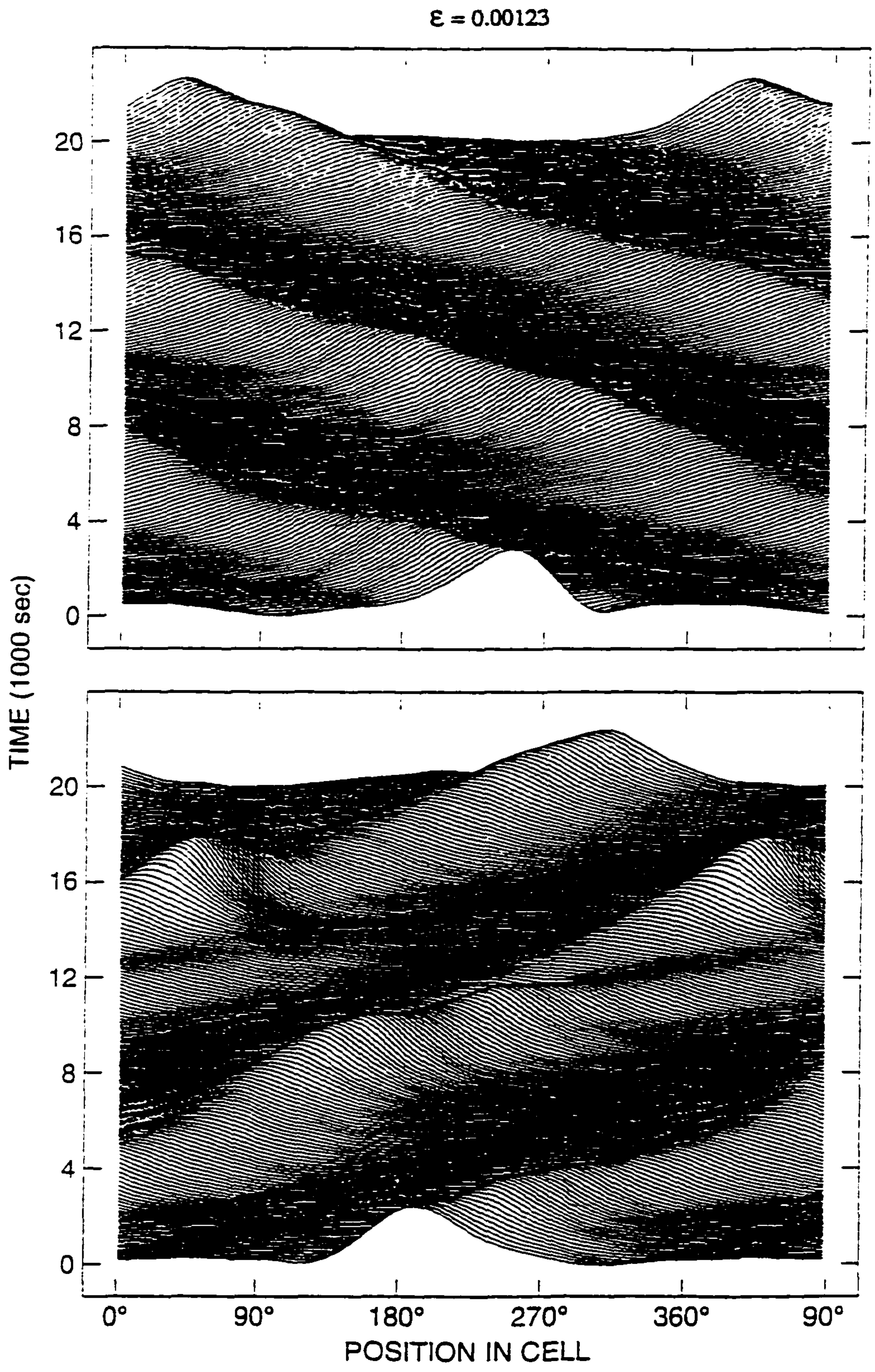

Figure 3.4: Hidden-line plot showing the evolution of the right-TW component of a CPWP state at $\epsilon = 0.00123(7)$. The vertical axis extends over a time $20000 sec = 390\tau_v$. Far clarity, 540^o of angle are shown.

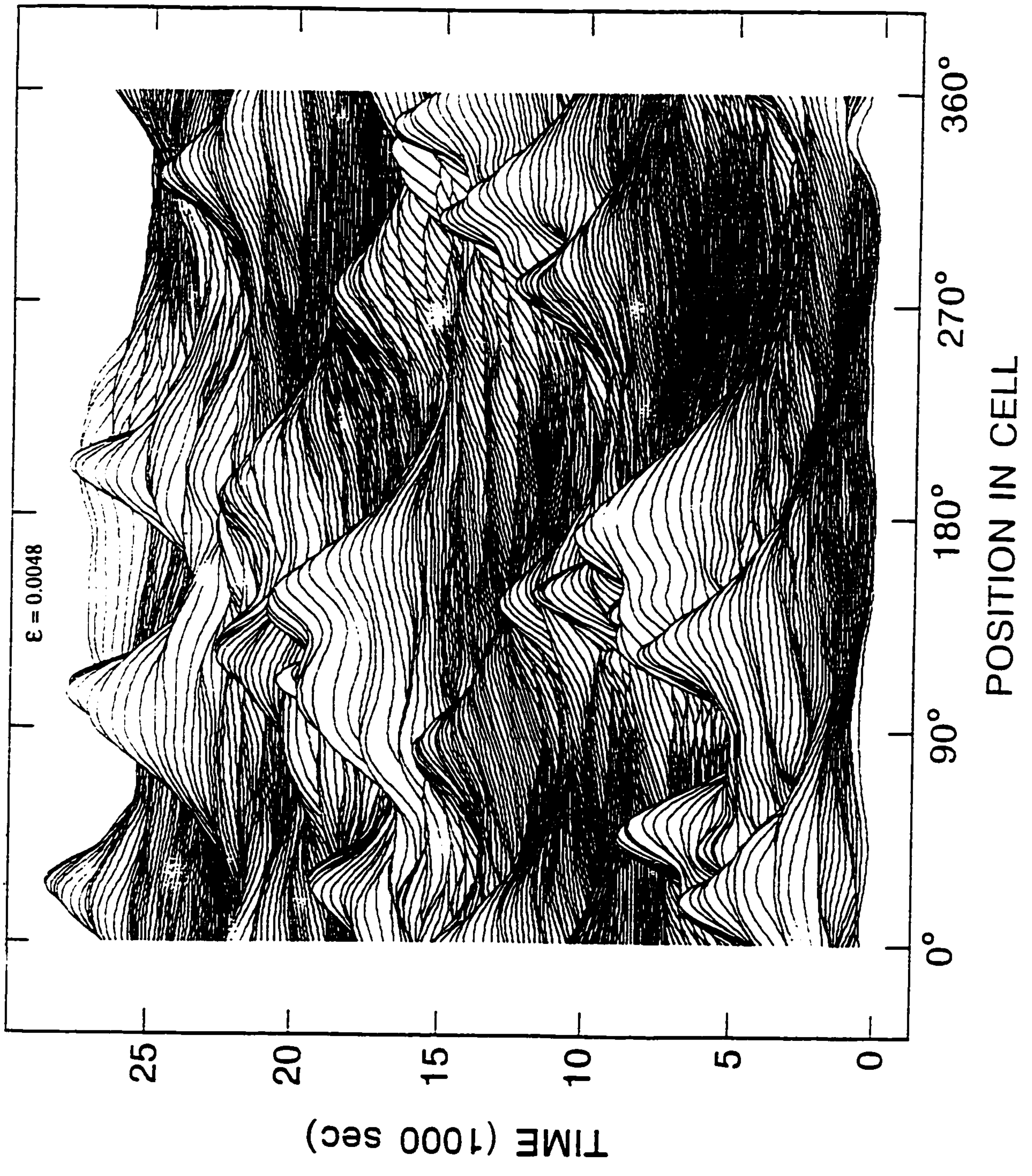

Figure 3.5: Hidden-line plot showing the evolution of the total demodulated TW amplitude for a state of dispersive chaos at $\epsilon = 0.0048$ over a period $25000 sec = 488\tau_v$.

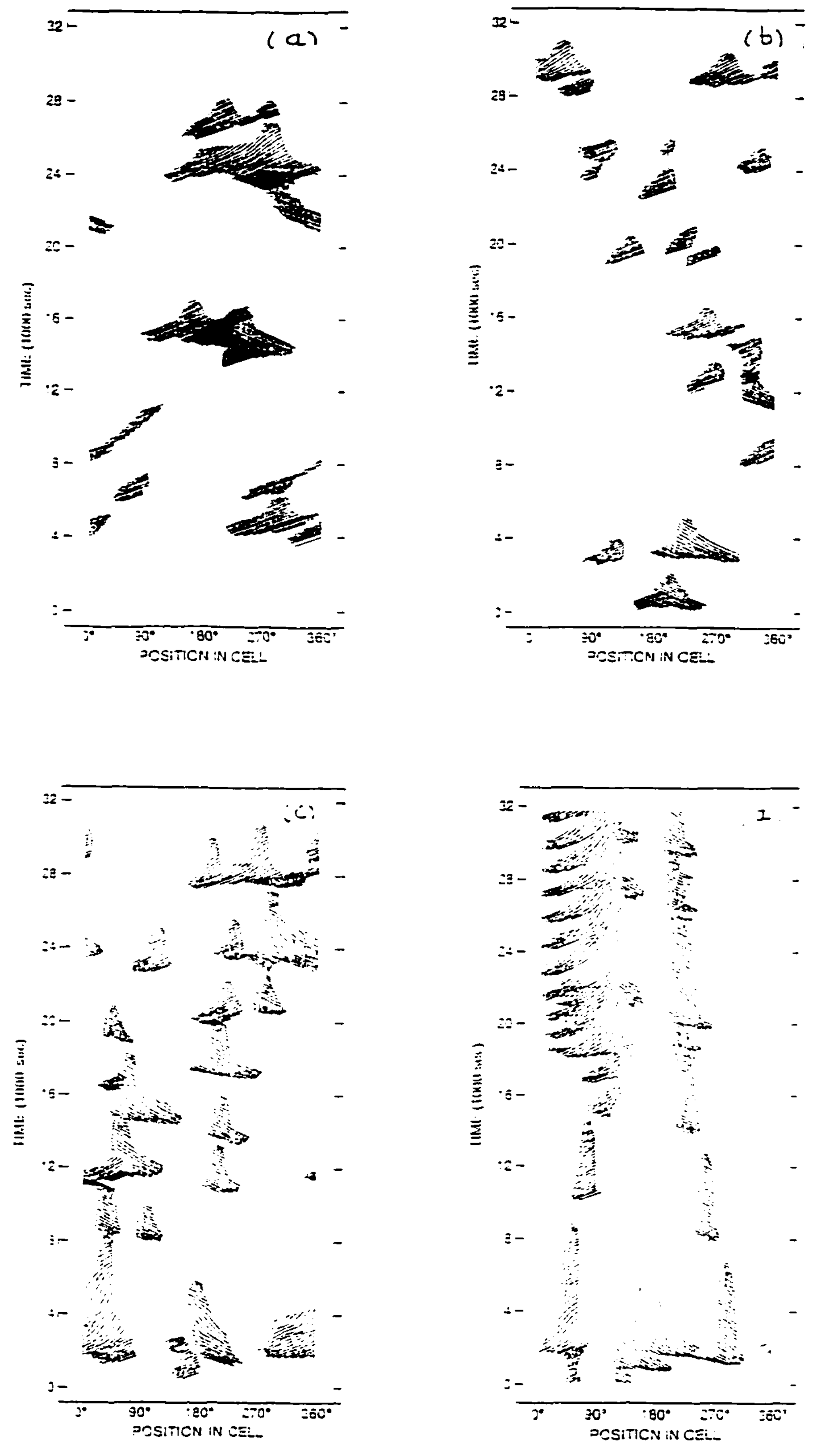

Figure 3.6: Spacetime diagrams of dispersive chaos. The vertical axis extends over $32000 sec = 625\tau_v$. (a) $\epsilon = 0.00200(6)$; (b) $\epsilon = 0.00323(5)$; (c) $\epsilon = 0.00744(5)$; (d) $\epsilon = 0.01098(8)$.

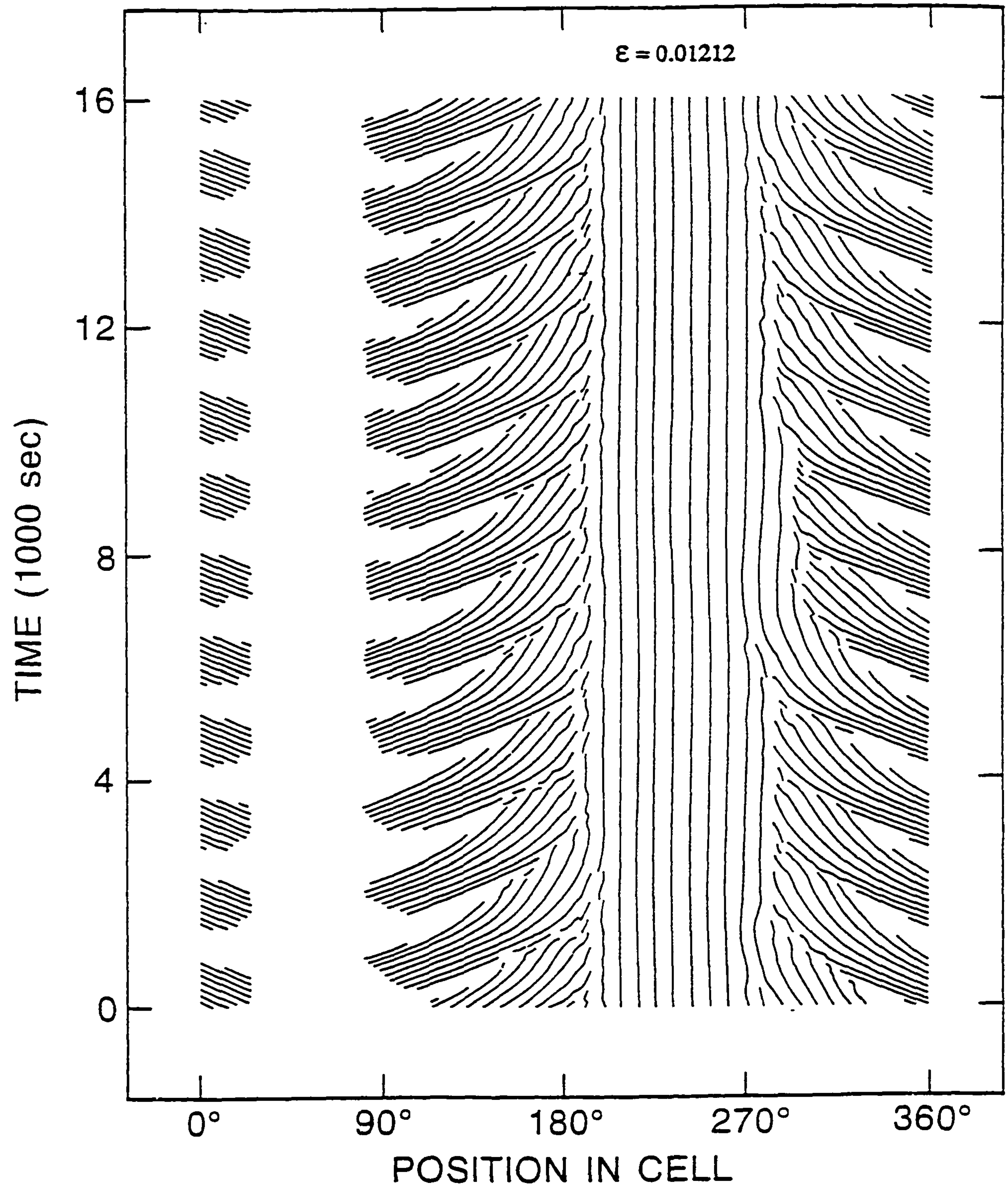

Figure 3.7: Coexisting state of TW bursts and steady rolls at $\epsilon = 0.01212(5)$. Time domain: $16000 sec = 312\tau_v$.

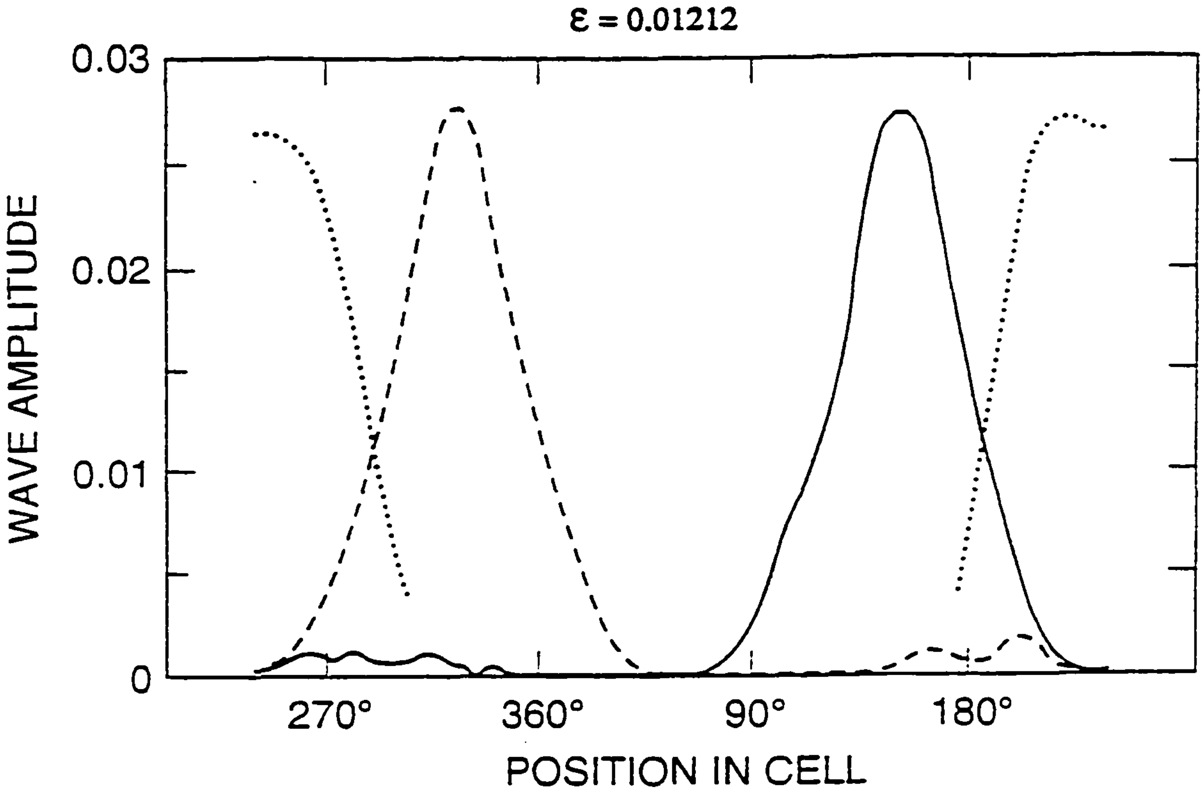

Figure 3.8: Time-averaged amplitude profiles for the TW/SR state at $\epsilon = 1212.10^{-5}$. For clarity, the horizontal axis has been shifted with respect to those figures. Solid curve: right-TW amplitude profile. Dashed curve: left-TW amplitude profile. Dotted curve: SR amplitude profile, reduced in vertical scale by a factor 5.5 and cut off at low amplitude for clarity.

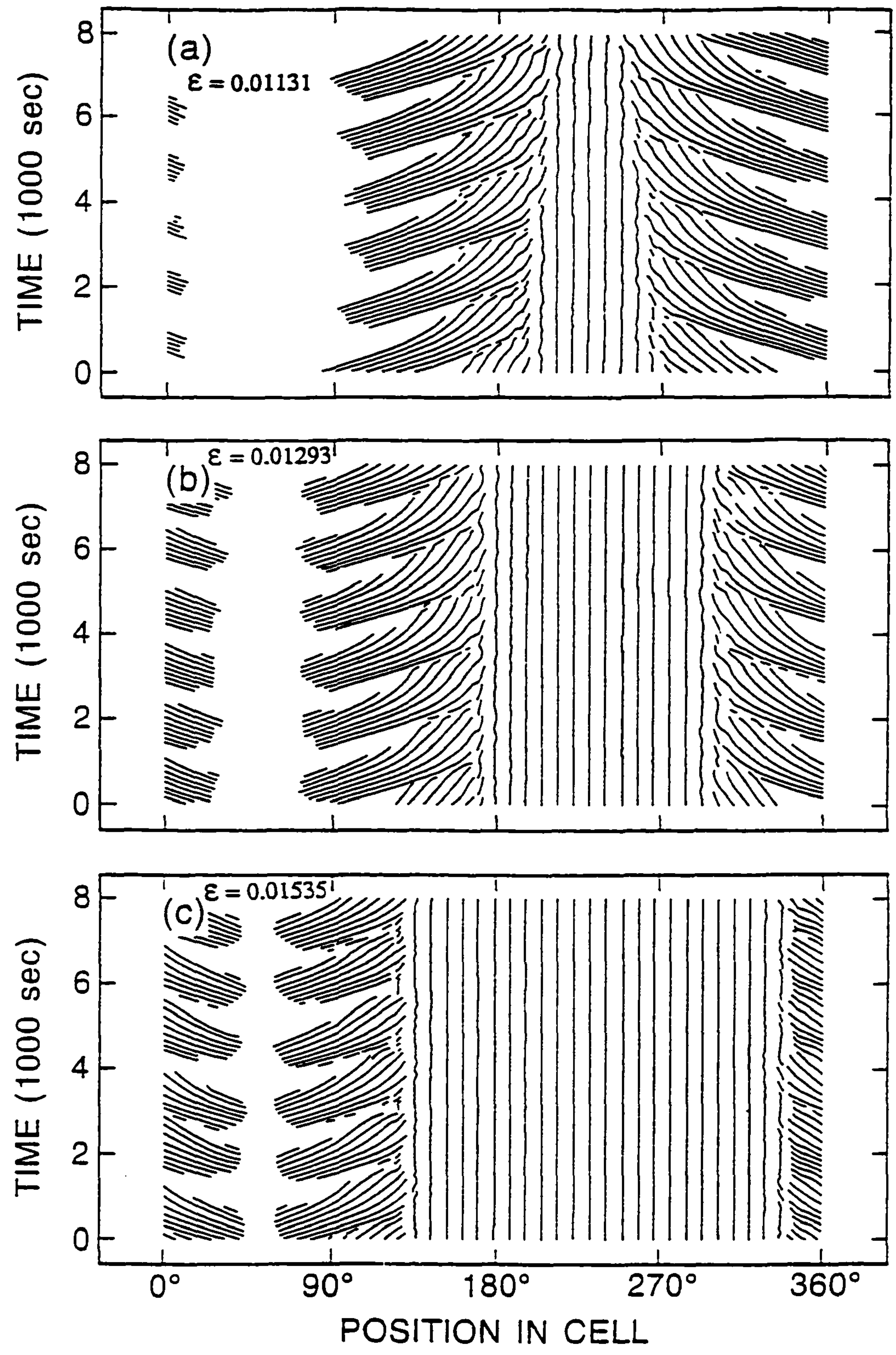

Figure 3.9: Evolution of the TW/SR state with Rayleigh number. Each frame covers a time domain $8000 sec = 156\tau_v$. (a): $\epsilon = 0.01131(5)$; (b): $\epsilon = 0.01293(5)$; (c): $\epsilon = 0.01535(5)$.

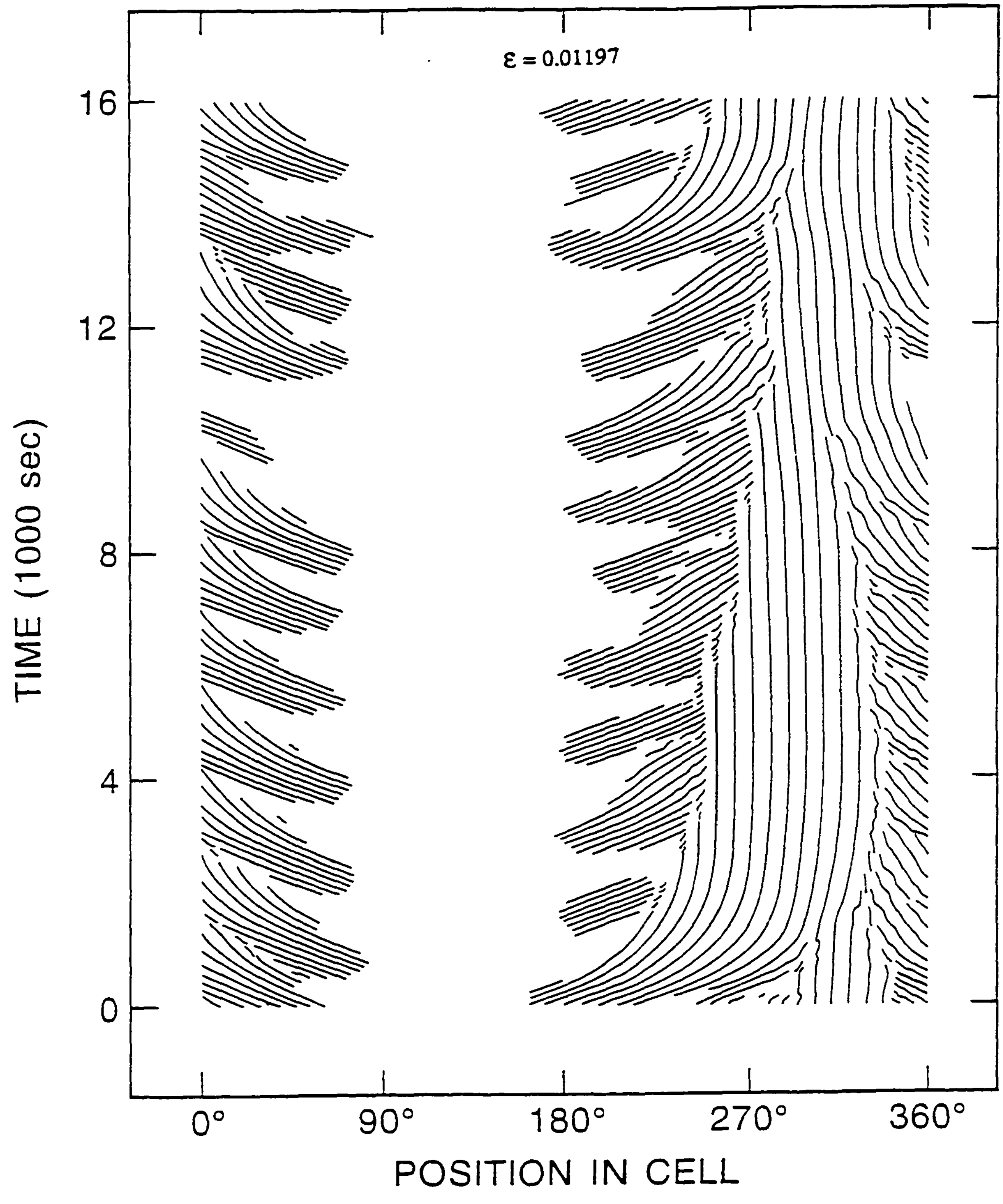

Figure 3.10: Spacetime diagram of an erratic TW/SR state at $\epsilon = 0.01197(8)$. The vertical axis covers an interval $16000 sec = 312\tau_v$.

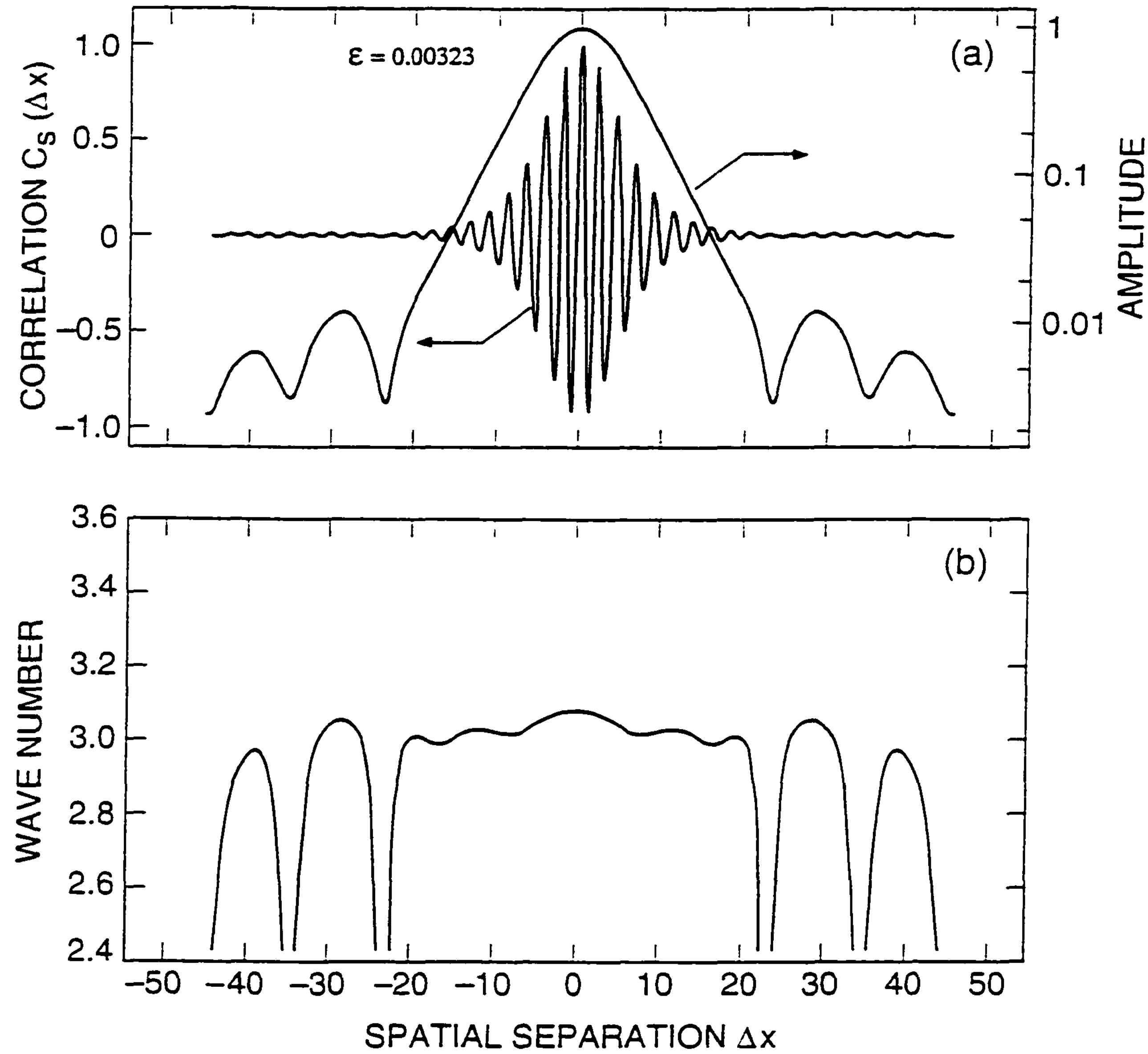

Figure 3.11: Time-averaged spatial correlation function $C_s(\Delta x)$ computed from the dispersive-chaos data at $\epsilon = 0.00323(5)$. (a) The oscillatory curve is $C_s(\Delta x)$. The smooth curve is the demodulated amplitude profile of the correlation function, plotted with a logarithmic vertical scale. The main body of this profile is approximately Gaussian. (b) Wavenumber profile of $C_s(\Delta x)$. The singularities are phase defects.

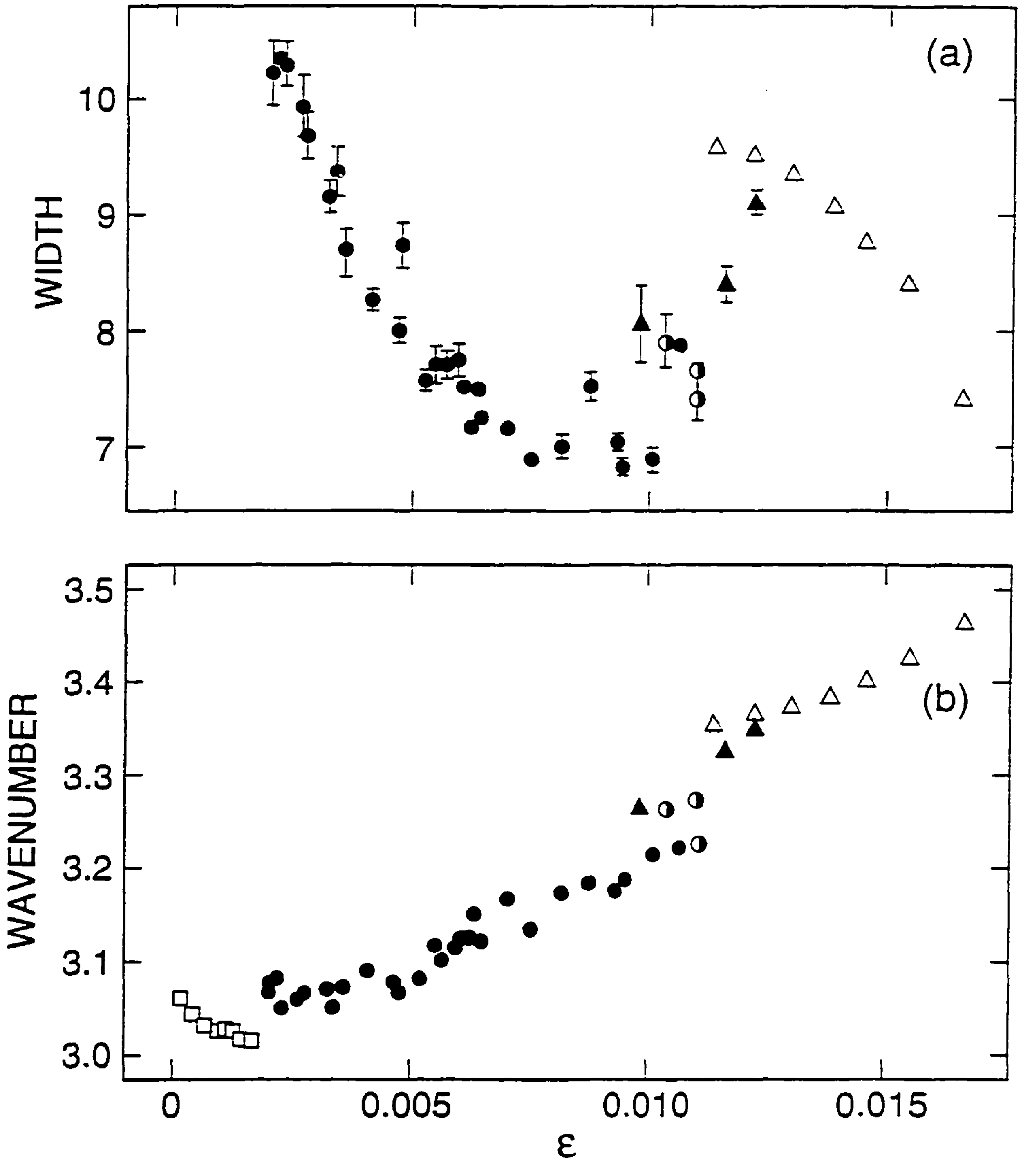

Figure 3.12: The width σ (a) and mean wave number k (b) extracted from fits to the time-averaged spatial correlation function $C_s(\Delta x)$ are plotted as functions of ϵ. The different symbols represent different dynamical states, as listed in Table 3.1. The uncertainties were estimated by performing the fits over spatial domains of varying sizes. For clarity, widths for CPWP states, which range from 15 to 35, are excluded from part (a).

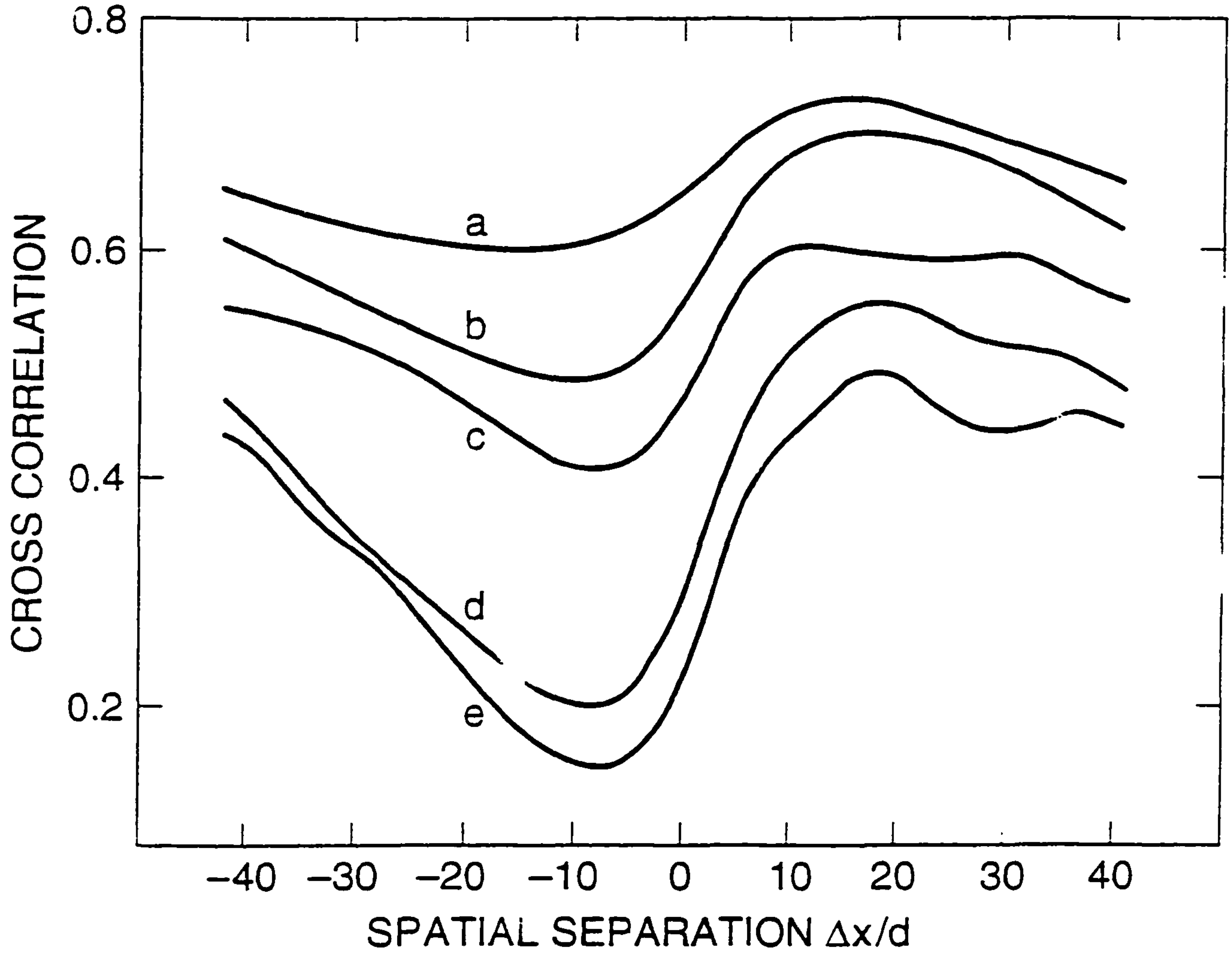

Figure 3.13: Time-averaged spatial cross-correlation functions computed from dispersive chaos data. (a) $\epsilon = 0.00200(6)$; (b) $\epsilon = 0.00323(5)$; (c) $\epsilon = 0.00516(5)$; (d) $\epsilon = 0.00744(5)$; (e) $\epsilon = 0.00934(7)$.

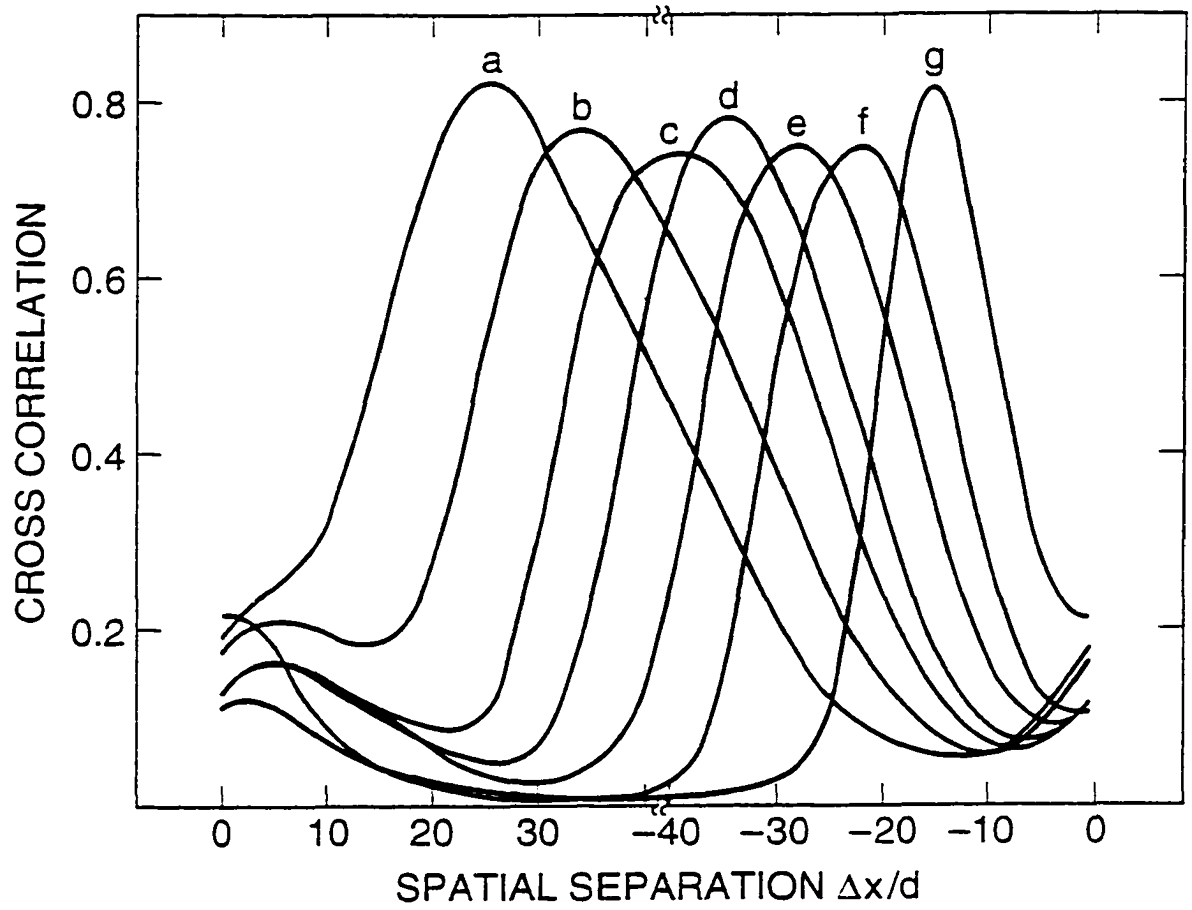

Figure 3.14: Time-averaged spatial cross-correlation functions computed from the hipass component of TW/SR data. (a) $\epsilon = 1131.10^{-5}$; (b) $\epsilon = 1212.10^{-5}$; (c) $\epsilon = 1293.10^{-5}$; (d) $\epsilon = 1370.10^{-5}$; (e) $\epsilon = 1446.10^{-5}$; (f) $\epsilon = 1535.10^{-5}$; (g) $\epsilon = 1650.10^{-5}$. For clarity, the horizontal axis has been shifted 180°.

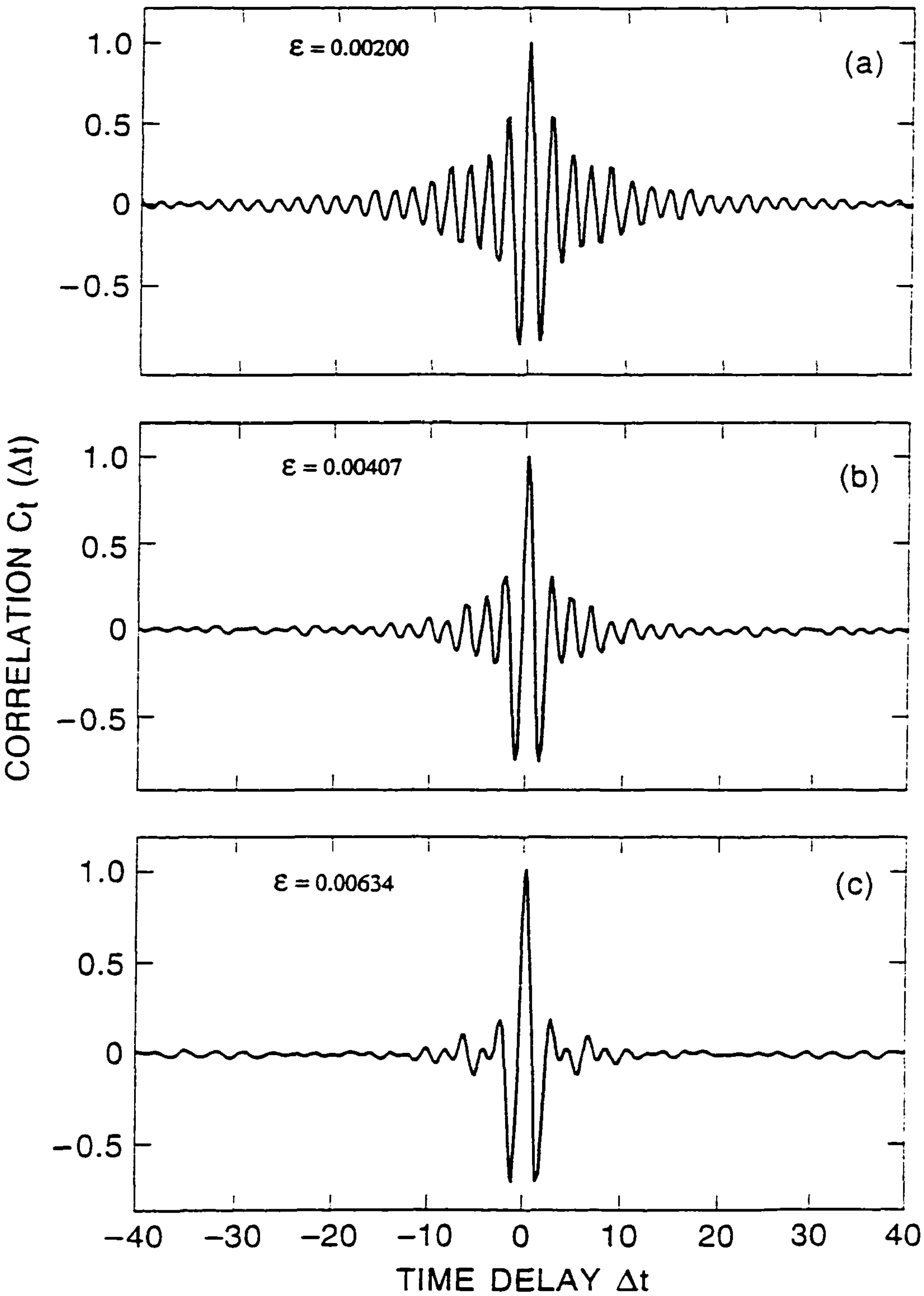

Figure 3.15: Space-averaged temporal correlation function $C_t(\Delta t)$ computed from the raw data in the regime of dispersive chaos. (a) $\epsilon = 0.00200(6)$; (b) $\epsilon = 0.00407(6)$; (c) $\epsilon = 0.00634(11)$. The phase-correlation time is short and decreases rapidly with ϵ.

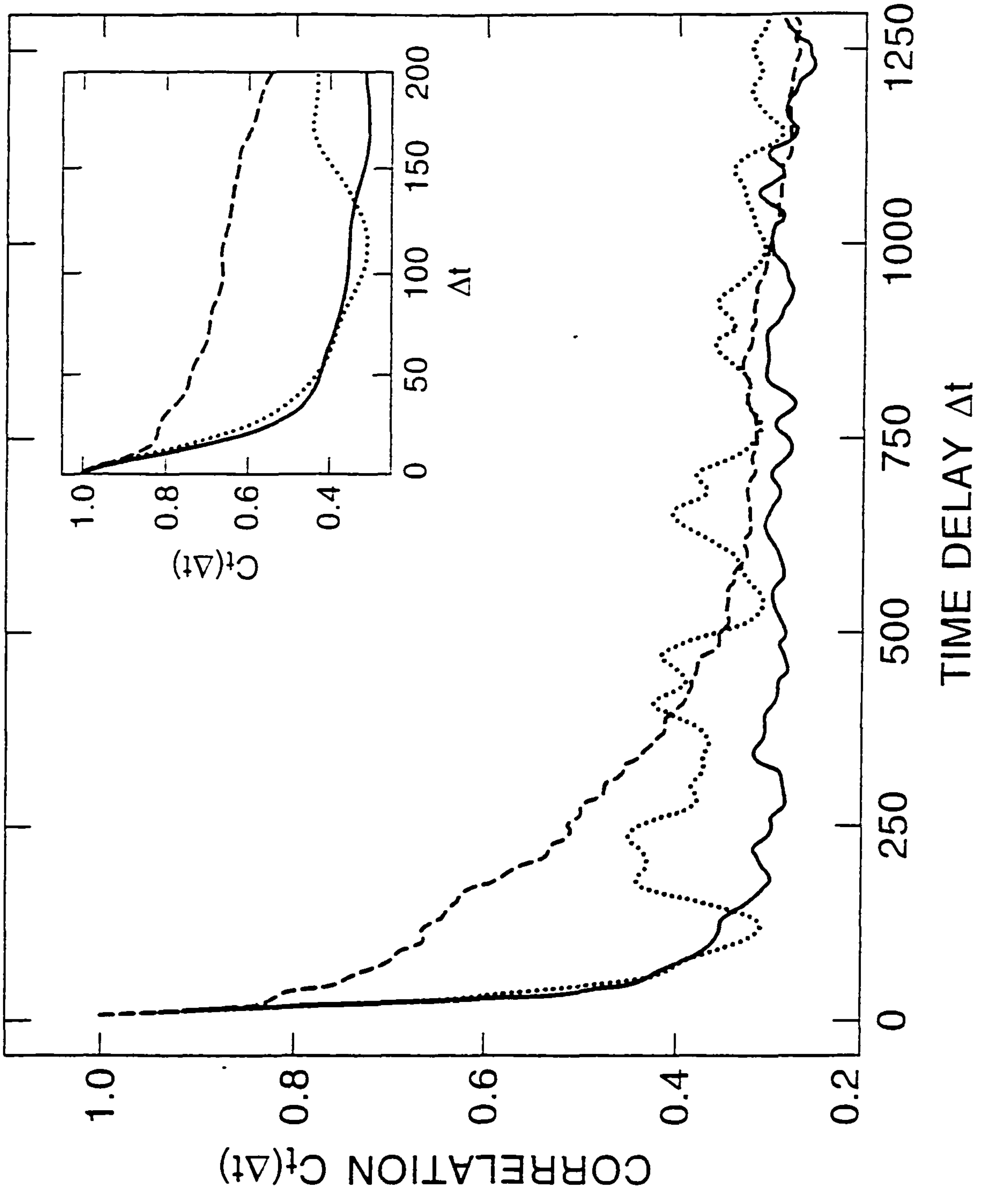

Figure 3.16: Space-averaged temporal correlation functions $C_t(\Delta t)$ for dispersive chaos states, computed from demodulated TW amplitude profiles. Each curve represents the average of the left- and right-TW components. The insert shows the behavior at short delay time. Dotted curves: $\epsilon = 200.10^{-5}$. Full curves: $\epsilon = 634.10^{-5}$. Dashed curves: $\epsilon = 1098.10^{-5}$.

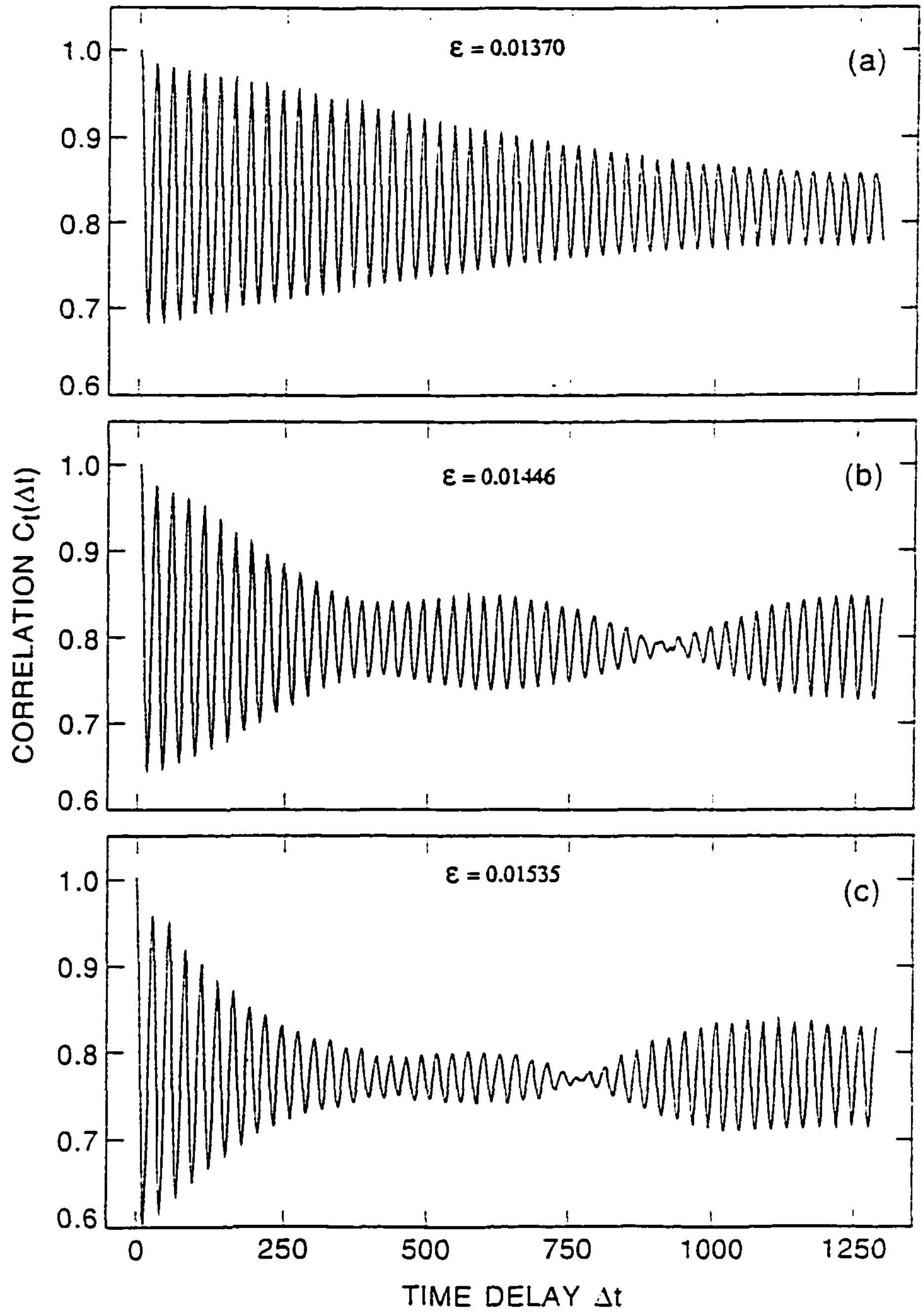

Figure 3.17: Space-averaged temporal correlation functions $C_t(\Delta t)$ for TW/SR states, computed from demodulated TW amplitude profiles of the hipass component of the raw data. Each curve represents the average of the left- and right-TW components: (a) $\epsilon = 0.01370(5)$: monoperiodic modulation with weak phase drift. (b) $\epsilon = 0.01446(5)$: quasiperiodic modulation. (c) $\epsilon = 0.01535(5)$: erratic modulation.

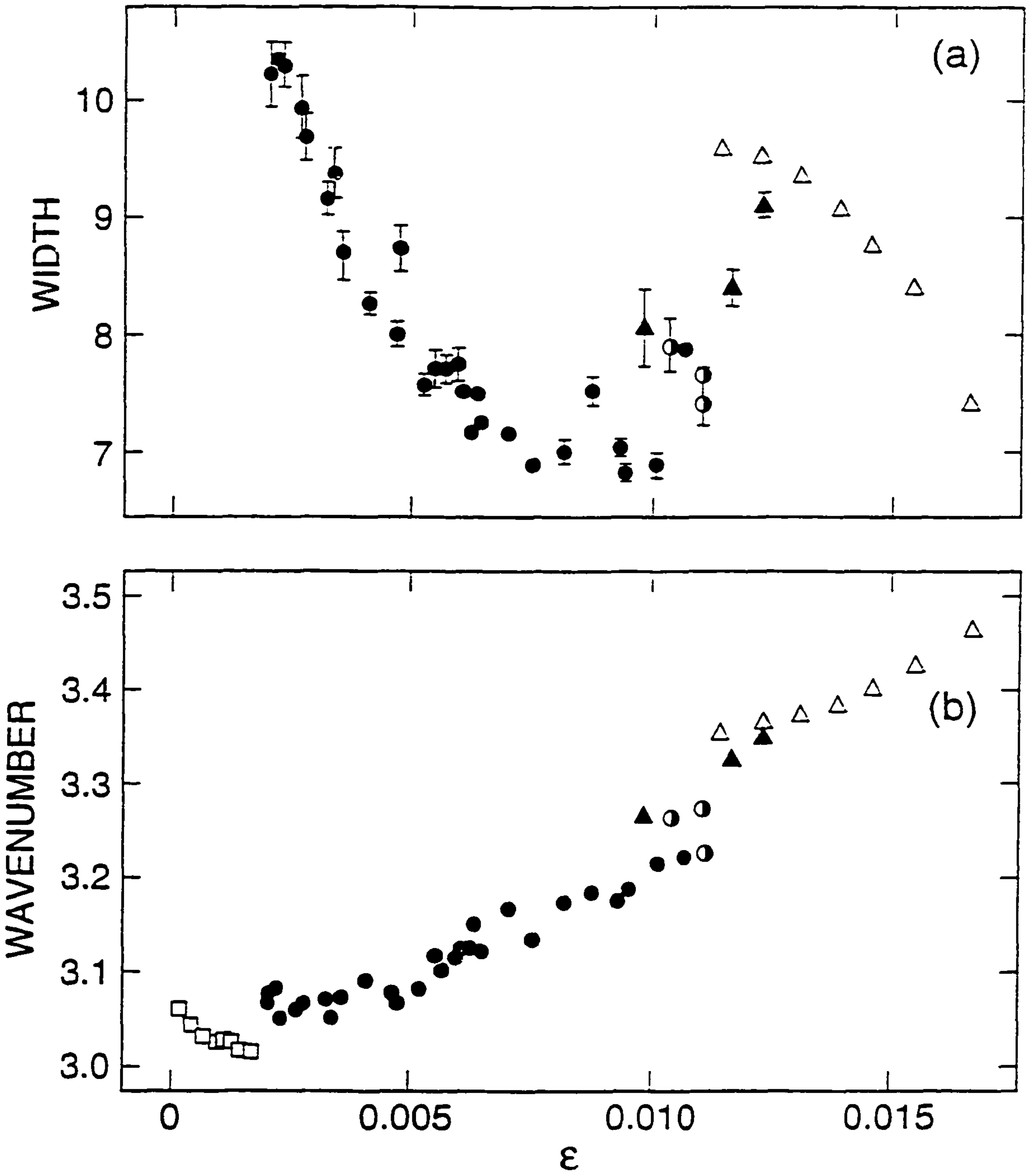

Figure 3.18: The dimensionless burst frequency f_b is plotted as a function of ϵ. In the dispersive chaos regime, f_b is computed by counting the number of bursts in each data set. In the CPWP and TW/SR regimes, f_b is computed from the temporal modulation spectrum by dividing the angular modulation frequency by π.

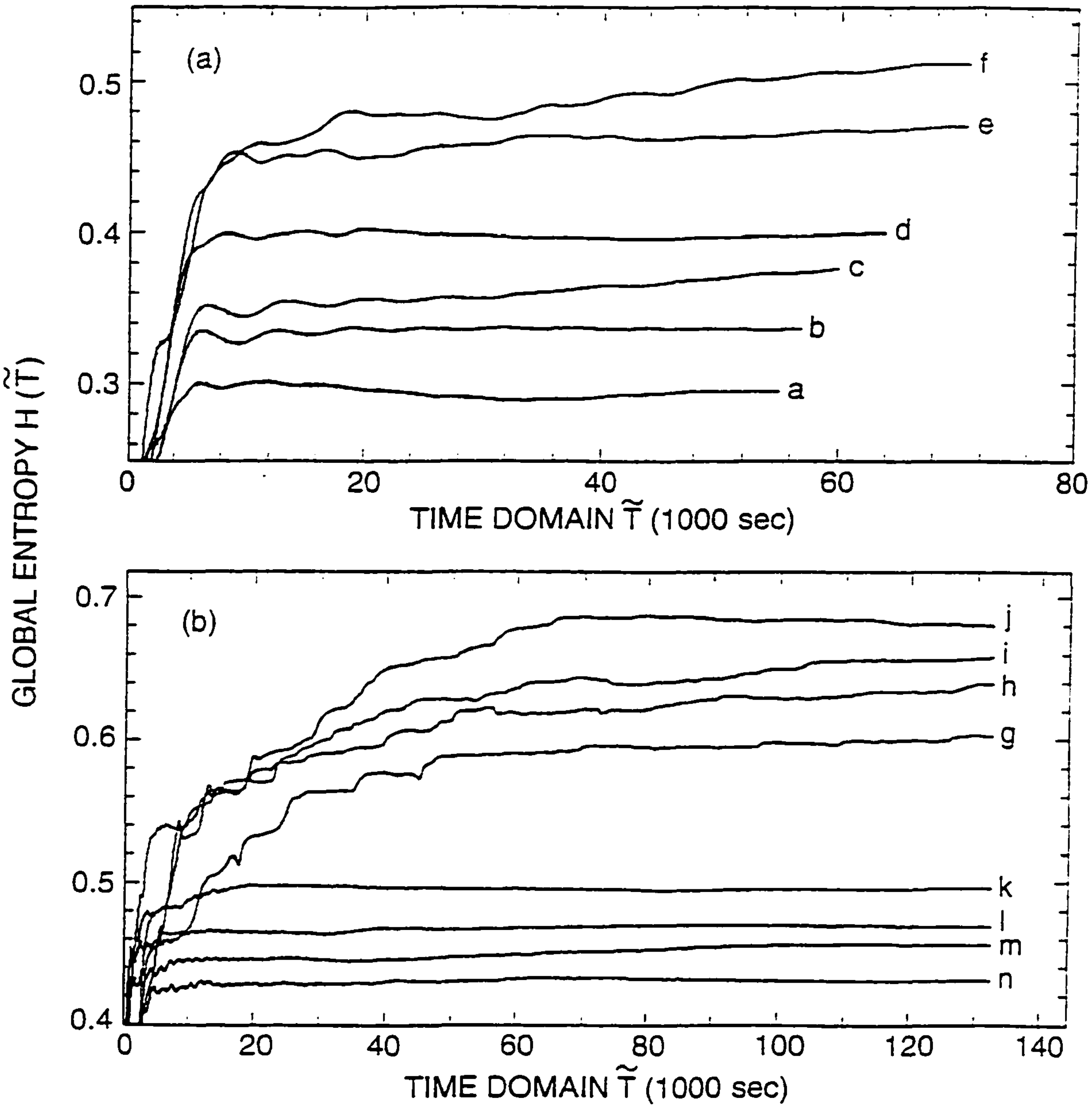

Figure 3.19: The saturation behavior of the global entropy H is illustrated by plotting $H(\tilde{T})$ as a function of the length $\tilde{T}$ of the time domain used for the calculation. ϵ increases monotonically on moving through the curves from a to n. (a) CPWP data. a: $\epsilon = 18.10^{-5}$; b: $\epsilon = 43.10^{-5}$; c: $\epsilon = 65.10^{-5}$; d: $\epsilon = 95.10^{-5}$; e: $\epsilon = 143.10^{-5}$; f: $\epsilon = 166.10^{-5}$. (b) Upper curves: dispersive-chaos data. g: $\epsilon = 200.10^{-5}$; h: $\epsilon = 407.10^{-5}$; i: $\epsilon = 634.10^{-5}$; j: $\epsilon = 1000.10^{-5}$. Lower curves: TW/SR data. k: $\epsilon = 1212.10^{-5}$; l: $\epsilon = 1370.10^{-5}$; m: $\epsilon = 1446.10^{-5}$; n: $\epsilon = 1535.10^{-5}$.

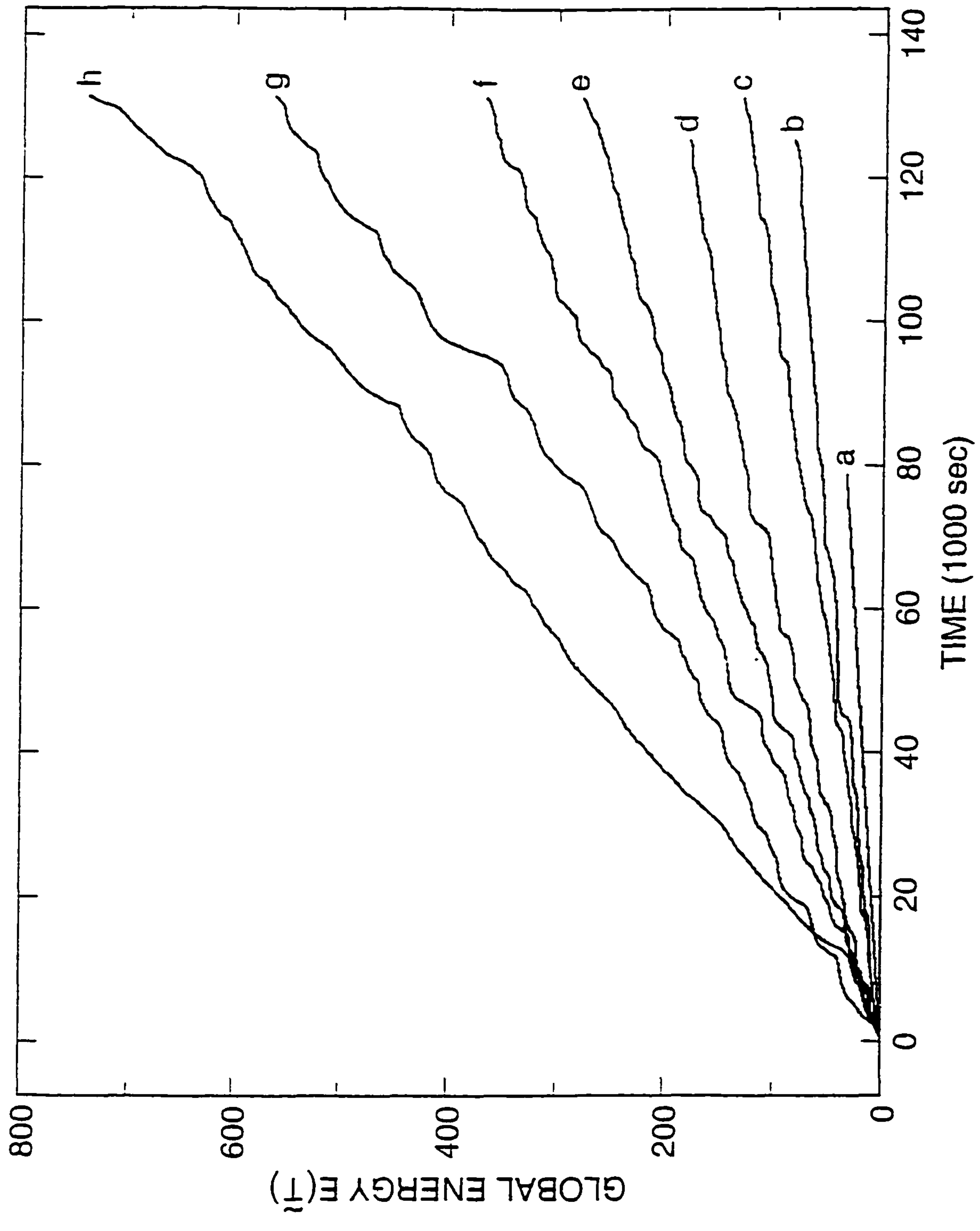

Figure 3.20: The global energy $E(\tilde{T})$ is plotted as a function of the length $\tilde{T}$ of the time domain used for the calculation. Curve a: $\epsilon = 95.10^{-5}$; b: $\epsilon = 200.10^{-5}$; c: $\epsilon = 323.10^{-5}$; d: $\epsilon = 407.10^{-5}$; e: $\epsilon = 634.10^{-5}$; f: $\epsilon = 744.10^{-5}$; g: $\epsilon = 1000.10^{-5}$; h: $\epsilon = 1098.10^{-5}$.

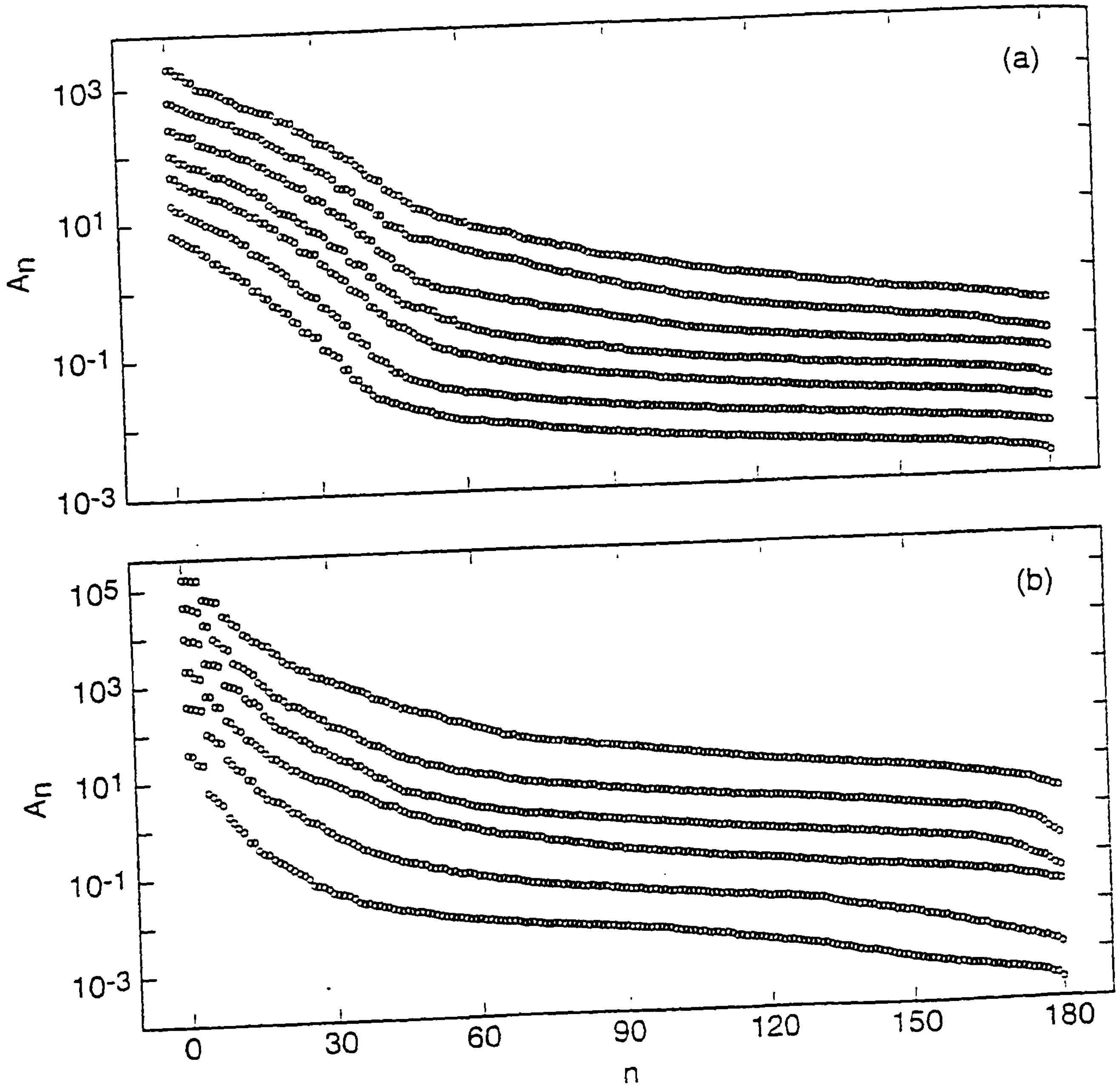

Figure 3.21: Eigenvalue spectra produced by BOD analysis. (a) Dispersive-chaos data. From bottom to top: $\epsilon = 200.10^{-5}$; $\epsilon = 323.10^{-5}$; $\epsilon = 407.10^{-5}$; $\epsilon = 516.10^{-5}$; $\epsilon = 634.10^{-5}$; $\epsilon = 744.10^{-5}$; $\epsilon = 934.10^{-5}$. Successive curves are displaced upwards by a factor of 2 for clarity. (b) TW/SR data. From top to bottom: $\epsilon = 1212.10^{-5}$; $\epsilon = 1293.10^{-5}$; $\epsilon = 1370.10^{-5}$; $\epsilon = 1446.10^{-5}$; $\epsilon = 1535.10^{-5}$; $\epsilon = 1650.10^{-5}$. Successive curves are displaced downwards by a factor of 4 for clarity.

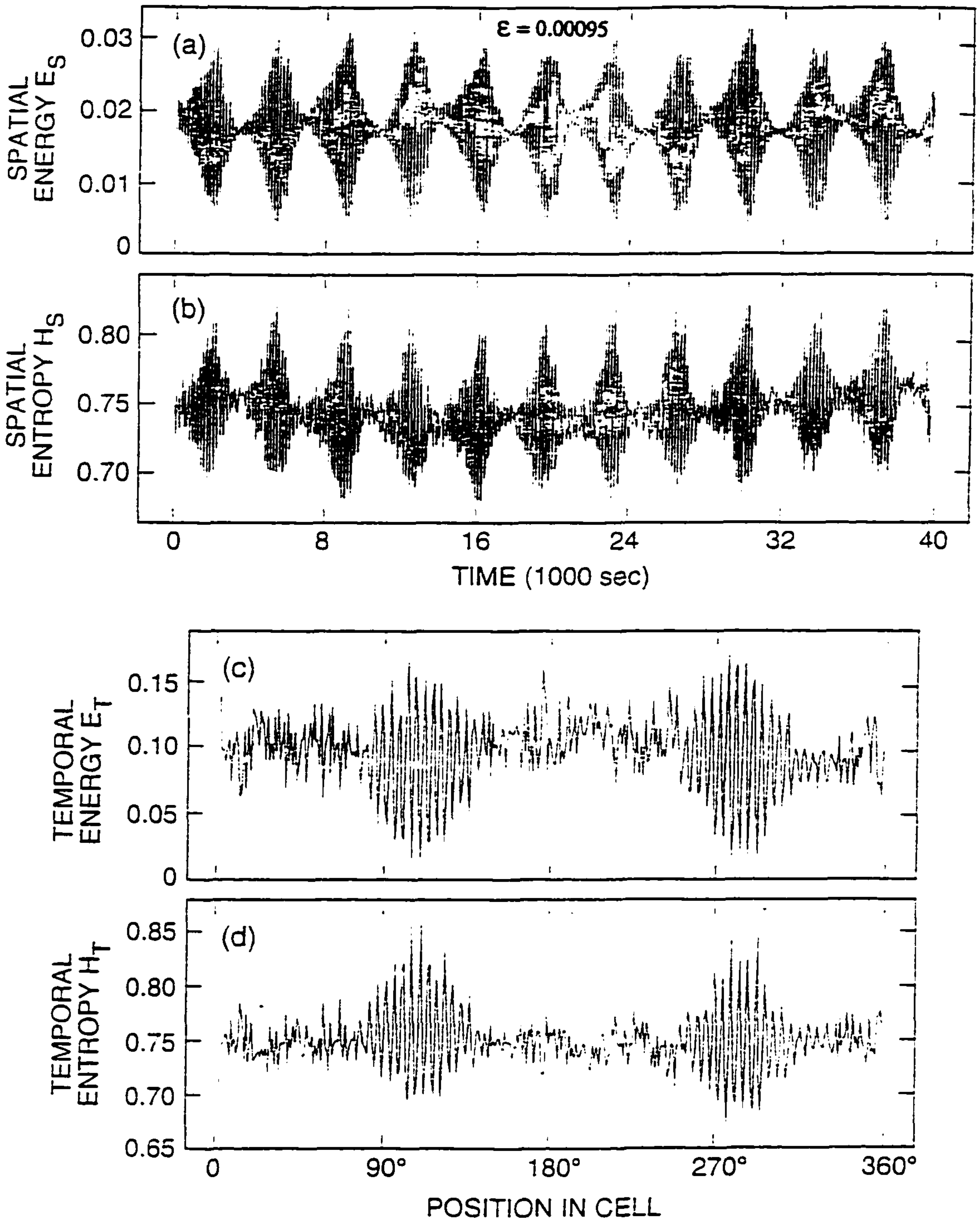

Figure 3.22: The top two frames show the instantaneous spatial energy $E_S(t)$ (a) and spatial entropy $H_S(t)$ (b) as functions of time for a CPWP state at $\epsilon = 95.10^{-5}$. For clarity, these plots and those in Figs. 3.23 and 3.24 cover only half of the temporal duration of the data set. The slow modulations (period 3533 sec) correspond to the propagation of the wave packets halfway around the cell. The bottom two curves show the temporal energy $E_T(x)$ and the temporal entropy $H_T(x)$ as functions of spatial position.

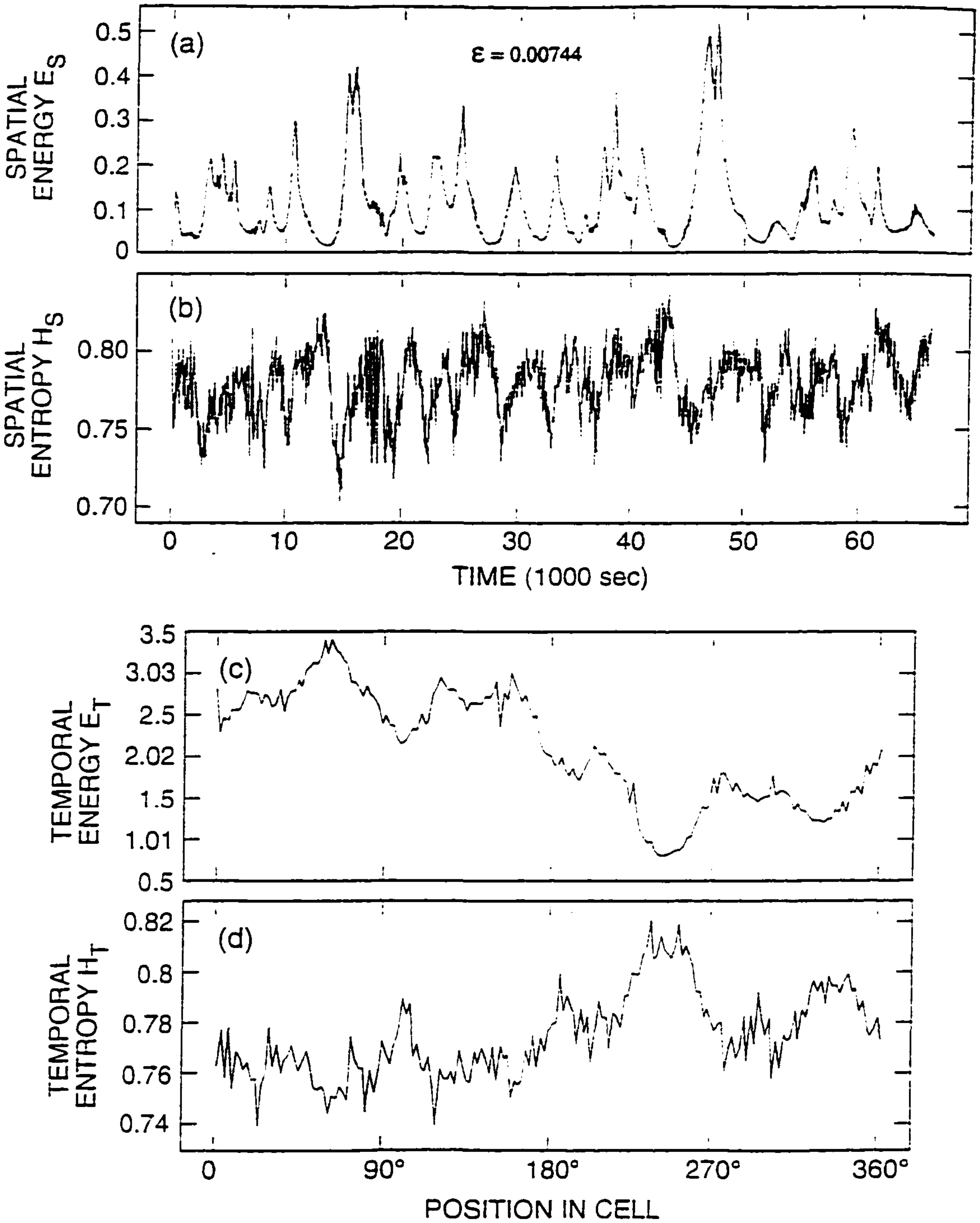

Figure 3.23: The spatial energy (a), spatial entropy (b), temporal energy (c), and temporal entropy (d) are plotted for the dispersive-chaos data set at $\epsilon = 0.00744(5)$. The spatial energy (a) and entropy (b) exhibit bursts and dips, respectively, caused by the appearance of TW bursts. The temporal energy and entropy exhibit large-scale spatial structure due to the finite number of bursts in the data set.

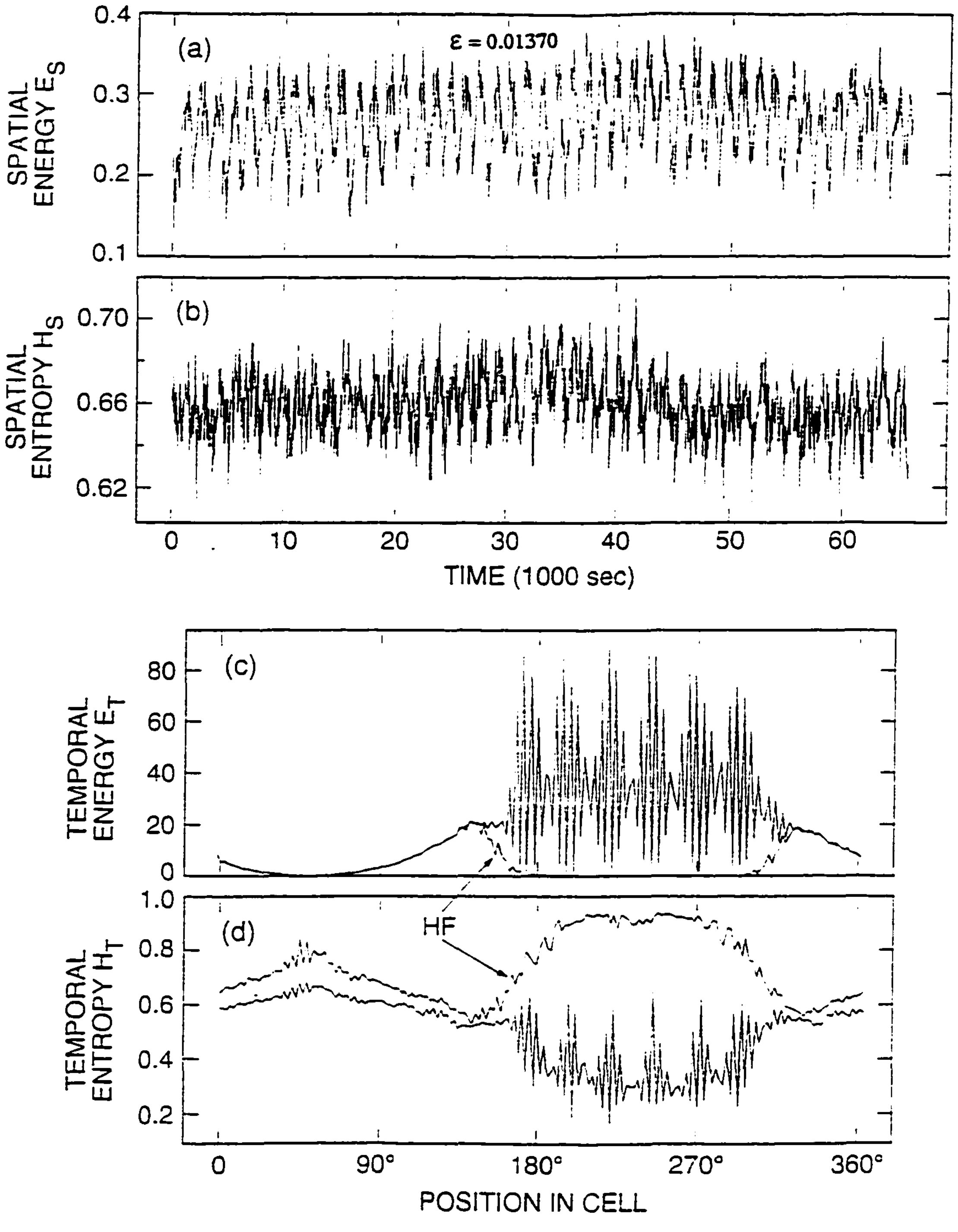

Figure 3.24: The spatial energy (a), spatial entropy (b), temporal energy (c), and temporal entropy (d) are plotted for a TW/SR data set at $\epsilon = 0.01370(5)$. In (c) and (d), the curves labeled "HF" were computed from data that had been passed through a temporal hipass filter to suppress the steady rolls seen between locations 160° and 310°. The other two curves were computed using data in which the SR component was retained.

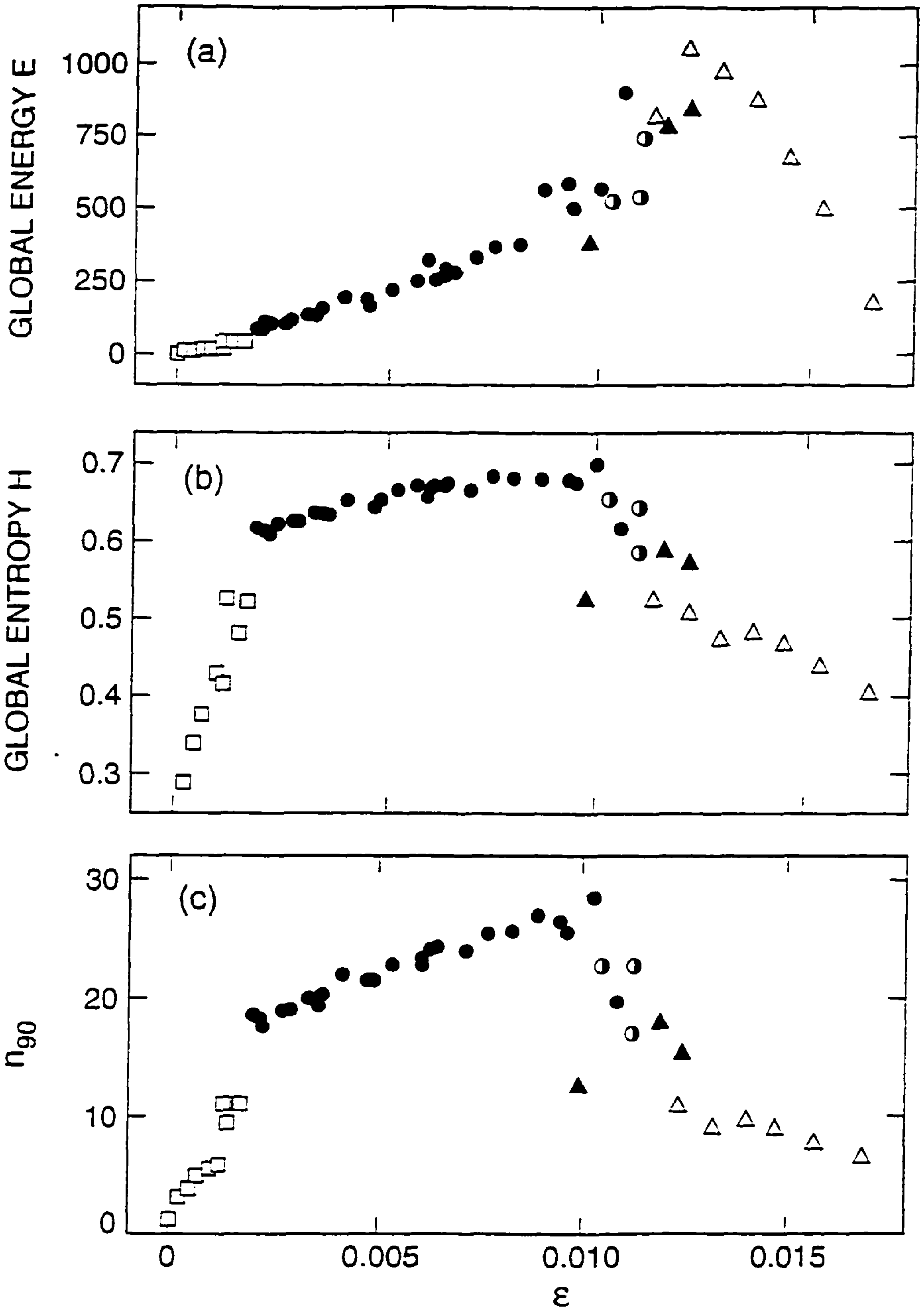

Figure 3.25: Global measures of dynamical behavior, derived from BOD analysis, are plotted *vs.* ϵ. (a) Global energy E; (b) Global entropy H; (c) Number of terms n_{90} in the BOD expansion required to recover 90% of the spectral energy of the original data. In the TW/SR state, the calculations were performed using temporal-hipass-filtered data to isolate the TW dynamics and suppress contributions from steady rolls. The CPWP, DC, and TW/SR states are readily distinguished by the ϵ dependence of these global quantities.

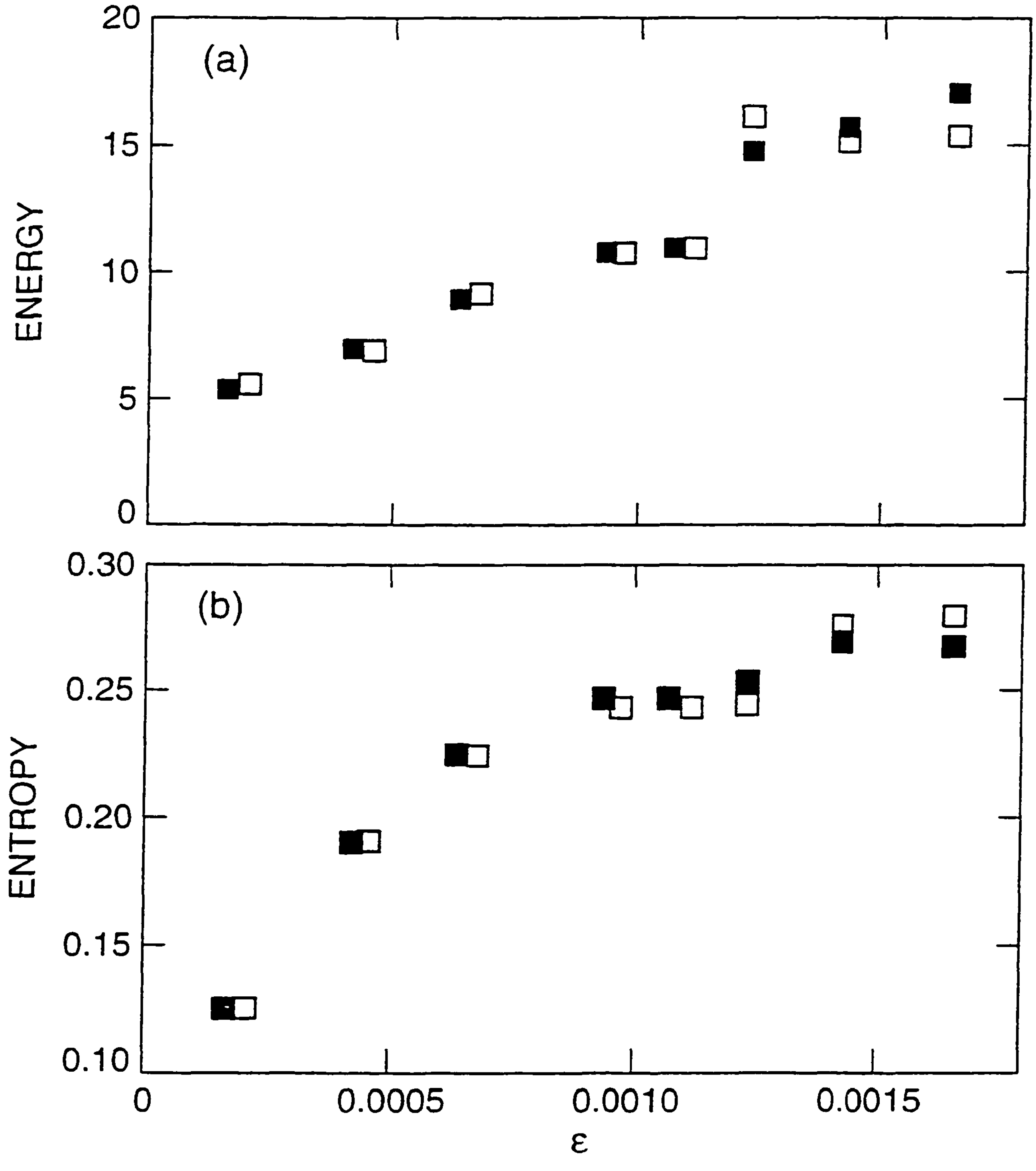

Figure 3.26: Evolution with ϵ of the global energy (a) and entropy (b) computed from demodulated left-TW (closed symbols) and right-TW (open symbols) amplitude profiles in the CPWP regime. Above $\epsilon \approx 0.0010$, the two TW components begin to evolve independently.

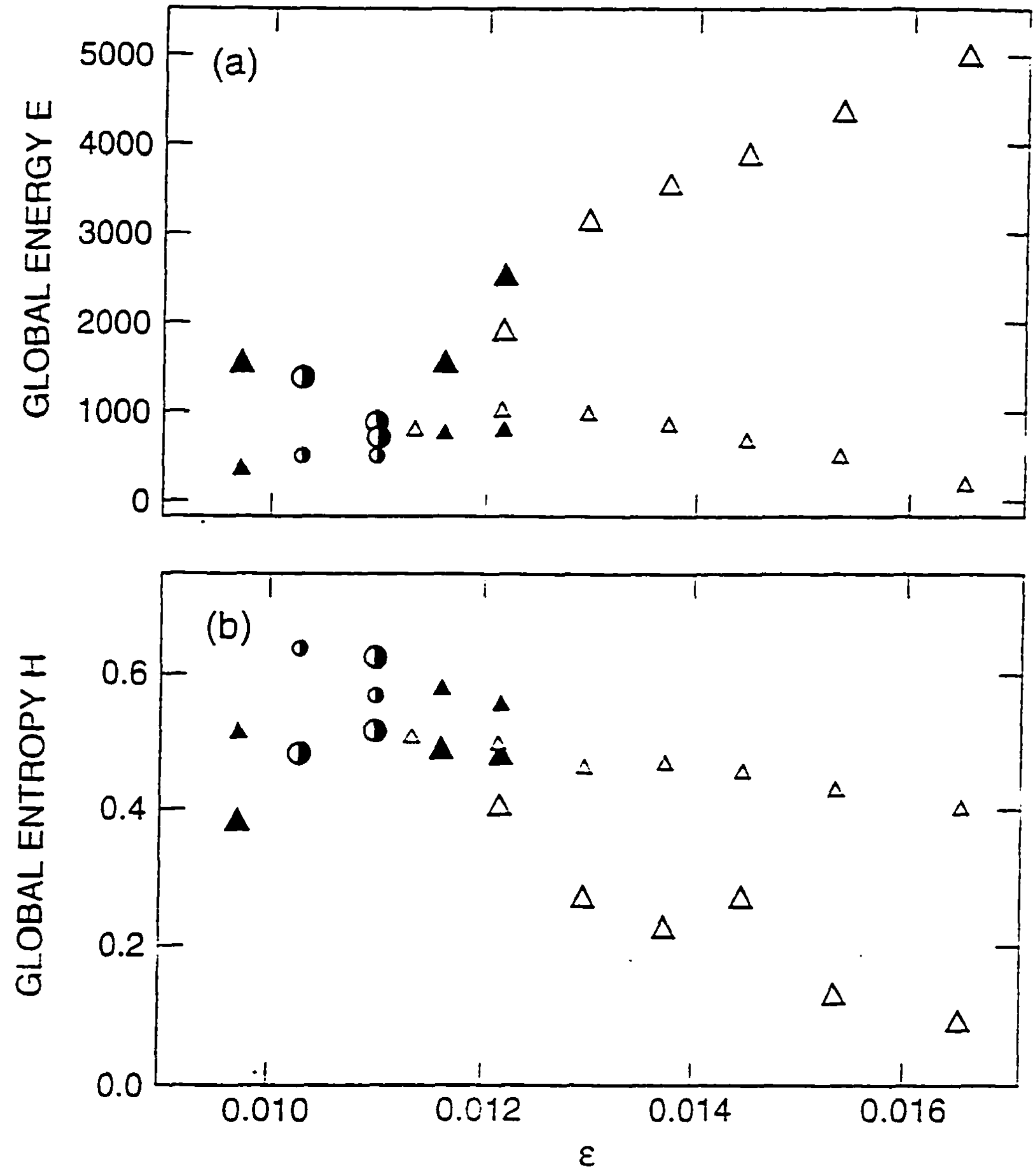

Figure 3.27: Effect of retaining or suppressing the contributions of steady rolls on the global energy (a) and entropy (b) in the TW/SR regime. In both of these graphs, the small symbols are taken from Fig. 3.25 and represent calculations performed on temporal-hipass-filtered data in which the SR component is suppressed. The large symbols represent the results of calculations performed on data in which this component was retained. Thus, the difference between the trends of the small and large symbols may be associated with the SR component. As ϵ is increased, the growing region of large-amplitude, steady rolls makes a large, positive contribution to the spectral energy and causes the entropy to decrease.

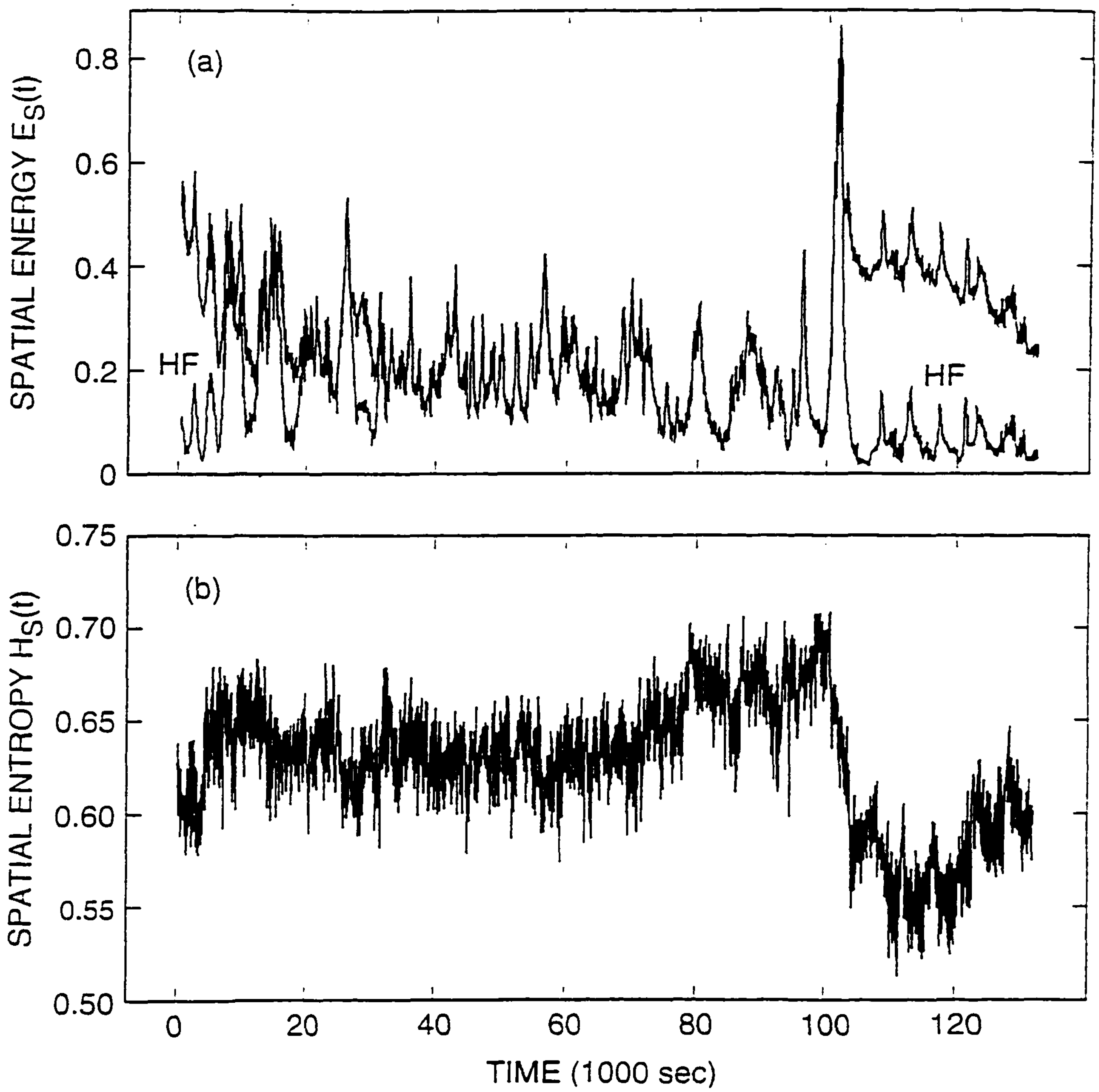

Figure 3.28: The spatial energy (a) and the spatial entropy (b) reveal switching of dynamics between DC and TW/SR at $\epsilon = 0.01097(8)$. At time 8000 sec, low-entropy, TW/SR dynamics gives way to a high-entropy DC state; the dynamics switch back at t = 101000 sec. These dynamical changes are signaled by opposing jumps in the spatial entropy and energy. In (a), the curve marked "HF" was computed using temporal-hipass-filtered data to suppress the contribution of steady rolls.

Chapter 4

Structures and Dynamics of Counterpropagating Waves

Introduction

This chapter aims at studying traveling waves patterns observed just above onset in thermal convection of binary fluids in a weakly-nonlinear regime. This regime is succeeded by a complicated space-time state termed *dispersive chaos*. Our goal in the following study is to gain some understanding of the underlying dynamics of the first state in an attempt to establish a possible route to the chaotic behavior in dispersive chaos.

Usually, reducing the study of the dynamics to a small phase space where sequence of transitions could be reminiscent of systems with a small number of degrees of freedom seems a natural approach. This, unfortunately, was not *a priori* very helpful, since, as has been explained earlier, classical (temporal) scenarios fail to account for the situation presented in these experiments. This study also aims at isolating the 'proper' mechanism that causes the appearance of the weakly chaotic behavior featured in the *Counterpropagating Wave Packets* (CPWP) regime. Dispersive chaos, with overwhelming strong nonlinear dispersion, presents complex space-time bursting events which, in addition to their traveling character, appear and collapse in somewhat random manner, thus featuring local space-time behavior which is hard to study using the tools of classical dynamical systems theory. Despite the simplicity of the counterpropagating wave packets, which consist of two localized pulse-like shaped profiles traveling in opposite directions, this regime presents intriguing dynamical behavior. Indeed, as the reduced Rayleigh number, ϵ, the main control parameter, is increased within the CPWP regime, some visually discernable *irregularities* appear. We are interested below in *precisely* determining both the nature of these irregularities as well as their effects on dynamics.

Even though these irregularities are quite weak and even weaker for low values of ϵ (near onset) which makes their detection difficult using spectral or demodulation techniques, that should not undermine their potential to affect the dynamics even at small Rayleigh numbers. Indeed, by performing dynamical analysis based upon the BOD techniques, their presence is revealed more clearly, and shows the essence of the role they play in the dynamics. Based on a simple representation,[1] we have been able to understand these irregularities, their nature and structures.

The underlying assumption of the theoretical approach is that some sort of expansion is possible, considering that CPWP is a weakly-nonlinear regime. Recall that CPWP consist of a pair of wave packets which travel around the annular cell in opposite directions with similar group velocities. Decomposing therefore the total wave field into left and right components thus permits the study of each component independently. Hence, we consider each component to be a perturbed uniformly traveling wave, such as

$$u_{L,R}(x,t) = u_o^{L,R}(x \pm ct) + \eta u_1^{L,R}(x,t), \tag{4.1}$$

where c is a known constant velocity, η is a smallness parameter, and u_1 is a space-time function the form of which will be specified later. For the moment we consider u_1 as s *space-time perturbation* whose presence can affect the dynamics and could pertain to some meaningful physics. In the same spirit as resonances studied in Ref. [2], u_1 makes some resonant interactions with the primary traveling wave u_o. Here, we propose a more specific form for u_1, and moreover we have developed a numerical algorithm to extract their shape in more general context of space-time resonances.

The outline of this chapter is as follows. In Section 4.1, we introduce spatio-temporal modulations of traveling waves as a representation. Space-time symmetries

---

[1] we sometimes use the terminology 'model' to refer to our representation

in relation to the model are presented in Section 4.2. We then discuss in Section 4.3 an important result concerning the global dimension of characteristic spaces before and after the occurrence of spatio-temporal modulations. In Section 4.4, we give biorthogonal equations for a spatio-temporally modulated traveling wave. In the case of non-resonant (spatial and temporal) modulations, a solution can be achieved. It is presented in Section 4.5. In other cases, depending on whether spatial and temporal resonances appear simultaneously or not, we can achieve some partial analytical results. They are discussed in Section 4.6. The effects that these spatio-temporal modulations have on the dynamics of a uniformly traveling wave are presented in Section 4.7. All these results are illustrated in a numerical example which is the subject of Section 4.8. In Section 4.9, this formalism is applied to data acquired from the experiments on binary fluid convection in the regime of counterpropagating wave packets, where similar behaviors are observed. Our findings are discussed in Section 4.10. Section 4.11 is a summary of this chapter.

4.1 A Spatio-temporal Representation

In this first section we introduce the precise meaning of spatio-temporal modulations on which we intend to base our theoretical modeling. Subsequently, we consider the slowly varying amplitudes, $A(x,t)$, obtained by removing the fast-varying phase which corresponds to convective rolls. For a wave profile which has a localized form and traveling with almost constant group velocity, we assume a representation of the signal of the form

$$A(x,t) = u(x-ct)g(x,t)$$

where $u(x-ct)$ is some 'averaged' uniformly traveling profile with the averaged speed c, and $g(x,t)$ the space-time function representing modulations.

4.1.1 Setting

We start by reviewing some characteristics of the counterpropagating wave packet regime in binary fluid convection to lay the foundations for our forthcoming discussion. This state constitutes the first dynamical state observed near onset and, despite their simple appearence, the dynamics involved are rather intricate. This regime consists of the superposition of wave packets traveling in opposite directions, termed conventionally right-going and left-going waves, see Figures 4.12–4.14. The behavior of both components is quite remarkable: the localized wave packets of both component, despite nonlinear interactions and linear dispersion, can sustain themselves for an extremely long time. This striking feature of this regime conveys the presence of stabilizing mechanism(s) leading to these long-lived wave packets. In addition, because both components can be separated using the demodulation procedure, it seems reasonable to look at each component independently. The amplitude profile of each component can be considered, to zeroth approximation, as a simple, uniformly-traveling wave:

$$u_{L,R}(x,t) = u_o^{L,R}(x \pm c_o t). \tag{4.2}$$

At this level of approximation the left-going wave can be considered exactly as the mirror image of the right-going wave. The latter can, then, be recovered from the left-going wave by a reflection symmetry ($x \to -x$) about x=0 and an appropriate shift, while reversing the sign of the group velocity c_o. The form (4.2) is, however, very simplistic, and in reality nonlinear mechanisms slightly affect the shape of the amplitude during the evolution. Our analysis will reveal that a much better approximation consists of spatially and temporally modulated right-going and left-going waves, and that one component cannot be recovered from the other by a mere reflection symmetry.

In developing the formalism of the spatio-temporal modulations, we consider a uniformly traveling component, which conceptually refers to one of the right- or left-going wave packets. Consider then a traveling wave propagating at a constant speed c_o which is modulated in space and time according to the following expression:

$$u_\epsilon(x,t) = u_o(x - c_o t) g_1(x) g_2(t). \tag{4.3}$$

We assume that the modulations are non-negative weakly-varying functions; with $g_1(x) > 0$, $\forall x \in X$, and $g_2(t) > 0, \forall t \in T$.

4.1.2 Possible Scenarios

The above proposed simplified model aims at establishing through some plausibility assumptions that the irregularities observed in the CPWP could well be represented through space-time modulations which are in part responsible for their dynamical behavior. Our aim is to try to extrapolate dynamical behavior of the CPWP as close as possible to dispersive chaos regime in an attempt to assess the extent to which spatio-temporal modulations play a role in complexity as well as to understand the route to complexity in this system. As the Rayleigh number is increased, we speculate that two scenarios may occur as the spatio-temporal modulations develop. The following scenarios are proposed on purely dynamical speculations, without any prior physical considerations. Scenario I has an intermediate transition in which either spatial or temporal modulation occur before their combined effect indicates a transition to chaotic behavior.

Scenario I

$$\text{Primary TW} \xrightarrow{1} \left\{ \begin{array}{l} \text{Spatial Modulation} \\ \text{or} \\ \text{Temporal Modulation} \end{array} \right. \xrightarrow{2} \text{Spatio-temporal Modulation} \rightarrow \text{Complexity}$$

Scenario II

$$\text{Primary TW} \xrightarrow{1} \text{Spatio-temporal Modulation} \rightarrow \text{Complexity}$$

The fundamental questions we address below are: How can we detect such scenarios and, once this is achieved, how can we characteristize these spatio-temporal modulations ? Do they reflect any physical behavior ?

Before going further with these questions, we briefly discuss in the following section symmetry related issues in this system.

4.2 Space-time Symmetries

Space-time symmetries are important in the understanding of this state, because of the simplicity of the geometry and the symmetries it dictates. These symmetries were literally described above. In the following we give them some mathematical flavor.

Reflection Symmetry

At a first approximation left and right traveling components can be considered as reflections of each other (*i.e.* the system preserves inversion symmetry), and thus can be written as

$$u_R(x, t_o) = u_L(x_o - x, t_o), \tag{4.4}$$

where x_o is an appropriate shift for some arbitrary time t_o. The coexistence of both components, left and right, in the CPWP regime represents a preservation of the symmetry related to the annular geometry of the cell as opposed to the rectangular cell where such coexistence is attributed to the presence of lateral boundaries which allow reflection of the traveling waves. Ideally, the reflection symmetry for the total wave field

$$u(x,t) = u_L(x,t) + u_R(x,t),$$

should be expressed in terms of the associated operator as

$$\tilde{S}U = US, \tag{4.5}$$

where the pair $(S, \tilde{S})$ is defined as

$$\begin{aligned} S\phi(x) &= \phi(x_1 + x_2 - x), \\ \tilde{S}\psi(t) &= \psi(t + \frac{T}{2}) \end{aligned}$$

where x_1 and x_2 represent the spatial locations where crossings between left and right components take place. The total wave field satisfies

$$u(x,t) = u(x_1 + x_2 - x, t + \frac{T}{2}).$$

Translation Symmetries

Each component has the continuous translation symmetry such that:

$$u_{R,L}(x,t) = u_{R,L}(x + x_o, t + t_o), \text{ such that } x_o \pm ct_o = 0.$$

where c is the group velocity. This symmetry is, however, broken if one considers the sum of both left and right components,

$$u(x,t) = u_L(x,t) + u_R(x,t). \tag{4.6}$$

Because of spatial periodicity, the translation symmetry reduces to a discrete one. Thus, if L denotes the spatial period and T the corresponding temporal period that is, L+c T=0, then, the following symmetry holds for the total field

$$u(x+\frac{L}{2},t+\frac{T}{2}) = u(x,t). \tag{4.7}$$

These symmetries remain true if only one assumes constant group velocity and that the shape of both left and right components remain unchanged during evolution.

Modulated Waves

Generally, the presence of spatio-temporal modulations of the form (4.3) in a traveling wave profile leads to a breaking of the symmetries (4.4), and (4.7). Under the form proposed above, (4.3), such symmetries can only be partially satisfied. If one considers each component independently, the left for instance, the symmetry relation (4.7) reads

$$\begin{aligned} u_L(x+\frac{L}{2},t+\frac{T}{2}) &= u_L(x,t) \\ g_1^L(x+L)u_L(x+ct)g_2^L(t+\frac{T}{2}) &= g_1^L(x)u_L(x+ct)g_2^L(t), \end{aligned}$$

which holds if the following conditions are satisfied

$$\frac{g_1^L(x+L/2)}{g_1^L(x)} = C, \tag{4.8}$$

$$\frac{g_2^L(t)}{g_2^L(t+T/2)} = C, \tag{4.9}$$

where C is a constant. For a spatially periodic domain C must equal 1, in which case the spatial and temporal modulations are simply L/2-periodic and T/2-periodic respectively. Any other constant value for C will not be physically plausible.[2]

4.3 Characteristic Spaces and Global Dimension

4.3.1 Some Notation

In this paragraph we first introduce some notations that will be used subsequently. The BOD operator associated with u_o is denoted by U_o. Hence, the matrix

---

[2] for unbounded domains, if $C > 1$ then the spatial modulation will monotonically increase while the temporal modulation will monotonically decay.

operator V_o reads

$$V_o = \begin{pmatrix} 0 & U_o^* \\ U_o & 0 \end{pmatrix}.$$

The action of both the spatial modulation, $g_1(x)$, and the temporal one, $g_2(t)$, define respectively two multiplicative operators G_1 and $\tilde{G}_2$ as follows

$$\begin{aligned} & G_1 : \mathcal{H}(X) & \rightarrow & \ \mathcal{H}(X) \\ \forall \varphi \in \mathcal{H}(X), \quad & (G_1\varphi)(x) & = & \ g_1(x)\varphi(x), \end{aligned}$$

and,

$$\begin{aligned} & \tilde{G}_2 : \mathcal{H}(T) & \rightarrow & \ \mathcal{H}(T) \\ \forall \psi \in \mathcal{H}(T), \quad & (\tilde{G}_2\psi)(t) & = & \ g_2(t)\psi(t). \end{aligned}$$

The spatio-temporal modulation operator, denoted by G, acting on $\mathcal{H}(X)\oplus \mathcal{H}(T)$ is defined by

$$G = \begin{pmatrix} G_1 & 0 \\ 0 & \tilde{G}_2 \end{pmatrix}.$$

Thus, we can write the operator associated with the modulated signal u_ϵ

$$V_\epsilon = G V_o G.$$

Since we are going to use the Fourier transform later on, we denote by $\{e_q\}$ and $\{\tilde{e}_p\}$ the spatial and temporal modes

$$\begin{aligned} e_q(x) &= e^{2i\pi q \frac{x}{L}} \\ \tilde{e}_p(t) &= e^{2i\pi p \frac{t}{T}}. \end{aligned}$$

The spatial and the temporal characteristic spaces associated with the system for $\epsilon \neq 0$ are denoted by $\chi_\epsilon(X)$ and $\chi_\epsilon(T)$, respectively. For $\epsilon = 0$, u_ϵ is reduced to the simple traveling wave case and the spaces are then $\chi_o(X)$ and $\chi_o(T)$.

4.3.2 Characteristic Spaces and Dimension

In this subsection we discuss an important result concerning the effect of spatio-temporal modulations on the global dimension of the characteristic spaces $\chi_o(X)$ and $\chi_o(T)$.

The following theorem states that the global dimension remains the same when a transition to spatio-temporally modulated dynamics occurs. This may appear at first sight surprising, as it is commonly believed that the appearance of modulations should increase the complexity and therefore the dimension. In order to understand how these modulations affect the dynamics, we apply them in two steps. First, we spatially modulate the primary traveling wave u_o, and then we apply the temporal modulation to the spatially modulated dynamics.

Theorem 4.1 *Let us consider the signal $u(x,t)$ given by*

$$u(x,t) = u_o(x - c_o t) g_1(x) g_2(t), \tag{4.10}$$

where $g_1(x)$ and $g_2(t)$ represent spatial and temporal modulations, respectively. We suppose that $g_1(x) \neq 0$, $\forall x$ and $g_2(t) \neq 0$, $\forall t$. We then have the following results

$$dim\chi_\epsilon(X) = dim\chi_o(X) = dim\chi_\epsilon(T) = dim\chi_o(T). \tag{4.11}$$

PROOF

To show this theorem, it is convenient to use vectorial quantities associated with the space-time dynamics, namely, $\vec{\xi}_t$ and $\vec{\eta}_x$. To better account for the action of spatio-temporal modulations, we apply the latter in two phases. We first apply the spatial modulation and then the temporal one. We consider the following spatially modulated signal

$$u_1(x,t) = u_o(x - c_0 t) g_1(x). \tag{4.12}$$

On the one hand, the spatial evolution associated with u_1 is given by

$$\vec{\eta}^1_x = g_1(x)\vec{\eta}^o_x. \tag{4.13}$$

This expression clearly shows that, for a fixed x, $\vec{\eta}^1_x \in \chi_o(T)$, which implies that the temporal characteristic space of u_1, $\chi^1(T)$, is a subspace of $\chi_o(T)$, i.e.

$$\chi^1(T) \subset \chi^o(T). \tag{4.14}$$

On the other hand, since we have assumed that $g_1(x) \neq 0, \forall x$, we can invert the formula (4.13) and get

$$\vec{\eta}_x^o = \frac{1}{g_1(x)} \vec{\eta}_x^1.$$

Hence, $\vec{\eta}_x^o \in \chi^1(T)$, and we can write

$$\chi_o(T) \subset \chi^1(T). \tag{4.15}$$

Consequently, relations (4.14) and (4.15) give

$$\chi_o(T) = \chi^1(T). \tag{4.16}$$

which implies that the dimension of both spaces is equal:

$$dim\chi_o(T) = dim\chi^1(T). \tag{4.17}$$

This global dimension is common, because of the isomorphism, to the spatial characteristic spaces as well and we have

$$dim\chi_o(X) = dim\chi^1(X). \tag{4.18}$$

This ends the first step of the proof. Note that the orbit corresponding to u_1 is obtained by the action of the operator G_1 on $\vec{\xi}_t^o$, namely

$$\vec{\xi}_t^1 = G_1.\vec{\xi}_t^o. \tag{4.19}$$

The second step consists of applying the temporal modulation to u_1:

$$u(x,t) = u_1(x,t)g_2(t). \tag{4.20}$$

Now, we consider the orbit of $u(x,t)$ which is given by

$$\vec{\xi}_t^\epsilon = g_2(t)\vec{\xi}_t^1, \tag{4.21}$$

hence, $\vec{\xi}_t^\epsilon \in \chi^1(X)$, which yields

$$\chi_\epsilon(X) \subset \chi^1(X). \tag{4.22}$$

We then invert the formula (4.21) since $g_2(t) \neq 0, \forall t$, and obtain

$$\vec{\xi}_t^1 = \frac{1}{g_2(t)} \vec{\xi}_t^\epsilon. \tag{4.23}$$

Hence, $\vec{\xi}_t^1 \in \chi_\epsilon(X)$, which implies

$$\chi^1(X) \subset \chi_\epsilon(X). \tag{4.24}$$

We then deduce from the relations (4.22) and (4.24) that

$$\chi^1(X) = \chi_\epsilon(X). \tag{4.25}$$

This implies

$$dim\chi^1(X) = dim\chi_\epsilon(X) \tag{4.26}$$

and therefore

$$dim\chi_o(X) = dim\chi_\epsilon(X) = dim\chi_o(T) = dim\chi_\epsilon(T).$$

■

Vectorial quantities of the modulated signal $u(x,t) = u_o(x - c_o t) g_1(x) g_2(t)$ read

$$\vec{\xi}_t^\epsilon = g_2(t) G_1 . \vec{\xi}_t^1, \tag{4.27}$$

$$\vec{\eta}_x^\epsilon = g_1(x) G_2 . \vec{\eta}_x^1. \tag{4.28}$$

Remark 4.2 *If the conditions, $g_1(x) \neq 0, \forall x$, and $g_2(t) \neq 0, \forall t$, are not satisfied, only the relations (4.14) and (4.22) remain valid, and we can conclude that the dimension of the spaces $\chi_\epsilon(X)$ and $\chi^1(T)$ are smaller or equal to that of $\chi_o(X)$ and $\chi_o(T)$.*

4.4 Bi-orthogonal Equations

Given a spatio-temporally modulated signal $u(x,t)$, that is, knowing the components u_o, g_1 and g_2, we would like to understand the interaction between the different Fourier modes of these components.

If the Fourier decomposition of the functions u_o, g_1 and g_2 is given by

$$
\begin{aligned}
u_o(x - c_o t) &= \sum_k u_o^k e_k(x) \tilde{e}_{c_o k}(t) && (4.29)\\
g_1(x) &= \sum_\ell g_1^\ell e_\ell(x) && (4.30)\\
g_2(t) &= \sum_m g_2^m \tilde{e}_m(t) && (4.31)
\end{aligned}
$$

then, combining the equations (4.29–4.31), we obtain

$$u(x,t) = \sum_{k,\ell,m} a_{k,\ell,m} e_{k+\ell}(x) e_{kc_o+m}(t) \qquad (4.32)$$

where $a_{k,\ell,m} = u_o^k g_1^\ell g_2^m$, u_o and g_1 are periodic functions with period L, and g_2 is periodic with period T.

We can conclude from the relation (4.32) that the primary traveling wave u_o realizes a coupling between the Fourier modes of the spatial modulation and those of the temporal modulation. The use of BOD equations show this fact as well. The presence of spatial and temporal modulations breaks the space-time translation symmetry of the traveling waves. This implies that the decomposition (4.32) does not coincide with the bi-orthogonal decomposition. In other words, it is not possible to reduce the three indices summation in (4.32) to a summation over one index only.

The topos as well as the chronos can be expressed in the Fourier basis:

$$
\begin{aligned}
\varphi(x) &= \sum_\alpha \varphi^\alpha e_\alpha(x), && (4.33)\\
\psi(t) &= \sum_\beta \psi^\beta \tilde{e}_\beta(t). && (4.34)
\end{aligned}
$$

The BOD eigensystem reads

$$
\begin{aligned}
U_\epsilon \varphi &= A\psi, && (4.35)\\
U_\epsilon^* \psi &= A\varphi, && (4.36)
\end{aligned}
$$

which, after calculations, yields the following equations:

$$
\begin{aligned}
\sum_{\substack{\alpha,\ell,m \\ c(\alpha+\ell)+m=\beta}} \varphi^\alpha g_1^\ell u_o^\alpha g_2^m &= A\psi^\beta, && (4.37)\\
\sum_{\substack{\beta,\ell,m \\ \frac{\beta+m}{c_o}+\ell=\alpha}} \psi^\beta g_1^\ell \overline{g}_o^{\frac{\beta+m}{c_o}} g_2^m &= A\varphi^\alpha. && (4.38)
\end{aligned}
$$

The system of equations (4.37)-(4.38) shows that it is not possible in the general case to have closed subsystems of equations. In other words, in general, we cannot have finite chains of resonances as was the case studied in Ref [2]. In a particular case, this is, however, possible: this situation corresponds to the case of non-resonant spatio-temporal modulations, as we show below. In this case, the Fourier sidebands due to spatial and temporal modulations do not overlap. In the binary fluid convection experimental data, particularly in the counterpropagating regime, resonances appear in both space and time. The study of this problem is deferred to Section 4.9.

4.5 Non-resonant Modulation

This case is the simplest that can be treated analytically. In this situation, spatial and temporal modulations appear in each topo and chrono. Indeed, using the Fourier expansion of the functions u_o, g_1, g_2, we obtain for the signal $u(x,t)$

$$\begin{aligned} u(x,t) &= \sum_{k,\ell,m} a_{k,\ell,m} e^{2\pi i(k+\ell)x} e^{-2\pi i(kc_o+m)t} && (4.39) \\ &= \sum_k u_o^k \, (\sum_\ell g_1^\ell e^{2\pi i(k+\ell)\frac{x}{L}}) \, (\sum_m g_2^m e^{-2\pi i(kc_o+m)\frac{t}{T}}) && (4.40) \end{aligned}$$

where $a_{k,\ell,m} = u_o^k g_1^\ell g_2^m$. We have used the fact that overlapping of the spatial and temporal Fourier sidebands due to the modulations does not occur. There is a set of topos and chronos of $u(x,t)$ which are simply the modulated topos and chronos of $u_o(x,t)$, *i.e.*

$$\begin{aligned} \varphi_k(x) &= a_k g_1(x) \varphi_k^o(x) && (4.41) \\ \psi_k(x) &= b_k g_2(t) \psi_k^o(t) && (4.42) \end{aligned}$$

where a_k and b_k are normalization constants. This is because the family φ_k as well as the family ψ_k are two orthonormal families as a consequence of the non-interaction of the sidebands (non resonant condition), i.e.

$$(e_{k+l}, e_{k'+l'}) = 0,$$

$$(\tilde{e}_{kc_o+m}, \tilde{e}_{k'+c_om'}) = 0.$$

for all k, k', l, l', m, and m'.

The relations (4.41) and (4.42) are no longer valid as soon as spatial and/or temporal resonances appear.

4.6 Resonant spatio-temporal modulations

4.6.1 Key remark

A pure traveling wave has constant spatial and temporal averages in the laboratory reference frame when defined on appropriate space-time domain. In the moving frame, the temporally-averaged spatial profile is nothing more than the traveling wave profile itself. For spatially and temporally modulated traveling waves, spatial and temporal averages are no longer constant functions. We thus expect that these averages are related to the spatial and temporal modulations present in the signal. Three cases can be distinguished, depending on whether resonances occur in space, in time, or in both space and time. They are the subject of the next subsections.

We consider a modulated signal of the form (4.3):

$$u(x,t) = (1 + \bar{g}_1(x))u_o(x - ct)(1 + \bar{g}_2(t)) \tag{4.43}$$

where $\int_X \bar{g}_1(x)dx = 0$, and $\int_T \bar{g}_2(t)dt = 0$.

Before studying the different cases we first proceed by integrating the signal $u(x,t)$ with respect to the space and time variables in the laboratory frame of reference as well as in the moving frame.

- Spatial average

$$\begin{aligned}
\frac{1}{L}\int_X u(x,t)dx &= \frac{1}{L}g_2(t)\int_X g_1(x)u_o(x-ct)dx && (4.44)\\
&= \frac{1}{L}g_2(t)\{\int_X u_o(x-ct)dx + \int_X \bar{g}_1(x)u_o(x-ct)dx\} && (4.45)\\
&= \frac{1}{L}Cg_2(t) + \frac{1}{L}g_2(t)\int_X \bar{g}_1(x)u_o(x-ct)dx && (4.46)
\end{aligned}$$

where

$$C = \frac{1}{L}\int_X u_o(x-ct)dx. \tag{4.47}$$

where C is a constant because of the spatial periodicity.

- Temporal average

  Similarly, the integral of the signal $u(x,t)$ over the time domain T is given by

$$\begin{aligned} \frac{1}{T}\int_T u(x,t)dt &= \frac{1}{T}g_1(x)\int_T g_2(t)u_o(x-ct)dt \quad (4.48)\\ &= \frac{C}{T}g_1(x) + \frac{1}{T}g_1(x)\int_T \tilde{g}_2(t)u_o(x-ct)dt. \quad (4.49)\end{aligned}$$

- Temporal average in the moving frame

  In the moving frame, the average over the time domain yields the following integral equation

$$\frac{1}{T}\int_T u(x+ct,t)dt = \frac{1}{T}u_o(x)\int_T g_1(x+ct)g_2(t)dt. \tag{4.50}$$

4.6.2 Spatial resonance

Proposition 4.3 *If the primary traveling wave is non resonant with respect to the temporal modulation, the spatial modulation can be recovered and is proportional to the temporal average of the signal* $u(x,t)$.

PROOF

The relation (4.49):

$$\int_T u(x,t)dt = Cg_1(x) + g_1(x)\int_T \tilde{g}_2(t)u_o(x-ct)dt$$

can be equivalently written as

$$\frac{1}{T}\int_T u(x,t)dt = \frac{g_1(x)}{T}\{C + \int_T \sum_{m,m'} \tilde{g}_2^m \hat{u}_o^{m'} e^{-it(m-cm')}e^{im'x}dt\}$$

$$= \frac{g_1(x)}{T}\{C + \sum_{\substack{m,m' \\ m,m' \neq 0}} e^{im'x}\tilde{g}_2^m \hat{u}_o^{m'} \int_T e^{-it(m-cm')}dt\}$$

$$= \frac{g_1(x)}{T}\{C + \sum_{\substack{m,m' \\ m,m' \neq 0}} \tilde{g}_2^m \hat{u}_o^{m'} e^{im'x}\delta_{cm',m}\}.$$

In the case where the second term of the right hand side is zero, namely

$$m \neq cm',\ \forall m, m'$$

we obtain the following relation

$$\frac{1}{T}\int_T u(x,t)dt = \frac{C}{T}g_1(x). \tag{4.51}$$

Remark 4.4 *For the case of quasi-periodic traveling wave, if one could extend the time domain in such a way that the normalized —dimensionless— velocity $|c|$ is large enough so that $m < |c|m', \forall m, m'$, then $\delta_{cm',m}$ is zero for any pair (m, m').*

4.6.3 Temporal resonance

The same analysis can be carried out for the case of non spatial resonance.

Proposition 4.5 *If the primary traveling wave is non resonant with respect to the spatial modulation, the temporal modulation can be recovered and is proportional to the spatial average of the signal $u(x, t)$.*

PROOF

$$\frac{1}{L}\int_X u(x,t)dx = \frac{g_2(t)}{L}\{C + \int_X \tilde{g}_1(x)u_o(x-ct)dx\} \tag{4.52}$$

$$= \frac{g_2(t)}{L}\{C + \int_X \sum_{k,k'} \tilde{g}_1^k \hat{u}_o^{k'} e^{ix(k'+k)}e^{-ik'ct}dx\} \tag{4.53}$$

$$= \frac{g_2(t)}{L}\{C + \sum_{\substack{k,k' \\ k,k' \neq 0}} e^{-ik'ct}\hat{u}_o^{k'}\tilde{g}_1^k\delta_{k',k}\} \tag{4.54}$$

In case where the second term of the right hand side is zero, namely

$$k \neq k',\ \forall k, k'$$

then the last equation reduces to

$$\frac{1}{L}\int_X u(x,t)dx = \frac{C}{L}g_2(t). \tag{4.55}$$

4.6.4 Extraction of modulations in the resonant case

In this subsection we investigate with the general case, namely the case of spatio-temporal resonances. In this situation we will not be able to extract either one of the modulations separately in the same way as non-resonant cases. Instead, we deal with all the equations:

$$\begin{aligned}
f_1(t) &= \int_X u(x,t)dx = g_2(t)\int_X g_1(x)u_o(x-ct)dx && (4.56)\\
f_2(x) &= \int_T u(x,t)dt = g_1(x)\int_T g_2(t)u_o(x-ct)dt && (4.57)\\
f_3(x) &= \int_T u(x+ct,t)dt = u_o(x)\int_T g_1(x+ct)g_2(t)dt. && (4.58)
\end{aligned}$$

This system of coupled integral equations is then solved iteratively. The iterative process based upon the system of equations above reads

$$\begin{aligned}
g_{2,n}(t) &= f_1(t)\left[\int_X g_{1,n-1}(x)u_{o,n-1}(x-ct)dx\right]^{-1} && (4.59)\\
g_{1,n}(x) &= f_2(x)\left[\int_T g_{2,n-1}(t)u_{o,n-1}(x-ct)dt\right]^{-1} && (4.60)\\
u_{o,n}(x) &= f_3(x)\left[\int_T g_{1,n-1}(x+ct)g_{2,n-1}(t)dt\right]^{-1}. && (4.61)
\end{aligned}$$

Reaching convergence depends on an appropriate choice of the initial conditions. Our first estimates for the profiles of the primary traveling wave, the spatial modulation and the temporal modulation are denoted $u_{o,0}(x)$, $g_{1,0}(x)$ and $g_{2,0}(t)$, which are simply $f_3(x)$, $f_2(x)$ and $f_1(t)$, respectively. For this particular choice, we have found that our scheme converged rapidly to the desired accuracy.

Because these input functions are only a representative form of the real signal, not all features of the signal are expected to be included. A detailed discussion of this point is presented below. Nonetheless, the signal reconstructed from the extracted functions should be capable of recovering features pertaining to the presence of spatio-temporal modulations.

We should mention that one can use the algorithm that we developed in this subsection to extract spatial and/or temporal modulations, even if resonances appear with respect to only one variable, either space or time. For the case of spatial resonance one recovers the spatial modulation after extracting the temporal modulation:

$$g_1(x) = \frac{u(x,t)}{g_2(t)}.$$

Similarly, in the temporal resonance the temporal modulation is given by

$$g_2(t) = \frac{u(x,t)}{g_1(x)}.$$

where $g_1(x)$ is extracted first through the algorithm.

4.6.5 Error estimate

The extraction therefore yields three components, the primary traveling wave profile, the spatial modulation and the temporal modulation. The signal, $u_{mod}(x,t)$, reconstructed from these components should in principle reproduce the original signal, $u(x,t)$. The goodness of fit to the original signal is measured numerically by means of the quantity δ defined as

$$\delta = \frac{1}{N_s * N_p}\left[\sum_{i,j} \left|\frac{u(i,j) - u_{mod}(i,j)}{u(i,j)}\right|^2\right]^{\frac{1}{2}} \tag{4.62}$$

where N_s and N_p are the number of spatial points and time steps respectively. The integers i and j are the space and time discretizations respectively.

4.7 Dynamics

In this section we study the effect of spatio-temporal modulations on the dynamics of the primary traveling wave u_o. We have concluded in Section 4.3.2 that the global dimension of characteristic spaces remain the same before and after the occurrence of spatio-temporal modulations. So we do not expect the dimension of the characteristic spaces to increase if modulations are involved.

First, we look at the effect of the spatial modulation on the orbit of the primary traveling wave u_o. In the Fourier basis, $\vec{\xi}^o_t$ is expressed as

$$\vec{\xi}^o_t = \sum_q u^q_o \psi^q_o(t) \vec{e}_q,$$

and thus the effect of the spatial modulation on $\vec{\xi}_t^o$ gives

$$G_1.\vec{\xi}_t^o = \sum_q u_o^q \psi_o^q(t) G_1.\vec{e}_q,$$

where $G_1.\vec{e}_q$ can be written as

$$G_1.\vec{e}_q = \sum_m g_1^m \vec{e}_{q+m}.$$

This last expansion shows that $\chi(X)$ has undergone a rotation in $\mathcal{H}(X)$ and that the dynamics is affected. The orbit $\vec{\xi}_t^o$ undergoes a non-unitary deformation: it is subject to a change of amplitude in the direction of $\vec{e}_q$ which depends on g_1^m. The family of vectors $\{G_1.\vec{e}_q\}$ is not orthonormal. Hence, the coefficients g_1^m represent a new repartition of energy among Fourier modes.

The action of the temporal modulation on the orbit $G_1.\vec{\xi}_t^o$ is also subject to a substantial distortion. The description of the dynamics in $\chi^\epsilon(T)$ is similar to that of $\chi^\epsilon(X)$ and obey the same mechanisms.

In summary, the spatio-temporal modulation manifests itself in the characteristic spaces through two effects. Globally, the spaces undergo rotations which deform the orbits. Then, additional deformations of the orbits take place because of the effects of stretching and contraction which depend on time for $\vec{\xi}_t^o$ in $\chi_\epsilon(X)$ and on space for $\vec{\eta}_c^o$ in $\chi_\epsilon(T)$.

4.8 Numerical Illustration

This section is intended to illustrate through a numerical example the effects that spatial and temporal modulations have on the BOD components. The simple traveling wave considered is defined in a spatially and temporally periodic domain. We consider a simple traveling wave u_o defined on a spatial domain L and a time domain T by

$$u_o(x,t) = \sum_k u_o^k cos(2\pi(\frac{k}{L}x - \frac{c_o k}{T}t)) \tag{4.63}$$

where the speed (normalized with respect to L/T) is taken $c_oT/L = 9$. The Fourier coefficients of u_o^k are of the form

$$\begin{cases} u_o^k = 10/k & for\ k{=}1,..,10 \\ 0 & for\ k \neq 1,..,10. \end{cases} \tag{4.64}$$

The spatial modulation $g_2(x)$ is given by

$$g_1(x) = 1 + 0.1 \sum_{\ell} g_1^{\ell} cos(2\pi\ell \frac{x}{L}), \tag{4.65}$$

where the coefficients g_1^{ℓ} are of the form

$$\begin{cases} g_1^{\ell} = 1/\ell & for\ \ell = 1, 2 \\ 0 & for\ \ell \neq 1, 2. \end{cases} \tag{4.66}$$

The temporal modulation, $g_2(t)$, is given by

$$g_2(t) = 1 + 0.1 \sum_{m} g_2^{m} cos(2\pi m \frac{t}{T}), \tag{4.67}$$

where the coefficients $g_2^m = 1/m$ are given by

$$\begin{cases} g_2^{m} = 1/m & for\ m = 2 \\ 0 & for\ m \neq 2. \end{cases} \tag{4.68}$$

Figure 4.1(a) shows the simple traveling wave $u_o(x)$. The spatial modulation, $g_1(x)$, and temporal modulation, $g_2(t)$ are shown in in solid lines in Figures 4.1(b) and 4.1(c) respectively. It is worthwhile to mention that in this numerical example the spatial and temporal modulations are considered to be small in amplitude as compared with the amplitude of the carrier wave. The modulated space-time dynamics is represented in Figure 4.2.

We first study the action of the spatial modulation on the TW $u_o(x - c_o t)$. The BOD spectrum associated with

$$u_1(x, t) = u_o(x - c_o t) g_1(x)$$

is shown in Figure 4.3. Clearly the dimension is equal to 20, which is the same as that of the signal u_o. We mentioned above that the application of a modulation breaks the traveling wave symmetry, namely the space-time translation symmetry. This fact is evident from the spectrum which does not present a total two-order degeneracy.

The bi-orthogonal temporal modes associated with $u_1(x, t)$ are shown in Figure 4.4 with their respective Fourier transforms. The latter show that the spectra $\widehat{\psi}_\alpha$ have non-zero components for all harmonics. This is due to the fact the space spanned by the chronos has undergone a rotation in the space $\chi_o(T)$. This rotation permits each chrono to have a non-zero projection on more than one Fourier mode.

The bi-orthogonal spatial modes of $u_1(x,t)$ and their respective Fourier transform are shown in Figure 4.4. It is important to note that, if the number of discrete modes involved in the problem is finite, then we can estimate this number accurately, as can be indeed done in this case. Notice that for $\alpha = 7$, the maximal value at which $\hat{\varphi}_7(k)$ is not zero is equal to 12 - this number corresponds to the maximum of $(k+\ell)$. In the present example, $(k+\ell)_{max} = 10+2 = 12$.

Let us now apply the temporal modulation to the spatially modulated signal $u_1(x,t)$. The dimension associated with the spatio-temporally modulated dynamics remains 20 as can be deduced clearly from Figure 4.6. The topos of the signal u, see Figure 4.8, have not changed with respect to the spatially modulated signal. Therefore, the characteristic spatial spaces are the same: $\chi_\epsilon(X) = \chi_1(X)$. However, the effects that the temporal modulation can have are clearly seen in the chronos. They are shown in Figure 4.7. The shape of the chronos have changed drastically. Their Fourier transform shows peaks for values of the frequency $\omega = kc_o \pm m$, exactly where the analytical model predicted -see Section 5.3.

4.8.1 Dynamics

Figure 4.9(a) shows the projection of the dynamics onto the subspace spanned by $(\vec{\varphi}_1^o, \vec{\varphi}_2^o)$ for the case of a simple traveling wave. The orbit is nothing but a circle since the temporal modes coincide exactly with Fourier modes. When the spatial modulation is applied, this space undergoes a rotation which can be observed because of the deformation that the circle undergoes. This is apparent in Figure 4.9(b) in the projection $(\vec{\varphi}_1, \vec{\varphi}_2)$. Figure 4.9(c) shows the case of the spatio-temporally modulated traveling wave. The effect of the temporal modulations on ξ_t, which consists of stretching and contraction, is shown by the splitting that the orbit $\vec{\xi}_t^\epsilon$ undergoes in the projection in the same plane.

We conclude that the effects observed in this numerical example confirm the predictions that we have established in the previous subsection 5.2.3. More importantly, we have shown that even in the case where the modulations are weak both in space and time, their effects on the dynamics, particularly in the resonant case, are drastic. This can be considered as both an advantage and a disadvantage. On the one hand, independently of how weak the modulations are, the previous formalism enables us to show their presence. On the other hand, this effect may be considered as a disadvantage when real data such as acquired from experimental systems or numerical computations are considered. In these cases, data might be contaminated by effects related to experimental artifacts or numerical procedures rather than being related to the physical processes. In such cases, one has to operate carefully and proceed with some preliminary checks which generally depend on the particular situation considered before drawing any conclusions. We specifically discuss this matter in the convection experiments below.

4.8.2 Extraction of modulations

In this paragraph, we consider the converse problem, that is, given the data of the modulated signal $u(x, t)$, we apply the numerical algorithm of section 4.6.4 to see how close the extracted profiles of primary traveling wave, spatial modulation and the temporal modulation are to the real ones. Figures 4.1(a,b,c) show how remarkably the extracted profiles, which appear in dotted lines, agree with the original functions in solid lines.

4.9 Analyses of Convection Experiments

4.9.1 Preamble

A comprehensive understanding of the physical processes that lead to the chaotic behavior seen in the regime following the counterpropagating wave dynamics as Rayleigh number is increased is a difficult problem and is far from being solved. Models based upon the Ginzburg-Landau equation can only reproduce some qualitative aspects of the dynamics even in the weakly nonlinear state of the CPWP regime. By using the formalism we have been developing in this chapter and by a direct analysis of the data acquired from the experiment, we hope to gain some further understanding of the dynamical interactions involved. We discuss the presence of spatio-temporal modulations, which is directly related to the increasingly complex dynamics in this regime.

However, our concern in the following analysis is that the presence of modulations is the reflection of some undesirable effects, which might be device related, or due to approximated procedures used during the collection of the data or during filtering procedures. Most of these effects have been discussed in the previous chapter. For the sake of completeness we review them here.

- *Experimental artifacts* such as large-scale, static, spatial non-uniformities constitute a major concern. In the present series of experiments, such non-uniformities have been considerably reduced by using a very uniform experimental system. We will discuss this issue in light of the extracted spatial modulations below, as they relate to spatial variations.

- *Filtering procedures* which are applied to acquired data before any other analysis could be performed, aim at eliminating any device related effects such as drifts, light intensity change etc. Their effects were discussed in Chapter 4 and other Refs. In this present work these effects are considered a minor issue as compared to spatial inhomogeneities in the cell and lie beyond the scope of the approach followed herein.

- *Complex Demodulations* which have been briefly discussed in the previous chapter, will only be discussed in relevance to the spatio-temporal model. The application of complex demodulation to raw data aims at obtaining the envelope function and thus should not affect the underlying physical properties of the signal, especially with regards to inducing modulation effects. In order to assess the extent to which these procedures affected our signals, we have chosen a typical set of data and altered the demodulation parameters by as much as ±10%. The resulting signal was then analyzed using the BOD techniques and passed through several procedures, particularly the ones related to modulations; see Section (5.9). The results obtained were encouraging in that we did not find any cause-effect between the use of complex demodulation procedures and the actual presence of modulations, except that a change in parameters in the demodulation procedure only resulted in minor change of the overall amplitude strength. Additionally, there were no significant changes in the dynamics viewed in characteristic spaces as compared to the unaltered dynamics.

- *Possible Origin* Finally, we turn to nonlinear interactions between the right-going and left-going waves. In time, these interactions have a stabilizing effect, since it leads to a decrease in their amplitudes that compensates the linear growth the components experience when far from each other. This type of interaction occurs twice in each temporal period. In the space domain, the physical locations of this interaction are diametrically opposite and might be related to the changes in amplitude profiles. We will dwell more on this subject in Section (5.10).

4.9.2 Entropies

The entropy variation as a function of the reduced Rayleigh number ϵ for each component, left and right, is represented in Figure 4.10. The latter shows that the entropy increases monotonically for both components. Of particular interest in this graph is the fact that the entropies, identical for $\epsilon < 95.10^{-5}$, differ slightly at higher ϵ. It seems that the irregularities present in both components for the same ϵ value do not contribute in the same way to the development of the space-time complexity as ϵ increases.

4.9.3 Correlations

- Correlation lengths

  The correlation length, ξ, defined as the width at mid-height of the temporally-averaged space-space correlation function, for the total wave field decreases with ϵ. Indeed, ξ decreases from about $L/4$ for $\epsilon = 18.10^{-5}$ to about $L/6$ for $\epsilon = 166.10^{-5}$.

- Two-point correlations

  The two-point correlations, $R(x, x')$ are calculated according to

$$R(x,x') = \frac{1}{T}\int_0^T u(x,t)u(x',t)dt,$$

where, $u(x,t)$ represents the total wave field : $u_L(x,t) + u_R(x,t)$.

Thus, because of the localized shape of both components, the maximum autocorrelation points should represent where the right and left wave packets intercept, namely x_1 and x_2. Figure 4.11 is consistent with this and shows higher correlation at these locations. Rather, what is unusual is that the amplitude of $R(x_1, x_1)$ and $R(x_2, x_2)$ are different, representing an amplitude change and more importantly a symmetry breaking.

4.9.4 Analysis of Experimental Data

We report in the tables below the Fourier analysis performed on temporal modes (chronos) obtained through the bi-orthogonal decomposition of the experimental signal for different values of ϵ, some of which are shown in Figures 4.15–4.26. Eight signals, of a typical temporal duration of 1600 time units, have been treated in the counterpropagating wave regime, spread over a range of $0.0020 \leq \epsilon \leq 0.00166$. We have performed the analysis on each left and right component separately as was discussed earlier.

Tables 4.1 and 4.3 summarize the most significant peaks of $\hat{\psi}^{\epsilon}_{\alpha}$ for the left and right components, respectively. The reduced Rayleigh number ϵ increases downward, in columns n indicates the order of the chronos. Each entry has two rows for the double-degenerate chronos. The underlined values correspond to peaks with the highest intensity. In Tables 4.2 and 4.4, we have summarized the frequencies of the temporal modulations. These numbers, noted m, correspond to the difference of peaks of Tables 4.1 and 4.3 to the fundamental frequency and its harmonics, that are 9, 18, etc. For most ϵ's, the presence of a common value for the $m's$, for the same ϵ, strengthens our assertion of the presence of temporal modulations.

The goal of this preliminary procedure is twofold. First, it is used to check whether the presence of modulations is a likely possibility. If so, we then secondly proceed to an estimation of the frequencies involved. The latter is the first quantitative information to be obtained about the temporal modulations. In addition, our results indicate that, in these experiments, we have spatial resonance, which makes the extraction of similar information from the topos difficult. To extract the shape of these modulations we use the numerical scheme developed earlier, Section 4.6.4.

4.10 Discussion

4.10.1 CPWP Preview

Detailed observations of the wave patterns in CPWP regime were reported in Section 3.3.1 of the previous Chapter. The wave-packet amplitude profiles evolve with approximately constant velocity and no apparent long term change in shape. As ϵ increases, the profiles grow stronger, narrower and more asymmetric. These features indicate growing nonlinearity. In a related matter, and of particular interest to us, is the appearance of irregularities in the wave profiles which become stronger as ϵ increases. The nature of these irregularities appears to be of two different types. The first type features undulations in the wave profiles. These undulations can sometimes be seen by simply following the crest of the traveling wave packet. However, strong evidence of their presence can only be achieved by performing the bi-orthogonal decomposition on the data and looking into resonance features characterized by the presence of sideband splitting in the power spectra of the chronos - see previous Section. We have represented them through deterministic space and time functions, which we have termed spatio-temporal modulations.

The second type of irregularity we are concerned with, which is readily observed at high values of ϵ, is the appearance of burst-splitting phenomenon. This is reminiscent of the behavior seen in dispersive chaos. A cusp-shaped amplitude null appears on the trailing side of the main body of the wave packet. By the formation of this amplitude null, the initial wave profile splits in two. This process of trailing-edge phase defect causing double bursting events is a signature of all the localized states observed in binary fluid convection. The leading burst lags behind, smears out and subsequently decays, while the trailing burst grows up and takes over. Thus far we note an important difference between the two types of irregularities and that is trailing bursts are a phenomenon taking place at the trough of the wave profiles whereas modulations are affecting high amplitudes, especially the main body of the traveling wave profiles.

4.10.2 Essence of the modulations

While the presence of spatio-temporal modulations was confirmed for all values of the Rayleigh number in the CPWP regime, the burst-splitting phenomenon could only be seen for $\epsilon > 95.10^{-5}$. This appears to be consistent with the the behavior of the entropies of left and right amplitudes, which are equal only below $\epsilon = 95.10^{-5}$ and different above. Thus, above $\epsilon = 95.10^{-5}$, the occurrence of burst-splitting phenomena adds to the complexity and moreover seems to contribute in a different way to the complexity in each component. Several factors are thus contributing to the increasing complexity in the CPWP regime. The most important is the left-right amplitude interactions, which lead to spatio-temporally modulated waves. Also, as the stress parameter increases, nonlinearity gets stronger, and erratic behavior due to the eruption of trailing bursts becomes important. These structures, wave profiles, modulations and bursts, all interact. Though the exact interaction of the trailing bursts with the primary traveling wave profiles is still unclear, we made considerable progress in understanding the nature of the spatio-temporal modulations.

Our purpose is to clearly interpret the spatio-temporal functions recovered through the proposed representation. The choice of the representation makes this task easier by allowing $g_1(x)g_2(t)$ to contain the dynamical part. The sustained shape of the TW profiles is modeled by a uniform traveling wave packet with constant group velocity. At small values of ϵ, a good representation is expected in the absence of burst-splitting phenomenon.

Figure 4.28 shows the shapes of the left (continuous) and right (dashed) spatial modulations extracted from the data for all values of ϵ in CPWP. Notice that the variation of the modulation amplitudes increase with ϵ, which seems to be consistent with the increasing complexity shown in the spatio-temporal maps of the signals. This fact strengthens our speculations that the primary TW's are destabilized through increasingly strong interactions.

4.10.3 Period-doubling Instability

We believe that modulations do not pertain to the presence of static non-uniformities in the cell. This conclusion can be drawn from the spatial profiles of the modulations. For that, the presence of any spatial defects in the cell will affect all TW packets. Static non-uniformities have tendencies to slow down TW packets, even put them to a standstill. This behavior was not found in the present series of experiments. Additionally, any repetitive phenomenon in modulations has to be carefully investigated. We found, however, a consistent presence of depressions in two locations in spatial modulations of both left and right components, for the first few ϵ values. These minima are found to coincide with the spatial positions where crossings between left and right components take place, noted earlier x_1 and x_2.

Nonlinear interactions between counterpropagating wave packets get stronger as their supports overlap, tending to suppress each other. Thus, it is physically plausible that depressions in the spatial modulations are the reflection of the damping in amplitudes of the wave packet suffered during their encounter. This is a clear evidence of the effects of nonlinearities, and agrees with qualitative arguments obtained from experimental observations. This phenomenon was incorporated in CGL equations, equations (4.5–4.6), by considering negative coefficient $h < 0$ for the cross terms. Interaction effects are considered stabilizing in view of the growth of the wave packet as they evolve separately after the overlap. Thus, the mere fact of the coexistence of left and right components turns out to be a vital ingredient for the sustaining of their profiles.

These depressions at locations x_1 and x_2 are not equally strong in amplitudes. This disparity results from the fact that the interaction between left and right component is slave to amplitude's growth. In other words, the higher the amplitude the stronger is the interaction, and vice versa. We refer to this process as *period-doubling instability.* This scheme results in stable oppositely traveling waves since crossings happen twice in every space-time period because of their similar group velocities. The temporal growth of both left and right amplitudes is also a crucial ingredient for the period-doubling behavior. If the temporal growth for both amplitudes is not phase coherent, a disruption of the double minima occurs and leads to dissimilar shapes in spatial modulations. Such cases occur starting at $\epsilon = 95.10^{-5}$, for which left and right temporal modulations are either out-of-phase, or seemingly unrelated at all. These temporal modulations for all values of ϵ are displayed in Figure 4.29. The disruption in period-doubling is also linked to the appearance of the burst-splitting phenomenon. Trailing bursts, which have noticeable spatial variations, interfer in a way with wave packet interactions. In addition, the increase in amplitudes of the TW packets is accompanied by stronger interactions, leading to more irregular spatial and temporal modulations.

In most of the temporal modulations, the number of oscillations seems to commensurate with the number of round-trips in the signals, rather than the period-doubling scheme. Because of this fact and of the lack of phase coherence between the left and the right temporal modulations for the same signal, it is inferred that temporal modulations variations are not directly linked to interactions. Because of their periodic behavior, they are more likely to be the reflection of temporal growth of TW amplitudes.

We have quantitatively tested how the representation mimics the data, by reconstructing the signal based on the extracted components, the uniform TW, the spatial and temporal modulations, and compared with the real signal by means of the root-mean-square difference, δ. We found that δ varies from 10^{-4} for $\epsilon = 18.10^{-5}$ to 10^{-3} for $\epsilon = 166.10^{-5}$. Additionally, features related to modulations were reproduced by the representation. An example of the reconstruction is shown in Figure 4.30 for the left component at $\epsilon = 143.10^{-5}$. Figure 4.31 is the original component. Clearly, most features of the TW, particularly the undulations at the crest, can be reproduced, and detailed comparison sounds reasonable.

4.10.4 Dynamical View-point

Figures 4.32-4.34 show the projection of the dynamics in the spatial characteristic spaces, $\chi(X)$, for two values of ϵ, 65.10^{-5} and 143.10^{-5}, for their left and right components respectively. Comparison with Figures 4.33 and 4.35, which correspond to the reconstructed signals using the representational form, shows similarity. The splitting of the orbits seen in the projections (ϕ_2, ϕ_3) and (ϕ_4, ϕ_5) is clearly reminiscent of modulation effects as seen in Figure 4.9(c) for the numerical example. Also, one can easily notice the splitting of the orbit, the thickness of which grows with ϵ indicating an increase in strength of modulations.

4.10.5 Symmetries

The symmetries in this state are investigated in light of the model and the TW patterns themselves. The latter are quasiperiodic patterns in time and therefore do not enjoy exact symmetries of the type we discussed earlier- see Section 4.2. Furthermore, the whole signal lacks the spatial reflection symmetry. These symmetries, spatio-temporal translations as well as spatial reflection symmetry, are also broken even at a low level, such as in spatial and temporal correlations. We do not expect our model to prove the presence of these symmetries; rather to provide explanations of which part of the extracted component is responsible for such symmetry breaking.

The left and right uniformly traveling profiles extracted through the model shown in Figure 4.27 behave like mirror images and thus are approximately reflection invariant. At high values of ϵ, the generation of bursting events at the tail of the main profiles breaks this symmetry, since these bursts evolve into structures of different size and duration. Figure 4.27(c) shows this fact clearly. Spatial modulations for low values of ϵ behave in the way we predicted in relations (4.8,4.9), namely a period-doubling function. This property is true only below $\epsilon = 65.10^{-5}$ where weak interactions are prevalent. However, even at such low values of ϵ, the symmetry of period-doubling is not exact, as the strength of the interaction in x_2 is weaker than at x_1, as noted above. As ϵ increases, the period-doubling instability contribute to more asymmetric spatial modulations.

The temporal modulations show 9 oscillations over the 9-round trip time interval of the signal. Therefore, not evident of period-doubling as in the case of spatial modulations. Temporal modulations for left and right components are quiet similar in behavior but could not be related by any symmetry.

In conclusion, the modulations do not generally reflect the type of symmetries we have discussed in Section 4.2. The symmetry breaking is due to the interaction rather than to the main TW profiles. Therefore the model we developed stresses the reflection symmetry between the primary traveling waves and the asymmetry in the spatial as well as temporal modulations which is responsible for the non periodic dynamics in the CPWP regime.

4.10.6 Model Limitations

The representation, based on modulations of a uniform TW, was successful in furthering our understanding of the complexity present in the wave packet regime. Basically two types of perturbations were related to complexity. The first type is due to nonlinear interactions between TW components. The second type are perturbations generated at the tail of the main traveling wave which lead to bursting events characterized by erratic behavior. The former process has been modeled through a simple representation via some plausible assumptions of which we now discuss the limitations.

- **Assumptions:**

Our model assumes a constant average group velocity. We estimated this velocity from spatial and temporal Fourier spectra of the demodulated amplitude profiles. By varying the constant group velocity by as much as ±20% in the extraction scheme, and computing the error δ, we found that the average velocity achieves good results. A typical example is shown in Figure 4.36, for $\epsilon = 0.00143$. The graph shows that δ is minimal for the average group velocity. Even though our representation is still valid for time-dependent velocities, we found that using constant average velocity to be efficient.

The other important assumption was that of a specific form of the space-time modulations. The choice of this form was dictated not only by the fact that the only traveling part is the primary traveling wave itself and thus any other time and spatial dependence could be modeled through $g_1(x)g_2(t)$, but also that this expression was easily implemented.

- **Limitations:**

As mentioned above, the main deficiency of our representation was its inability to capture properly the burst-splitting phenomena exhibited at higher Rayleigh numbers. The trailing burst can, however, be partly extracted. It corresponds to the little hump at the trail of the extracted primary TW wave profile. The main hindrance was that trailing bursts possess a different group velocity, as they lag behind the main body of the TW profile. Furthermore, their amplitude shows a substantial growth followed by a decay. The time duration and extent of these events vary over the course of the TW evolution.

The second limitation comes from the model itself. The left hand of the system of the integral equations (5.57)-(5.59) is formed by functions set to represent the signal. These functions are obtained by integrating the signal in space, time and in the moving frame of the TW. The degree to which these functions f_1, f_2 and f_3 reflect the detailed texture of the signal is not trivial and remains an open question. The fast convergence of the iterative scheme shows, however, that the extracted components are a rather robust solution to the system of integral equations.

In this attempt to understand the nature of the complexity of the CPWP regime, there are a few important conclusions. First, it is clear that the presence of spatio-temporal modulations has a direct effect on the dynamics and is involved in the increase of complexity. The nature of the spatial as well as the temporal modulations is presumed to pertain to nonlinear interactions between the right- and left-going components. The appearance of burst-splitting events which become more clear as ϵ increases, are similar to those in dispersive chaos regime and contribute to complexity. They seem to take place as wave packets get narrower. These phenomena, as mentioned before, are of local character and exhibits space-time variations. The trailing bursts apparently have a slightly smaller velocity than the average group velocity of the wave packets. Thus, a model based upon considering yet another traveling component which accounts for the burst splitting might be appropriate, such as

$$u_{mod_2}(x,t) = g_1(x)u(x-ct)u'(x-c't)g_2(t). \tag{4.69}$$

The difficulty is that, unlike c, the velocity c' is not *a priori* known. In addition, these bursts sustain their shapes only for more or less one round trip.

4.11 Summary

In this chapter, we have shed some light on probable causes which lead to space-time complexity in oppositely propagating waves. The presence of the space-time modulations stems from the fact that nonlinear interaction between left and right components tends to suppress each component during their overlap, compensating the linear growth they experience when far from each other. The application of the spatio-temporal model to each component considered separately clearly shows the effects related to nonlinear interactions as well as linear growth in spatial and temporal modulations respectively. Both theoretical and numerical studies conducted in this chapter showed the effects on the dynamics and ways to find evidence of the presence of space-time modulations. This evidence is found by using the BOD techniques. The application of the Fourier decomposition on the chronos and topos relative to a one-directional modulated wave offers the evidence of the modulations through the presence of sideband splitting in frequencies and/or wave numbers respectively. These findings were illustrated through a numerical example to test the applicability of the model. The extraction of modulation functions could be achieved analytically in cases where resonances between the the main traveling wave profile and the modulations takes place with either the spatial or temporal modulation. Otherwise, the extraction of both modulations is performed by means of a numerical algorithm to solve a set of integral equations.

The novelty in this work is the detection and the extraction of spatial and temporal modulations. These were found to be an inherent part of the dynamics of the counterpropagating regime of binary fluid convection. The proposed representation successfully reflected the effects of nonlinear interactions on the wave packets. Despite the drawbacks of not being able to account fully for the bursting events, the extracted components reproduced most of the textures present in the experimental signal. We particularly note our success in extracting modulations from localized wave packet, non-monochromatic wave. Additionally, these modulations, notably the spatial ones, were clearly reflecting nonlinear interactions between the oppositely traveling waves through depressions at crossing locations. The combined effects of nonlinear interaction and amplitude growth termed *period-doubling instability* was a major contributor to the rising complexity in addition to trailing bursts phenomena.

As a final note, from the scenarios we have proposed earlier, Scenario II is likely the one occurring in this series of experiments in the absence of more data sets for ϵ values close to onset.

n / $\epsilon 10^5$	1, 2	3, 4	5, 6	7, 8	9, 10
18	$\underline{9}$	$\underline{18}$	$\underline{27}$	$\underline{36}$	$\underline{45}$
	$\underline{9}$	$\underline{18}$	$\underline{27}$	$\underline{36}$	$\underline{45}$
43	$\underline{9}$	$\underline{18}$	23,$\underline{27}$,31	8.10.17.19,$\underline{36}$.41.45	36,$\underline{45}$.54.63
	$\underline{9}$.18.27.36	$\underline{18}$.27	23,$\underline{27}$,31.45.49	10.19.32,$\underline{36}$.41.45.49	36,$\underline{45}$.54.63
65	$\underline{9}$.18.26.36	$\underline{18}$.27,35	$\underline{27}$.35.44	$\underline{36}$.44.53	36,$\underline{45}$.54
	$\underline{9}$.18.26,36	$\underline{18}$.27	18,$\underline{27}$.35.44	$\underline{36}$.44.53	36,$\underline{45}$.54
95	$\underline{9}$,18,27	9,$\underline{18}$,27	$\underline{27}$,36,40,45	23,$\underline{36}$. 40,49.54	32,$\underline{45}$,49.54.58.63
	$\underline{9}$.18.27	9,$\underline{18}$,31	$\underline{27}$,36,40,45	23,$\underline{36}$.40.49.54	32,$\underline{45}$.54.58.63
109	$\underline{9}$,18,27	9,$\underline{18}$,27.36	14.18,$\underline{27}$,36	23.27.$\underline{36}$.45.48.54	32,$\underline{45}$.59.63
	$\underline{9}$.18.27.36	9,$\underline{18}$.27.36	14.18,$\underline{27}$,36.41	23.27.$\underline{36}$.45.48.54	32,$\underline{45}$.58.64
123	$\underline{9}$,18,27.29,45	11,$\underline{18}$,26.36	18.20,$\underline{27}$,35,47	29,$\underline{37}$.44.56	44.46
	$\underline{9}$,18,29.45	9.11,$\underline{18}$.26.36	20,$\underline{27}$,35.47	29,$\underline{37}$. 44.56	$\underline{44}$.46
143	$\underline{9}$,18,20,27,29.36	9,$\underline{18}$,27	18.24,$\underline{27}$,36.45.47	27,$\underline{36}$.45.47.54.56	16.21.36.42,$\underline{45}$.54.63
	$\underline{9}$.11.18,20.27.29	9,$\underline{18}$,27.36.38	18.24,$\underline{27}$,36.44.46.53	27.33.$\underline{36}$.45.47.54.56	21.25.36.42,$\underline{45}$.54.63.
166	$\underline{9}$,31	$\underline{17}$	$\underline{26}$,35,48,57	26,$\underline{35}$.57.61	21,$\underline{43}$.66
	$\underline{9}$.31	$\underline{17}$	$\underline{26}$.35.48.57	26,$\underline{35}$.57.61	21,$\underline{43}$.66

Table 4.1: Left-going amplitude $A_L(x,t)$

ϵ	m
18.10^{-5}	0
43.10^{-5}	±1, ±4
65.10^{-5}	-1
95.10^{-5}	4
109.10^{-5}	-4.3
123.10^{-5}	±1, 2
143.10^{-5}	±1, ±2, 3
166.10^{-5}	-1,-2,3,4

Table 4.2: Values of m for the left-going component

n $\epsilon 10^5$	1.2	3.4	5.6	7.8	9.10
18	$\underline{9}$.11	$\underline{18}$,20 .27	$\underline{27}$,29	$\underline{36}$	$\underline{45}$,47
	$\underline{9}$,11	$\underline{18}$,20 .27.36	$\underline{27}$,29,36	$\underline{36}$.38	$\underline{45}$,47
43	$\underline{9}$.18.27.36.45	9,$\underline{18}$,36.46	23,$\underline{27}$,36.45	32, $\underline{36}$, 45,68	32.36,$\underline{45}$,54.63
	$\underline{9}$.18.27,36	9,14,$\underline{18}$,36,45,54	23,$\underline{27}$,36.45.54	32.36,$\underline{45}$,54	32.36.$\underline{45}$,54
65	$\underline{9}$,18.53	$\underline{18}$.25.35,54.63	17,$\underline{27}$,36.53	17.27,$\underline{35}$, 35,54	17.27.35,$\underline{44}$.63
	$\underline{9}$.18,26.36	8,$\underline{18}$.25,35	$\underline{27}$,36	17.27,$\underline{35}$, 35,54.63	19.27.34,$\underline{44}$.54.63
95	$\underline{9}$,18.36.45	9,$\underline{18}$.36	15,$\underline{27}$,36.45	15,$\underline{36}$, 45.48.55	24.$\underline{45}$,54.63
	$\underline{9}$.18.27.45	$\underline{18}$,36	15,$\underline{27}$,36.45	24,$\underline{36}$, 45,48.54.63	24.36,$\underline{45}$.54
109	$\underline{9}$,18.27,45	$\underline{18}$,27.31,36	18,$\underline{27}$,31.36,40.54.63	22.27,$\underline{36}$,40.49	31.37.$\underline{45}$,63.67
	$\underline{9}$.18.27.31.36.45	$\underline{18}$,27.31,36.45	18,$\underline{27}$.31,36.40.45	$\underline{36}$.40.45,49.58	$\underline{45}$,63.67
123	$\underline{9}$,11,18.27.36.43	$\underline{18}$,27.34.37	$\underline{26}$,28,35.44.53	$\underline{37}$.44	8.19.43,$\underline{45}$.65
	$\underline{9}$,11.19.26.37.53	$\underline{18}$,27.34,37,53	17,26,$\underline{28}$,35.45.53	$\underline{37}$,44	19.26.43,$\underline{45}$.65
143	$\underline{9}$,18.21	$\underline{18}$.27.30.39.48	18,$\underline{27}$,36.45.48	27,$\underline{36}$.45 48.54,57.63	24.33.36.$\underline{45}$.54
	$\underline{9}$.12.18	$\underline{18}$,27.30,48	18,$\underline{27}$,36.45,48.57	27,$\underline{36}$.45 48.54.57.63	15.24.36,$\underline{45}$.54.63
166	$\underline{9}$,18	9,$\underline{18}$.26.35	$\underline{27}$,35,43.52	27,$\underline{35}$,44,53	26.35.$\underline{44}$.53.61
	$\underline{9}$.18.26	9.$\underline{18}$.26.35.43	18, $\underline{27}$,35	27.$\underline{35}$.44.53	21,$\underline{43}$,66

Table 4.3: Right-going amplitude $A_R(x.t)$

ϵ	m
18.10^{-5}	2
43.10^{-5}	$\pm 1, \pm 4$
65.10^{-5}	-1
95.10^{-5}	± 3
109.10^{-5}	$\pm 1, \pm 4$
123.10^{-5}	$\pm 1, \pm 2$
143.10^{-5}	± 3
166.10^{-5}	$-1,-2,\pm 4$

Table 4.4: Values of m for the right component

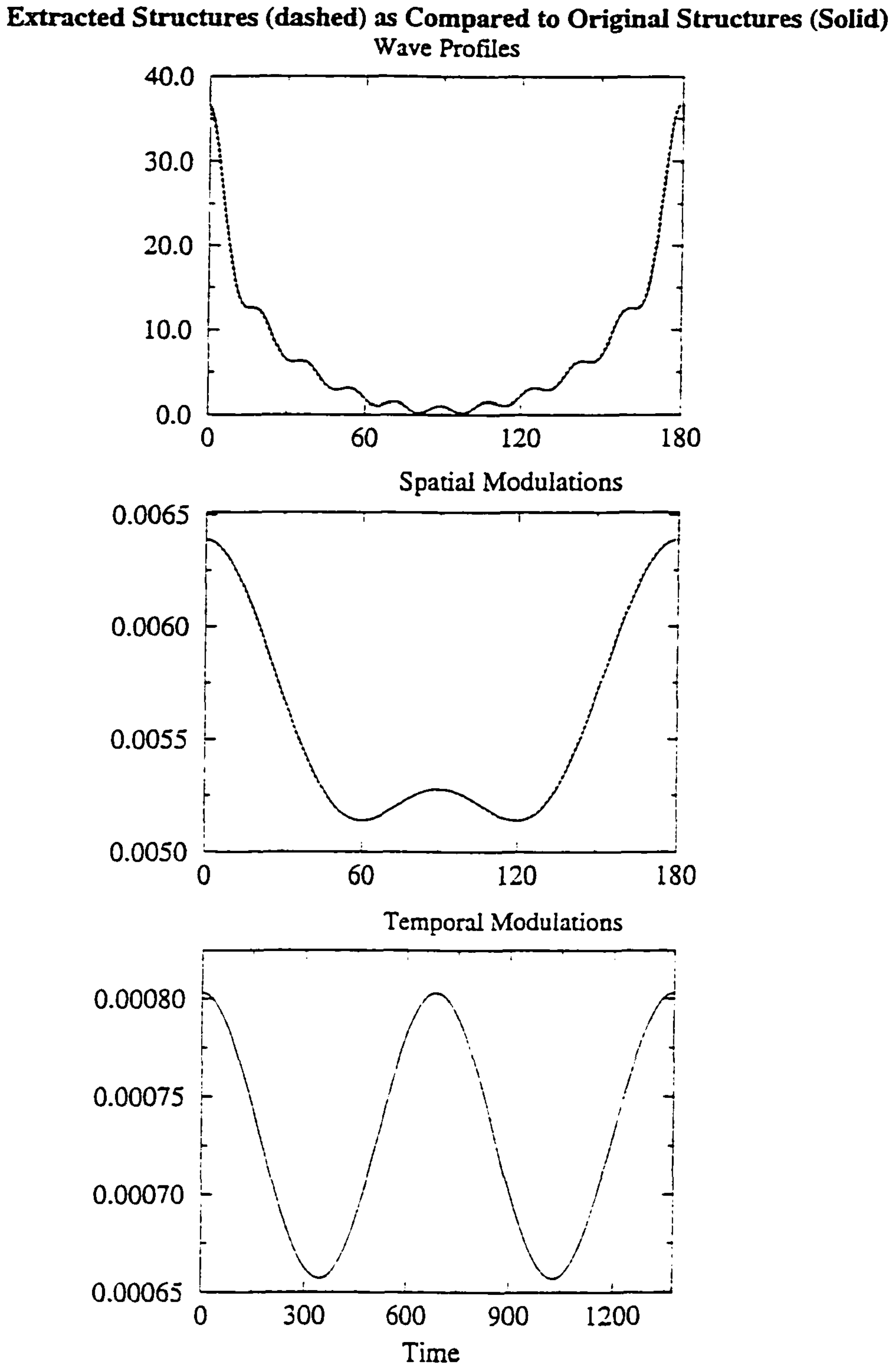

Figure 4.1: Representation of: (a) the reference dynamics $u_o(x,t)$, (b) the spatial modulation $g_1(x)$ and (c) the temporal modulation $g_2(t)$ from the numerical example. In solid lines are the original profiles, while dotted lines are obtained through numerical extraction.

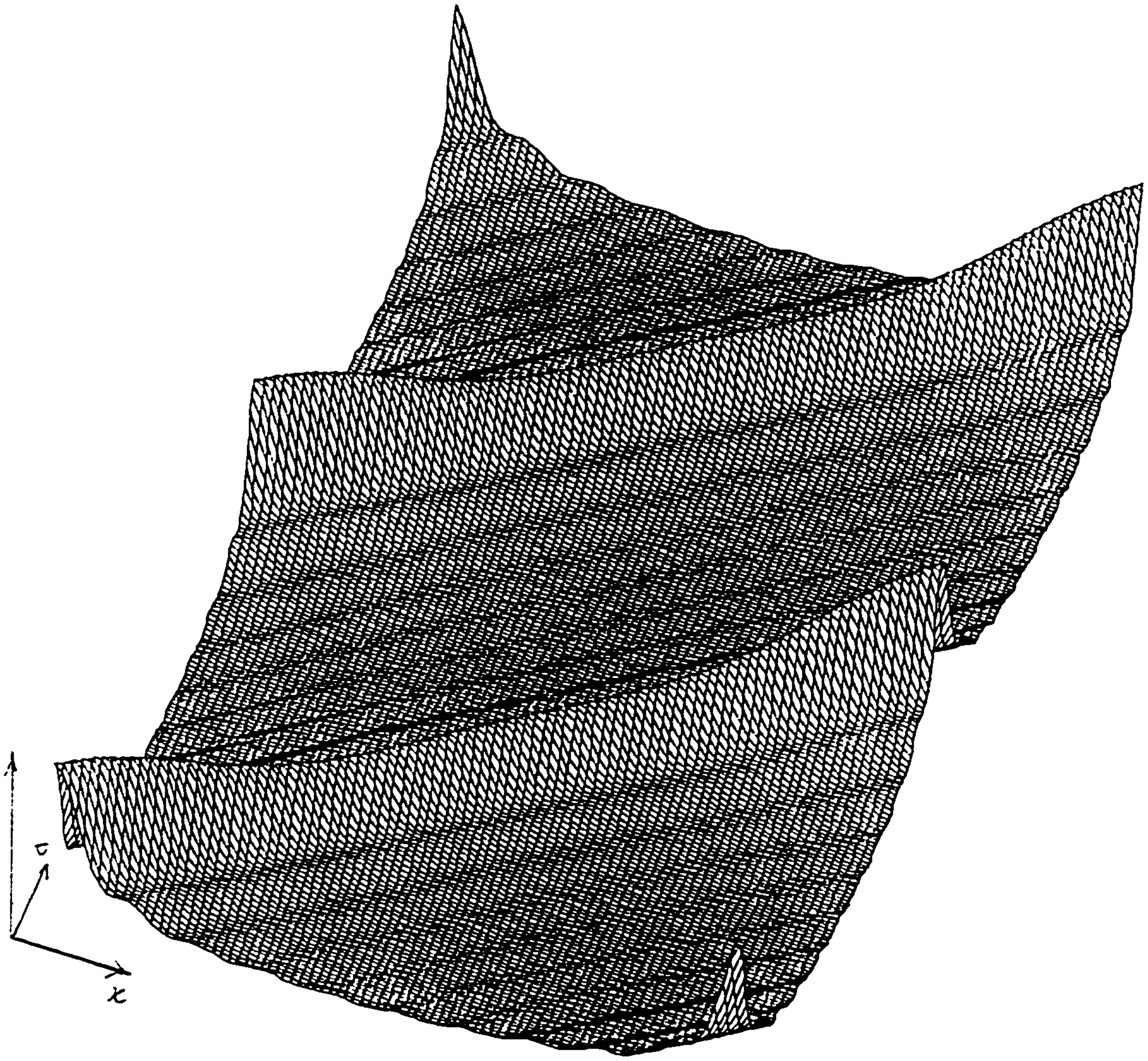

Figure 4.2: Three-dimensional representation of the modulated signal: $u(x,t) = u_o(x - c_o t)g_1(x)g_2(t)$, used in the numerical example.

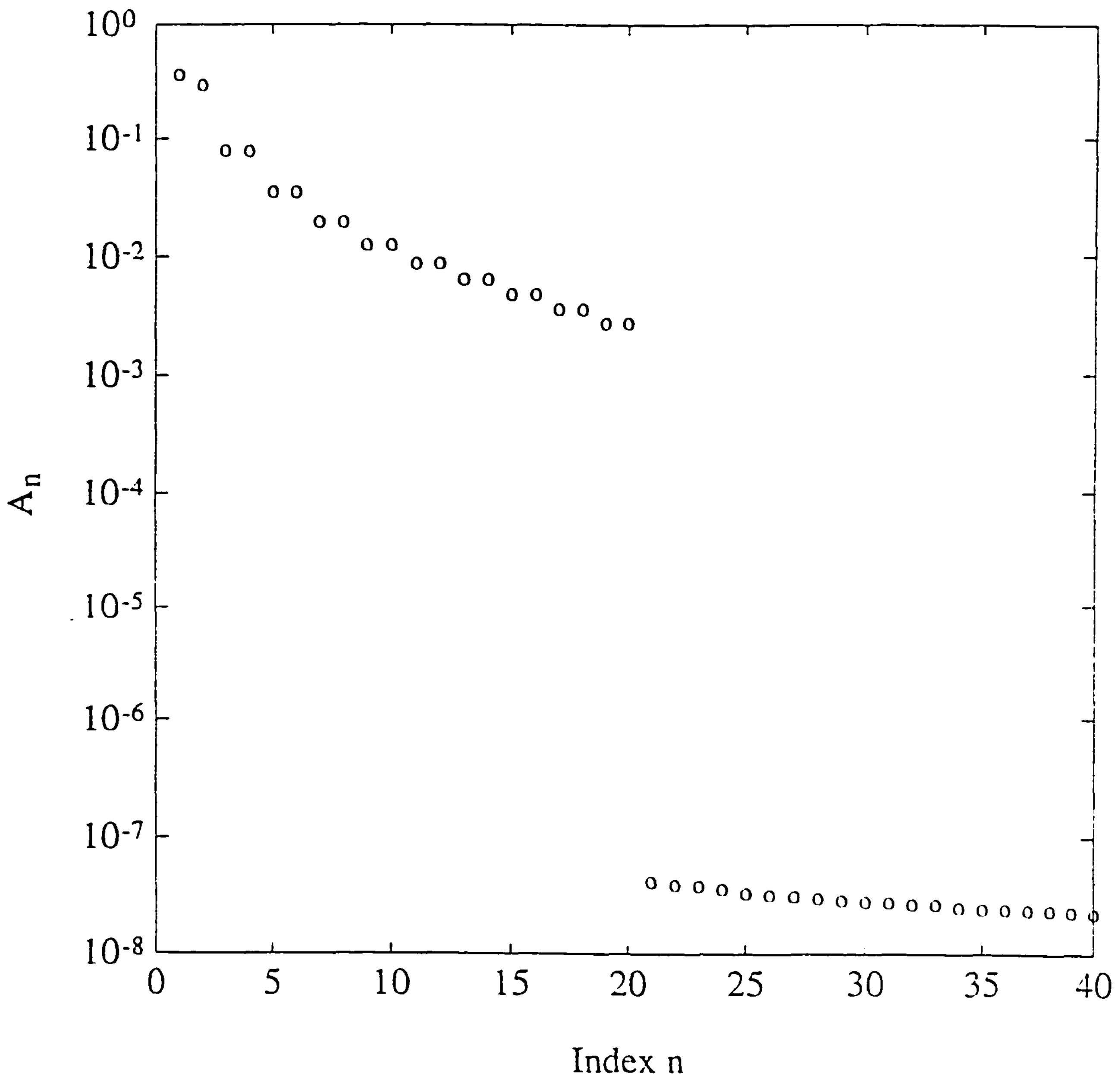

Figure 4.3: The bi-orthogonal spectrum of the spatially modulated traveling wave: $u_1(x,t) = u_o(x - c_o t)g_1(x)$.

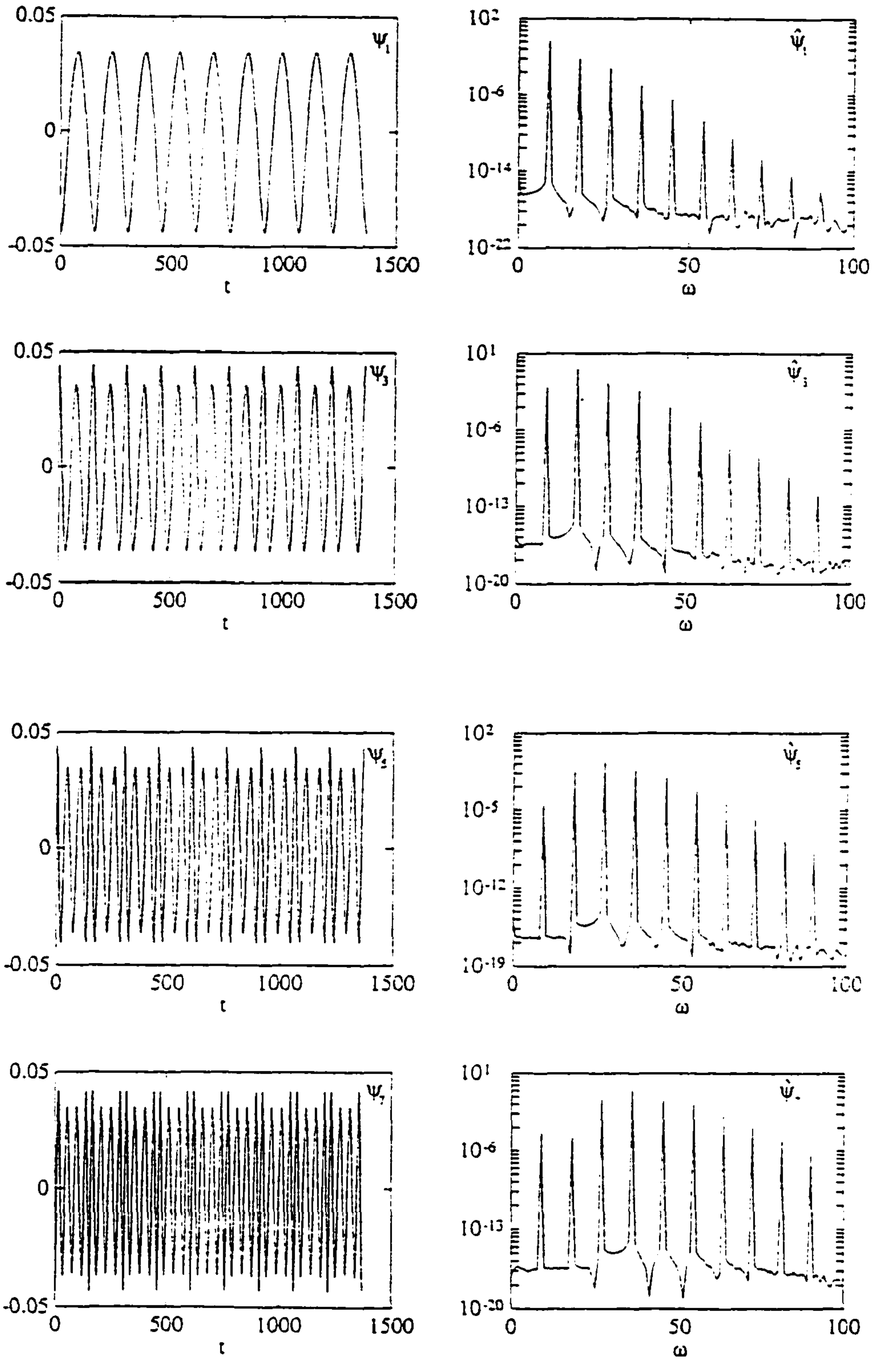

Figure 4.4: The temporal modes (chronos) and their respective Fourier transforms for the spatially modulated traveling wave $u_1(x,t)$.

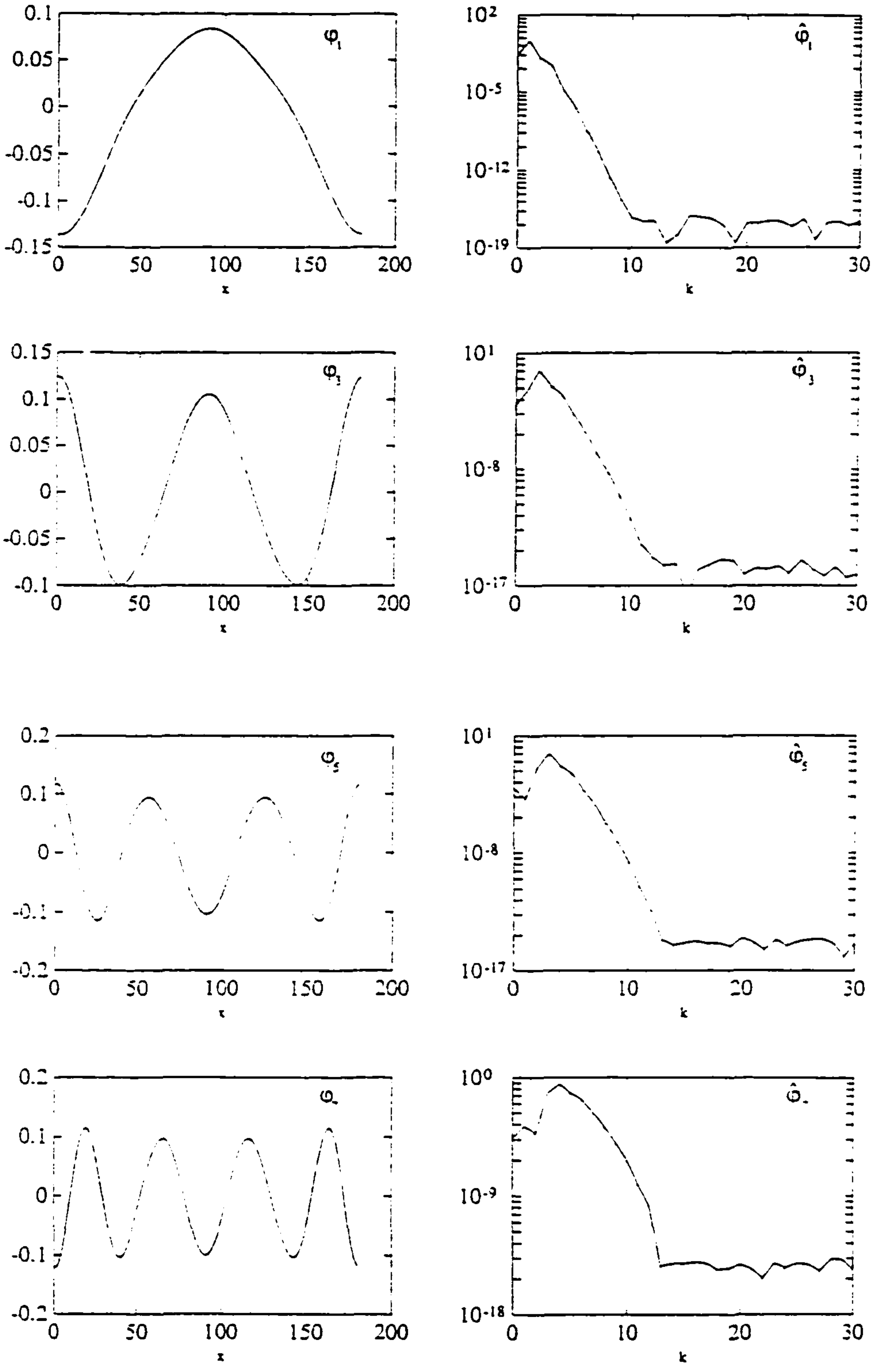

Figure 4.5: The spatial modes (topos) and their respective Fourier transforms for the spatially modulated traveling wave $u_1(x,t)$.

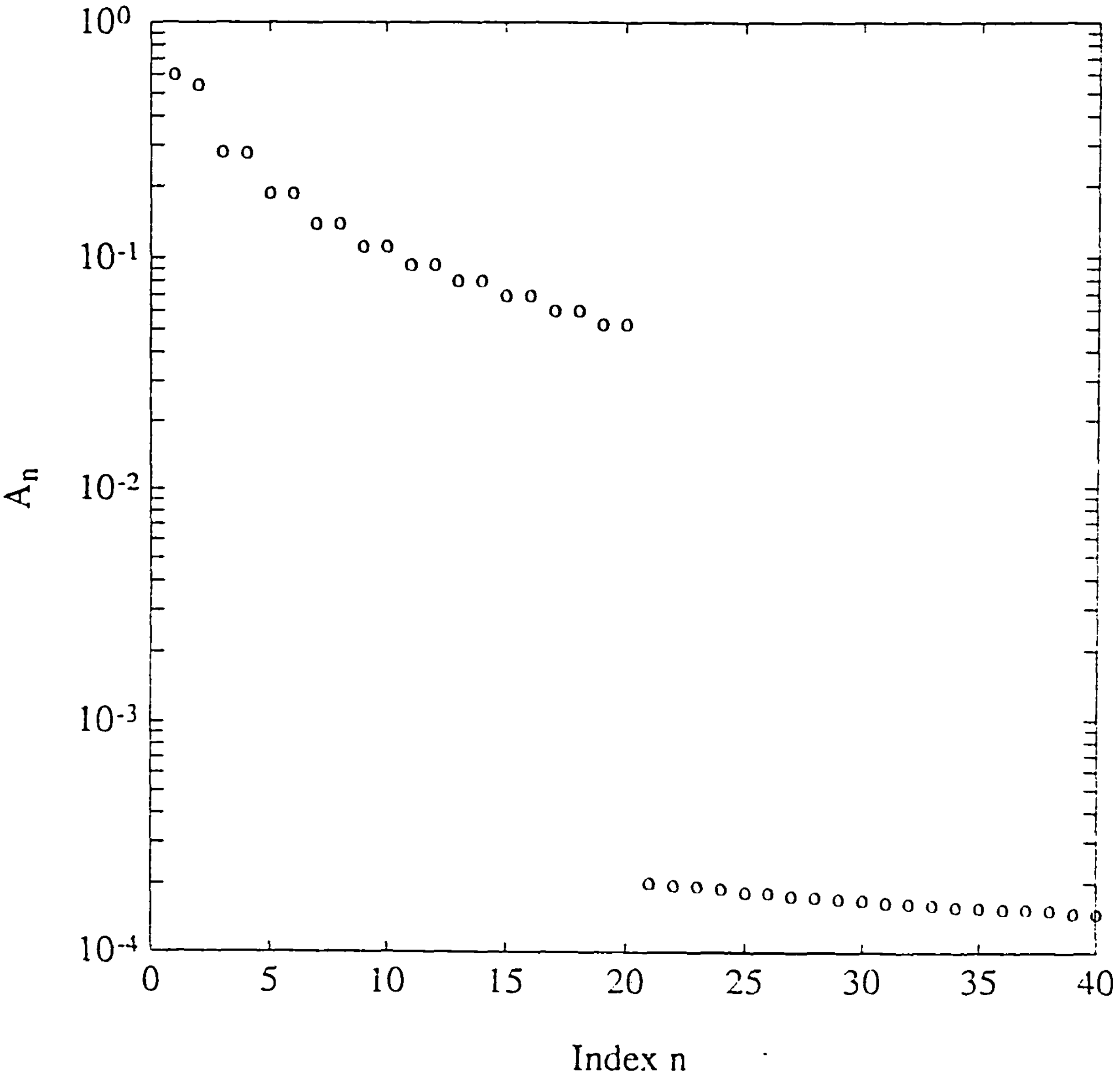

Figure 4.6: The biorthogonal spectrum for the spatially and temporally modulated traveling wave: $u(x,t) = u_o(x - c_o t)g_1(x)g_2(t)$.

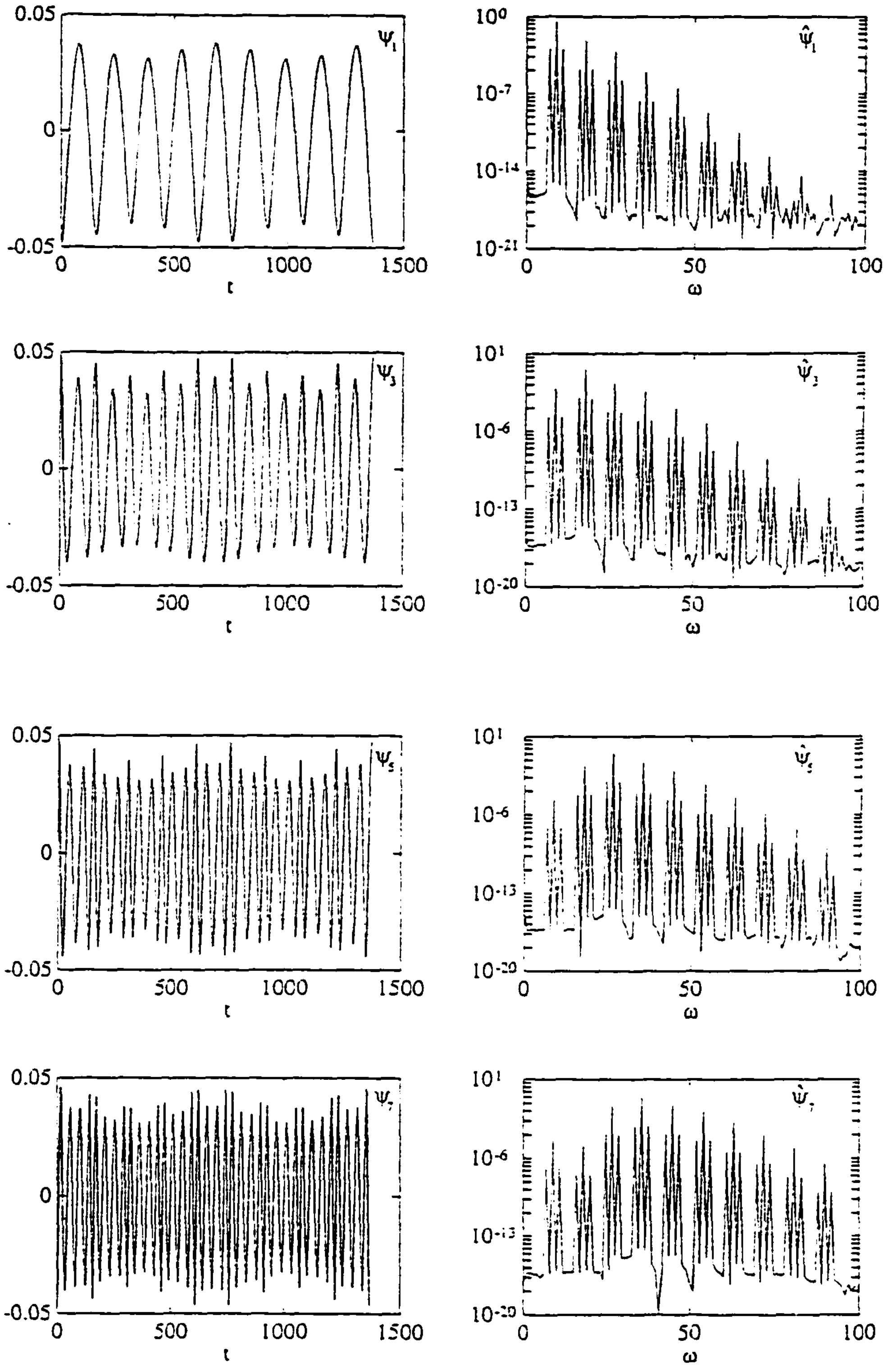

Figure 4.7: The temporal modes (chronos) and their respective Fourier transforms for the spatially and temporally modulated traveling wave $u(x, t)$.

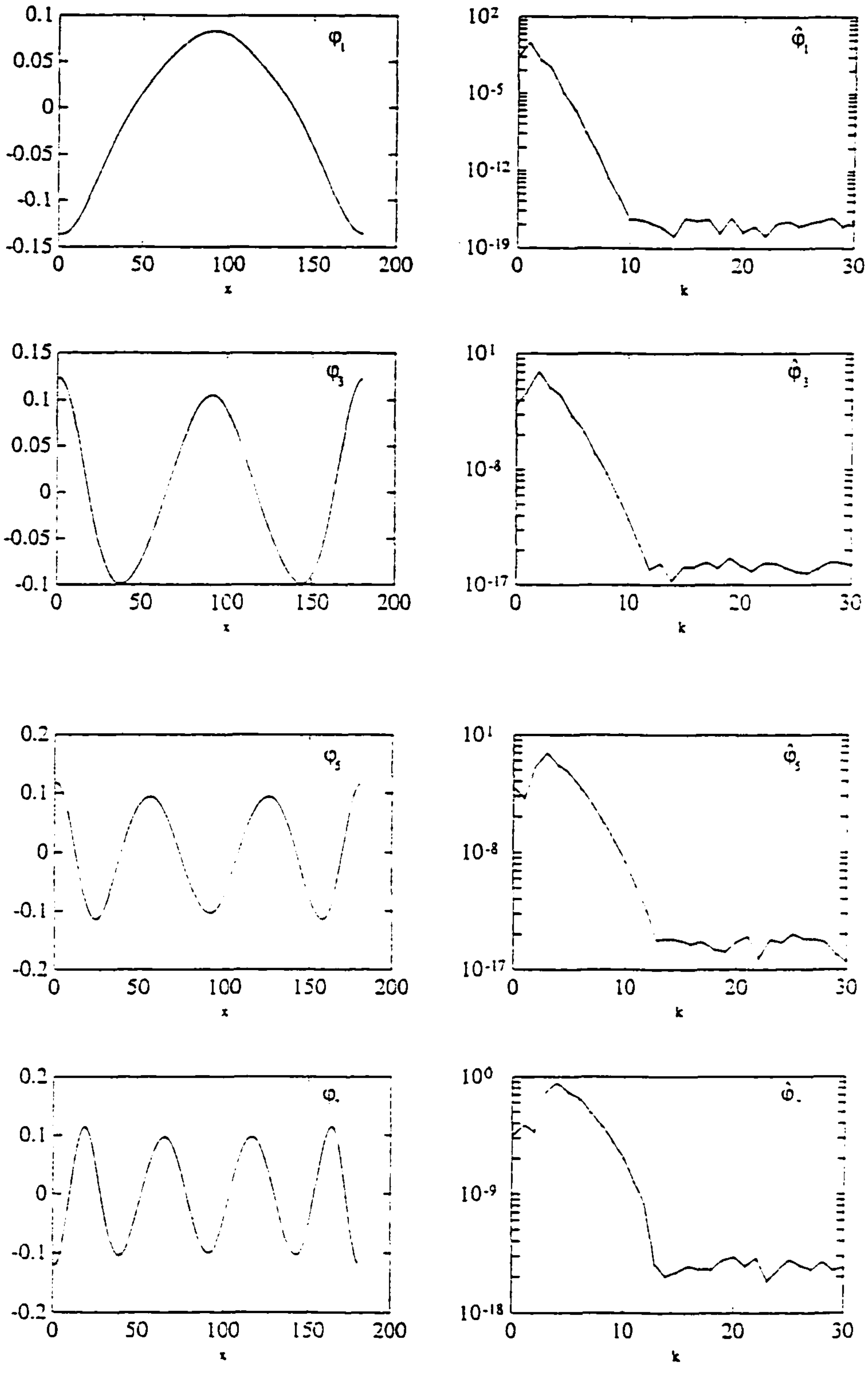

Figure 4.8: The spatial modes (topos) and their respective Fourier transforms for the spatially and temporally modulated traveling wave $u(x,t)$.

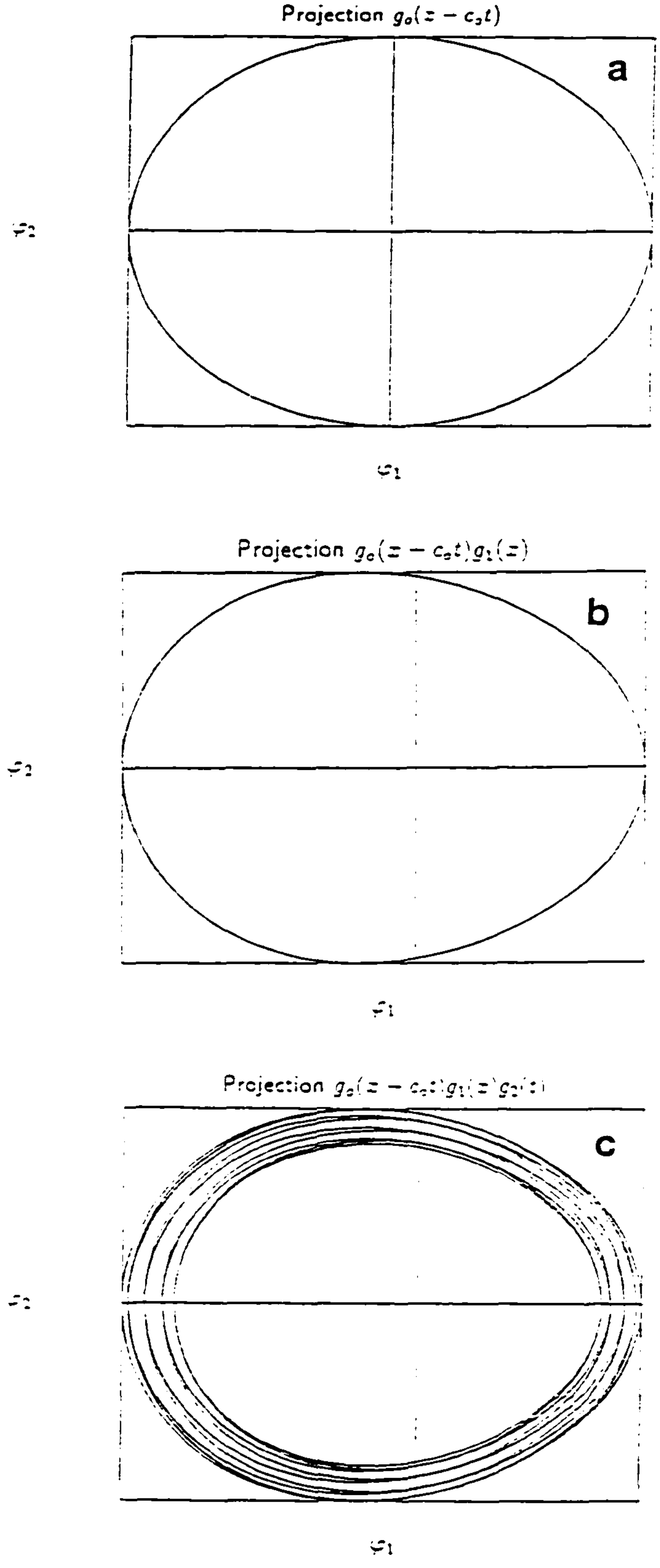

Projection $g_0(z - c_0 t)$

Projection $g_0(z - c_0 t) g_1(z)$

Projection $g_0(z - c_0 t) g_1(z) g_2(t)$

Figure 4.9: Projection of the dynamics onto the plane $(\vec{\varphi}_1, \vec{\varphi}_2)$ of the spatial characteristic space for, (a) uniform traveling wave (b) spatially modulated traveling wave (c) spatio-temporally modulated traveling wave.

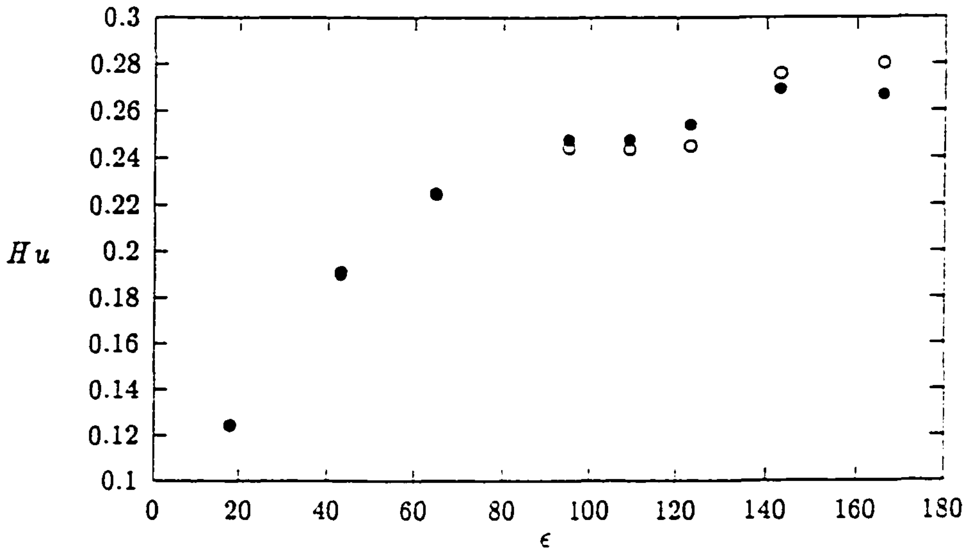

Figure 4.10: The global bi-orthogonal entropy for both left and right amplitudes as a function of the reduced Rayleigh number ϵ for the binary fluid experiments. The full and open circles correspond to the left and right amplitudes respectively.

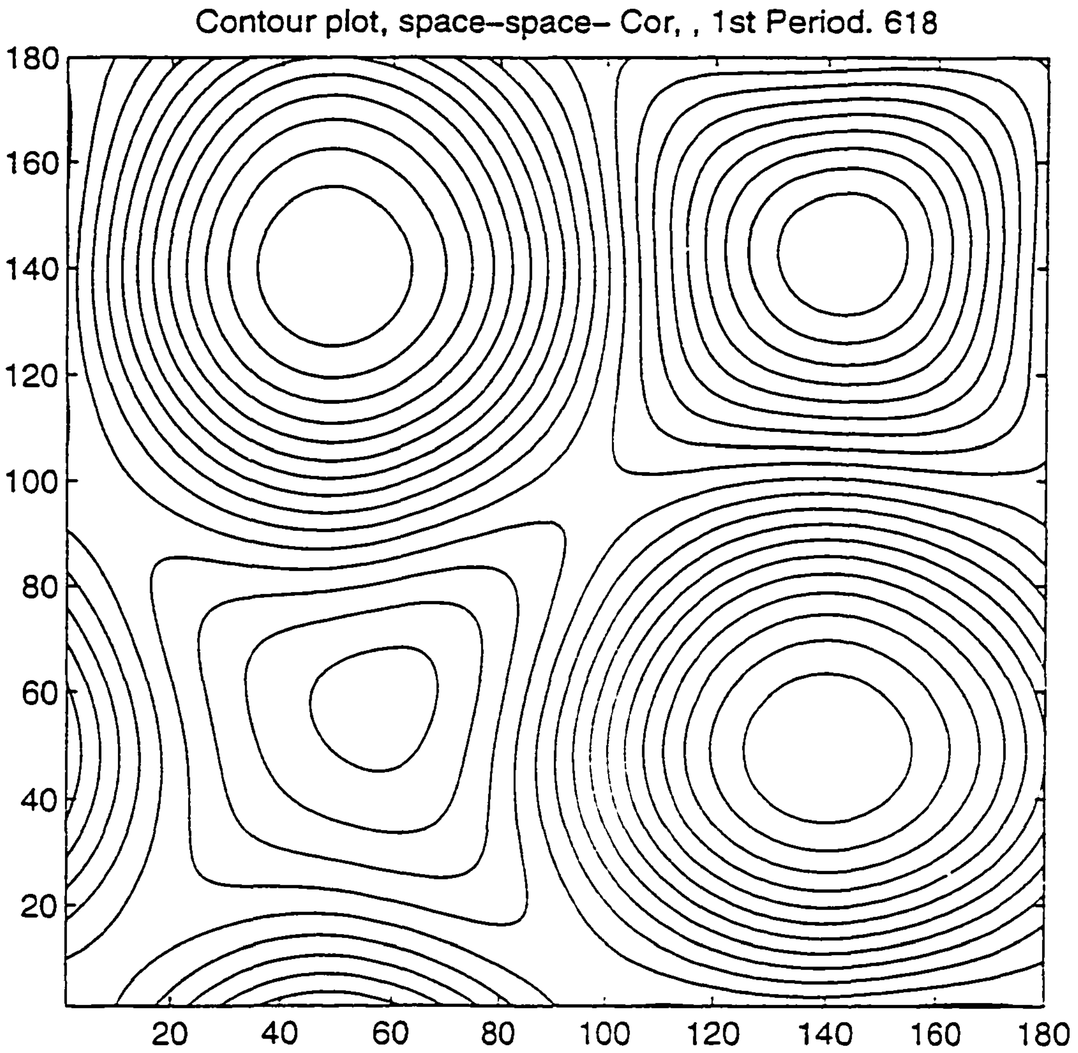

Figure 4.11: Space-Space Correlation computed for one round trip period for $\epsilon = 0.00018$.

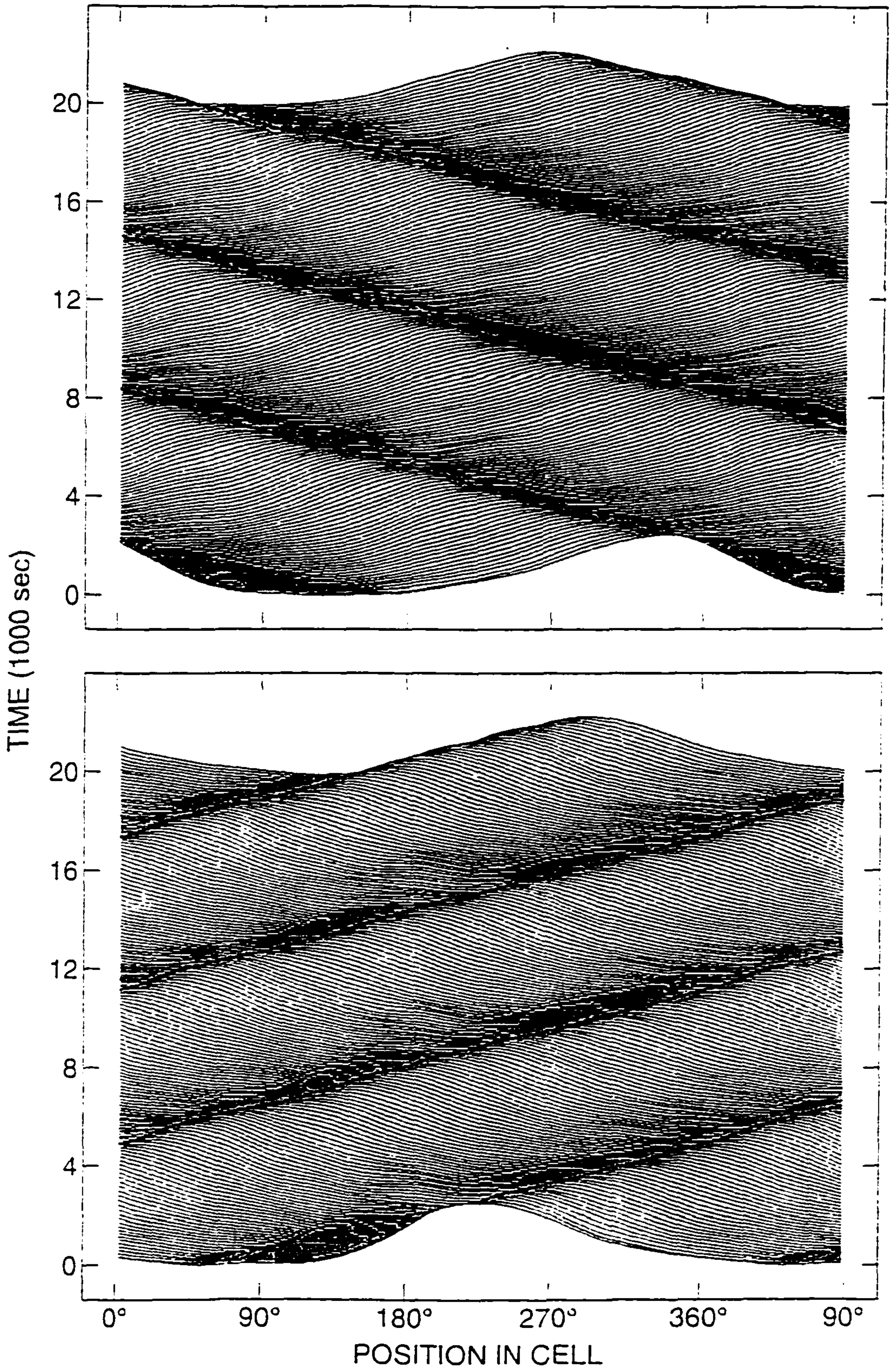

Figure 4.12: Left- and right-going amplitudes from binary fluid convection experiments for the reduced Rayleigh number value $\epsilon = 43.10^{-5}$.

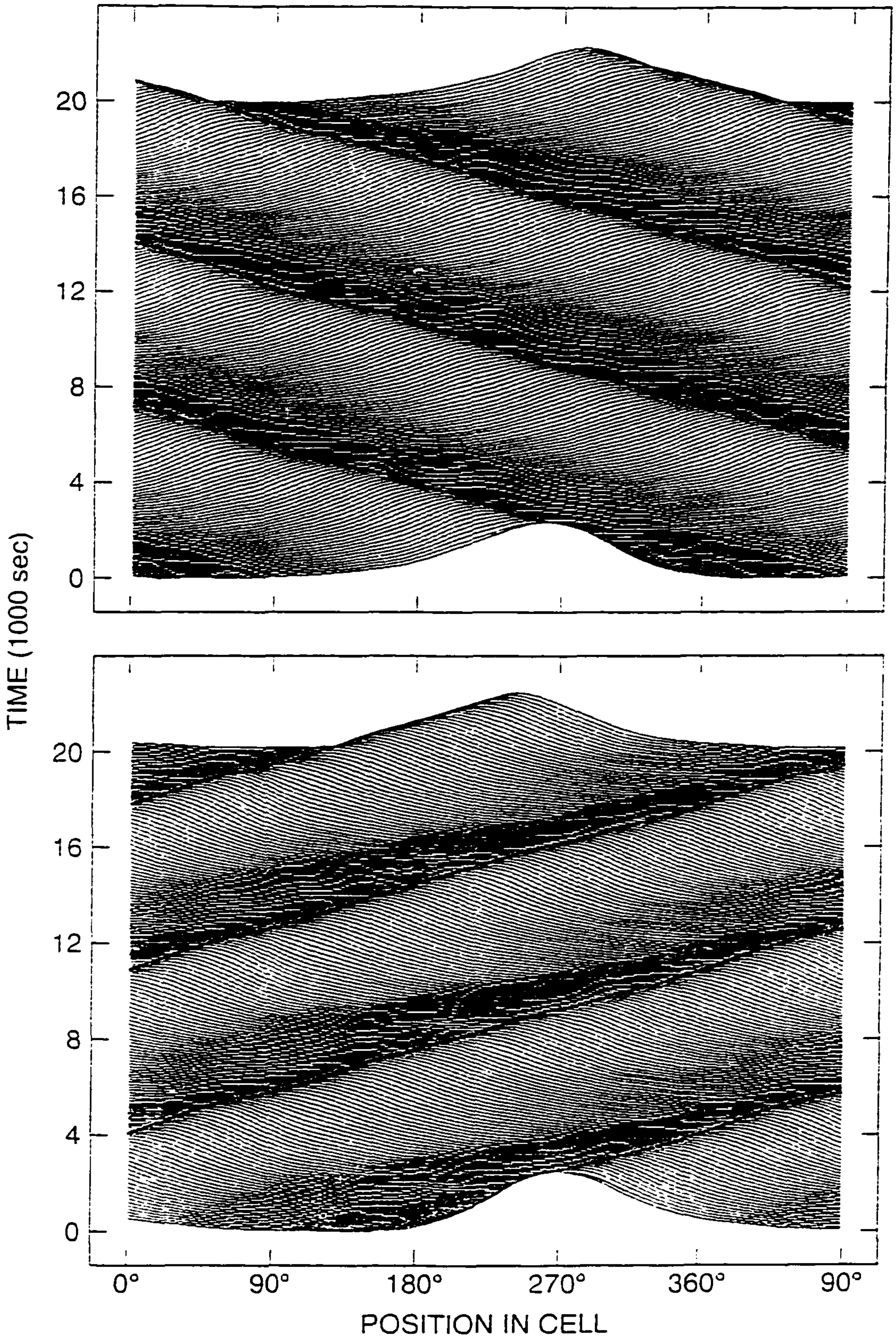

Figure 4.13: Left- and right-going amplitudes from binary fluid convection experiments for the reduced Rayleigh number value $\epsilon = 65.10^{-5}$.

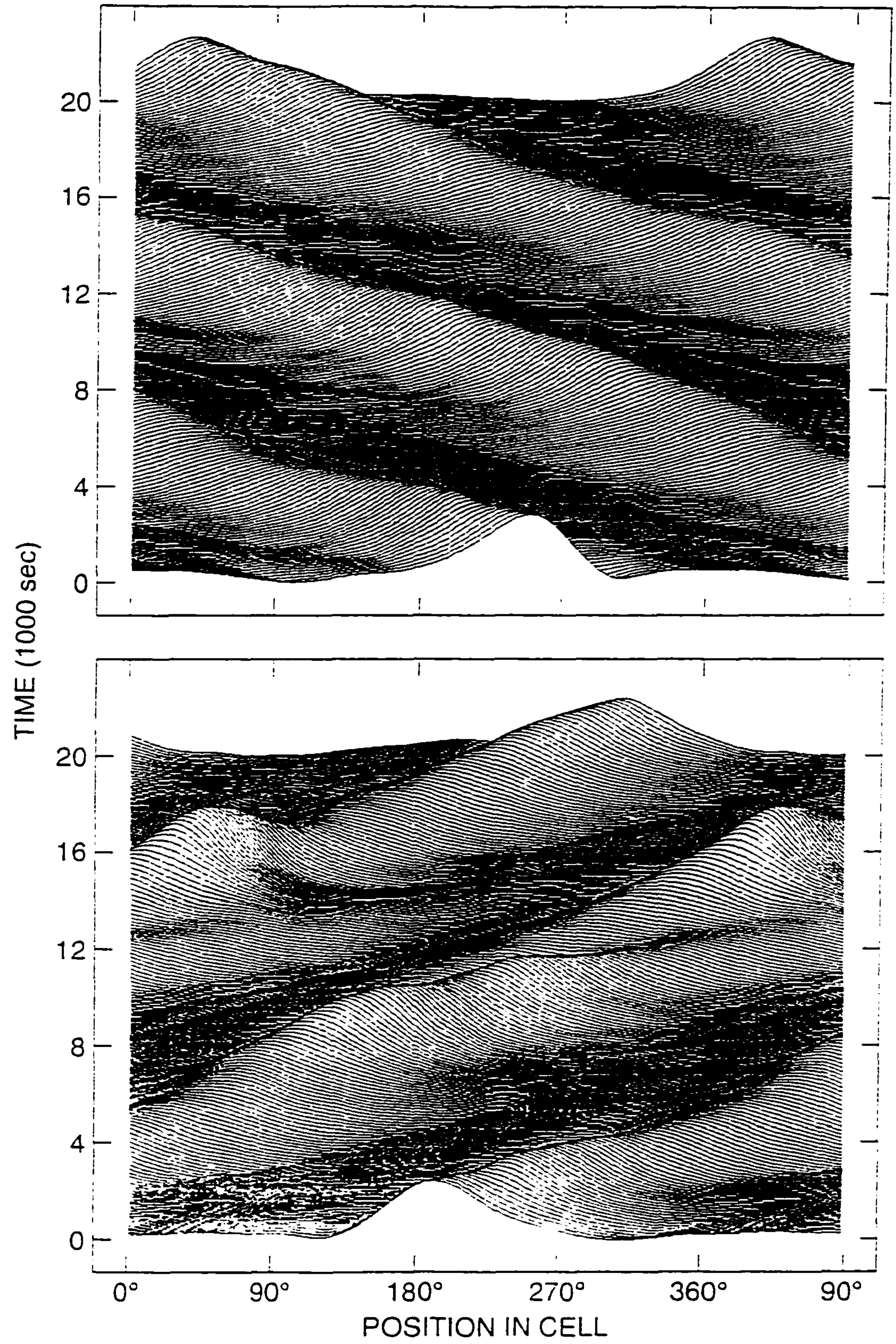

Figure 4.14: Left- and right-going amplitudes from binary fluid convection experiments for the reduced Rayleigh number value $\epsilon = 123.10^{-5}$.

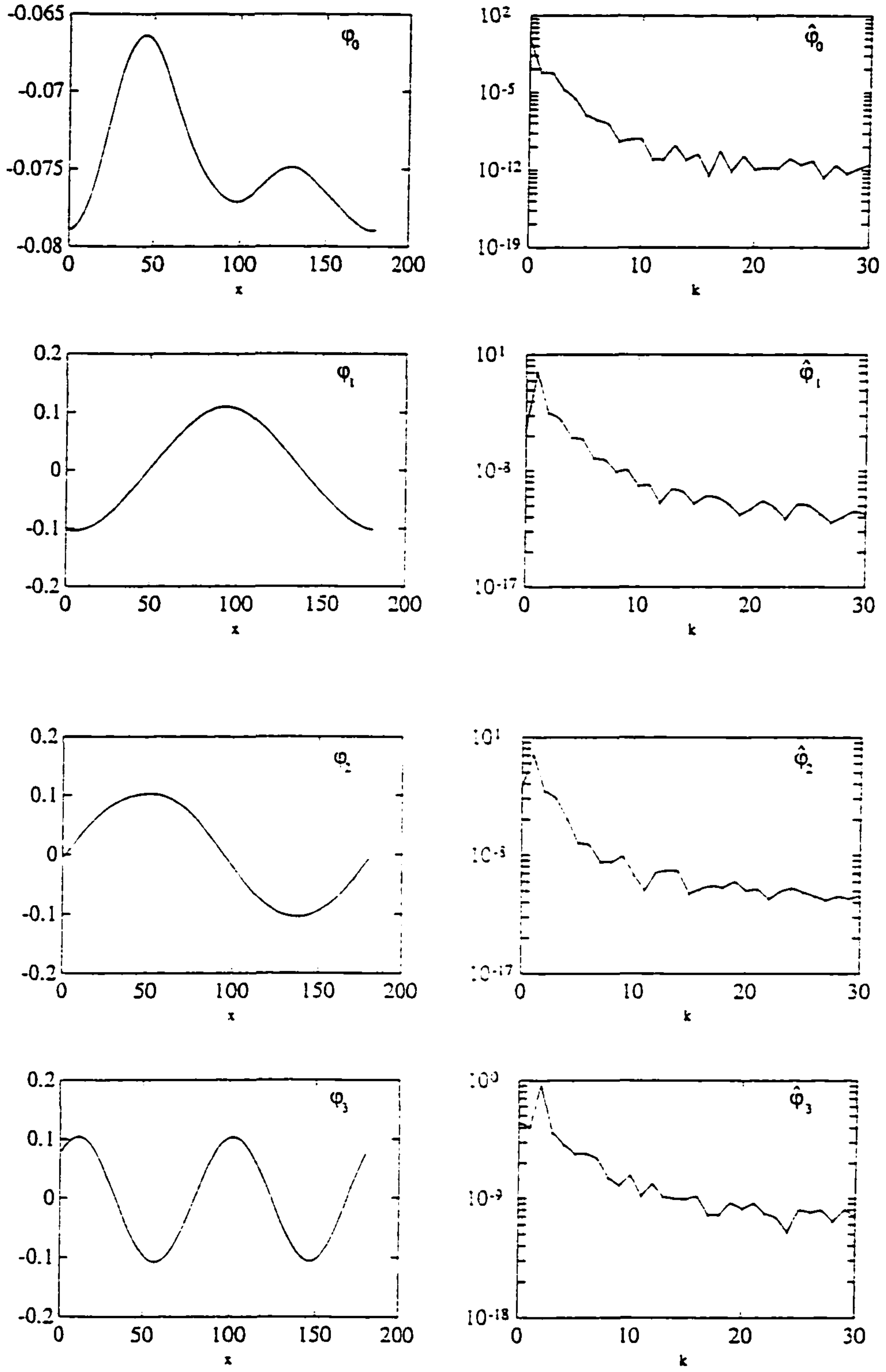

Figure 4.15: Topos and their respective Fourier transforms of the left TW for the reduced Rayleigh number value $\epsilon = 43.10^{-5}$.

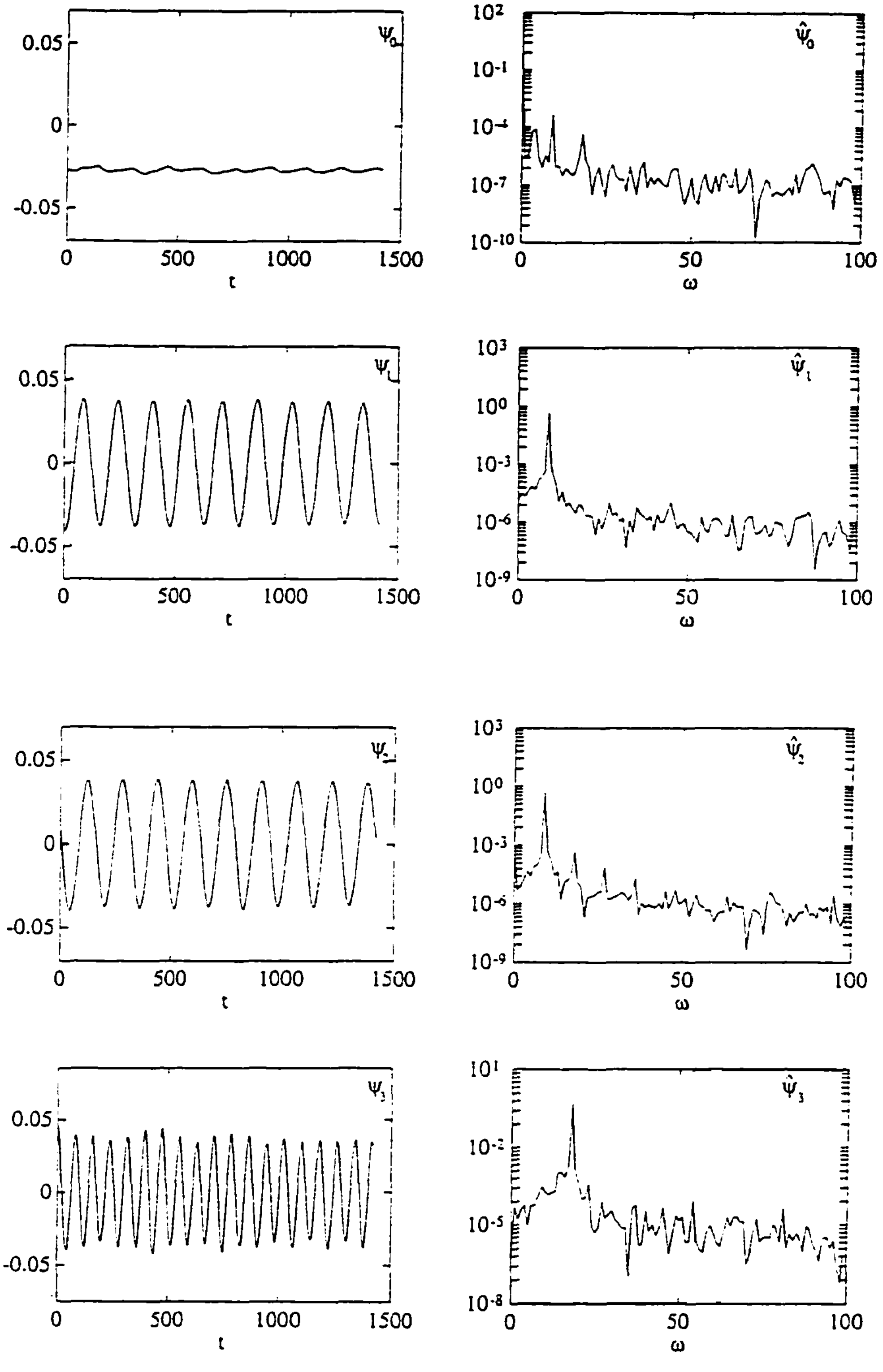

Figure 4.16: Chronos and their respective Fourier transforms of the left TW for the reduced Rayleigh number value $\epsilon = 43.10^{-5}$.

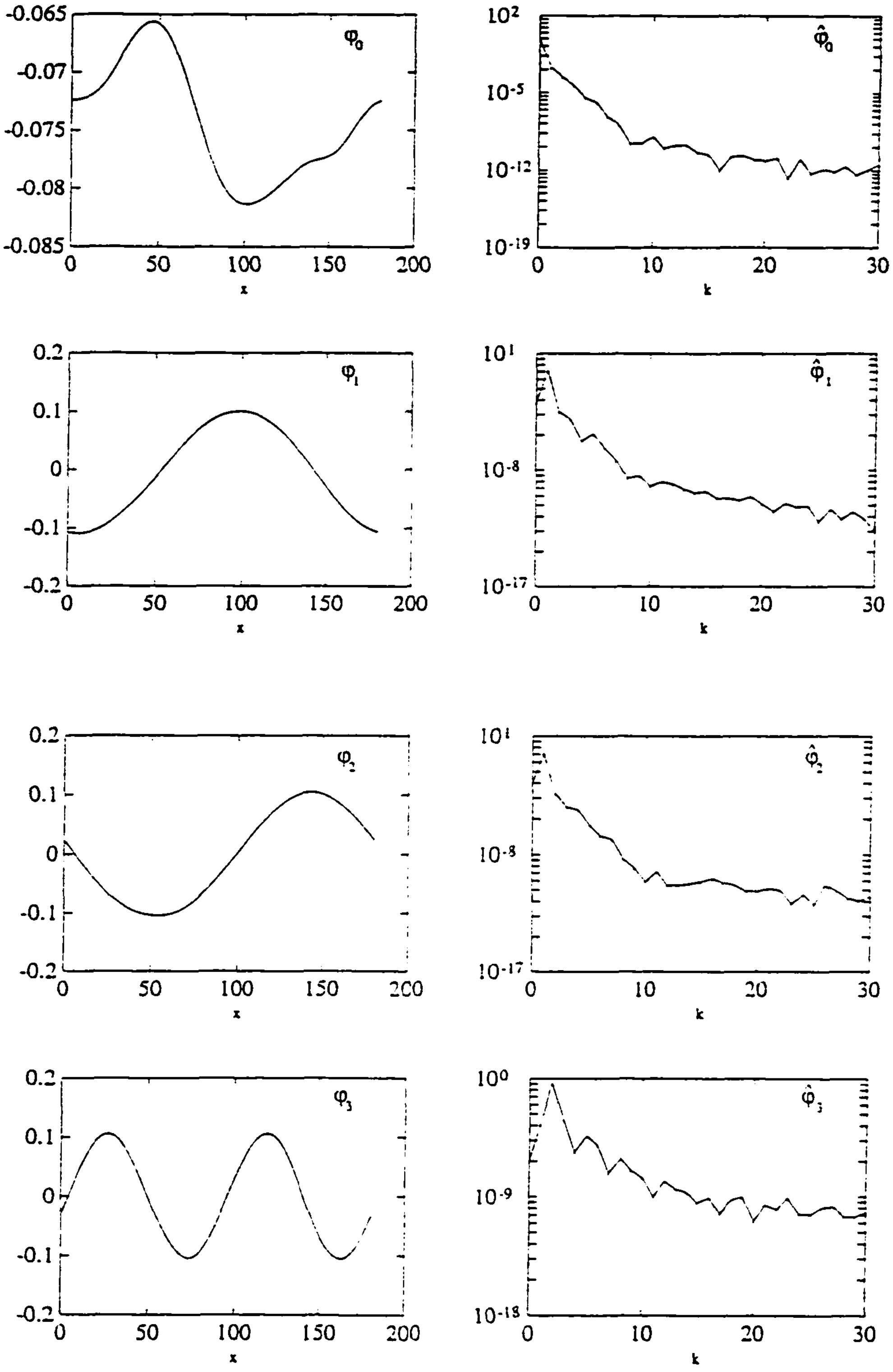

Figure 4.17: Topos and their respective Fourier transforms of the right TW for the reduced Rayleigh number value $\epsilon = 43.10^{-5}$.

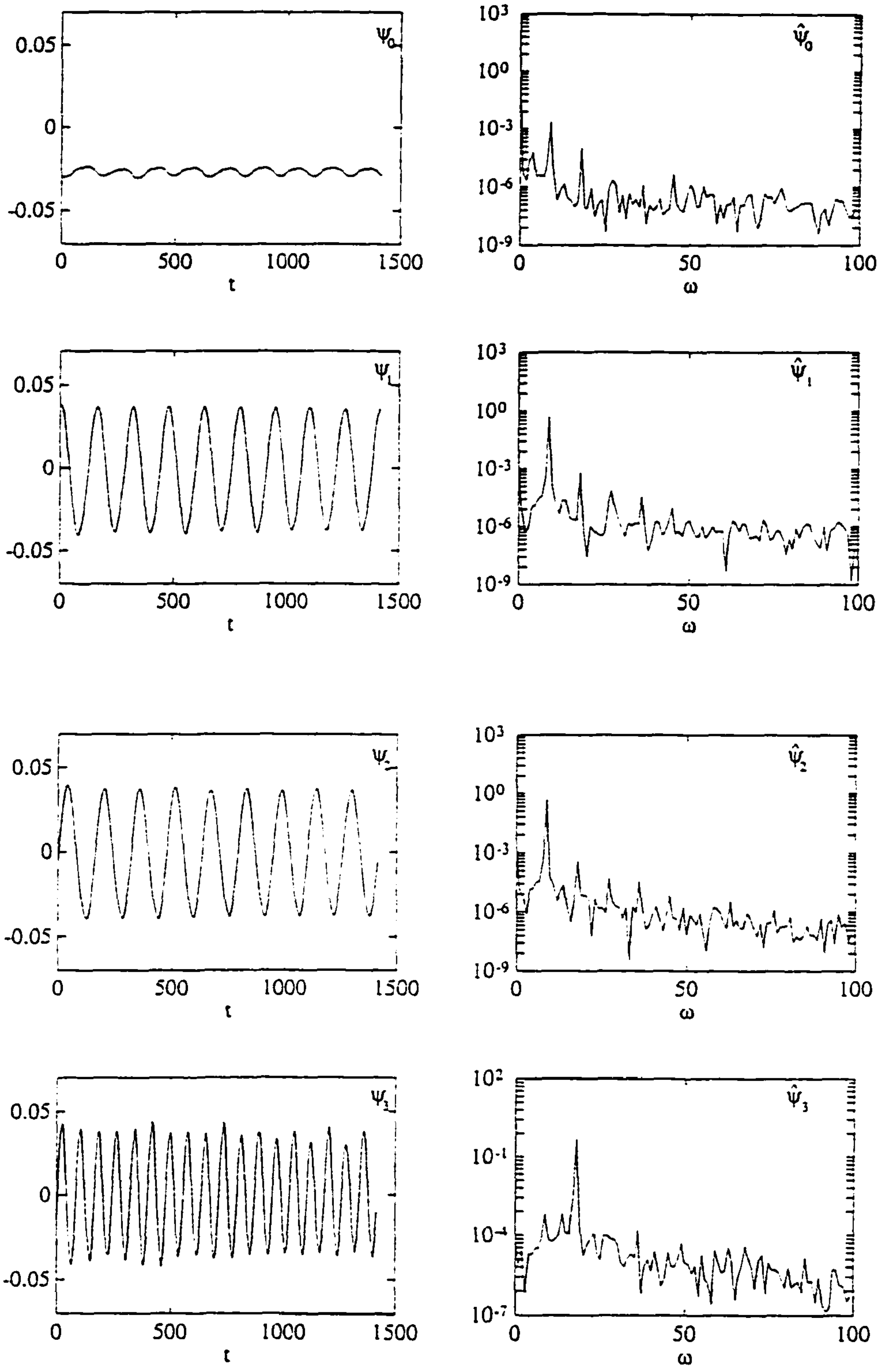

Figure 4.18: Chronos and their respective Fourier transforms of the right TW for the reduced Rayleigh number value $\epsilon = 43.10^{-5}$.

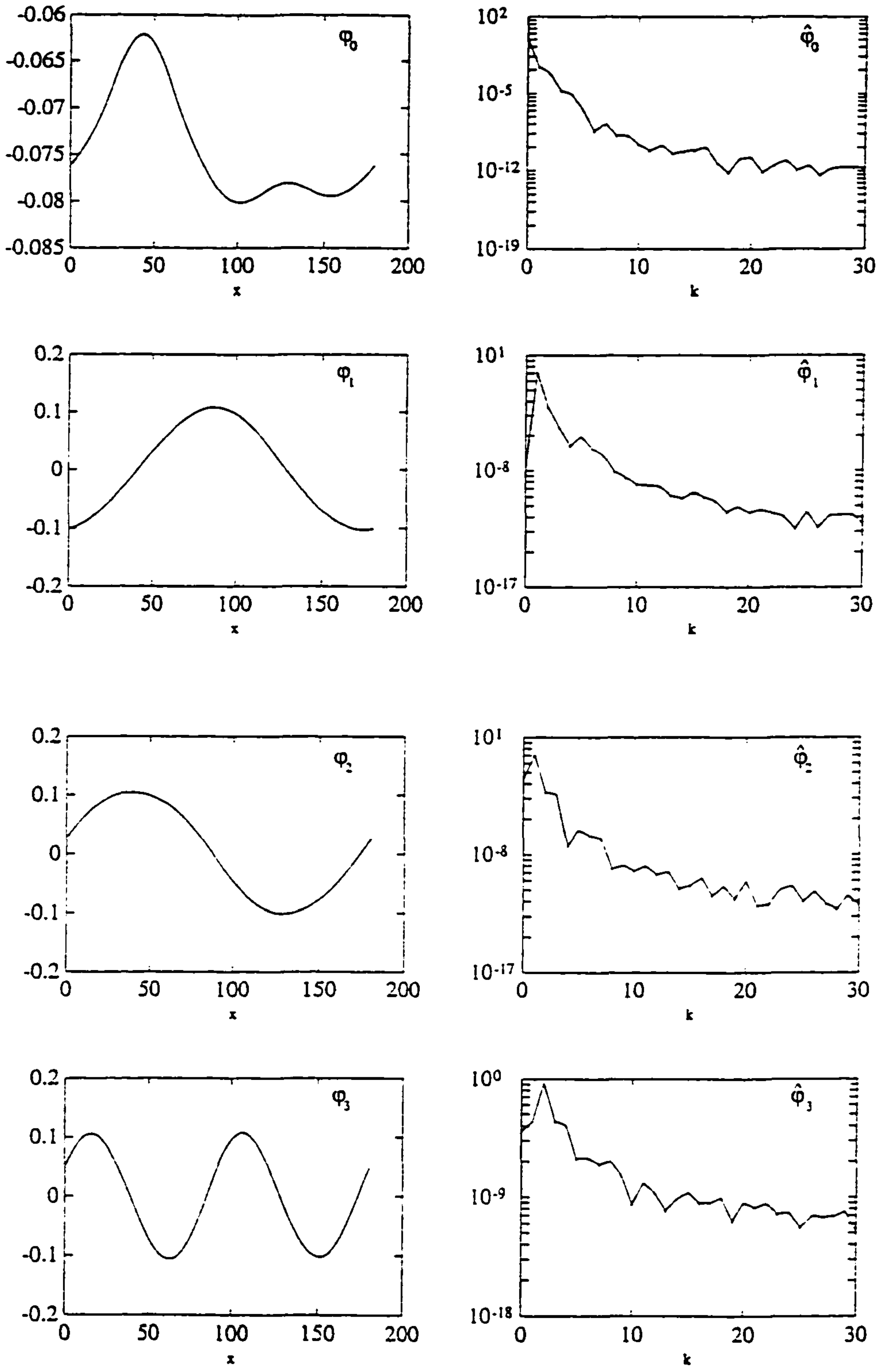

Figure 4.19: Topos and their respective Fourier transforms of the left TW for the reduced Rayleigh number value $\epsilon = 65.10^{-5}$.

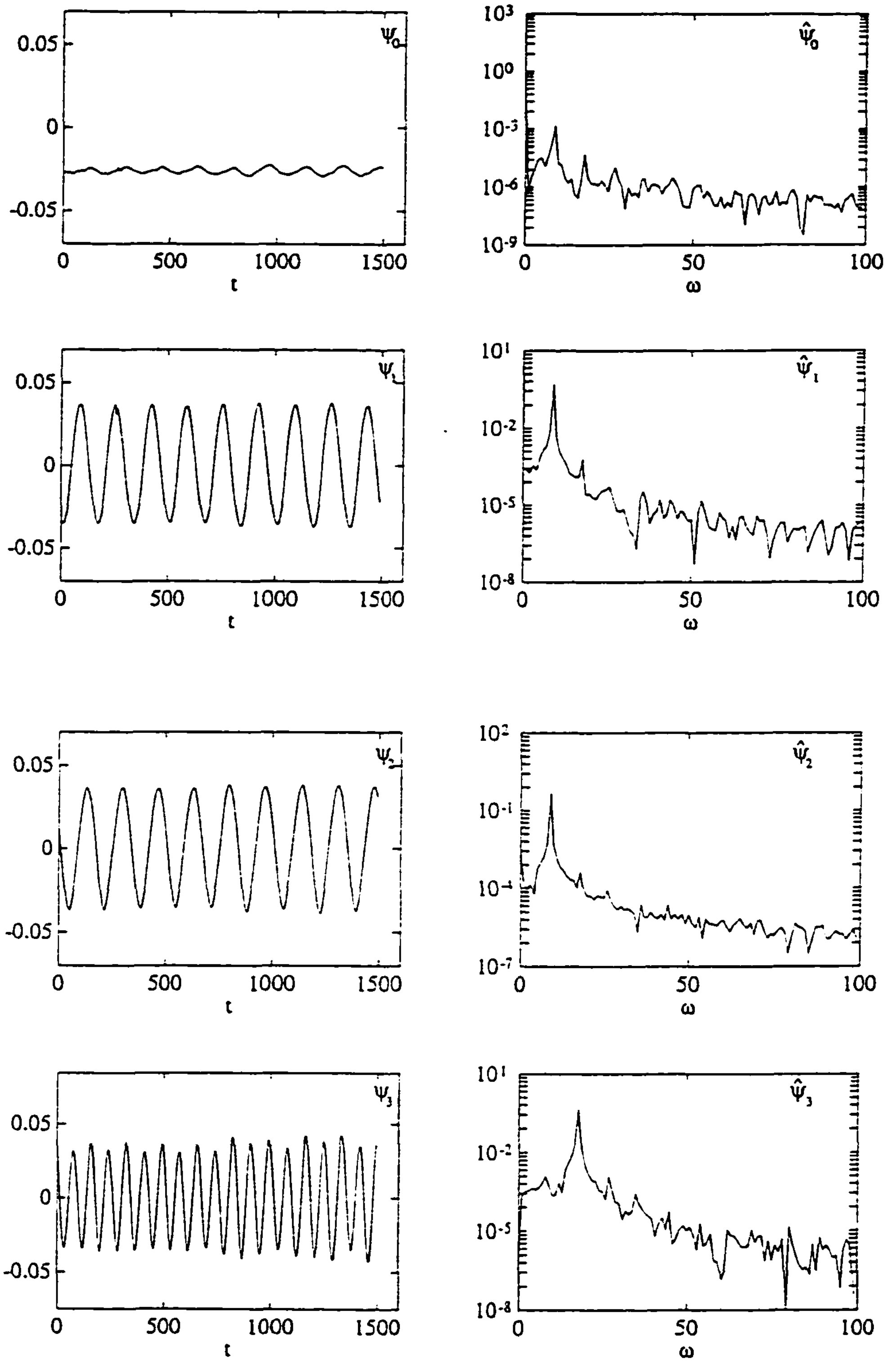

Figure 4.20: Chronos and their respective Fourier transforms of the left TW for the reduced Rayleigh number value $\epsilon = 65.10^{-5}$.

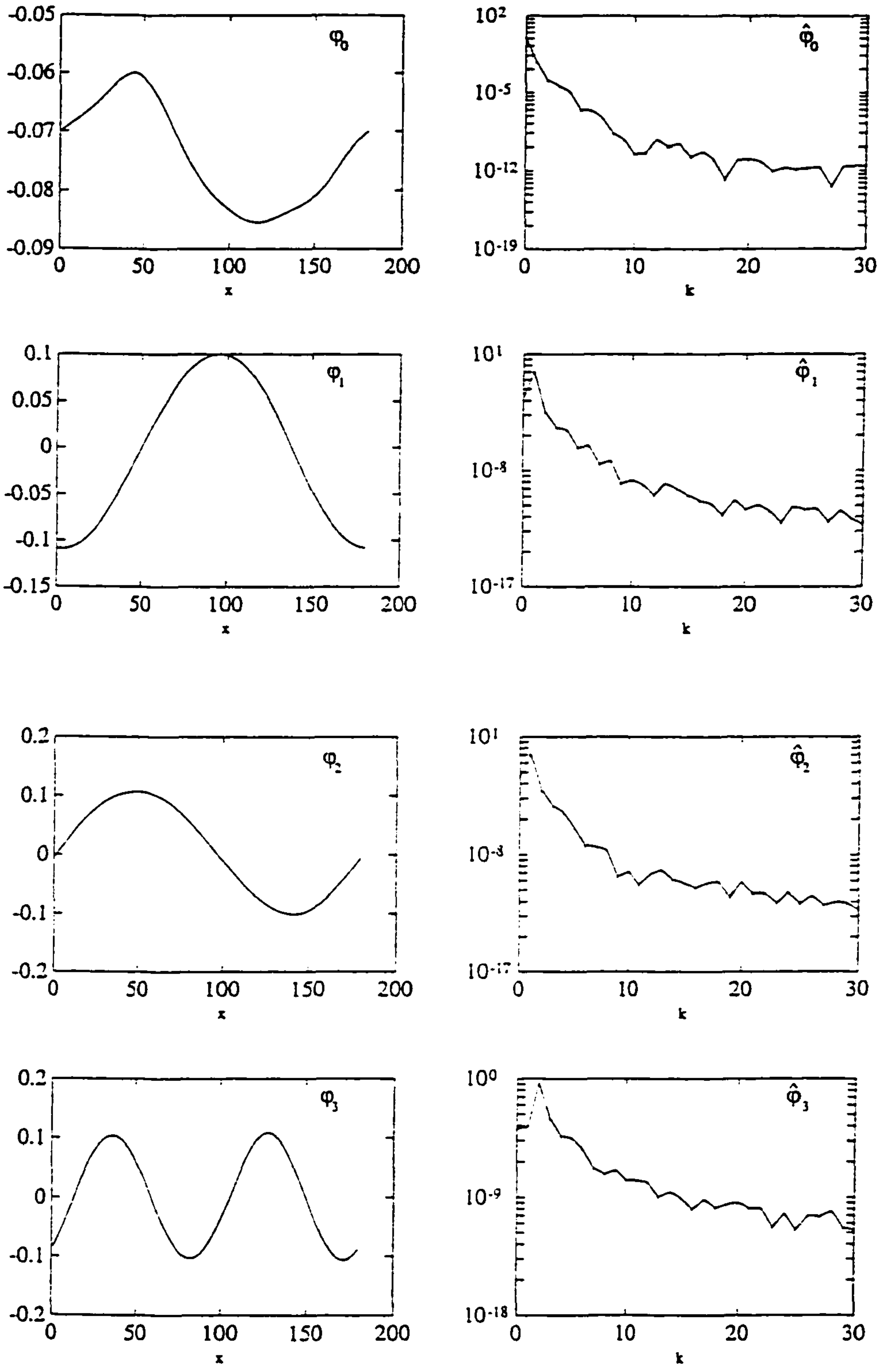

Figure 4.21: Topos and their respective Fourier transforms of the right TW for the reduced Rayleigh number value $\epsilon = 65.10^{-5}$.

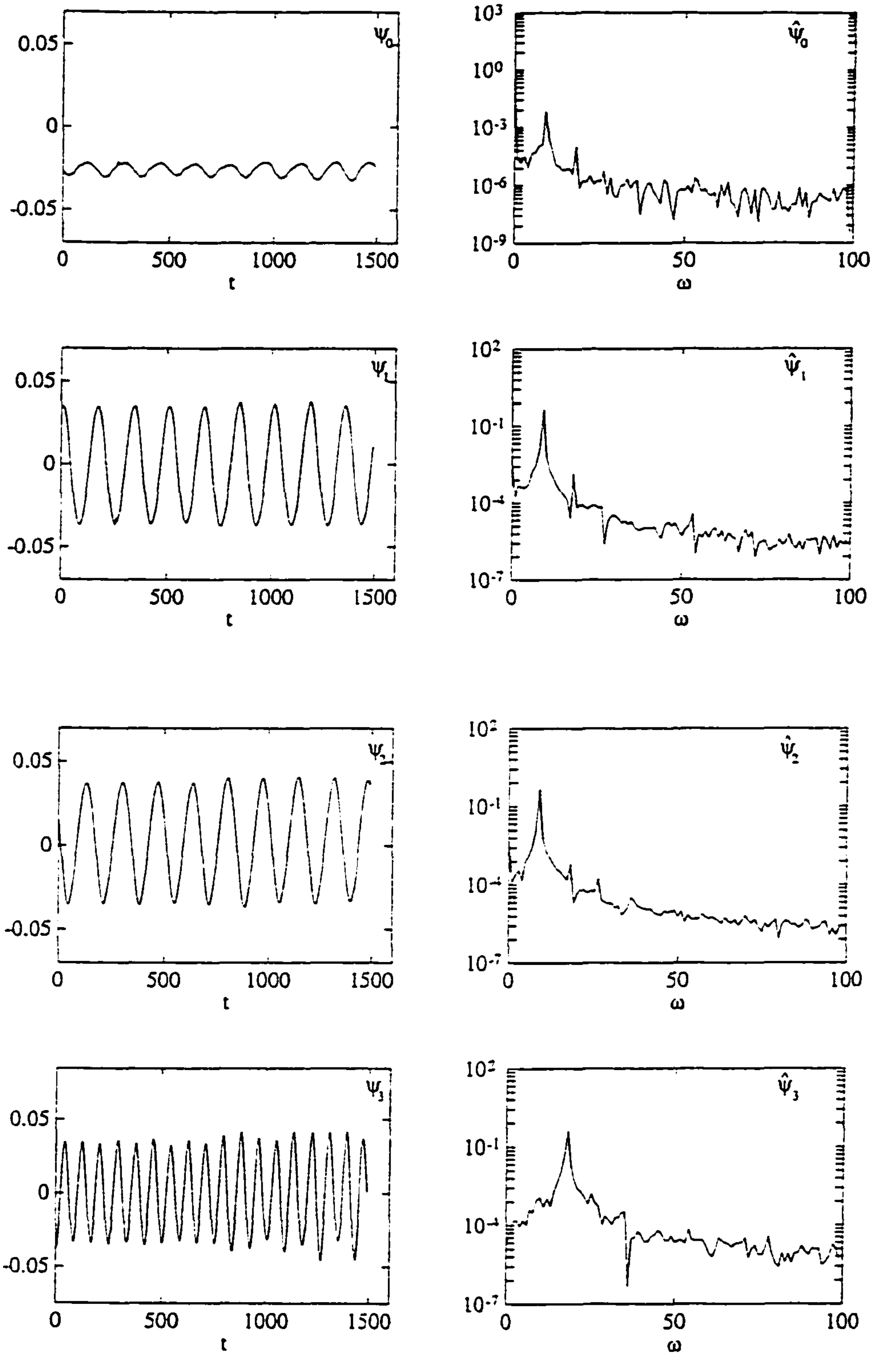

Figure 4.22: Chronos and their respective Fourier transforms of the right TW for the reduced Rayleigh number value $\epsilon = 65.10^{-5}$.

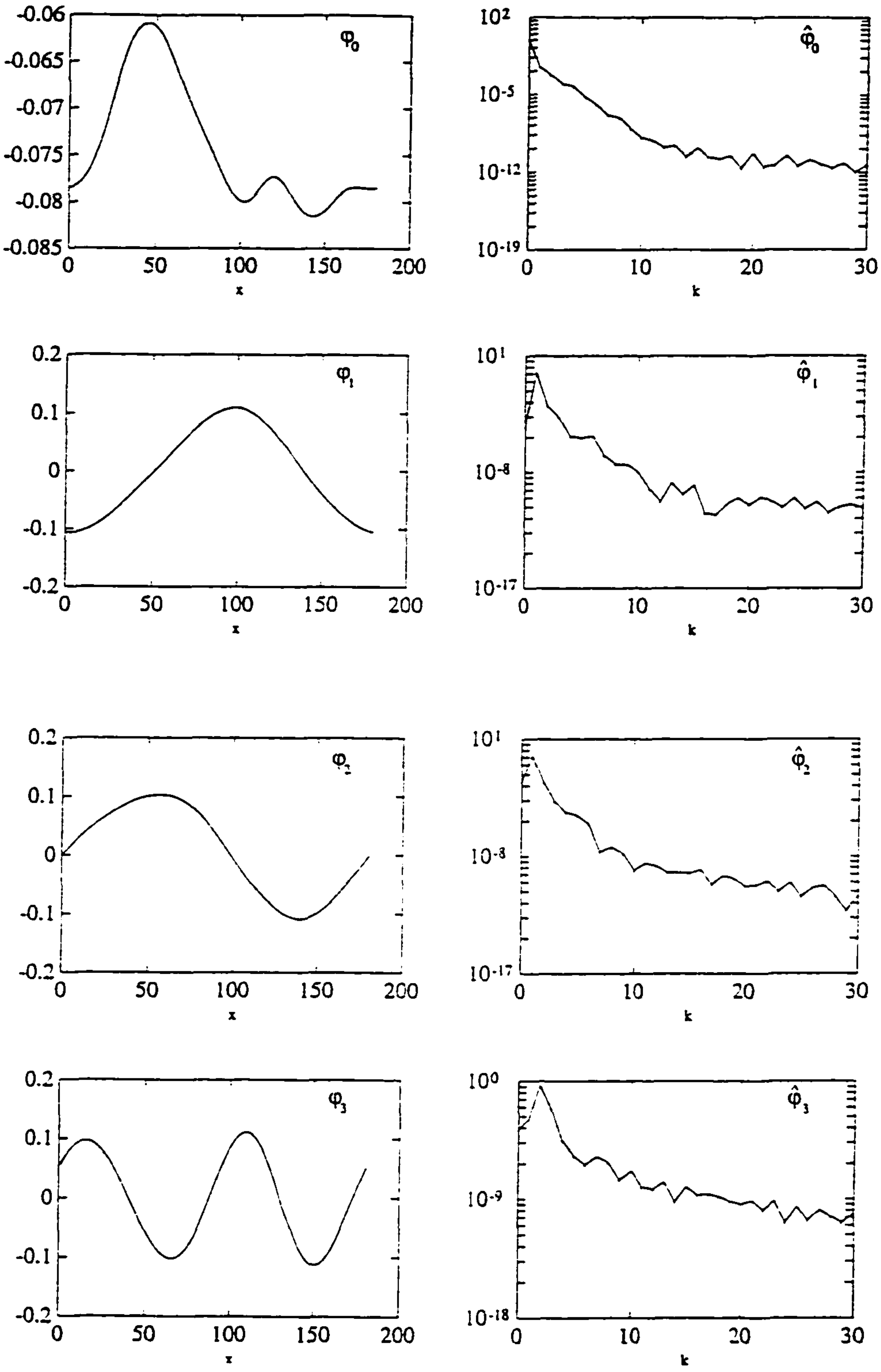

Figure 4.23: Topos and their respective Fourier transforms of the left TW for the reduced Rayleigh number value $\epsilon = 123.10^{-5}$.

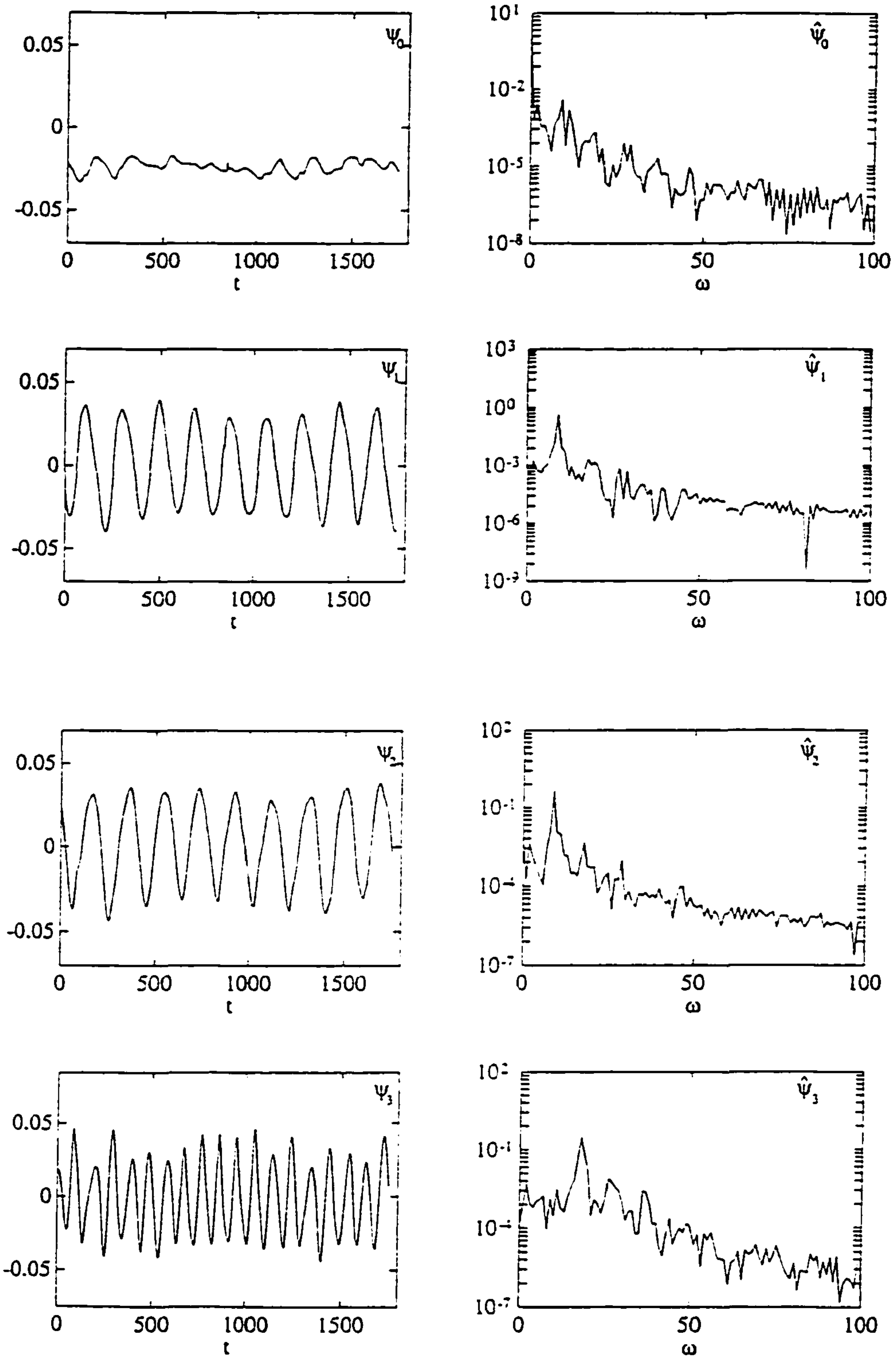

Figure 4.24: Chronos and their respective Fourier transforms of the left TW for the reduced Rayleigh number value $\epsilon = 123.10^{-5}$.

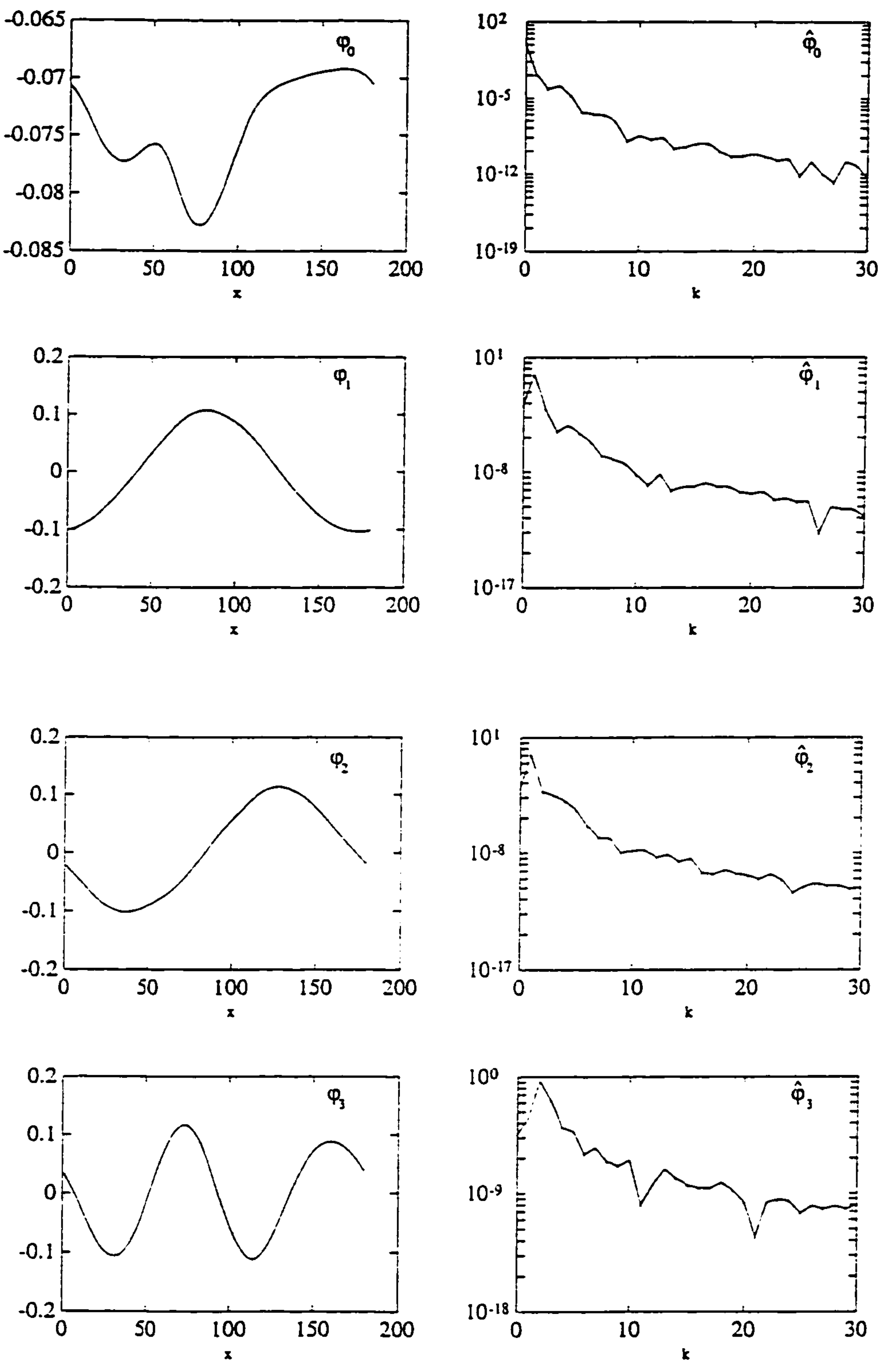

Figure 4.25: Topos and their respective Fourier transforms of the right TW for the reduced Rayleigh number value $\epsilon = 123.10^{-5}$.

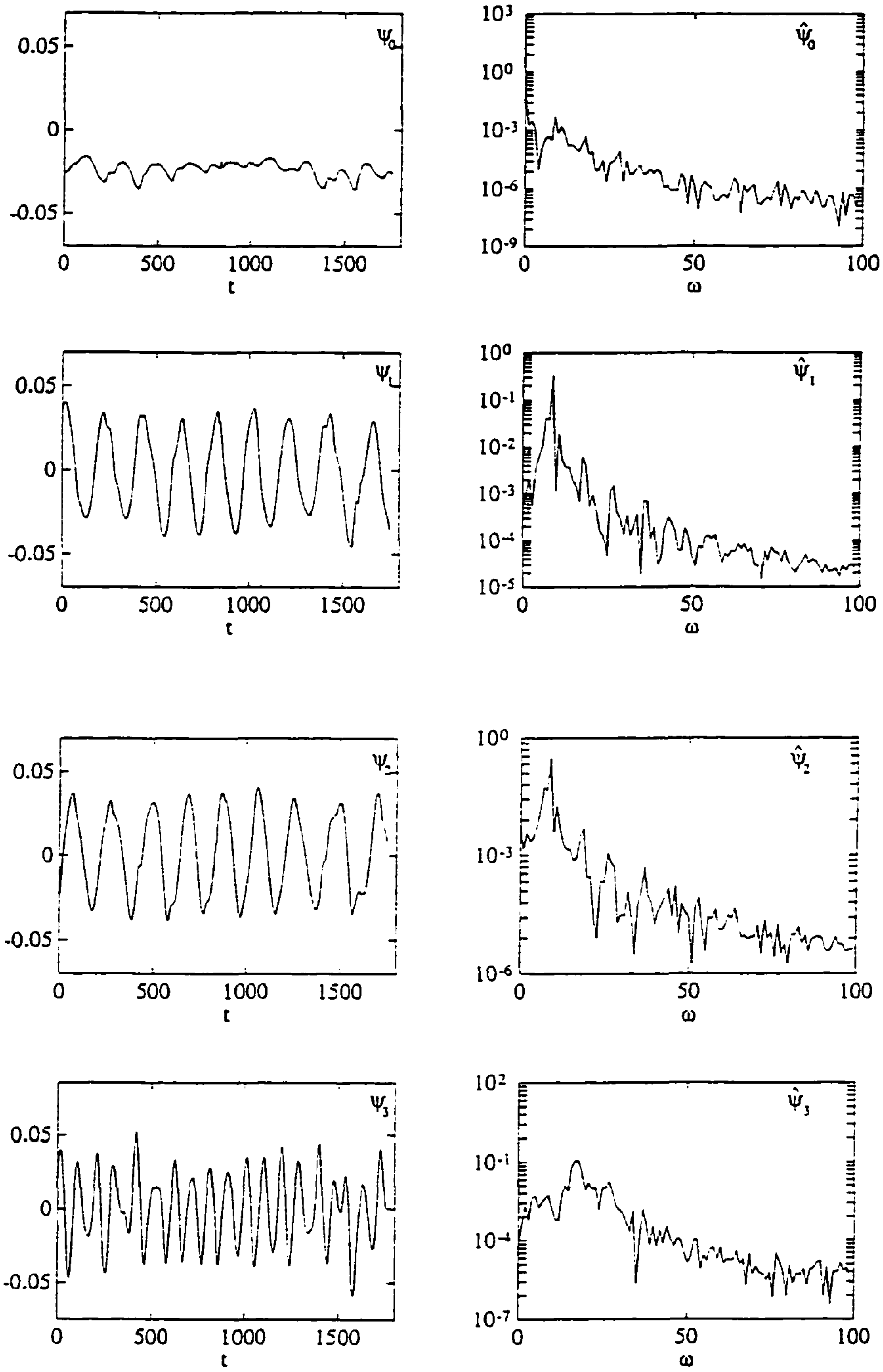

Figure 4.26: Chronos and their respective Fourier transforms of the right TW for the reduced Rayleigh number value $\epsilon = 123.10^{-5}$.

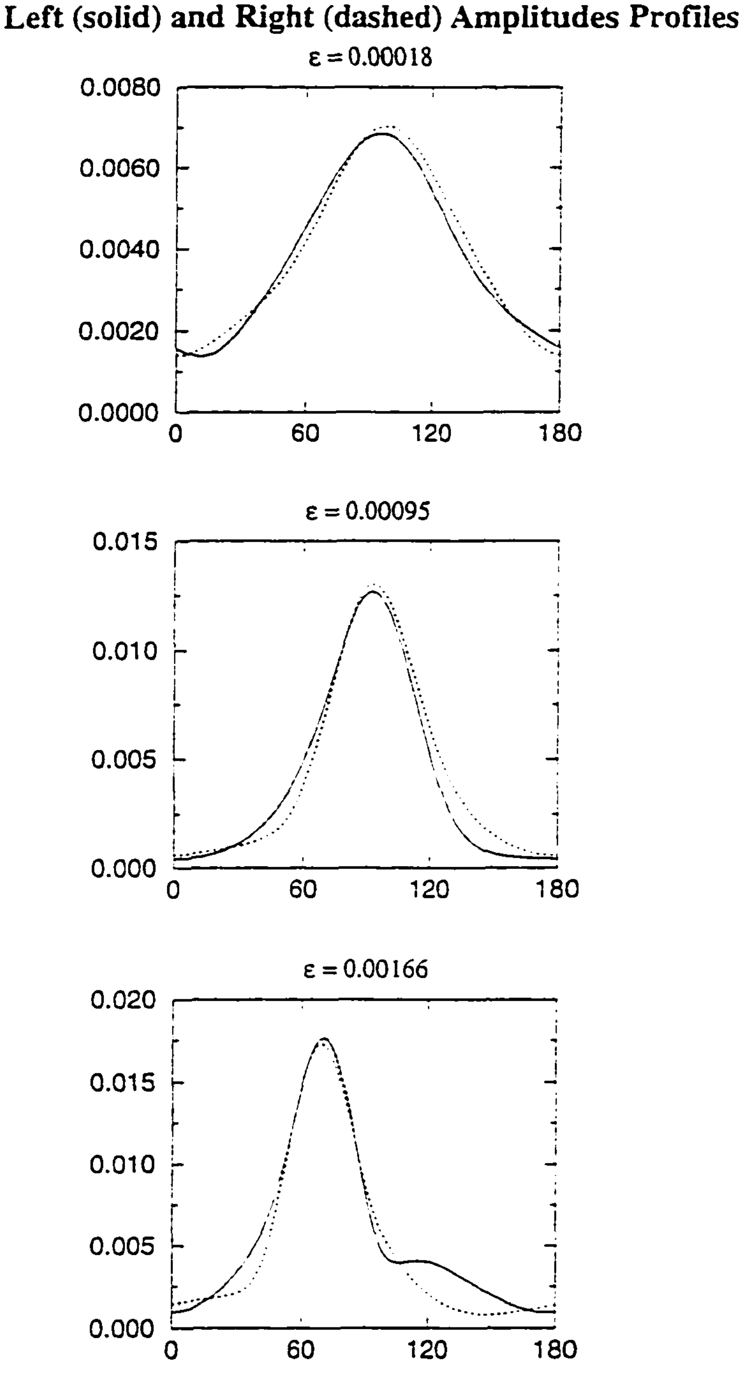

Figure 4.27: The extracted profiles of the primary TW, for $\epsilon = 0.00018$, $\epsilon = 0.00095$ and $\epsilon = 0.000166$. Left and right primary components are represented in solid and dotted line respectively.

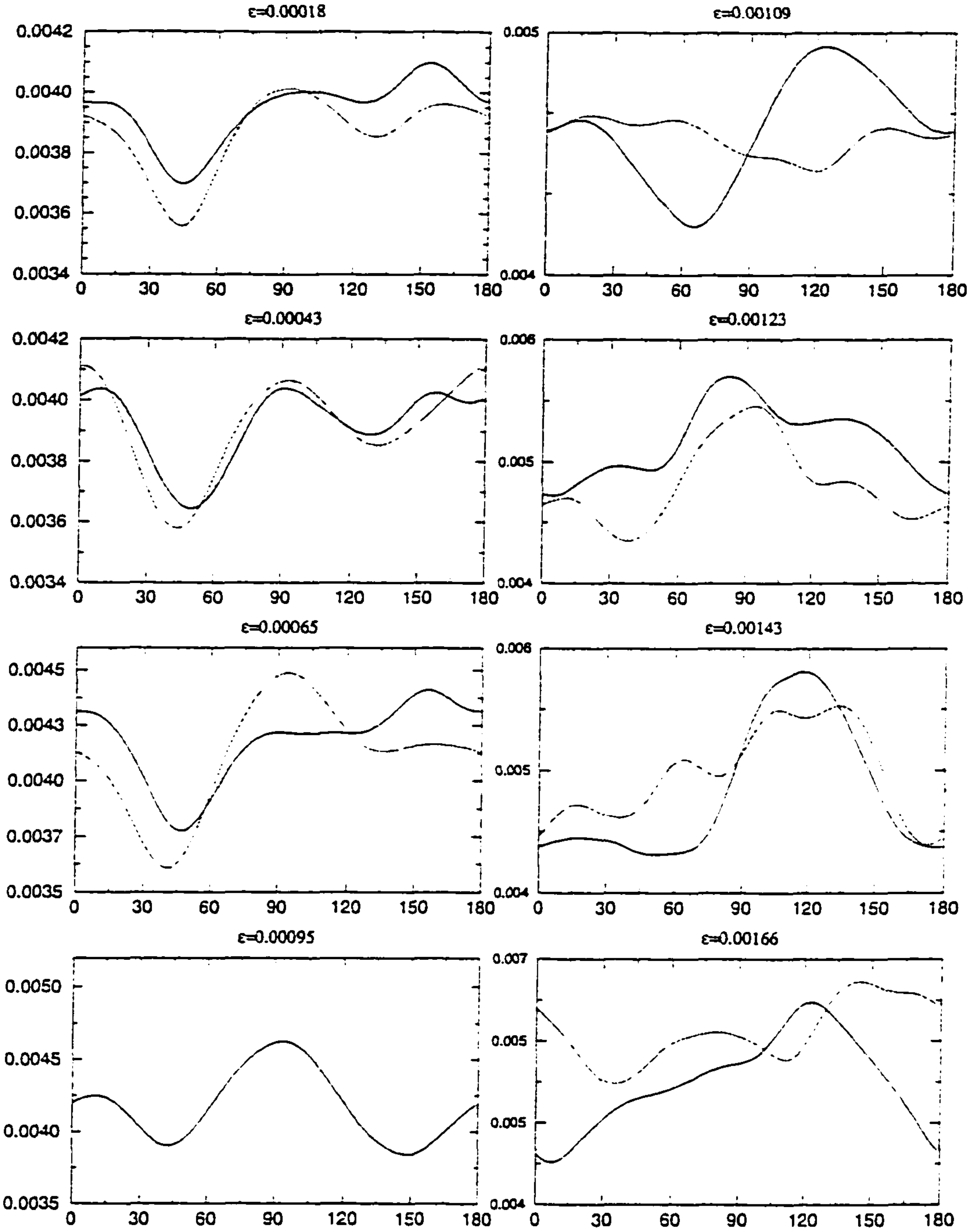

Figure 4.28: Spatial modulations extracted from the binary fluid experimental signals for all the reduced Rayleigh number values.

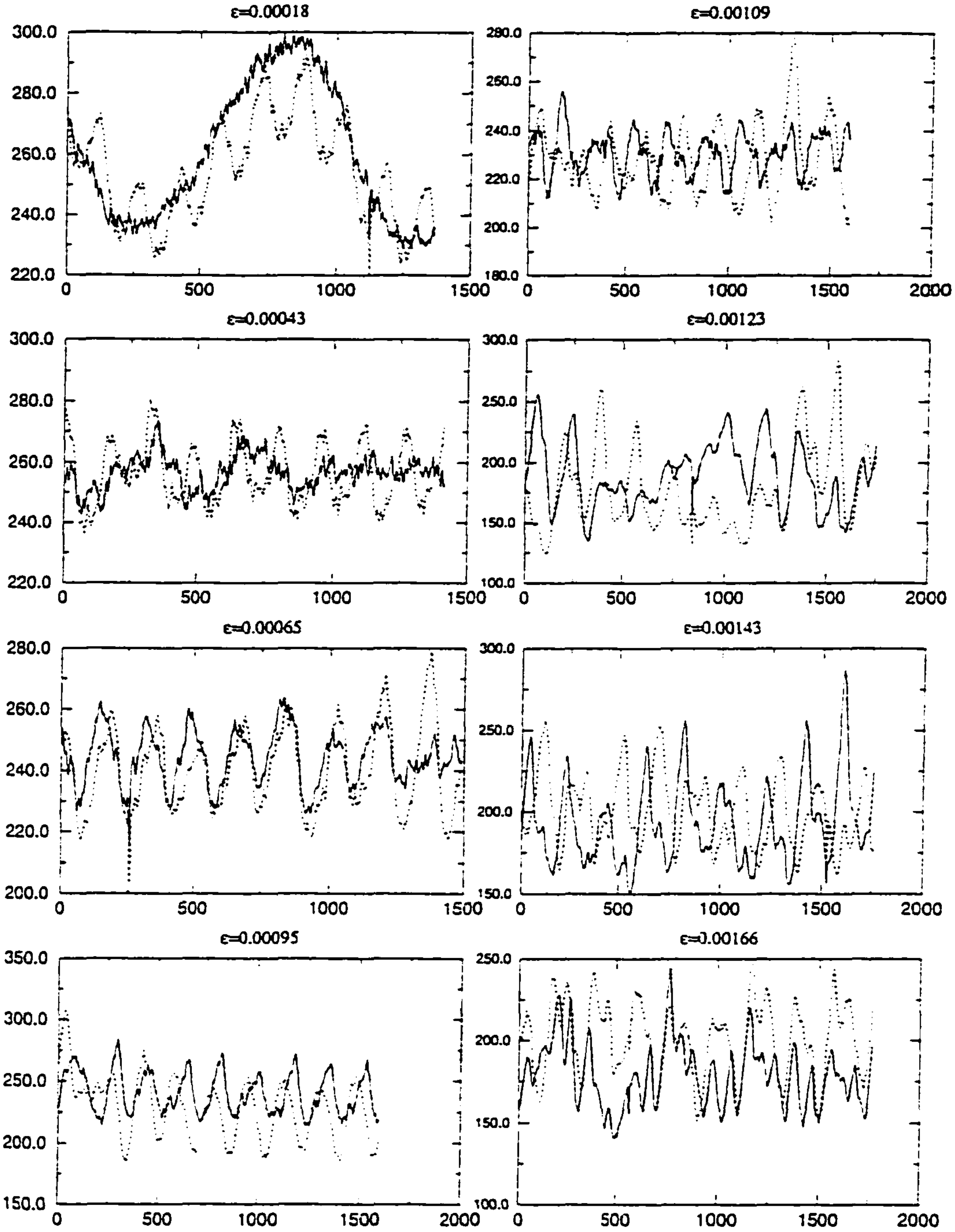

Figure 4.29: Temporal modulations extracted from the binary fluid experiments signals for all the reduced Rayleigh number values.

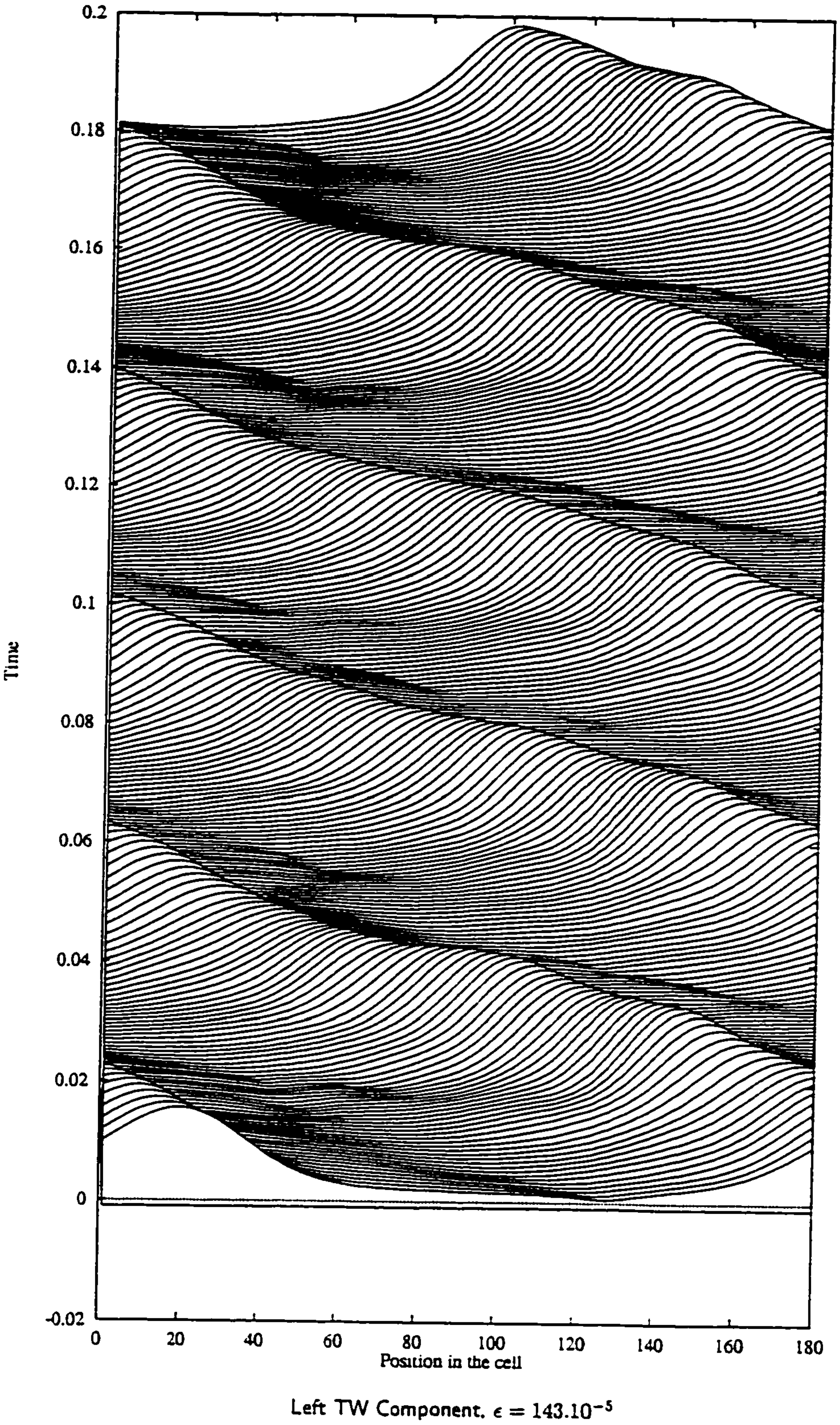

Figure 4.30: Left-going wave in the binary fluid experiments for the reduced Rayleigh number value $\epsilon = 143.10^{-5}$

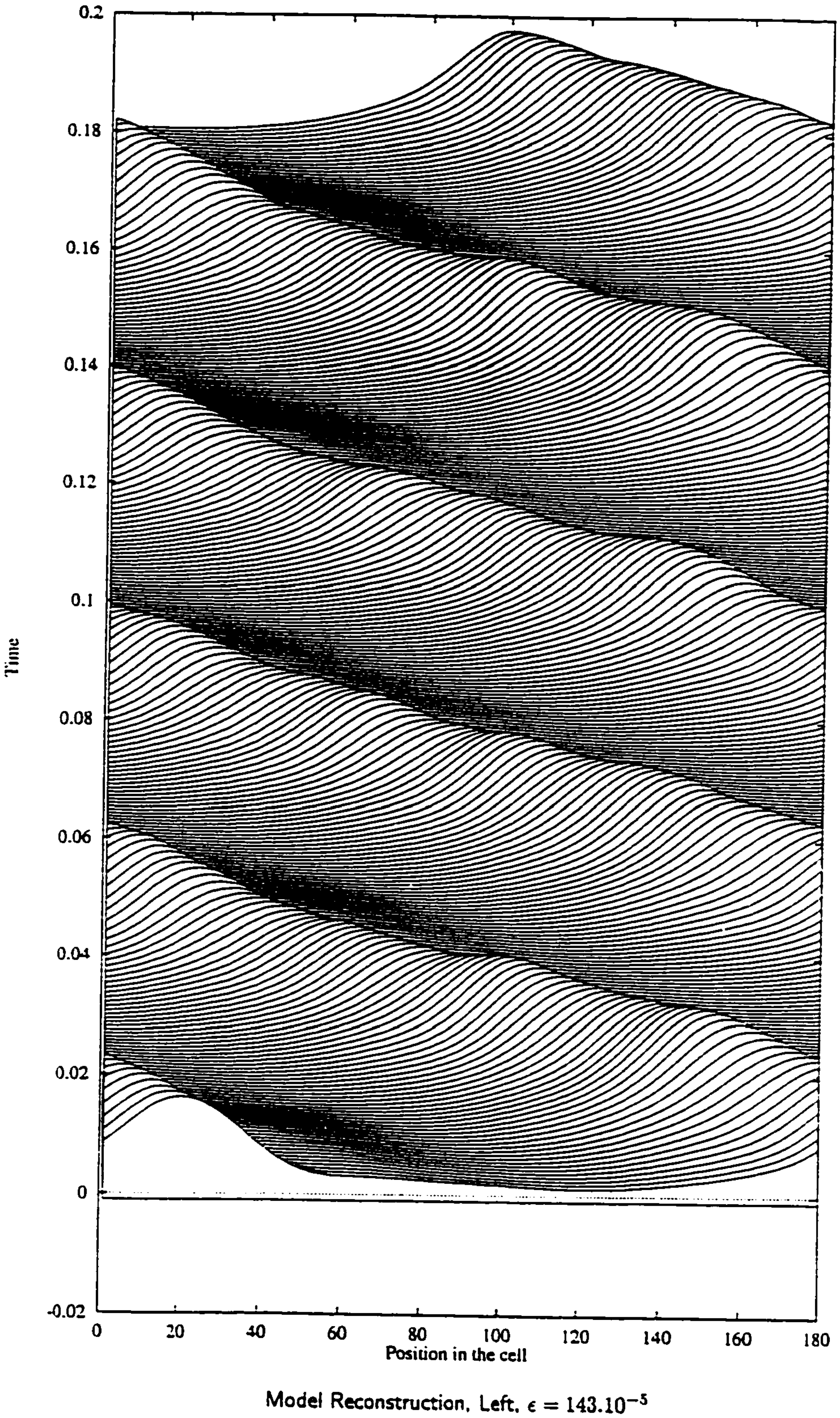

Figure 4.31: The reconstructed left-going wave for $\epsilon = 143.10^{-5}$ though the representational model.

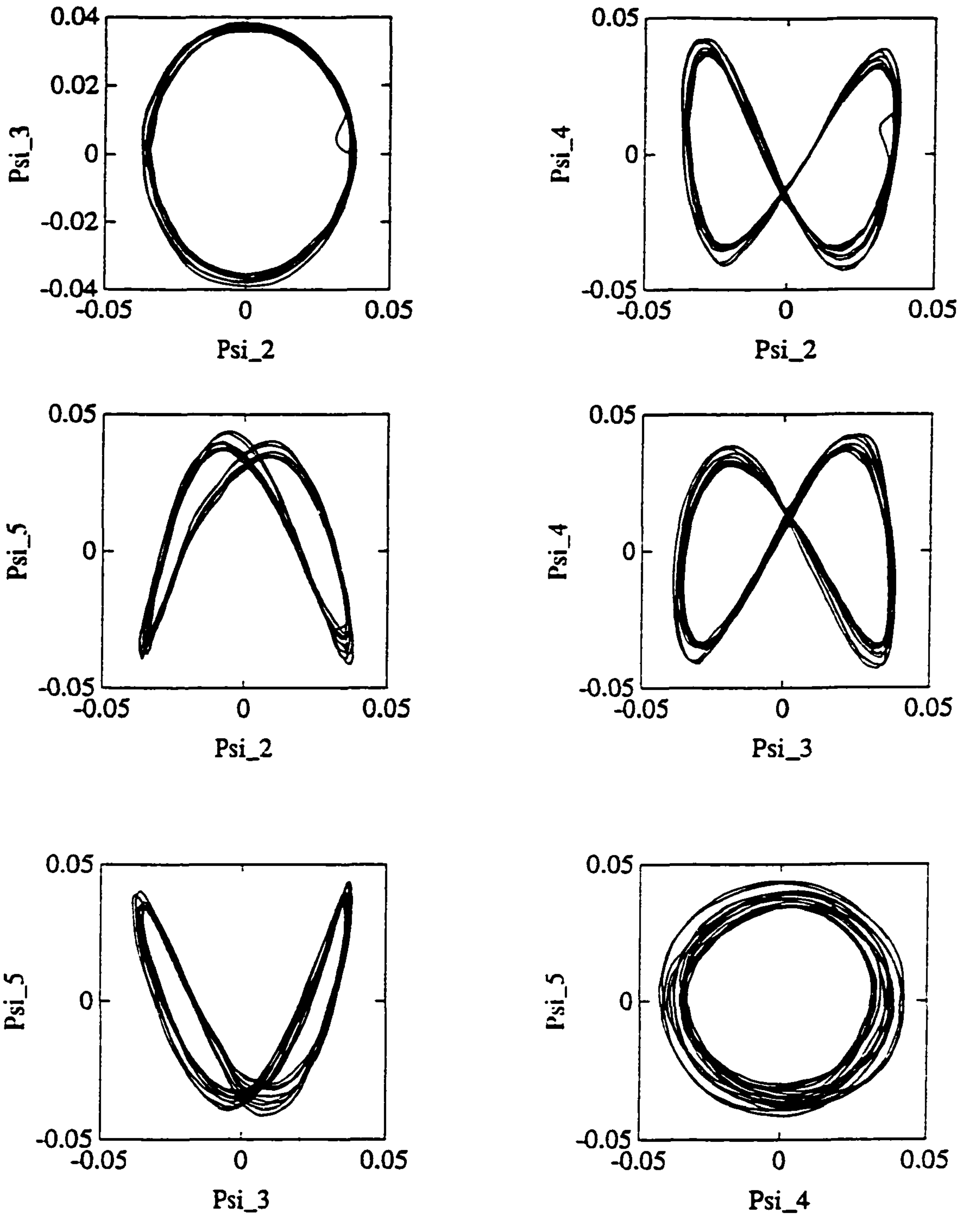

Figure 4.32: Projection of the dynamics onto the planes $(\vec{\varphi}_i, \vec{\varphi}_j)$, for $i, j = 2, .., 5$, for $\epsilon = 65.10^{-5}$, from the experimental data.

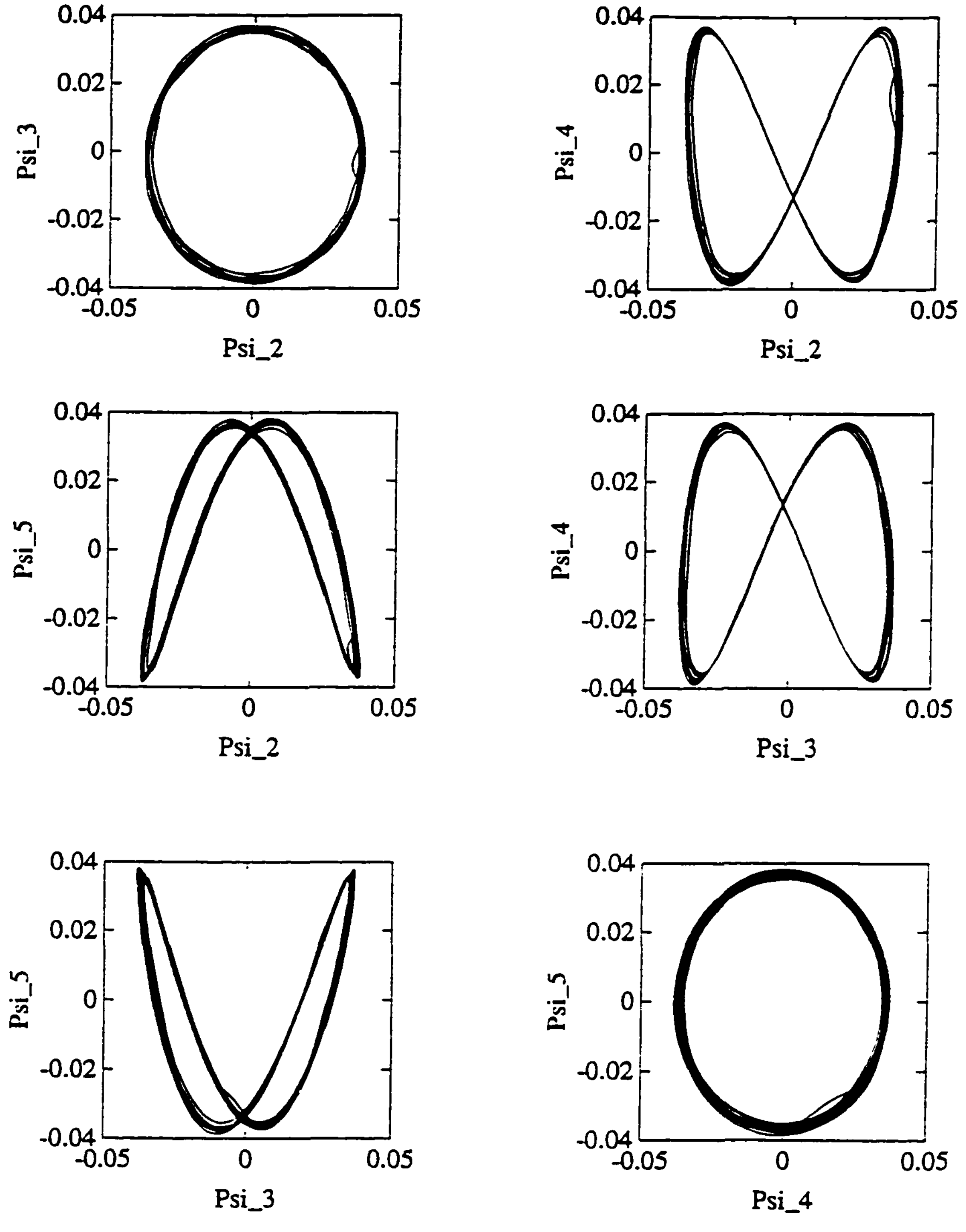

Figure 4.33: Projection of the dynamics onto the planes $(\vec{\varphi}_i, \vec{\varphi}_j)$, for $i, j = 2, .., 5$, for $\epsilon = 65.10^{-5}$, from the model,

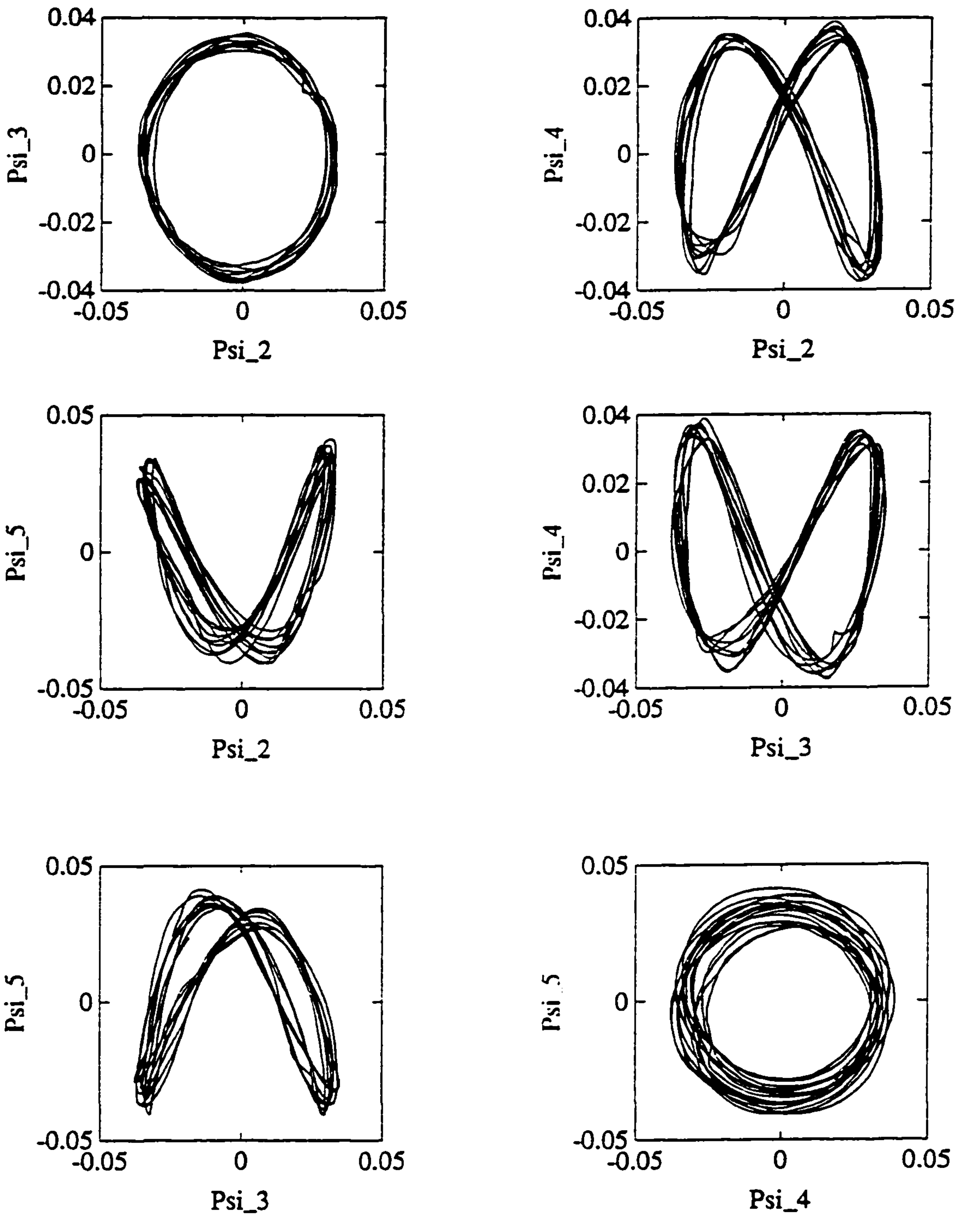

Figure 4.34: Projection of the dynamics onto the planes $(\vec{\varphi}_i, \vec{\varphi}_j)$, for $i, j = 2, .., 5$, for $\epsilon = 143.10^{-5}$, from the experimenal data.

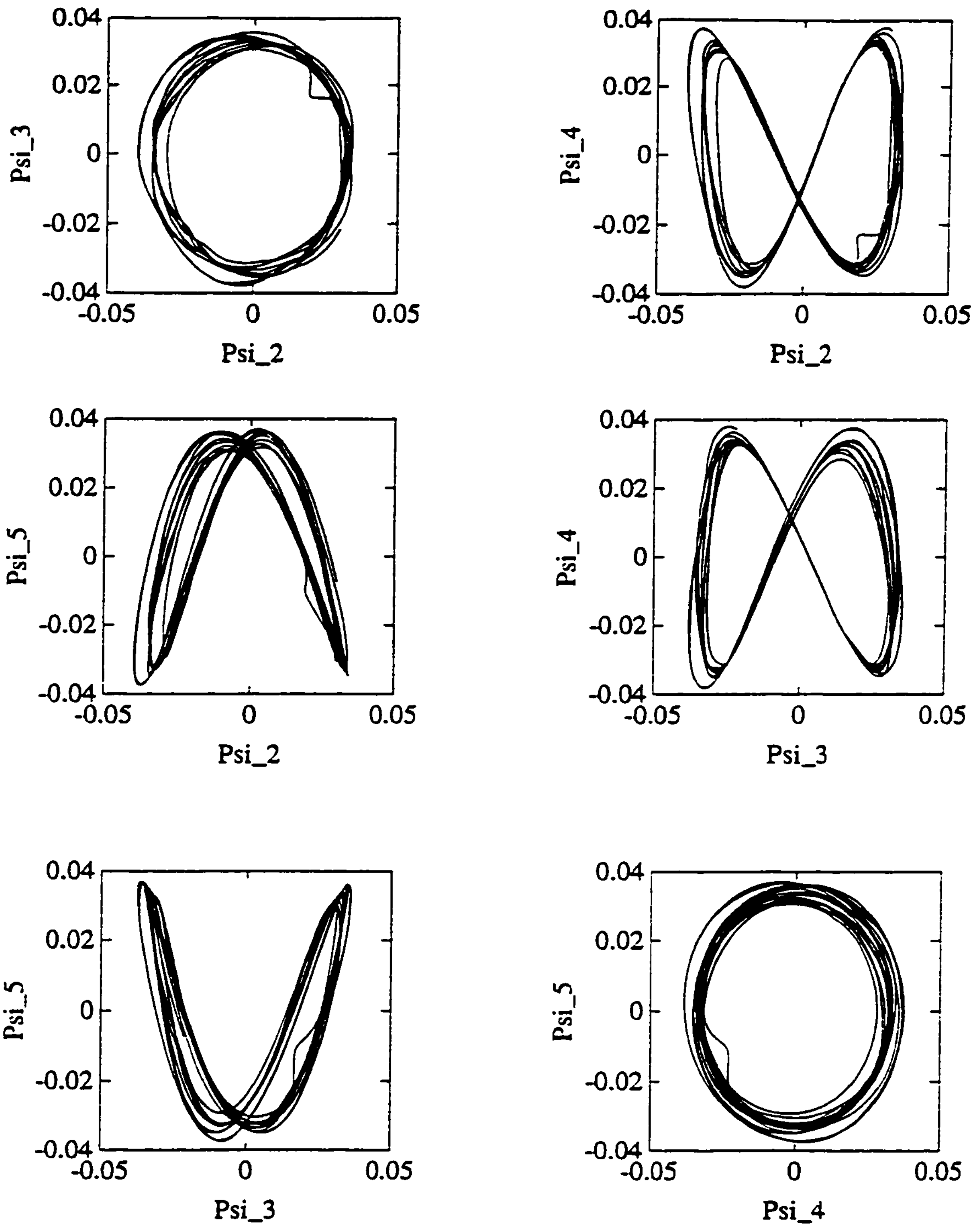

Figure 4.35: Projection of the dynamics onto the planes $(\vec{\varphi}_i, \vec{\varphi}_j)$, for $i, j = 2, .., 5$, for $\epsilon = 143.10^{-5}$, from the model.

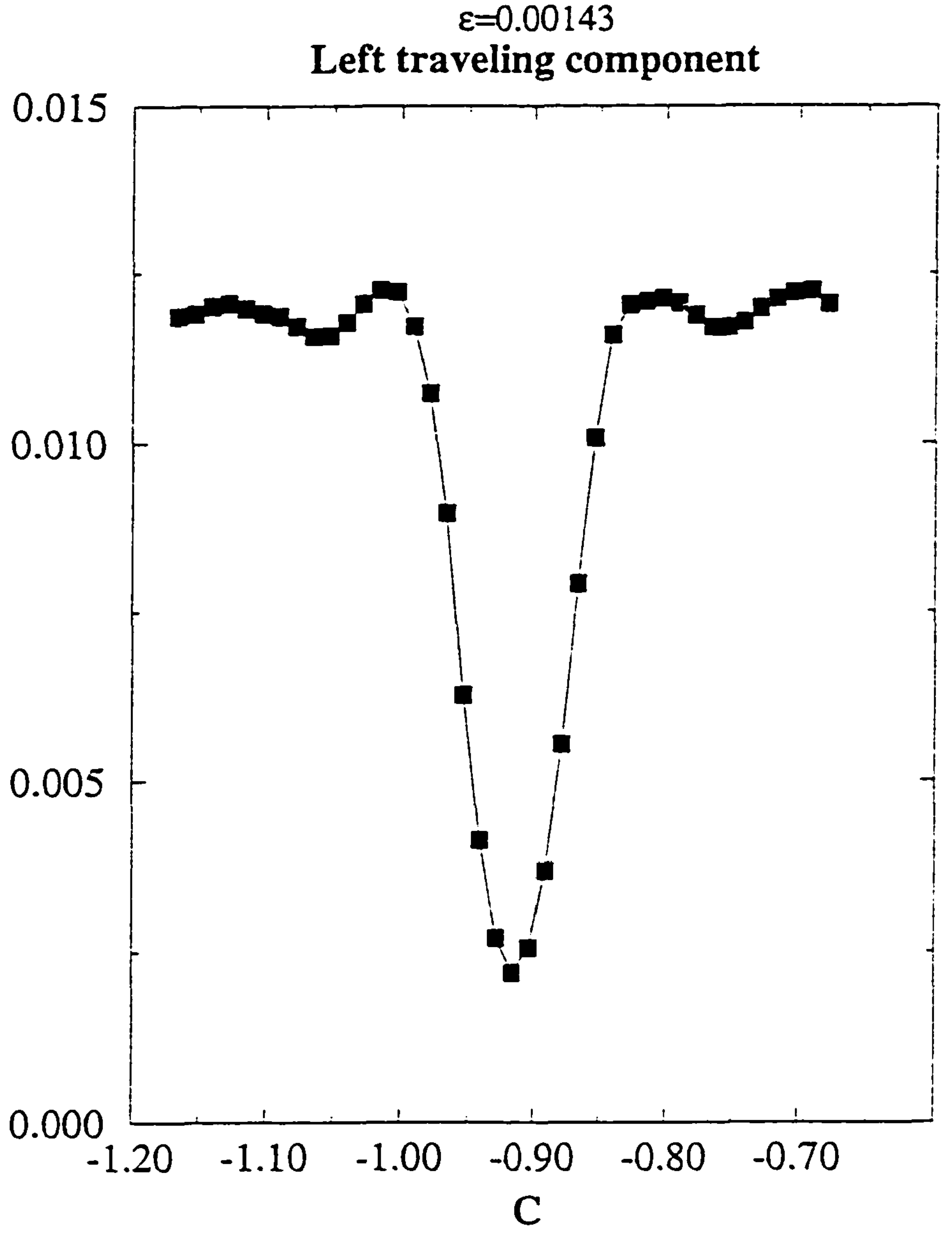

Figure 4.36: The rms difference, δ, between the experimental signal and reconstructed signal obtained through the model, plotted versus the averaged group velocity used in the algorithm.

Conclusion

The work we have undertaken consisted of developing the necessary tools first, for quantitatively characterizing the increasing complexity in spatiotemporal systems, and second, for recognizing the mechanisms of transitions in those systems. Our achievements have gone beyond these and were extended to generate simple representations for the occurrence of these complex behaviors and mimic the spatio-temporal dynamics exhibited.

We have used the Bi-orthogonal Decomposition (BOD), which has the ability to account for the deterministic behavior of complex spatio-temporal phenomena. The BOD provides several quantifiers of the space-time complexity. These can be reflected in the energy and the entropy which are computed from the BOD spectra. However, the entropy seems to be more sensitive to transitions from one regime to another. Other quantifiers include dimension, energy as well as entropy related functions. For a geometric picture of the deterministic dynamics, the bi-orthogonal modes, termed topos and chronos, span spatial and temporal characteristic spaces where adequate studies can be performed. To provide the link from the formalism of the BOD and numerical work to experiments, we have studied the effects of varying space-time windows on the BOD components. Of particular importance is the entropy for which we have shown that, by considering sufficiently large time domains, we allow the entropy to saturate, thus reaching an asymptotic value. The latter represents a fairly accurate value of the space-time complexity for the given dynamics. Although these findings are applicable to any space-time dynamics, we have emphasized in our discussions the case of nonlinear wave phenomena. These were the subject of the third chapter. We were interested in studying the propagation of waves from the BOD viewpoint. We have been able to determine quantitative characteristics of traveling waves (TW), such as the different uniform TW waves composing the wave field, their speeds, and shapes. Also, we have found that the interaction between the different waves manifests itself in space-time resonances. These resonances appear as invariant subspaces under the biorthogonal operator.

We have applied the BOD formalism to study the spatio-temporal complexity in the binary fluid convection. The entropy enabled us to quantify the space-time complexity and accurately detect the transitions seen in these experiments. The use of the spatial and temporal energies and entropies, which are useful in studying the properties of the dynamics, reveal features which can be related to the properties of TW bursts, such as their growth for instance. Although the BOD reduces the representation of the data to the smallest spaces possible, a difficulty presented by most of our data is one of high dimensionality, particularly in the dispersive chaos regime, where the dimension can reach 50. This regime has resisted our efforts in extracting, quantitatively, the spatio-temporal shape of the burst. In contrast, we have been much successful in the counterpropagating regime, the dimension of which is of the order 10, studied in detail in the last chapter. Also, the use of conventional statistical methods provided valuable information, especially from the correlation functions.

In the last chapter we have studied the development of structures and dynamics of the first regime observed above onset, namely the counterpropagating regime as the reduced Rayleigh number, ϵ, is increased. Two localized wave packets are observed to travel in opposite directions for an extended period of time. As ϵ is increased, some irregular behavior appears. By perfoming a systematic study of the spatial and temporal BOD modes of many data sets for different reduced Rayleigh number values, we attributed the appearence of these irregularities to the occurrence of spatial and temporal modulations. Then, these modulations, together with the primary traveling wave profile, were extracted. The variation of the amplitudes of these modulations is seen to increase with ϵ. A representational model based upon a primary traveling wave perturbed through spatial and temporal modulations yields satisfactory description of the dynamics. A reconstruction of the space-time dynamics based upon the modulations and the traveling wave profiles seems to reproduce major features present in the original signal. Despite the high quality of the data we have analyzed, we were worried that these modulations might have been just the reflection of some experimental artifacts such as static nonuniformities in the cell for instance. Luckily, after several checks we concluded that such artifacts are unimportant, and that these modulations are an inherent part of the dynamics.

Bibliography

[1] V. I. Arnold. Geometrical methods in the theory of ordinary differential equations, Springer Verlag (1987), Second Edition.

[2] N. Aubry, F. Carbone, R. Lima and S. Slimani. Wave propagation phenomena from a spatio-temporal viewpoint: resonances and bifurcations, J. Stat. Phys. 76, 1005 (1994).

[3] N. Aubry, M. P. Chauve and R. Guyonnet. Transition to turbulence on a rotating flat disk. Phys. Fluids 6(8), 1994.

[4] N. Aubry, R. Guyonnet and R. Lima. Spatio-temporal analysis of complex signals: theory and applications, J. Stat. Phys. 64: 683-739 (1991).

[5] N. Aubry, R. Guyonnet and R. Lima. Spatio-temporal symmetries and bifurcations via biorthogonal decompositions. J. Nonlinear Sci. 2: 183-215 (1992).

[6] N. Aubry, R. Guyonnet and R. Lima. Turbulence spectra, J. Stat. Phys. 67: 183-215 (1992).

[7] N. Aubry, P. Holmes, J. L. Lumley and E. Stone. The Dynamics of Coherent Structures in the Wall Region of a Turbulent Boundary Layer, J. Fluid Mech. 192: 115-173 (1988).

[8] N. Aubry and W. Lian. Exploiting symmetries in Applied and Numerical Analysis, Lectures in Applied Mathematics, eds. E. Allgower, K. Georg and R. Miranda (1993).

[9] N. Aubry and W. Lian. Self-similarity of compressible turbulence, FED-Vol. 183 (1992).

[10] N. Aubry, W. Lian and E. S. Titi. Preserving symmetries in the proper orthogonal decomposition, SIAM Journal on Statistical and Scientific Computing 14, No. 2: 483-505 (1993).

[11] W. Barten, M. Lucke, and M. Kamps. Phys. Rev. Lett. 66, 2621 (1991); M. Lucke, W. Barten, and M. Kamps, Physica D61, 183 (1992).

[12] G. Berkooz, P. Holmes and J. L. Lumley. The proper orthogonal decomposition in the analysis of turbulent flows, Annu. Rev. Fluid Mech. 25: 539-575 (1993).

[13] K. S. Breuer and L. Sirovich. The use of the Karhunen-Loève procedure for the calculation of linear eigenfunctions, J. Comp. Phys. Vol 96, No 2 277-296, (Oct 1991).

[14] C. S. Bretherton and E. A. Spiegel. Phys. Lett. 96A, 152 (1983).

[15] D. S. Broomhead and G. P. King. Physica D20, 217 (1986).

[16] Nian-Zheng Cao. 1993, Analysis and reduced simulations of laminar/turbulent wake flows, Ph.D. Thesis, The City University of New York.

[17] P. Collet and J. P. Eckmann. Instabilities and Fronts in Extended Systems. Princeton Series in Physics; Princeton University Press, Princeton, New Jersey (1990).

[18] S. Ciliberto and M. Caponeri. Phys. Rev. Lett. 64, 2775 (1990).

[19] M. P. Chauve and P. Legal. Physica D (1991).

[20] P. Coullet and J. Lega. Defect-mediated turbulence in wave patterns, Europhys. Lett. 7: 511-516 (1988).

[21] M. C. Cross. Phys. Rev. A 38, 3593 (1988); Physica D37, 315 (1989).

[22] A. Deane, G. E. Karniadakis, I. G. Kevrekidis and S. A. Orszag. Low dimensional models for complex geometry flows: Application to grooved channels and circular cylinders, Phys. Fluids A. 3: 2337 (1991).

[23] J. A. Glazier and P. Kolodner. Phys. Rev. A 43, 4269 (1991).

[24] J. Guckenheimer and P. Holmes. Nonlinear oscillations, Dynamical Systems and Bifurcations of Vector Fields, Springer-Verlag (1986).

[25] T. Kato. Perturbation theory for linear operators, Springer-Verlag (1976), 2nd edition.

[26] M. Kirby and D. Armbruster. Reconstructing phase space from PDE simulations, Z. Angew Math Phys. 43: 999-1022 (1992).

[27] P. Kolodner, D. Bensimon, and C. M. Surko. Phys. Rev. Lett. 60, 1723 (1988); D. Bensimon, P. Kolodner, C. M. Surko, H. Williams, and V. Croquette, J. Fluid Mech. 217, 441 (1990).

[28] P. Kolodner. Drifting pulses of traveling-wave convection, Phys. Rev. Lett. 66, 9 (1991).

[29] P. Kolodner. Phys. Rev. A. 44, 6448 (1991).

[30] P. Kolodner. Phys. Rev. Lett. 69, 2519 (1992).

[31] P. Kolodner. Phys. Rev. A 46, 6431 (1992).

[32] P. Kolodner. Phys. Rev. E 47, 1038 (1993).

[33] P. Kolodner and J. A. Glazier. Phys. Rev. A 42, 7504 (1990).

[34] P. Kolodner and C. M. Surko. Phys. Rev. Lett. 61, 842 (1988); J. Fineberg, E. Moses, and V. Steinberg, Phys. Rev. Lett. 61, 838 (1988); P. Kolodner, C. M. Surko, and H. Williams, Physica D37, 319 (1989); V. Steinberg, J. Fineberg, E. Moses, and I. Rehberg, Physica D37, 359 (1989).

[35] P. Kolodner, A. Passner, C. M. Surko and R. W. Walden. Phys. Rev. Lett. 56, 2621 (1986).

[36] P. Kolodner, C. M. Surko and H. Williams. Dynamics of traveling waves near the onset of convection in binary fluid mixtures, Physica D 37: 319-333 (1989).

[37] P. Kolodner, J. A. Glazier, and H. L. Williams. Phys. Rev. Lett. 65, 1579 (1990); J. A. Glazier, P. Kolodner, and H. Williams, J. Stat. Phys. 64, 945 (1991).

[38] P. Kolodner, and H. Williams. Complex Demodulation Techniques for Experiments on Traveling-wave Convection, in Proceedings of the NATO Advanced Research Workshop on Nonlinear Evolution of Spatio-temporal Structures in Dissipative Continuous Systems, F. H. Busse and L. Kramer, eds., NATO Advanced Study Institute, Series B2, Vol. 225 (Plenum, New York), p. 73. (1990).

[39] P. Kolodner, H. Williams, and C. Moe. J. Chem. Phys. 88, 6512 (1988).

[40] W. Lian and N. Aubry. FED-Vol. 151 (ASME), 129 (1993).

[41] R. Lima. Describing the dynamics with a bi-orthogonal decomposition, Chaos **2** (3), 1992.

[42] M. Loève. Probability Theory, Van Nostrand, New York (1955).

[43] J. L. Lumley. The structure of inhomogeneous turbulent flows, in: Atmospheric turbulence and radio wave propagation, eds. A.M. Yaglom and V.I. Tatarski:, Moscow: Nauka: 166-178 (1967).

[44] J. L. Lumley. Stochastic Tools in Turbulence, Academic (1970).

[45] W. I. Neuman, D. K. Campbell and J. M. Hyman. Identifying coherent structures in nonlinear wave propagation, Chaos 1: 77-94 (1991).

[46] A. C. Newell. in Nonlinear Wave Motion, Lectures in Applied Mathematics, Vol. 15, A. C. Newell, ed. (AMS, Providence, 1974), p. 157.

[47] H. Riecke. Phys. Rev. Lett. 68, 301 (1992); Physica D61, 253 (1992).

[48] M. Reed and B. Simon. Methods of Modern Mathematical Physics I: Functional Analysis, Academic Press (1980).

[49] S. Slimani, N. Aubry, R. Lima, and P. Kolodner, in preparation.

[50] R. Z. Sagdeev, D. A. Usikov, G. M. Zaslavsky. Nonlinear physics from the pendulum to turbulence and chaos, Contemporary Concepts in Physics (vol. 4), Harwood Academic Publishers (1988).

[51] W. van Saarloos and P. C. Hohenberg. Phys. Rev. Lett. 64, 749 (1990); Physica D56, 303 (1992); Erratum: Physica D69, 209 (1993).

[52] S. Sanghi and N. Aubry. Interaction mode models of near wall turbulence, J. Fluid Mech. 247: 455-488 (1993).

[53] H. Segur. Who cares about integrability ?, Physica D 51: 343-359 (1991).

[54] L. Sirovich. Q. Appl. Math 5, 561 (1987) and references therein.

[55] L. Sirovich. Chaotic dynamics of coherent structures, Physica D 37: 126-145 (1989).

[56] S. Slimani, N. Aubry, P. Kolodner and R. Lima. Biorthogonal decomposition analysis of dispersive chaos in binary fluid convection, in: Bifurcation Phenomena and Chaos in Thermal Convection, Proc. of ASME Winter Annual Meeting 92, Anaheim (Ca), Nov. 9-13, 1992, eds. H. H. Bau, L. Bertram and S. A. Korpela. New York: ASME: 39-46 (1992).

[57] J. J. Stoker. Water waves, Pure and Applied Mathematics, vol. 4, Interscience Publishers, Inc., New York.

[58] G. B. Whitham. Linear and nonlinear waves, Pure and Applied Mathematics, a Wiley-Interscience Series of texts, Monographs and Tracts (1974).

[59] B. L. Winkler and P. Kolodner. J. Fluid Mech. 240, 31 (1992); K. D. Eaton, D. R. Ohlsen, S. Y. Yamamoto, C. M. Surko, W. Barten, M. Lucke, M. Kamps, and P. Kolodner, Phys. Rev. A 43, 7105 (1991).

[60] P. Kolodner, S. Slimani, N. Aubry and R. Lima. Physica D 85 (1995) 165-224.

IMAGE EVALUATION
TEST TARGET (QA-3)

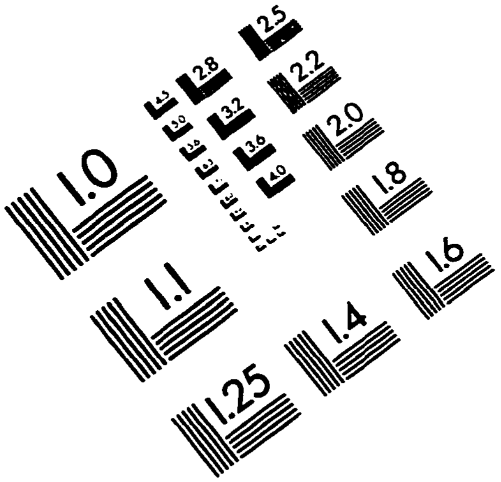

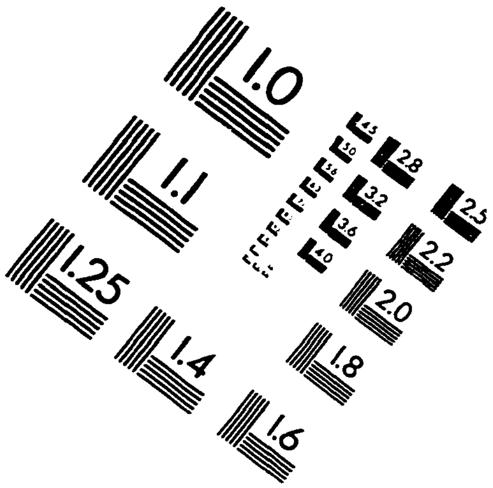

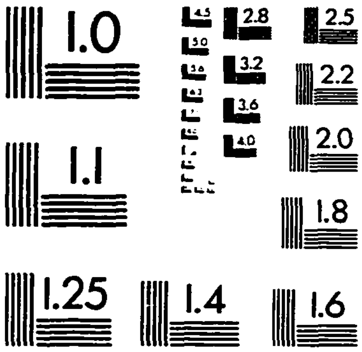

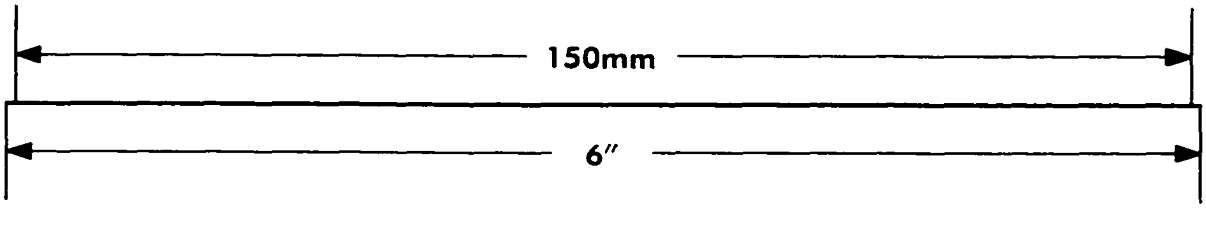

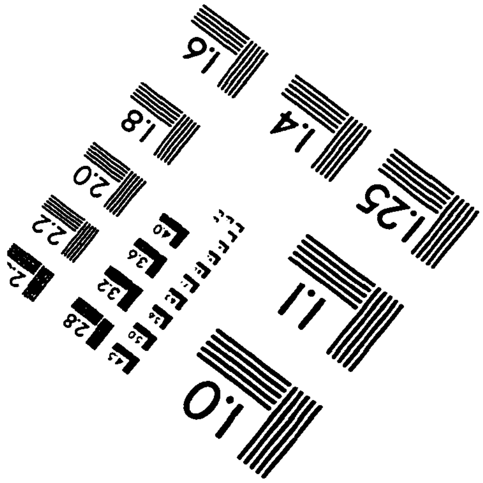

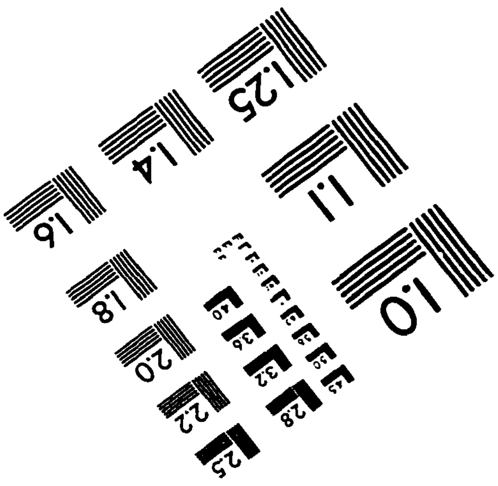

APPLIED IMAGE, Inc
1653 East Main Street
Rochester, NY 14609 USA
Phone: 716/482-0300
Fax: 716/288-5989